STRUCTURAL AND BIOCHEMICAL CHARACTERIZATION OF PROTEIN DRUG TARGETS FROM HUMAN PATHOGENS

Ph.D. THESIS

by

MADHUSUDHANARAO KATIKI

DEPARTMENT OF BIOTECHNOLOGY
INDIAN INSTITUTE OF TECHNOLOGY ROORKEE
ROORKEE - 247667, INDIA
AUGUST, 2018

STRUCTURAL AND BIOCHEMICAL CHARACTERIZATION OF PROTEIN DRUG TARGETS FROM HUMAN PATHOGENS

A THESIS

Submitted in partial fulfilment of the requirements for the award of the degree

of

DOCTOR OF PHILOSOPHY

in

BIOTECHNOLOGY

by

MADHUSUDHANARAO KATIKI

DEPARTMENT OF BIOTECHNOLOGY
INDIAN INSTITUTE OF TECHNOLOGY ROORKEE
ROORKEE – 247 667 (INDIA)
AUGUST, 2018

©INDIAN INSTITUTE OF TECHNOLOGY ROORKEE, ROORKEE- 2018
ALL RIGHTS RESERVED

INDIAN INSTITUTE OF TECHNOLOGY ROORKEE
ROORKEE

CANDIDATE'S DECLARATION

I hereby certify that the work which is being presented in the thesis entitled "**STRUCTURAL AND BIOCHEMICAL CHARACTERIZATION OF PROTEIN DRUG TARGETS FROM HUMAN PATHOGENS**" in partial fulfilment of the requirements for the award of the Degree of Doctor of Philosophy and submitted in the Department of Biotechnology of the Indian Institute of Technology Roorkee, Roorkee is an authentic record of my own work carried out during a period from July, 2012 to August, 2018 under the supervision of **Dr. Pravindra Kumar**, Associate Professor, Department of Biotechnology, Indian Institute of Technology Roorkee, Roorkee.

The matter presented in this thesis has not been submitted by me for the award of any other degree of this or any other Institution.

(MADHUSUDHANARAO KATIKI)

This is to certify that the above statement made by the candidate is correct to the best of my knowledge.

(Pravindra Kumar)
Supervisor

Date:

The Ph.D. Viva-Voce Examination of Mr. MADHUSUDHANARAO KATIKI, Research Scholar, has been held on ..... .

Chairman, SRC External Examiner

This is to certify that the student has made all the corrections in the thesis.

Supervisor Head of the Dept./Chairman, ODC

ABSTRACT

My Ph.D. research objectives mainly focus on the characterization of the structure-function relationships of few of the protein drug targets from human pathogens including multidrug-resistant gram-negative bacteria and protozoans that may direct us towards the development of novel, potential, broad-spectrum antimicrobials with new modes of actions or improved efficacy. Current human society is completely dominated by the MDR/XDR/PDR pathogenic bacteria and several other infectious agents for which there is dearth of treatment strategies (antibiotics/drugs/vaccines) and hence there is a demand for new drug molecules or vaccines with alternative modes of action or improved efficacy and characterization of new drug targets. As proteins are the driving horses of the cellular life of any living organism, it is a good idea to target the protein components (involving in the any of several essential metabolic/signaling/structural pathways) of the pathogen of any disease/infection. In this course of Ph.D. research, I have worked on three promising drug targets including two bacterial proteins enoyl-ACP Reductase (ENR) from *Moraxella catarrhalis* (*Mc*FabI) and Oxa-58 carbapenemase from *Acinetobacter baumannii*, and one protozoan protein deoxyhypusine hydroxylase (DOHH) from *Leishmania donovani*. *M. catarrhalis* and *A. baumannii* are known to cause severe nosocomial infections and several other pathological conditions. Several clinical strains of these two gram-negative pathogenic bacteria also exhibit resistance to many known classes of antibiotics and hence designated as multidrug-resistant bacteria. *L. donovani* causes visceral leishmaniasis (VL), the lethal form of leishmaniasis, in several economically poor countries and there are no parasite-specific drugs/vaccines. The proteins FabI and Oxa-58 are successfully characterized from the respective pathogens, using structural and biochemical techniques, and provided us with crucial structural information which may be useful in the development of novel structure based antimicrobial development. We are working on several methods to crystallize the *Ld*DOHH protein and it is structurally modeled, followed by the search for new structural compounds which may exhibit anti-leishmanial activity.

The bacterial type II fatty acid biosynthesis pathway, which is differing very much from the animal and human type I fatty acid biosynthesis pathway in its structural organization, has been validated to be a potential drug target pathway. All its catalytic steps are being catalyzed by individual proteins and many of these are proven as promising drug targets including the enoyl acyl carrier protein reductase (ENR). Moraxella catarrhalis is possessing the FabI (ENR I) isoform of the ENR and is a validated drug target against which many of the currently known

inhibitors including triclosan, isoniazid and diazaborines are exhibiting antimicrobial activities. In my current work I have structurally and biochemically characterized the FabI protein from *M. catarrhalis* (*Mc*FabI) to elucidate its structural elements essential for the substrate binding and catalysis, which can be subsequently exploited for the structure-based drug designing. The structure of the *Mc*FabI is obtained in its apo form and NAD and triclosan bound ternary complex form also. Virtual screening of the libraries of small druggable molecules was carried out using these structural features and obtained few lead molecules. We also observed that 17-β estradiol (E2), a human major female sex hormone, is also binding with higher score and energy, and hence we have characterized its interactions with the *Mc*FabI enzyme. The biochemical analysis revealed that E2 is potentially binding to this enzyme with a kD value of ~0.5 μM and inhibiting the enzyme activity with a ki value of 38.1 μM. E2 was also observed to be exhibiting antimicrobial properties against *M. catarrhalis*. These results altogether are indicating that the direct antimicrobial activities of E2 might be contributing to the sex differences in resistance to infectious diseases in many organisms, including humans, and supporting the fact that females are more resistant than their male counterparts.

The β-lactamase enzymes have been the major contributors of the antibiotic resistance in many of the multidrug resistance bacteria including *Acinetobacter baumannii*, one of the leading cause of nosocomial infections and deaths worldwide. Among these enzymes also, the carbapenem hydrolyzing class D β-lactamases (CHDLs) are the major concern in the context of constantly accelerating antimicrobial resistance, as they are able to hydrolyze the carbapenem antibiotics which have been the first line of defence against these MDR bacterial pathogens. *A. baumannii* is producing several groups of CHDLs including OXA-23, OXA-24, OXA-58 and OXA-48, and few others. In our current study, we are aiming at elucidating the active site elements that are crucial in facilitating the substrate recognition and subsequent catalysis. We determined the crystal structure of OXA-58 from *A. baumannii* (*Ab*OXA-58) in complex with one of the carbapenem mimetic 6α-hydroxymethyl penicillin (6α-HMP) and obtained a stable acyl-enzyme complex intermediate. Analysis of these structures revealed that the active site of OXA-58 is exhibiting great amount of plasticity during its substrate recognition and a hydrophobic bridge formed over the active site cleft is very crucial in the carbapenem substrate recognition and its hydrolysis. The structural analysis of the point mutation variants of *Ab*OXA-58 protein also revealed that the enzyme can use alternative active site residues to form the hydrophobic bridge in the absence of any of the earlier. These discoveries are very

important in understanding the carbapenem hydrolysis and helpful in designing structure-based inhibitors against these β-lactamase enzymes.

The hypusine biosynthesis pathway, participating in the posttranslational modification of a lysine residue on eukaryotic initiation factor 5A (eIF5A) leading to its maturation by having the hypusine residue, from many parasitic organisms was validated as a potential drug target. This pathway includes two enzymatic steps catalyzed by deoxyhypusine synthase and deoxyhypusine hydroxylase (DOHH), and both these enzymes are validated drug targets. Our study focuses on the characterization of the structural and biochemical elements of the DOHH enzyme from *Leishmania donovani* (*Ld*DOHH), a protozoan parasite responsible for causing many forms of leishmaniasis, including its most lethal form "visceral leishmaniasis (VL)", disease in humans and other animals. This enzyme was analyzed biochemically for its oligomeric forms in solution and secondary structural features. Crystallization trials were made rigorously to obtain its 3-dimensional structure and the protein was modelled using computational tools. The *Ld*DOHH model structure was analysed and used for virtual screening of small molecule libraries in search of new anti-leishmanial drug molecules. We found few hit compounds, including the compounds 43, 712 and 1366, and analysed for their binding modes and strengths, their interaction patterns and conformational stability in bound state. These analyses showed that these compounds were binding tightly in the active site and may be promising molecules for testing their anti-leishmanial activities.

ACKNOWLDGEMENTS

I take this great opportunity to thank and appreciate countless personalities who helped, guided, supervised, supported and encouraged me throughout the unforgettable journey of my Ph.D. course. It's the time to mention that during this journey I worked on many scientific projects, learnt on plenty of scientific concepts, got introduced to many unknown and unbelievable surprises of science, gained pretty good knowledge, enjoyed several aspects of professional and personal life, suffered and struggled several moments and finally survived this ever so enjoyable Ph.D. course.

First of all, I sincerely thank Prof. Pravindra Kumar for indispensable guidance, supervision, support and help from the day of joining until the last day of my Ph.D. course. I spent 6-year long period of time in his laboratory working on several projects under his invaluable guidance, which allowed me to learn many experimental and practical aspects of science which I hadn't experienced before. It's a great opportunity for me to work in his well-equipped and well-funded laboratory having instrumental facilities for all the needed experimental works of our projects. He encouraged and supported me throughout the course by involving in many projects on going in our laboratory and the regular weekend discussions were very much helpful in improving our experimental approaches towards fruitful results. He also provided us with several opportunities to interact with national and international scientists during the conferences and courses conducted under his leadership. I learnt several concepts of crystallography through discussions with Prof. Pravindra Kumar and they are very helpful for working in this field. His suggestions are always intellectual, encouraging, exciting and fruitful. I am very much obliged and thankful to him for all the help and support throughout the course.

I had also guidance from Prof. Shailly Tomar since the beginning of my Ph.D. course. I had training in the experimental parts of my Ph.D. projects and also learnt several aspects of Ph.D. course through constant discussions with her. I had been a part of weekend discussions with her for a long time and one way I should say that I had been supervised by her too. I also worked with her in the experimental maintenance of several instruments and learnt many concepts of designing and executing the biophysical experiments. I had a continuous help and support from her laboratory and students. I should sincerely thank her for all the help, support and encouragement from her throughout the course.

I had several scientific discussions with Prof. Ashwani Kumar Sharma who also helped and supported me throughout my Ph.D. course. He encouraged me at many points of the course which boosted me a lot to work efficiently and balancing many sides of the course. I learnt many concepts of biochemistry through the discussion with him. I had a lot of support and help from his laboratory and students which is unforgettable. I thank him sincerely for his continuous encouragement, help and support.

I express my gratitude to Prof. Ramesh Chandra for being kind and helpful throughout my Ph.D. course. I had been in his contact from the beginning of the course and being a member of my student research committee, I had discussions with him several times in regard of my projects. I had good interaction with him in regard of the instruments' maintenance at MCU lab, IIC and I should be very thankful to him for providing us with a comfort stay during the course.

I am obliged to Prof. RP Singh who helped me a lot at several points of the course. Being the chairman of my student research committee, he used to initiate enthusiastic discussions during all my presentations, as part of the course evaluation, that are very helpful in improving my projects and experiments further. His evaluations and suggestions during these presentations are very reasonable, intellectual and fruitful. I sincerely thank him for all the suggestions, encouragement and support.

I had so much help and support from Prof. Partha Roy. Being a member of my student research committee, he is very much encouraging and supportive, and he used to suggest me several insights into my experiments. His discussions during the presentations of my course evaluation are highly valuable and helpful. I express my sincere gratitude for his help throughout the course.

I should be thankful to Prof. Kiran Srinivas Ambatipudi for being a source of constant help, support and encouragement. I participated in intense discussions with him in regard of few projects carried out in collaboration and learnt many new concepts of mass spectrometry other areas of biotechnology. I could also spend time with him talking in my mother tongue which used to give me immense pleasure and recreates me a lot. I am very grateful to him and thank him sincerely for all the support and inspiration.

I had help from Prof. Rama Krishna Peddinti, Dept. of Chemistry, also. I visited him several times to do experiments in collaboration with him and had very exciting discussions. He is very much kind and helpful, and I had many suggestions in regard of the experimental proceedings

of those collaborative projects. I had help and cooperation from his laboratory and students as well. I am very much thankful to him for all the support and help.

I sincerely thank Prof. D. Golemi-Kotra and Prof. Madhubala Rentala for their kind help and support in the collaborative projects. I learnt many scientific lessons while workibg on these projects.

I am very obliged and thankful to Prof. R. Rukkumani for her guidance and during my M.Sc. course at Pondicherry university. I am sincerely grateful to Mr. Kasinaidu Reddy for being the mentor of my career since my childhood. He is the one who introduced me to the educational society and taught me many lessons of life.

I am very thankful to Dr. Deepak Patil, Dr. Shivendra Pratap, Dr. Aditya Dev, Dr. Pramod Kumar, Dr. Sonali Dindwal, Dr. Manju Narwal, Dr. Satya Tapas, Dr. Megha Aggrawal, Dr. P. Selva Kumar, Dr. Vivekanand, Dr. Prabat Tomar, Dr. Nidhi Sharma, Dr. Anamika Singh, Dr. Preeti Verma, Dr. Pradeep Kumar, Dr. Paramesh Lambadi, Dr. Rajinikant Sharma, Dr. Supriya Patil, Dr. Tapas Bhattacharya, Dr. Umesh and Dr. Santosh Kumar, for their unconditional help, support and love since the day-1 of my course.

I should be always thankful to my beloved friends Snehasish Das, Alok Patel, Rajat Mudgal, Atin Sharma, Tomagna Ghosh, Shailendra Singh Kichi and Rajesh Sharma.

I am grateful to all my lab members and friends Vijay Kumar Sharma, Harvijay Singh, Anchal Sharma, Neha Singh, Ramanjit, Rakesh, Pooja Kesari, Anjali Malik, Benazir Fatma, Neetu, Poonam Dhankad, Vikram Dalal, Jai Krishna Mahto, Monica Sharma, Vishakha Singh, Akshay Parik, Vedita Singh. Their support is crucial in achieving my objectives.

I have to be very much grateful and thankful for the constant support from Dr. Shivendra Pratap and Ms. Neetu, who helped me in every possible way throughout the course. These two are my immediate helping hands from whom I could expect help at any point of time. I learnt so many scientific lessons from Dr. Shivendra Pratap and had a brotherly support from him. I will be always thankful to him and Ms. Neetu.

I thank Zia Tariq, Kiran Kumar, Deepesh, Ankit Verma, Sachin, Ankit Kushwal, Shahid Alam, Nandita Bodra, Kanika Gupta and Shubham Dubey for their help and support.

I thank all my friends Sai Venkatesh, Chinna Rao, Eswar Reddy, Suresh, Dr. Appala Naidu Srinivas, Nishank Reddy, Anil Kumar, Venkatesh, Indumati Patta, Laxmi and Onnur Reddy for being my good friends during my career.

I also thank Priyanka Priyadarshini, Deepshika and Satakshi for being my good colleagues.

I thank the staff of Biotechnology department for their constant support.

I am always in debt of my parents Shri. Krishna and Shrimati. Parvathi for their endless love and every possible thing they are doing for me. I am because of them. I thank my brother Venkatesh and all family members whose support was unconditional throughout my career till date. I am grateful to Narannaidu Katiki, Simhachalam Marisarla, Siva Reddy and Jairam for being my close friends since my childhood, without whom my journey till Ph.D. couldn't possible. I thank my village Bhagemmapeta and fellows for their love, memories, inspiration and encouragement in my life.

I thank IIT Roorkee for supporting me financially and all the platforms and facilities it provided me for my 6-long year Ph.D. journey.

Madhusudanarao Katiki

LIST OF PUBLICATIONS

Garima S, **Katiki M**, Sankar P, Rukkumani R (2012). "Antihyperglycaemic and antihyperlipidaemic effect of wheatgrass on streptozotocin induced type 2 diabetic rats". J. Pharm. Res. 5, no. 5 (2012): 2580-2583.

Pratap S, **Katiki M**, Gill P, Kumar P, Kotra DG (2016). "Active-Site Plasticity Is Essential to Carbapenem Hydrolysis by OXA-58 Class D β-Lactamase of *Acinetobacter baumannii*." Antimicrobial Agents and Chemotherapy 60, no. 1 (2016): 75-86.

Neetu, Sharma A, Kesari P, **Katiki M**, Kumar P, Kumar P (2016). "Purification and characterization of 11S globulin from Kutaj (*Holarrhena antidysenterica*)." Journal of Proteins Proteomics 7, no. 4 (2016): 297-303.

Kesari P, Neetu, Sharma A, **Katiki M**, Kumar P, Gurjar BR, Tomar S, Sharma AK, Kumar P (2017). "Structural, Functional and Evolutionary Aspects of Seed Globulins." Protein and Peptide Letters 24, no. 3 (2017): 267-277.

Kumar P, Kesari P, Dhindwal S, Choudhary AK, **Katiki M**, Neetu, Verma A, Ambatipudi K, Tomar S, Sharma AK, Mishra G and Kumar P (2017). "A novel function for globulin in sequestering plant hormone: Crystal structure of *Wrightia tinctoria* 11S globulin in complex with auxin." Scientific Reports 7, Article number: 4705 (2017).

Katiki M, Neetu, Pratap S, Kumar P. Studies on FabI from *Moraxella* uncovered new insights into estradiol's direct antimicrobial actions which may contribute to sex differences in resistance to infections. (Under communication).

Katiki M, Neetu, Pratap S, Kotra DG, Kumar P. Structural studies on OXA-58 point mutants from *Acinetobacter baumannii* revealing the alternative mechanisms exploited for achieving β-lactam hydrolysis even in the presence of the point mutations of the known catalytic residues. (Manuscript in preparation).

Paper/Poster Presentations and Participation in International and National Conferences

Participated in the International conference on Biomolecular forms and functions, a celebration of 50 years of the Ramachandran map (2013), Indian Institute of Sciences, Bangalore, India.

Participated in the 42nd National seminar on crystallography and International Workshop on Application of X-ray Diffraction for Drug Discovery (NSC-42) (2013), Jawaharlal Nehru University, New Delhi, India.

Katiki M, Kesari P, Gupta K, Madhubala R, Tomar S, Kumar P (2014) Characterization of Deoxyhypusine Hydroxylase as a drug target for visceral leishmaniasis caused by *Leishmania donovani* using computational methods, International Conference/Workshop on Recent advances in structure biology and drug discovery (RASBDD-IITR-2014), Indian Institute of Technology Roorkee, India.

Katiki M, Pratap S, Gill P, Kotra DG and Kumar P (2016). Crystal structure of OXA-58 class D β-Lactamase of *Acinetobacter Baumannii* in complex with carbapenem mimetics revealing the active site structural elements essential for carbapenem hydrolysis by this enzyme, International conference and workshop on structure-based drug designing and applications to infectious diseases, University of Hyderabad, India.

Katiki M, Pratap S, Gill P, Kotra DG and Kumar P (2016). Structural studies on OXA-58 of *Acinetobacter Baumannii* revealing the active site structural elements essential for carbapenem hydrolysis by this enzyme, 44th National seminar on crystallography (NSC-44) IISER Pune, India.

CONTENTS

PAGE NO.

LIST OF FIGURES

LIST OF TABLES

LIST OF ABBREVIATIONS

6αHMP	6α-hydroxymethyl penicillin
6αHOP	6α-hydroxyoctyl penicillin
ACP	Acyl carrier protein
AGE	agarose gel electrophoresis
AKR superfamily	Aldo-keto reductase protein superfamily
Ala	alanine
APS	Ammonium persulfate
BLAST	Basic local alignment search tool
BME	β-mercaptoethanol
BSA	bovine serum albumin
BPB	bromophenol blue
CBB	Coomassie brilliant blue
CCA	Crotonyl coenzyme A
Ccp4i	Computational collaborative project 4
CD	Circular dicroism
Cfu	Colony forming units
CHDLs	Carbapenem hydrolyzing class D β-lactamases
CLSI	Clinical and Laboratory Standards Institute
DHS	Deoxyhypusine hydroxylase
DTT	Dithiothreitol
DOHH	Deoxyhypusine hydroxylase
DSC	Differential scannniing calorimetry
ENR	Enoyl acyl carrier protein reductase
ESBL	Extended spectrum β-lactamase
EST	Estradiol
EtBr	Ethidium bromide
FAB	Fattyacid biosynthesis
FPLC	Fast performance protein liquid chromatography
Fs	Femto seconds

GPU	Graphical processing unit
GnHcl	Guanidine hydrochloride
HBS	HEPES-buffered saline
HE motif	Histidine-Glutamate motif
Hrs	Hours
HSDs	Hydroxysteroid dehydrogenases
H-bonds	Hydrogen bonds
IP	Image plate
ITC	Isothermal titration calorimetry
kDa	Affinity constant
K_M	Michaelis Menten constant
KPSI	kilopounds-force per square inch (cell disruption pressure)
LGA	Lamarckian genetic algorithm
LB broth	Luria Bertani broth
LPG	Lipophosphoglycan
LN2	Liquid nitrogen
Lys	Lysine
MDR	Multi-drug resistance
MD simulation	Molecular dynamics simulation
Met	Methionine
MH broth	Muller Hinton broth
MIC	Minimum inhibitory concentration
mL	Millilitre
mm	Millimeter
mM	Millimolar
mns	Minutes
Molrep	Molecular replacement
MWCO	Molecular weight cutoff
NADH	Nicotinamide adenine dinuceotide reduced
NPT	Constant Number of particles, Pressure and Temperature
ns	Nano seconds
NTA	Nitrilo tri acetic acid
NVT	Constant Number of particles, Volume and Temperature

ORF	Open reading frame
OXA	Oxacillinase
PDR	Pan-drug resistance
PME	Particle mesh Ewald
PBS	Phosphate-buffered saline
PCR	Polymerase chain reaction
PDB	Protein data bank
PEG	Polyethylene glycol
pbc	Periodic boundary condition
Phe	Phenyl alanine
RNS	Reactive nitrogen species
ROS	Reactive oxygen species
RLPG	Receptor-Ligand Pharmacophore Generation
Refmac	Macromolecular refinement
RMSF	Root mean square fluctuation
RMSD	Root-mean-square displacement
Rpm	Revolutions per minute
RSR	Real space refinement
RSRZ	Real space refinement zone
RU	Response units
SDR superfamily	Short-chain dehydrogenase reductase superfamily
SDS-PAGE	Sodium dodecyl sulfate-polyacrylamide gel electrophoresis
Ser	Serine
Spc	Simple point charge
SP	signal peptide
SPR	Surface plasmon resonance
TCL	Triclosan
TEVP	Tobacco Etch virus protease
TLS	Translation-libration-screwmotion refinement
Trp	Tryptophan
Tyr	Tyrosine
UV	Ultra-violet

V	volts
V_{max}	Maximum velocity
Val	Valine
μL	Microlitre
XDR	Extensive-drug resistance

CHAPTER 1

Review of Literature

1.1. Introduction:

1.1.1. Humans' cohabitation with microbes:

The cohabitation of human beings with the microbes can be categorized among the variety of ecological relationships of living organisms of the ecosystem (biome) on this planet earth, depending on the microbial partner, including commensalism, mutualism and parasitism. All the types of microbes spending living relationship with human beings are collectively defined as human microbiome [(human microbiota), (human flora)] and these microbes include viruses, bacteria, protists and fungi, among which many are commensals or mutualistics, while few are parasites.

1.1.2. Evolution and survival among the living forms of ecosystem:

The driving force of the evolution and survival among living forms is the common goal to achieve the nature's measurements of the natural selection by qualifying its acting/working principle of the "Survival of the fittest", which was explained, as the mechanism of natural selection, by Darwin, in the Darwinian evolutionary theory. In order to qualify the natural selection through "Survival of the fittest" principle, living forms compete for the limited space and energy sources available on this lone living planet; and this competition maybe intra-specific or inter-specific. The microbes grow rapidly and multiply at very high rates, which demands a never-ending (continuous) need for high amounts space and energy sources. As a consequence, they try to inhabit and occupy every space and energy source, living or non-living, available in their surroundings and encountered in their way; and also make several types of living relationships with the living sources of space and energy. If they encounter any resistance from the surrounding living-forms, a form of space and energy source for microbes, while inhabiting and making relationships with them, the microbes try to harm and parasitize them by causing physical damage including diseases as a mechanism of offence.

The humans, although belonging to the higher orders of living kingdom and dominating the current ecosystem, are also major victims of this microbial offence. The human body, including most of its component cells, tissues, organs, organ systems and biofluids, is serving as a predominant source of space and energy for microbes; and it hosts 3 times of non-human cells

to human cells (1). Major portion of these non-human cells include commensal and mutualistic microbes comprising the normal flora (normal microbiota), while the rest constitutes human pathogenic parasites.

113. Human pathogens and infectious diseases:

Humans are surrounded by countless types of infectious agents including prions, viruses, bacteria, protists and fungi. The list of pathogens causing infectious diseases in humans is endless as new strains are emerging constantly with new abilities and advanced virulence factors (2). Bacteria and viruses are the major groups of human pathogens and the list of human pathogens and infectious diseases is always get updated with the time by several worldwide health organizations including the world health organization (WHO). The human infections can be classified into several groups based on different factors (3), including the causative agent of the infection (viral, bacterial, fungal, protozoan), environmental source (soil, air, vector, animal, hospital), the duration of infection (acute, chronic), the geographical spread of infection (epidemic, endemic, pandemic) and the body locality of infection (systemic, local). Currently ESKAPE group of pathogens (*Enterococcus faecium*, *Staphylococcus aureus*, *Klebsiella pneumoniae*, *Acinetobacter baumannii*, *Pseudomonas aeruginosa*, and *Enterobacter* species) (4), nosocomial infections (5) and the neglected tropical diseases (NTDs) (6, 7) are few of the major concerns of the modern human society.

1.1.4. Human defenses to infectious diseases:

The current human society is facing a constant threat of infectious diseases which occasionally erupts into epidemics and endemics. The unwanted parasitic relationship of few microbes is constantly fought by the defense systems of human body, which majorly includes the immune system (8). But the microbial parasites try to overcome the human defenses by causing diseases and physically damaging its defense components and rest body components. We also treat the infections by using the antibiotics/antimicrobials, discovered by humans, with potential biocidal effects against those human pathogens (9-10). These antibiotics can be natural or synthesized and may be with narrow-spectrum or broad-spectrum actions.

1.1.5. Microbial resistance to human defenses:

The human body tries to defend itself from the potential harm and diseases by using its native immune system, but the microbial pathogens try to evade the host defence components by several mechanisms. Even for the non-native (external) defence mechanisms including the

antibiotics, antimicrobials, drugs, vaccines, and immunotherapeutics used by the human hosts to treat infections/diseases; the pathogens started developing resistance in several ways. The resistance of microbes to human's external defence mechanisms including the antibiotics and several classes of antimicrobials is generally called as "antimicrobial resistance (AMR)" or "antibiotic resistance (ABR)" (11-12). Depending on the extent of resistance exhibited by these microorganisms, AMR is classified into several classes including multidrug-resistant (MDR), extensively drug-resistant (XDR) and pandrug-resistant (PDR) according to the international standard definitions (13). The infectious agents cause diseases, through certain virulence factors including toxins and host metabolic enzymes' inhibitors, as a foremost level offence against human body when they face resistance for their spatial colonization or energy source utilization from the human cells/tissues/organs/organ systems. The microbial pathogens escape the host native defence, the immune system, by modulating/masking their cellular surface antigens, as a first level of resistance towards the host defences. The infectious agents also defend the non-native defence strategies of the human host including antibiotics/ antimicrobials/ drugs/ vaccines/ immunotherapeutics, through several macromolecular components including antibiotic-degrading enzymes and drug-efflux pumps, as a second level of resistance (14-15).

These drug-resistant strains of pathogens are mostly occurs in the hospital environments, but also spreading in the human communities (i.e. residential areas) (16). Hence it's a growing concern for the current day human society, as the antimicrobials available are very limited and in fact dwindling due to constantly increasing drug-resistance and lack of new drugs' discovery (16). It's also an acceptable truth that discovery/development of new drugs/anti-infactives, vaccines and diagnostic tools is also a major drawback in the management of infections due to drug-resistant pathogens.

The multi-drug resistant gram-positive bacteria including Staphylococcus aureus and Enterococci, especially the methicillin-resistant S. aureus (MRSA) (17), vancomycin-resistant S. aureus (VRSA) (18) and vancomycin-resistant Enterococci (VRE) (19), have been the major concern of infection control and only area of focus for the new antimicrobial discovery for a long time until the neglected drug-resistance threat from gram-negative bacteria was recognized (20).

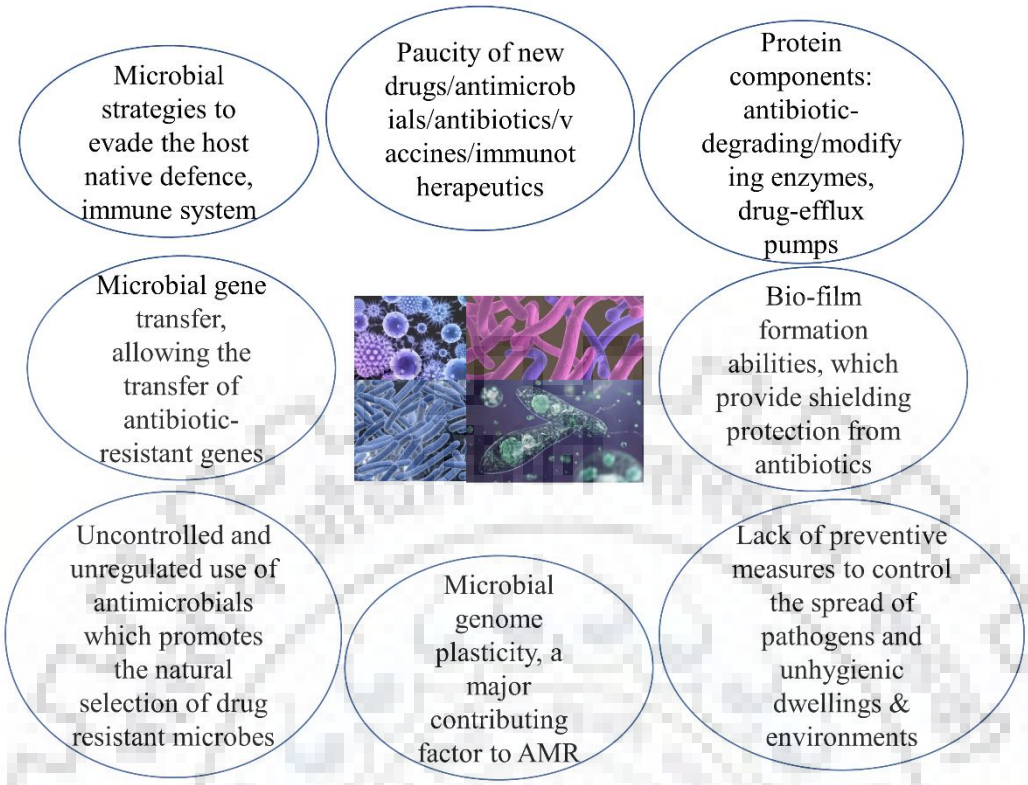

Figure 1.1: Major factors contributing to antimicrobial resistance (AMR).

1.1.6. Human strategies to overcome the antimicrobial resistance:

Humans are constantly accelerating their efforts to innovate novel antimicrobial molecules by using advanced technologies (21-22). These novel molecules may be with improved antimicrobial efficiencies, extended broad-spectrum activities, novel modes of inhibition mechanisms, decreased side effects and cost-effective (23-24). Humans employ several types of drug discovery tools to invent new antimicrobials, including structure-based drug discovery (SBDD) tools (25-26) [computer-aided drug discovery (CADD) (27-28), fragment based drug designing (FBDD) (29-31) and ligand based drug designing (LBDD) (32-33)], synthesizing novel groups of small molecules, finding new drug targets, searching and screening the libraries of natural compounds, modifying the existing antimicrobials, combinatorial therapies, immunotherapies, repurposing the existing drugs and using the metagenomics tools and many other microbiology tools to dig the natural sources (34).

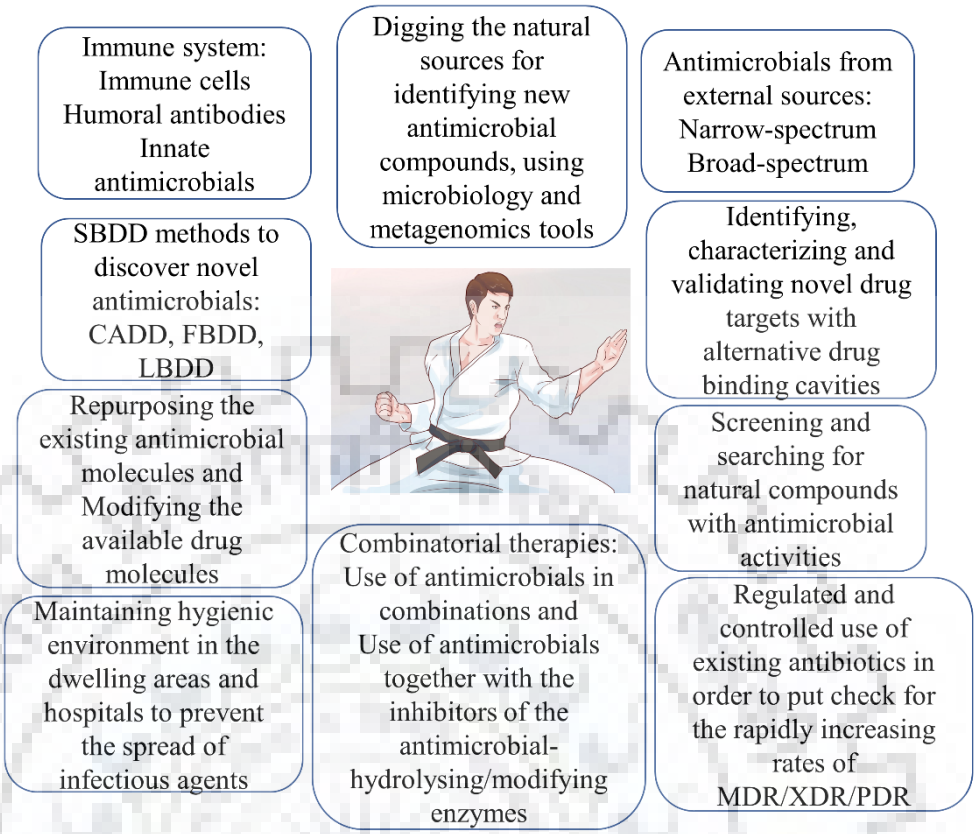

Figure 1.2: Human defence mechanisms to fight the antimicrobial resistance (AMR).

1.2. *Moraxella catarrhalis* infections in humans:

Moraxella catarrhalis is a fastidious, gram –negative, aerobic diplococcus bacterium. It is a human restricted opportunistic respiratory tract pathogen (35-37). It predominantly occurs in hospital environments and causes several nosocomial infections (38-39). It morphologically resembles the commensal *Neisseria* species and hence used to be called as *Neisseria catarrhalis*. Taxonomically it was been assigned to several taxa including *Micrococcus catarrhalis*, *Neisseria catarrhalis*, *Branhamella catarrhalis* and *Moraxella catarrhalis* (40-41). Finally, it is ended up and popularly called with the taxonomic name *Moraxella catarrhalis*. It used to be thought of *M. catarrhalis* as an upper respiratory tract communal, but since late 1970s it has been established that it is a common respiratory tract pathogen. It is one of the common causes of otitis media (OM) in infants and children, and exacerbations of chronic obstructive pulmonary disease (COPD) in adults; which are the two most common infectious diseases caused by this pathogen (42-44). It is also responsible for several other community-acquired infections including pneumonia (45-46), bacteremia (47-49), sepsis (50-51), sinusitis

(52-53), meningitis (54-56), bacterial conjunctivitis (57) and few other invasive infections. Its transmission majorly occurs through nosocomial modes in hospitals among patients.

1.2.1. Otitis media (OM):

M. catarrhalis, along with another two associated respiratory tract pathogens *Streptococcus pneumoniae* and nontypeable *Haemophilus influenzae*, is one of the predominant causes of acute otitis media (AOM) and is responsible for an approximately 15-20% of the AOM episodes (35, 41). Its clinical symptoms include fever and red bulging of tympanic membrane, and its diagnosis involves tympanocentesis, a gold standard for etiology determination (58). If children experienced more than 4 episodes of AOM or 8 months of middle ear effusion in an year are said to be otitis prone and are confirmed with "recurrent OM or OM with effusion (OME)" if they possess middle ear fluid without any clinical signs of AOM. Otitis prone children frequently experience conductive hearing loss which may subsequently causes delays in speech and language development. *M. catarrhalis* frequently causes OME than AOM (59-60).

1.2.2. Chronic obstructive pulmonary disease (COPD):

According to the known etiology records, 50% of the COPD exacerbations are caused by the bacterial infections, including the *M. catarrhalis* infections also, while the rest by viral infections and noninfectious causes (61-63). The COPD exacerbations due to *M. catarrhalis* infections include the symptoms of dyspnea, fever, fatigue, rhonchi, sputum production and purulence and decreased air entry (35, 61). *M. catarrhalis* also found in the distal airways of lower respiratory tract and new strains of this pathogen observed with many episodes of COPD exacerbations in case of adults (39).

1.2.3. Hospital- and community-acquired infections by *M. catarrhalis*:

Several nosocomial and community-acquired infections including pneumonia, bacteremia, septicemia, sinusitis, meningitis, endocarditis, cellulitis, septic arthritis and few other invasive infections, are also known to be caused by *M. catarrhalis* (35-39). Approximately 20% of the acute bacterial sinusitis is known to be caused by *M. catarrhalis* in children, while very few cases in adults, and are clinically indistinguishable from that caused by *S. pneumoniae* and *H. influenza* (52-53). It causes pneumonia in elders suffering from cardiopulmonary diseases and rarely bacteremic illness.

1.2.4. *M. catarrhalis* pathogenesis:

M. catarrhalis, along with *H. influenza*, *Pseudomonas aeruginosa* and *S. pneumonia*, is a common pathogen associated with multiple pulmonary diseases. The seroresistant lineage of *M. catarrhalis* is known to be strongly associated with the virulence of this pathogen (64-65). Migration of *M. catarrhalis* from their usual colonization spot of nasopharynx to the middle ear through Eustachian tube and acquisition of new strains are the crucial events in the pathogenesis of otitis media (OM) and exacerbations of COPD by this pathogen (35, 66). The virulence-associated phenotypes and genotypes vary greatly among the strains found in children/infants from that of adults. Several kinds of adhesins, from its outer membrane, are known to participate in the adherence of *M. catarrhalis* strains to the respiratory tract epithelial cells, which is the initial and crucial step in its colonization and subsequent infection (67-71). These adhesins help the pathogen to hack the host extracellular matrix and avoid the bullets of host immune system that try to clear the pathogen along with the mucus, by directly binding to the patches of matrix through its components such as collagen, laminin, fibronectin and vitronectin or indirectly adhering to the epithelial cells via their binding to the same set of matrix components (72-73). The membrane vesicles (MVs), released by the pathogen during its infection to host macrophages, dampen the immune responses, triggered by the MVs released by those host macrophages, and enhance the pathogen adherence and survival (74).

It was discovered that *M. catarrhalis* also invades the bronchial epithelial cells and type2 alveolar cells to spend an intracellular life, although it's been thought to be an exclusively extracellular pathogen. And it also present intracellularly in the pharyngeal lymphoid tissue, which provides a potential reservoir for its persistence in the human respiratory tract (35).

1.2.5. Colonization by *M. catarrhalis*:

It usually colonizes the human upper respiratory tract and rarely the lower tract components, and human respiratory tract is its major ecological niche. Its colonization follows an age dependent pattern which is observed to be high and common in infants and children (nasopharyngeal colonization), while lower in adults (70, 75). The colonization patterns also changes based on few other several factors including pneumococcal vaccination (the use of pneumococcal conjugate vaccines) and rates of otitis media. Few *M. catarrhalis* strains colonize the lower respiratory tract in case of adults with COPD and they secrete highly inflammatory antigens into the airways which subsequently cause airway inflammation, the hallmark of COPD (76-77).

1.2.6. *M. catarrhalis* biofilms:

M. catarrhalis has the ability to form biofilms which confers greater amounts of resistance towards several classes of antibiotics and human immune defences (78). It usually produces biofilms in the middle ears of children with OM and majorly account for the recurrent and chronic OM. Although *M. catarrhalis* biofilms were found in the middle ear fluids, their role in pathogenesis is yet to be investigated (79-80). *M. catarrhalis* strains also participate in the microbial biofilm formation in the sinus tissue in patients with chronic rhinosinusitis with nasal polyposis (CRSwNP) infection (35, 81).

1.2.7. Current treatments available against *M. catarrhalis* infections:

It involves treating the individual symptoms of *M. catarrhalis* infections observed with patients, and follow the WAW (wait and watch) approach. The current treatment methods majorly involve the use of several oral antibiotics, including fluoroquinolones, 2nd and 3rd generation cephalosporins, macrolides, tetracyclines, and amoxicillin-clavulnate, for which the *M. catarrhalis* strains haven't developed resistance yet (82-84). The fluoroquinolones used for treating *M. catarrhalis* infections include sitafloxacin, tosufloxacin, levofloxacin and garenoxacin; while the extended-spectrum cephalosporins include cefixime, cefuroxime, loracarbef, cefaclor and cefpodoxime; and the macrolides include azithromycin, erythromycin and clarithromycin (85-88). The combinatorial therapy, including amoxicillin-clavulnate and trimethoprim-sulfamethoxasole, is also being used successfully to treat the infections due to drug-resistant *M. catarrhalis* strains. Amoxicillin-clavulnate and levofloxacin were also proven to be potent antibiofilm agents that can significantly reduce/inhibit the biofilm formation by *M. catarrhalis* strains (89-93).

1.2.8. Vaccination against *M. catarrhalis* infections:

Vaccines are the major alternative options to prevent the emergence of multi/extended/pan-drug resistance in *M. catarrhalis* strains, due to the currently increased use of antibiotics to treat its infections. Currently there is no licensed vaccine available for *M. catarrhalis*, but many promising candidate vaccine antigens are in final stages of clinical trials, while few others are in final stages of development (94-95). At present, the conjugate vaccines, including pneumococcal conjugate vaccines (PCVs) and PHiD-CV, are only used for treating the clinical *M. catarrhalis* strains during its infections (96-97). Maternal immunization of pregnant women is proposed to be an effective strategy to protect the infants from the respiratory tract infections,

including the OM due to *M. catarrhalis* in infants (97-98). The usual route of vaccination trials is subcutaneous.

1.2.9. *M. catarrhalis* resistance to human immune defences:

M. catarrhalis employs multiple mechanisms to evade the host innate immune defences, among which complement inactivation plays major role in conferring resistance to human serum (35, 67-68, 99-100). The adhesins produced by *M. catarrhalis* strains to bind to the host extracellular matrix and epithelial cells also play major roles in pathogen escape from its clearing, along with the mucus, from the host respiratory tract, by the host immune reactions (67-73). The membrane vesicles (MVs) released by the pathogen during its infection, also dampen the host immune responses and enhance its adherence and survival (74).

1.2.10. Antimicrobial resistance in *M. catarrhalis*:

1.2.10.1. Resistance to β-lactams:

M. catarrhalis strains acquired BRO-1 and BRO-2 types of β-lactamases at very early times of antibiotic resistance era, but remained susceptible to many of the rest antibiotic classes till date (101-103). It was discovered long time back that *M. catarrhalis* is resistant to penicillins, including ampicillin, and 1st generation cephalosporins. These β-lactamases render > 95% of *M. catarrhalis* clinical strains resistant to ampicillin (104-106).

1.2.10.2. Resistance to fluoroquinolones:

Among the fluoroquinolones used for the treatment, *M. catarrhalis* strains developed resistance towards levofloxacin, while susceptible to rest (107-108). Fluoroquinolones resistance mechanism in *M. catarrhalis* involves mutations in the quinolone resistance-determining region (QRDR) of GyrA and GyrB, the DNA gyrase protein subunits, and ParC and ParE, the topoisomerase IV protein subunits, and certain multi-drug efflux pump systems that cause reduced accumulation of fluoroquinolones in the cells (109-110).

1.2.10.3. Resistance to colistin and polymixins:

Resistance to colistin and polymixins, the last-resort antibiotics, is also identified in *M. catarrhalis*. This intrinsic colistin resistance (ICR) is known to be rendered by the chromosomally encoded lipid A phosphoethanolamine transferases (PEtN), whose crystal structure also reported from *M. catarrhalis* (ICR-Mc or ICR^{Mc}) recently this year (111-112).

Plasmid-borne mobilized colistin resistance (MCR-1/2) elements also reported from this pathogen (113).

1.2.10.4. Resistance to macrolides:

Decreased susceptibilities of *M. catarrhalis* strains to the macrolides including azithromycin, clarithromycin and erythromycin were reported from different parts of the world and majorly from China mainland (114-116). Increased prevalence of marolide-resistant *M. catarrhalis* strains has been reported in recent years from the Mainland China. There were two clonal complexes (CCs) CC363 and CCN10 reported, from China, to be the drug-resistant clones possessing the highly concentrated macrolide-resistant clinical *M. catarrhalis* strains (117-120).

M. catarrhalis strains, at present time, are relatively not resistant to many classes of antibiotics, but the constantly increasing use of antibiotics in the current times is posing inevitable emergence of extensively drug-resistant (XDR) and pandrug-resistant (PDR) strains of this human pathogen (106-118).

1.2.11. Current progress in drug discovery and vaccine development for *M. catarrhalis* infections:

Vaccine development for treating *M. catarrhalis* infections is very challenging and limited, due to the fact that many respiratory diseases caused by *M. catarrhalis* strains, including otitis media (OM) and exacerbations of COPD, are polymicrobial diseases which usually include co-infection with other major pulmonary tract pathogens nontypeable *H. influenzae* (NTHi) and *S. pneumonia*, and also the OM-associated respiratory viruses (121-125). *M. catarrhalis* vaccine development has also lagged behind that for NTHi and *S. pneumonia*, the other two common causes of OM and exacerbations of COPD (126-128). The lack of good animal models for *M. catarrhalis* further complicates this challenge of vaccine development against its clinical strains, although chinchilla been shown a novel promising animal model for testing *M. catarrhalis* vaccine antigens, and as the mouse pulmonary clearance model, the widely used animal model for assessing vaccine antigens of *M. catarrhalis*, does not simulate the human respiratory diseases and the protective response observed with this model is not yet been correlated with protection in humans (129-131).

Several anti-biofilm drugs and therapies are also in development stage (132). At present many vaccine candidates, including several types of adhesins, surface molecules and porins, to treat clinical *M. catarrhalis* strains are in their development stage (133-137).

Several drug discovery tools are in use for finding novel antimicrobials and drug targets from *M. catarrhalis* including high-throughput screening (HTS) and CADD/SBDD/LBDD/FBDD tools. Many drug targets including fatty-acid synthesis, DNA replication, protein modification, protein elongation, protein termination, RNA elongation, cell division, glycolytic pathway, amino-acid synthesis, protein secretion, cell-wall synthesis, tRNA synthetases and whole-cell antibacterial assays are being used for antibiotic discovery against *M. catarrhalis* infections (138-142). Several other techniques including combination therapy, repurposing the old antibiotics and medication strategies are also being employed in optimizing the drug discovery approaches (143-147).

1.2.12. Fatty acid biosynthesis pathway as drug target:

Fatty acid biosynthesis occurs through 2 different systems in humans and bacteria with the major structural differences in their component enzymes (148-149). In humans, fungi and higher order animals it occurs through the type I fatty acid biosynthesis pathway which is catalyzed by a single large polypeptide, containing the catalytic/functional domains for catalyzing all the individual steps of the pathway, called fatty acid synthase-I (FAS-I). While, in bacteria (prokaryotes) and plants it occurs by type II fatty acid biosynthesis pathway which is executed by the individual enzymes catalyzing the individual steps and called as fatty acid synthase-II (FAS-II), which is also known as dissociated type II FAS systems (Figure 1.3) (150-154). Very few organisms, having the need for the synthesis of specialized fatty acid compounds like mycolic acids, express both types of fatty acid biosynthesis systems including *Mycobacterium tuberculosis*, *Toxoplasma gondii* and *Eimeria tenella*. However, the type I FAS that occurs in microbes is called as microbial type I FAS and in animals it is the animal/mammal type I FAS, which significantly exhibit structural and localization/compartmentation differences (155-156). Microbial FAS-I, also called as the bacterial FAS-I family, is narrowly distributed within the Actinomycetales genera *Mycobacterium*, *Corynebacterium* and *Nocardia*, and is still poorly understood (157-158). The FAS-I enzymes can have all of the active sites present in a single protein (as in mammals and mycobacteria) or split between two interacting proteins (as in fungi and *Corynebacterium ammoniagenes*). These extensive differences in the structural organization of the FAS component enzymes can be exploited for antimicrobial drug discovery (159-160).

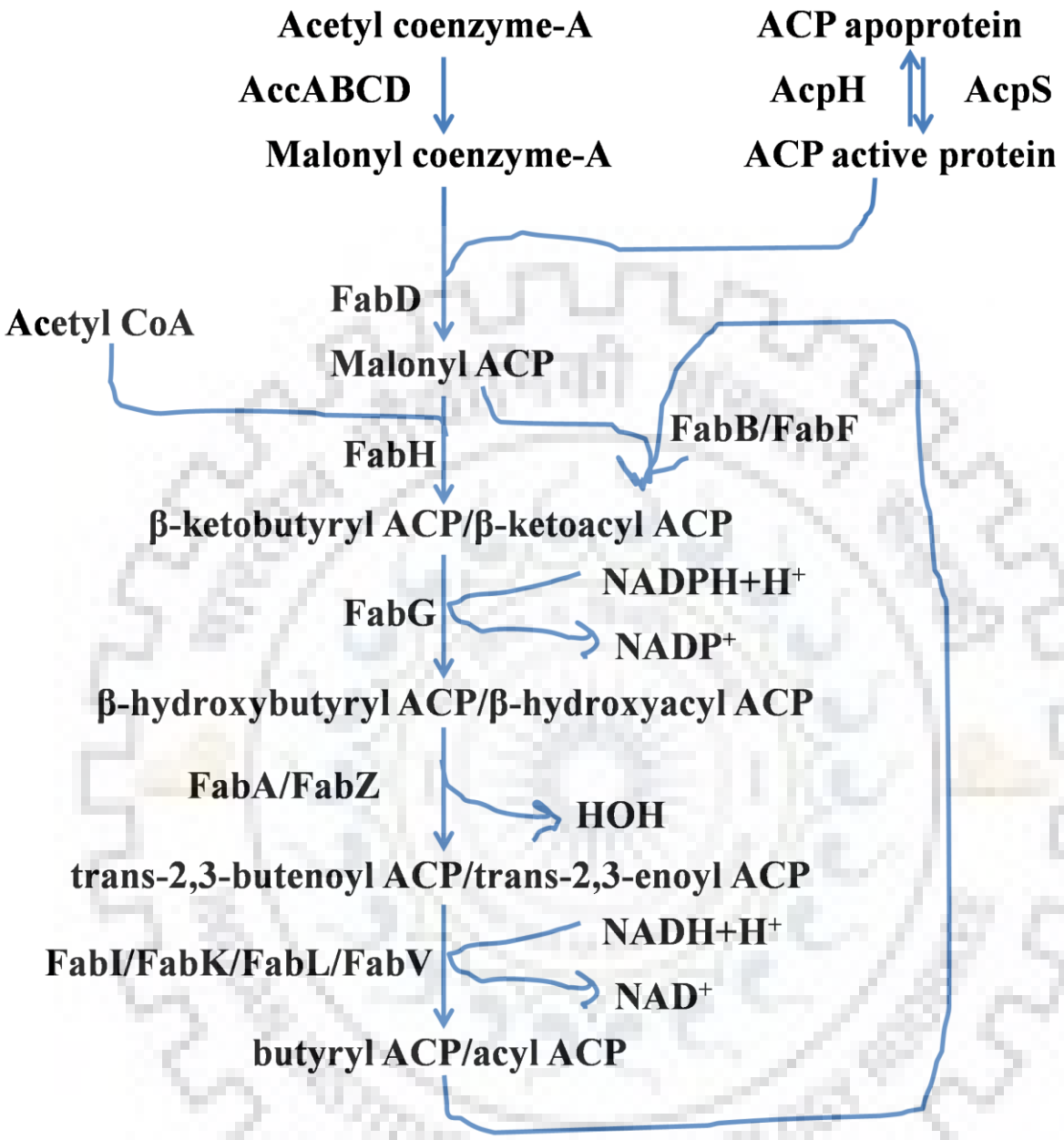

Figure 1.3: The type II fatty acid biosynthesis pathway in bacteria. The component individual enzymes are AccABCD: the four gene products of acetyl coenzyme-A carboxylase, ACP: acyl carrier protein, AcpS: ACP synthase, AcpH: ACP hydrolase, FabD: malonyl-CoA-ACP transacylase, FabH/FabB/FabF: β-ketoacyl ACP synthase III/I/II, FabG: β-ketoacyl ACP reductase, FabA/FabZ: β-hydroxyacyl ACP dehydratase, FabI/FabK/FabL/FabV: enoyl ACP reductase (ENR) I/II/III/IV.

Type II fatty acid biosynthesis system had been proved to be a potential drug target from several pathogenic bacteria, and can be targeted at several essential steps. This pathway was extensively studied from various bacteria including *Escherichia coli*, *M. tuberculosis*, *Staphylococcus aureus* and *Plasmodium falciparum* (148-149, 162-163). Several component enzymes of this pathway including FabH/FabB/FabF (β-ketoacyl-ACP synthases III, and I and II; catalyzing the first and subsequent condensation reactions respectively), FabG (β-Ketoacyl-ACP reductase), FabZ/FabA (β-hydroxyacyl-ACP dehydratase) and FabI/FabK/FabL/FabV (enoyl-ACP reductases (ENRs)) were validated as promising drug targets in designing broad-spectrum inhibitors (148-149, 161-167). Many potential inhibitors, inhibiting different steps of this pathway were discovered and few are currently serving the human community in fighting severe infectious diseases (168-170).

The microbial type I FAS system is also studied extensively and proved as a promising drug target due to its structural and functional differences with the animal/mammalian FAS-I (155-160).

Table 1.1. Reductases of type II fatty acid biosynthesis pathway in bacteria.

Reductase isoform	Name	Cofactor dependency	Length (No. of aas)	Protein family
BKR	FabG	NADPH	450-470	SDR
ENRI	FabI	NAD(P)H	260-280	SDR
ENRII	FabK	NAD(P)H FMN (flavoprotein)	300-330	AKR
ENRIII	FabL	NAD(P)H	250-270	SDR
ENRIV	FabV	NAD(P)H	400-420	SDR

1.2.13. Enoyl ACP reductase enzymes and inhibitors:

The final reduction step of the type II fatty acid biosynthesis pathway is catalyzed by the ENR enzymes which had been proven to be promising drug targets, as many of the known inhibitors

including triclosan, isoniazid and diazaborines, are exercising their antimicrobial actions by inhibiting this enzyme (171-174). It has four known isoforms, observed in different pathogenic bacteria, including FabI (ENR isoform I), FabK (ENR isoform II), FabL (ENR isoform III) and FabV (ENR isoform IV). Few bacteria possess more than one isoform of ENR including *Enterococcus faecalis*, *M. tuberculosis* and *Pseudomonas aeruginosa* possessing FabI and FabK; *Bacillus subtilis* and *Bacillus cereus* containing FabI and FabL; *Burkholderia pseudomallei* having FabI and FabV; and *Listeria monocytogenes* harboring FabI, FabK and FabL (175-186). FabI (ENR isoform I) is the predominantly occurring ENR isoform in wide range of bacteria, including *M. catarrhalis*. Its functional, structural characterization and crystal structures are reported from various bacterial, plant and protozoan species, and extensively studied from *E. coli* (175-176, 187-190), *M. tuberculosis* (191-197), *S. aureus* (198-202), *Helicobacter pylori* (203), *Bacillus subtilis* (204), *Bacillus cereus* (205), *Bacillus anthracis* (206-207), *P. aeruginosa* (208-209), *Francisella tularensis* (210-211), *Acinetobacter baumannii*, *Thermus thermophilus* (212), *B. pseudomallei* (184), *Candidatus Liberibacter* (213), *Chlamydia trachomatis* (214), *L. monocytogenes* (182), *Brassica napus* (177, 215-216), *P. falciparum* (217-219), *T. gondii* (220) and *E. tenella* (221), and show remarkable structural similarity at their active sites.

Several classes of inhibitors, targeting the ENR enzymes from many pathogenic bacteria, were discovered and many of them are in development phase, while few reached upto the clinical trials phase (222-226). Extensive drug discovery studies carried out on the FabI enzymes from the gram negative bacteria including *E. coli*, *M. tuberculosis* and *P. aeruginosa*, gram positive bacteria including *S. aureus* and *Bacillus*, and protozoa including *P. falciparum* which have been the targets for developing antimicrobials with improved efficiencies and/or novel modes of actions (227-234).

Hence, our current study is focusing in understanding the structural and biochemical attributes of this enzyme from *M. catarrhalis* (*Mc*FabI), with the hope of exploiting those molecular features in structure-based drug designing of broad-spectrum antimicrobials.

1.3. Infections by *Acinetobacter baumannii*:

Acinetobacter baumannii is an opportunistic nosocomial pathogen in humans and predominantly exists in the health-care settings. It causes several bloodstream and ventilator-associated infections, including hospital-acquired pneumonia (HAP), for example, in the

health-care facilities (235). While other species of the genus *Acinetobacter* are often found in soil samples (leading to the common misconception that *A. baumannii* is a soil organism and ubiquitous organism, too), it is almost exclusively isolated from hospital environments (236-237). *A. baumannii* has a reputation of low virulence, but emerged as MDR pathogen due to its natural MDR phenotype and capability of acquiring new mechanisms of resistance (236-239). It's one of the major causes of the hospital-derived nosocomial and community-acquired infections in humans, especially the people with compromised immune systems. *A. baumannii* causes several types of hospital-acquired infections including pneumonia, bacteremia, secondary meningitis, bloodstream infections (BSIs), urinary tract infections (UTIs), central nervous system infections (CNSIs) and surgical site infections (SSIs) as manifestation of *Acinetobacter* nosocomial infection (240-241, 260). It mainly aims the moist tissues such as cut skin or mucous membranes and causes bacteremia followed by septicemia which may finally lead to death if left untreated (237). MDR *A. baumannii* usually causes infections like bacteremia, pneumonia, meningitis, wound and urinary tract infections.

Pathogenecity of *A. baumannii*:

When it is in adverse or stress conditions it rapidly mutates its genome to develop resistance and thereby to survive in those unfavorable conditions. Hence its genome can be plastic which majorly contributes to the development of MDR in *A. baumannii* strains (235). The potential of this organism to respond swiftly to changes in selective environmental pressure (selective antibiotic pressure, for example) contributes to the rapid global emergence of *A. baumannii* strains resistant to all β-lactams, including carbapenems. It also has a potential to upregulate its innate resistance mechanisms and potential of acquisition of foreign determinants. The genetic complexity, genetic agility and broad resistance armamentarium of *A. baumannii* and its wide array of drug resistance determinants and its ability to effectively regulate these according to selective environmental pressures clearly demand respect. Much of the success of *A. baumannii* to be multidrug-resistant can be directly attributed to its plastic genome, which rapidly mutates when faced with adversity and stress (235-236, 262, 281). The WHO has included carbapenem-resistant *A. baumannii* in the critical group in the list of bacteria that pose the greatest threat to human health, prioritizing research and development efforts for new antimicrobial treatments. The molecular features that promote environmental persistence, including desiccation resistance, biofilm formation and motility, and the most recently identified virulence factors, such as secretion systems, surface glycoconjugates and micronutrient acquisition systems

collectively enable these pathogens to successfully infect their hosts (235-236, 262, 281, 300, 303, 305).

1.3.1. Colonization by *A. baumannii*:

A. baumannii has the ability to colonize the oral tracts, oropharyngeal tracts, skin, open wounds, body fluids and mucous membranes of the oral and respiratory tracts (242). It has the potential to colonize both biotic as well as abiotic surfaces that helps in its survival, persistence and widespread in adverse clinical settings also (243). All the clinical isolates tested have the ability to adhere to epithelial cells and subsequently colonize. According to the centers for disease control and prevention (CDC) criteria, the definition of *A. baumannii* colonization is its presence without any significant clinical symptoms of active infection (244-245). About 15-20% of clinical isolates of *A. baumannii* develop colonization rather than active infections, making the assessments confused between infection and colonization (246). The factors promoting the colonization of *A. baumannii* include ICU admission, invasive ventilation and trauma unit admission. The colonization of *A. baumannii* strains subsequently leads to the active infections in the later stages. *A. baumannii* is considered as a relatively avirulent organism that frequently colonizes the bodyfluids (247) and hence is often identified in the sputum and blood samples (248). Subsequently it's also difficult to assess the attributable mortality of *A. baumannii* which appears to be as much a colonizer as it is a true pathogen (247).

1.3.2. Bio-film formation by *A. baumannii*:

Maximum proportion of *A. baumannii* clinical strains isolated from hospital-settings form the biofilms and these biofilm-forming strains of majorly responsible for the catheter-related urinary or bloodstream infections and shunt-related meningitis (249). These strains exhibit adherence, colonization and biofilm forming properties (250). Formation of biofilms by *A. baumannii* strains helps for their survival in environments like hospital settings including ICUs despite of the adverse/unfavorable conditions such as desiccation, nutrient starvation and antimicrobial treatments (251). *A. baumannii* strains have the ability to form biofilms on biotic surfaces including tracheal tubes, epithelial cells and fungal filaments as well as on multiple abiotic surfaces, in healthcare facilities, including glass, polypropylene, titatinium and polystyrene (251-252). Biofilms helps *A. baumannii* survival in adverse conditions and their persistence and dissemination in/across hospital environments and also acts as a potential virulent factor in *A. baumannii* pathogenesis, and thereby increasing its probability of causing

nosocomial infections (253). Biofilm formation by *A. baumannii* clinical strains is also known to play significant role in acquiring their antibiotic resistance, as the antibiotic resistance observed in biofilm producing *A. baumannii* strains is significantly higher than the non producers (254-257). There is also an evidence for the trade-off between antibiotic resistance and desiccation tolerance, in case of both clinical and environmental isolates of *A. baumannii* strains; and the fact that biofilm formation enhances the desiccation tolerance; but it particularly promotes antibiotic resistance only in case of clinical isolates and not in environmental isolates (258-259).

1.3.3. Current treatment strategies for *A. baumannii* infections:

Many classes of antibiotics including penicillins, cephalosporins, tetracyclins, aminoglycosides and quinolones have been the choice for treating infections due to *A. baumannii*, historically, for which they were susceptible to; but with time they started developing resistance to many of these antibiotics (260-261). Even after the development of resistance against several classes of antibiotics, the carbapenems, including imipenem, meropenem and doripenem, retained their antibiotic activities and become the major/only choice of treatment in many clinics worldwide (261-262). With the constantly rising antibiotic resistance in *A. baumannii* strains, the treatment, gradually, became dependent on the strain of its clinical isolate and the extent of its drug-resistance (i.e. the antibiotic susceptibility profile of the isolate); and the antibiotics which retained antimicrobial activities, including carbapenems (majorly imipenem, meropenem and doripenem), aminoglycosides and amikacin, were being used. In the subsequent time periods, *A. baumannii* strains also developed drug-resistance towards the last-line antibiotics carbapenems and maximum of the rest antibiotics (262-263), making the preference of antibiotics shifted to other therapeutic options including colistin, polymixins, aminoglycosides, derivatives of penicillins and tetracyclins, tigecycline, for example and the β-lactamase inhibitors, sulbactam, tazobactam and clavulanic acid, for example (248, 262-267). The resistance towards colistin is also observed in many parts of the world and the increasing use of this antibiotic worldwide is also posing a major threat of resistance further (262). Antibacterial phage therapy, bactericidal gene transfer therapy, cathelicidins, nanoparticle technology and photodynamic therapy are also in use, while radioimmunotherapy is yet to be implemented (237).

Due to severe broad-spectrum drug-resistance and lack of new antibiotics, the treatments also involve the use of the inhibitors of *A. baumannii* adherence, colonization and biofilm formation, oroidin analogues, for example (268-269). Alternatively, the *A. baumannii*

infections are currently treated by deploying the combinatorial antibiotic therapies, instead of using any single antibiotic, as most of its strains are developing resistance to many of the antimicrobial categories including the carbapenems which are the major tools to treat its infections for longer periods of time. These combinatorial therapies usually include a combination of one β-lactam antibiotic and one β-lactamase inhibitor, for example ampicillin/sulbactam and amoxicillin/sulbactam (248, 264). Colistin is also used in combination therapy along with tigecycline or gentamycin (262), as it is having advantages over its monotherapy. It is very crucial to notice that there should be always a strong experimental data to support and favor the combined therapy for treating MDR *A. baumannii* using any combination of antibiotics/drugs (270). Combinations of antimicrobials, in double or triple therapy, are becoming the cornerstones of treatment for *A. baumannii* infections, as the colistin-tigecycline-meropenem triple therapy is highly efficient than the double or monotherapies and also safe when the susceptibility profile of the pathogen is not known (271).

Lot more new strategies been deployed in the treatments of MDR/XDR/PDR *A. baumannii* strains' infections due to the unique physiologic characteristics of patients, which can alter the drugs' pharmacokinetics and pharmacodynamics (272). These strategies include (1) the antibacterial dosing which exploit the pharmacokinetic and pharmacodynamic parameters of antibiotics to tailor their dosing (248), (2) the extended/prolonged infusion of β-lactams which exhibits the advantage of achieving drug concentrations above the MIC for a greater time in case of less-susceptible pathogens (248, 272) and (3) effective antimicrobial/antibiotic stewardship (AMS) which is a method that includes appropriate selection, dosage, route and duration of antimicrobial therapy (273); and antimicrobial/antibiotic stewardship programmes (ASWPs) which analyse the clinical and microbiological data on *A. baumannii* strains and assist the preauthorization of antibiotics at the patient level; and also educate and persuade the prescribers of antibiotics to follow evidence-based prescribing (274).

Altogether the current repertoire of antibiotics/drugs available as choices to treat A. baumannii infections include polymixins, tigecycline, sulbactam, rifampicin, minocycline, fosfomycin and few of the newly discovered peptide agents; along with the new approaches of prudent usage of antibiotics including extended infusion of β-lactams and tailored antibiotic dosing (248, 267, 275). And the treatment of infections due to non-MDR *A. baumannii* strains involves aminoglycosides in combination with a β-lactam (262). Polymixins, including colistin, are standing as the last-resort option for treating infections due to all carbapenem-resistant bacteria, although resistance is emerging gradually towards this class of antibiotics also.

1.3.4. Drug-resistance in *A. baumannii*:

A. baumannii is a prominent member of the ESKAPE group of pathogens which are prevalent in healthcare settings and very well known to exhibit substantial drug resistance (4). *A. baumannii* strains were sensitive to most of the common antibiotics till 1970s, but exhibited resistance to carbapenems and rest of the antibiotic classes available (276-278). According to the international standard definitions of multidrug-resistant (MDR), extensively drug-resistant (XDR) and pandrug-resistant (PDR) bacteria (13), *A. baumannii* clinical isolates belonging to all 3 categories were reported worldwide, India, China, Africa, America, Asia and Europe (276-295). *A. baumannii* strains employ numerous mechanisms to attain resistance to any adverse conditions encountered in their way of survival (236, 262, 281, 300). The most prevalent mechanism of β-lactam resistance in *A. baumannii* is enzymatic degradation by β-lactamases. However, in keeping with the complex nature of this organism, multiple mechanisms often work in concert to produce the same phenotype. The nonenzymatic mechanisms of β-Lactam resistance, including carbapenem resistance, include changes in outer membrane proteins (OMPs), multidrug efflux pumps, and alterations in the affinity or expression of penicillin-binding proteins (PBPs). The resistance mechanisms toward other classes of antibiotics such as aminoglycosides, quinolones, tetracyclines and glycylcyclines, polymyxins and other antibiotics, include the aminoglycoside-modifying enzymes, ribosomal (16S rRNA) methylation, tetracycline-specific efflux, modification to target binding sites, ribosomal protection and multidrug efflux (236, 262, 281, 296-300).

Among all the resistance mechanisms exhibited by *A. baumannii* clinical strains, the carbapenemases, extended-spectrum β-lactamases (ESBLs) and 16s rRNA methylases, conferring resistance to carbapenems, broad-spectrum cephalosporins and all clinically relevant aminoglycosides respectively, are the most important causes of concern (300). The following are the major mechanisms of antibiotic/antimicrobial resistance in *A. baumannii*.

1.3.4.1. Resistance to β-lactams (cephalosporins and carbapenems, majorly) in *A. baumannii*:

In this section, resistance mechanisms of *A. baumannii* towards β-lactam carbapenems and broad-spectrum β-lactam cephalosporins are explained majorly, while little focus on penicillins and monobactams. Resistance to β-lactams in *A. baumannii* is primarily conferred by the production of β-lactamases including ESBLs (class A β-lactamases), MBLs (class B β-lactamases) and oxacillinases (class D β-lactamases), while the AmpC-type cephalosporinases

(class C β-lactamases) contribute only a very low level resistance to cephalosporins (260, 262-263). *A. baumannii* strains also employ few non-enzymatic mechanisms of antibiotic resistance to β-lactams including antibiotic target site modifications, efflux pumps and porin channel downregulation/deletion (298).

1.3.4.2. Class A β-lactamases:

1.3.4.2.1. Class A extended-spectrum β-lactamases (ESBLs) in *A. baumannii*:

The class-A ESBLs are proven to majorly confer resistance towards broad/expanded-spectrum cephalosporins. PER-, GES- and VEB-type β-lactamases are the common Ambler class A ESBLs identified in *A. baumannii* (236-263). PER-1, 2, 3, 7 and 8 types of ESBLs were reported in *A. baumannii* from different parts of the world (260-264). VEB-1, 3 and 7 types were reported in *A. baumannii* from France, Iran and Taiwan; and GES-11, 12 and 22 types were reported from different parts of the world and majorly Middle East (284, 301). SHV-, TEM- and CTX-M-type ESBLs were rarely reported in *A. baumannii*, including SHV-5 and 12, TEM-92 and 116, and CTX-M-2, 15 and 43 types. RTG-4, a novel atypical ESBL was also identified in from France (296-300). The genes of these ESBLs are spread either on bacterial chromosomal or plasmid DNA.

1.3.4.2.2. Class A carbapenemases in *A. baumannii*:

Although carbapenemase activity is not the intrinsic property of Ambler class A ESBLs, few are known to possess and among which only GES-14 and KPC-2, -3, -4 and -10 were identified with carbapenemase activity in *A. baumannii* strains (300).

1.3.4.3. Class B β-lactamases:

Being also known as metallo-β-lactamases (MBLs), Ambler class B β-lactamases are not the most commonly identified carbapenemases in *A. baumannii*, and only either IMP-, VIM-, SIM- or NDM-type MBLs reported. IMP variants including IMP-1, -2, -4, -5, -6, -8, -11, -14 and -19; VIM variants including VIM-1, -2, -4, -6 and -11; and NDM variants including NDM-1 and -2 were reported in *A. baumannii* from different parts of the world (297-300). The SIM-1 carbapenemase is reported only from *A. baumannii*. IMP-, VIM-, SIM-type MBLs, that exhibit carbapenemase activity, are also considered as class B carbapenemases.

1.3.4.4. Class C β-lactamases:

A. baumannii naturally produces AmpC-type cephalosporinases, which confer very low level cephalosporin resistance, and no acquired AmpC-type genes are identified in this species so far. AmpC variants with extended cephalosporinase activity including the ADC-type (*Acinetobacter*-derived cephalosporinase) enzymes ADC-33 and -56, which were termed as the extended-spectrum AmpC (ESAC) enzymes, were also reported (263, 300, 302).

1.3.4.5. Class D β-lactamases:

Enzymes of this heterogeneous class, exhibiting diverse structural and functional properties, are also known as oxacillinases and many class D β-lactamases possess an intrinsic property of carbapenemase activity and hence are also called as carbapenem-hydrolysing class D β-lactamases (CHDLs) (236, 263). The broad-spectrum class D β-lactamases hydrolyzing expanded-spectrum cephalosporins are also known as extended-spectrum oxacillinases (ES-OXA) and none of the ES-OXAs identified in *A. baumannii* so far.

A. baumannii possess only one group of naturally occurring class D β-lactamases, OXA-51-like enzymes, and 5 subgroups of acquired class D β-lactamases including OXA-23-, OXA-40-, OXA-58-, OXA-143 and OXA-235-like enzymes. All these enzymes are classified as CHDLs, but exhibit weak carbapenemase activity and confer only reduced susceptibility to carbapenems. The cluster of OXA-51-like enzymes include OXA-51, -64, -65, -66, -68, -69, -70, -71, -78, -79, -80 and -82, and are inherent in *A. baumannii*, locating on its chromosomal genomic DNA (236, 263, 281, 303). The OXA-23 subgroup consists of OXA-23 (ARI1), -27, -49 and -73, which are the most widespread CHDLs in *A. baumannii* and responsible for major nosocomial outbreaks worldwide. The group of OXA-40-like enzymes in *A. baumannii* consists of OXA-40 (formerly known as OXA-24), -25, -26 and -72; the OXA-58 subgroup of CHDLs consists of structurally related OXA-58, -96 and -97; and the novel OXA-235-like enzymes include OXA-235, -236 and -237. Most of these enzymes are chromosome- or plasmid-encoded, while OXA-58 is always plasmid-born, and very few are transposon- or integron-encoded (236-237, 262-264, 281, 296-300).

1.3.4.6. Resistance to aminoglycosides in *A. baumannii*:

Among the different mechanisms of aminoglycosides resistance exhibited by *A. baumannii* strains, the enzymatic methylation modification of the 16S rRNA, the binding target of aminoglycosides, by 16S rRNA methylases is the most common one. ArmA enzyme is the most commonly identified 16S rRNA methylase in *A. baumannii*, while few isolates are reported to be producing the RmtB also (236, 263, 281). These methylases confer a high level

resistance to most of the aminoglycosides being used in the clinics to treat *A. baumannii* infections. The aminoglycoside-modifying enzymes (AMEs) including acetyltransferases, nucleotidyltransferases and phosphotransferses, produced by the gene cassettes located within the integrons, also contribute to the aminoglycosides resistance in *A. baumannii* (299-300).

1.3.4.7. Resistance to fluoroquinolones and quinolones in *A. baumannii*:

The constitutive expression of efflux pumps and membrane impermeability offer a very low intrinsic resistance to fluoroquinolones in *A. baumannii*. But mutations in the DNA gyrase and topoisomerase-IV enzymes, resulting in antibiotic target site modifications, confer high level fluoroquinolones resistance (236, 260, 263-264). In addition to these mechanisms, overexpression of AdeABC and AdeIJK resistance-nodulation-cell division (RND) efflux pump systems encoded by *adeABC* and *adeIJK* operons, and AbeM efflux system, belonging to the multi-antimicrobial extrusion (MATE) protein family, co0ntribute to the high level acquired resistance to fluoroquinolones (297-298, 300). These efflux systems also contribute in the resistance to other classes of antibiotics, including aminoglycosides, tetracyclines, trimethoprim and chloramphenicol (304, 305).

1.3.4.8. Resistance to tetracyclines and glycyclines in *A. baumannii*:

A. baumannii usually exhibits efflux pumps mediated resistance towards most of the tetracyclines, which majorly involves the *tet* gene-encoded TetA and TetB efflux pumps (236, 263). Upregulation of the synergistically acting *A. baumannii*-specific multidrug RND efflux pump systems AdeABC and AdeIJK are also responsible for the resistance towards many of the tetracyclines and glycyclines (glycylcyclines) including the tetracycline derivatives like tigecycline, a current potential therapeutic option to treat several MDR *A. baumannii* clinical starins (281, 297-298, 300, 303). The Trm methyltransferase and AdeFGH efflux pump may also involve in conferring resistance to tigecycline. The ribosomal protection protein TetM confers resistance to minocycline, but identified rarely in *A. baumannii* clinical isolates (300, 303).

1.3.4.9. Resistance to polymyxins and colistin in *A. baumannii*:

We have renewed our clinical interest in polymyxins in the last decade because of accelerating numbers of MDR gram negative bacteria and dearth of novel antimicrobials. Resistance to polymyxins including colistin (polymyxin E), by *A. baumannii*, involves 2 mechanisms: mutations in the PmrAB two-component regulatory system leading to alterations in the lipid A

component of lipopolysaccharide (LPS), and mutations in the enzymes involving in the LPS biosynthesis resulting in complete loss of LPS production (236, 263, 281, 300). Colistin-resistant PDR *A. baumannii* strains are reported from Korea, Spain, Iran and USA, and colistin heteroresistance also observed in *in vitro* models (306-308).

1.3.4.10. Resistance to macrolides, chloramphenicol and trimethoprim/ sulfamethoxazole in *A. baumannii*:

The AbeM and AbeS multi-drug efflux pump systems, belonging to the MATE and BIMP families respectively, are responsible for the macrolide resistance in *A. baumannii* (297-298). The chloramphenicol resistance also majorly conferred by the efflux pumps of RND family, including AdeABC and AdeIJK; MFS family, including CmlA and CraA; and BIMP family, including AbeS (281, 300, 309). Dihydrofolate reductase and dihydropteroate synthase enzymes are conferring trimethoprim resistance, along with the contributions from the RND family efflux pumps including AdeABC and AdeIJK.

1.3.4.11. Non-enzymatic mechanisms of resistance in *A. baumannii*:

There are multiple non-enzymatic mechanisms contributing to the high level antibiotic resistance in *A. baumannii*, which majorly include efflux pumps overexpression, downregulation/deletion of porin channels and modifications/alterations in the antibiotic target sites.

1.3.4.12. Outer membrane proteins (OMPs):

CarO and OprD are the two outer membrane proteins (OMPs) which usually transport the β-lactams across the bacterial outer cell membrane, and *A. baumannii* downregulates or deletes the expression of these two OMPs resulting in the membrane impermeability or a very low and hampered transport of these β-lactams across the membrane which finally confer β-lactam resistance (236, 281, 300).

1.3.4.13. Efflux pumps:

Different efflux pump systems belonging to the RND, MATE, MFS and BIMP families play major roles in contributing to antimicrobial resistance in *A. baumannii* strains. Overexpression of the AdeABC multi-drug RND efflux pump system, encoded by *adeABC* operon, confer resistance towards almost all classes of antibiotics including β-lactams, tetracyclines and glycyclines, fluoroquinolones and aminoglycosides (236, 263, 297). Among the other RND

efflux pump systems, AdeIJK also confer resistance to tetracyclines and glycyclines. The MATE family AbeM efflux pump system contributes to fluoroquinolones resistance, while AdeM to aminoglycosides and quinolones. The BIMP family multi-drug efflux pump system AbeS confers resistance to quinolones, chloramphenicol and macrolides. The *tet* gene-encoded TetA and TetB efflux pumps of MFS family also contribute to the tetracyclines resistance (237, 262, 281, 300).

1.3.4.14. Antibiotic-binding site modifications:

A. baumannii also brings certain structural modifications in the penicillin-binding proteins (PBPs), the binding sites for β-lactams, which also contribute additional resistance towards this class of antibiotics. Alterations in the tetracyclines binding sites through the involvements of TetM proteins also confer tetracycline resistance to *A. baumannii* (236, 263). Mutations in the *gyrA* and *parC* genes that result in the structural modifications of the DNA gyrase and Topoisomerase IV enzymes, the binding sites of fluoroquinolones, also majorly contribute to the fluoroquinolones resistance (281, 296-300). Enzymatic methylation modification of the 16S rRNA, the target of aminoglycosides, by 16S rRNA methylases encoded by *armA*, *rmtA*, *rmtB*, *rmtC*, and *rmtD* genes is a major mechanism of aminoglycosides resistance.

1.3.4.15. Acquired resistance in *A. baumannii*:

Major proportion of the antibiotic resistance mechanisms used by *A. baumannii* is acquired; while very few are native/inherent to this pathogen. Among the β-lactamases, only the chromosomally encoded AmpC cephalosporinases (Ambler class C β-lactamases) and the OXA-51 group of CHDLs (Ambler class D β-lactamases) are native to *A. baumannii*, and all rest are acquired (236-237, 262-264, 281, 296-300). The insertion sequence (IS) IS*Aba1*, present upstream of the bla_{AmpC} gene and appears to act as a promoter that greatly enhances AmpC expression which can finally confer resistance to all penicillins and extended-spectrum cephalosporins in *A. baumannii*, is also acquired (298). Many of the genes encoding the efflux pumps and involving in the antibiotic target site modifications or the expression regulation of the porin channels are also acquired by *A. baumannii* strains. Acquisition of the genes involving in the antibiotic resistance occurs principally through horizontal gene transfer and these genes are either the plasmids-, transposons (jumping jenes)- or integrons-encoded (236, 262, 281, 296-300). All these acquired resistance mechanisms act synergistically to confer the antibiotic resistance to the pathogen. The genomic analysis of several MDR clinical isolates of *A. baumannii* also revealed multiple large genomic islands including AbaR1, R2, R3 and R5,

which contain great number of resistance genes thought to be acquired from other pathogenic resistant bacteria (298).

1.3.5. β-lactamase inhibitors (BLIs) as antibiotics to fight *A. baumannii* infections:

The current repertoires of β-lactamase inhibitors (BLIs), that are clinically used to treat the infections caused by the β-lactamase producing *A. baumannii* clinical strains, include clavulanic acid, tazobactam, sulbactam and avibactam. Among these, clavulanic acid, tazobactam and sulbactam are themselves β-lactams, while avibactam is a diazabicyclooctanone (DBO) (310-312). In addition to these several new groups of β-lactamase inhibitors have been identified with potential activities to inhibit the *A. baumannii* clinical strains and these include ETX2514, a broad-spectrum diazabicyclooctanone β-lactamase inhibitor, WCK4234, WCK5222, LN-1-255, relebactam and vabrobactam, among which many are in last-stage development currently (313-318).

1.3.5.1. Traditional BLIs:

The BLIs, clavulanic acid, tazobactam and sulbactam, that are structurally and chemically β-lactams in nature are usually recognized as traditional BLIs. Sulbactam exhibits its antibiotic properties through the inhibition of certain penicillin-binding proteins (PBPs) including PBP1 and PBP3 (310-311, 319-320).

Clavulanic acid and tazobactam do not inhibit the overexpressed the AmpC enzyme and hence do not exhibit any inhibitory actions against the AmpC hyperproducing *A. baumannii* strains. But sulbactam can inhibit *A. baumannii* strains in the absence of IS*Aba1* insertion sequence, which is responsible for the overproduction of AmpC-type cephalosporinases in *A. baumannii* (310, 320-327).

1.3.5.2. Non-β-lactam BLIs:

The BLIs that are not β-lactams in their chemical nature are grouped as Non-β-lactam BLIs. This group, at present, majorly includes the diazabicyclooctanone (DBO) derivatives/variants that exhibit potential broad-spectrum inhibitory activities against β-lactamases including several of the CHDLs. Avibactam, ETX2514, and WCK4234 are the major DBOs with proven broad-spectrum β-lactamase inhibitory activities (313-318).

1.3.5.3. Resistance towards BLIs in *A. baumannii*:

The traditional BLIs are active against only very few class-A β-lactamases and no proven activity against other classes. The reason behind this maybe that the traditional BLIs, being β-lactams themselves, also turn into the substrates of β-lactamases, making them good substrates for hydrolysis by these enzymes and poor inhibitors (310, 328-330). Hence the traditional BLIs are routinely used in clinics in combinations with the β-lactam antibiotics, ampicillin-sulbactam, amoxicillin-clavulanic acid and piperacillin-tazobactam, for example, and are resulting in significant antibacterial activities against several MDR strains (312, 319-327, 329).

1.3.6. Human efforts and drug development to fight back AMR in *A. baumannii*:

Humans are constantly evaluating the virulence mechanisms of this pathogen and understanding the molecular attributes contributing to its multi-drug resistance (MDR) (331-339). Based on these, continuous trials are being undertaken to develop new antibiotics with increased potencies to inhibit a currently recognized mechanism of resistance or novel modes of antimicrobial actions (340-371). With regard to the former, attention has been directed toward new β-lactamase inhibitors, especially those targeting the Ambler class D OXA type carbapenemases (serine oxacillinases) (CHDLs) and Ambler class B MBLs, as well as toward inhibitors of aminoglycoside-modifying enzymes and multidrug efflux pumps (235-236, 281, 300). The emergence of MDR *A. baumannii* emphasizes the urgency of developing alternative treatment strategies. These anti-virulence strategies include antibacterial phage-therapy, metabolic interference therapy, bactericidal gene transfer therapy, photodynamic therapy, radioimmunotherapy, antimicrobial peptide therapy, nanoparticle technology and vaccine strategies (248, 262, 267, 272, 275, 341, 343, 347, 351, 355, 359). Several new approaches are also being employed to fight the AMR in *A. baumannii* including combination therapy, repurposing the old antibiotics, digging the unexplored repertoire of antimicrobials and continuous discovery of synthetic antimicrobial compounds (343, 369-370). The β-lactams are being used in combination with the β-lactamase inhibitors to fight the antibiotic resistance conferred to *A. baumannii* by the β-lactamases, the major contributors to MDR phenotype (248, 262, 270, 272, 310-330, 343). Antimicrobial stewardship (AMS) programs are widespread and actively involving in the control of AMR by educating and guiding the antibiotic prescribers and users on the evidence based usage of the antibiotics (273-275, 350). Many drug targets are being explored and characterized successfully to exploit in the drug discovery programs which mainly involve the techniques of CADD/SBDD/LBDD/FBDD tools, including molecular modeling, HTS and VS, and chemical synthesis of novel antimicrobial molecules (352-353, 362, 366, 368, 372). Continuous efforts are being made by humans to discover and develop

novel β-lactam antibiotics, carbapenems, β-lactamase inhibitors and β-lactam enhancers (373-376).

1.3.7. Carbapenems, carbapenem-resistance, carabapenemases and carabapenemase inhibitors:

Among the several chemical classes of antibiotics, including β-lactams, aminoglycosides, quinolones/fluoroquinolones, polymyxins, sulfonamides, macrolides, tetracyclines, glycylcyclines, oxazolidinones, cyclic lipopetides, glycopeptides and lipiarmycins, β-lactams, including penams (such as penicillins), penems, carbapenems, cephems (such as cephalosporins) and monobactams, are the most potent and popular antibiotics that are being widely used to treat broad range of infectious diseases (373, 377-379). With the constantly growing antibiotic resistance against many classes of antibiotics and emergence of MDR/XDR/PDR pathogenic strains, carbapenems, including imipenem, meropenem, doripenem, ertapenem and tebipenem, became the major choice of treatment due to their inherent antimicrobial properties against those antibiotic resistant bacteria (374, 380-403). Resistance is emerged towards many of the carbapenems following their widespread usage for treating the MDR/XDR/PDR pathogens, which is mainly conferred by the carbapenemases, the carbapenem-hydrolyzing β-lactamase enzymes, while it is also conferred by few naturally-occurring enzymes including CphA, L-1, FEZ-1, CGB-1, EBR-1, JOHN-1, THIN-B and IND series (404).

Carbapenemases are observed from all the 4 Ambler classes of β-lactamases and the MBLs are the first ever discovered carbapenem-hydrolyzing β-lactamases which are the source of acquired β-lactam antibiotic resistance in several gram-negative bacteria of clinical relevance (404-410). Later on, several other classes of carbapenemases contributing to MDR phenotype in several pathogens were discovered and characterized from many bacterial pathogens including *A. baumannii*. The carbapenemases are encoded by either chromosomes, plasmids, transposons or integrons; and either inherent/native to the bacteria or acquired. The class A carbapenemases including KPC, GES, SME, NMC, IMI, BIC and SFC; the class B carbapenemases including IMP, VIM, NDM, GIM, KHM, SPM, SIM, DIM, AIM and TMB; the class C carbapenemases including CMY, ACT, DHA and ADC; and the class D carbapenemases including the oxacillinases are extensively studied from *A. baumannii*, *P. aeruginosa*, *K. pneumoniae* and *Enterobacteriaceae* (404-416). The mechanisms of resistance being conferred to bacteria by all classes of carbapenemases are studied in detail and the underlying principles are deciphered (417-429). The Ambler class D β-lactamases, which are

also called as oxacillinases and carbapenem-hydrolyzing class D β-lactamases (CHDLs), are the major concern of the current day human society due to their continuous evolution with broad-spectrum carbapenemase/β-lactamase activities. The CHDLs, which are also known as the class D serine carbapenemases, including the OXA-51, OXA-23, OXA-24/40, OXA-48, OXA-58, OXA-143, OXA-235, OXA-55, OXA-50, OXA-60 and OXA-62 subfamilies/clusters, are characterized and widely studied from MDR/XDR/PDR strains of different pathogenic bacteria (430-486). The structural, functional and mechanistic features of several OXA enzymes, including OXA-1, 2, 9, 10, 11, 12, 13, 15, 16, 18, 19, 23, 24/40, 25, 26, 27, 46, 48, 51, 58, 134, 143, 145, 146, 163, 181, 205, 235, 139 and 245, have been studied thoroughly and provided a great platform to develop structure/mechanistic based β-lactamase inhibitors towards several antibiotic-resistant pathogenic strains (430-486).

1.3.8. Oxa-58 β-lactamase from *A. baumannii*:

The Oxa-58 is one of the acquired β-lactamases and a CHDL enzyme found in clinical isolates of *A. baumannii* from different parts of the world (444-448, 454, 463, 466, 473, 484). It is a serine β-lactamase which hydrolyzes a variety of β-lactam antibiotics, including penicillins, cephalosporins, and the last resort carbapenems, the most promising tools to treat this MDR pathogen, and conferring resistance to most of those antibiotics (444-448, 454, 463, 466, 473, 484). It is one of the major factors contributing to MDR phenotype and hydrolyzing many classes of β-lactams including the β-lactamase inhibitors that are β-lactams in their chemical nature. The hydrolytic mechanism of different classes of β-lactams, including the carbapenems, by Oxa-58 from *A. baumannii* (*Ab*OXA-58) is elucidated in detail by DG Kotra group (428). It is very crucial to understand the structural basis for the mechanism of β-lactam hydrolysis by these enzymes in order to take further actions towards controlling the constantly accelerating multidrug resistance in *A. baumannii* and many other human pathogens exhibiting MDR/XDR/PDR phenotypes. Hence, we are focusing on understanding the active site structural and catalytic elements essential for the hydrolysis of carbapenems by the *Ab*OXA-58 enzyme, by using the carbapenem structural mimetics including 6α-hydroxymethyl penicillin (6α-HMP) and 6α-hydroxyoctyl penicillin (6α-HOP), which are the very well proven probes of hydrolytic mechanisms of β-lactamases (421).

1.4. Human diseases by *Leishmania donovani* and drug targets:

Leishmania donovani is a protozoan parasite that lives an obligative intracellular parasitic life in human macrophages/mononuclear phagocytic cells and causes a popular disease called leishmaniasis, which is also categorized as one of the neglected tropical disease (NTD) (487-493). It also causes the similar disease in certain domestic animals, and hence the disease is considered as zoonotic disease in humans and anthroponotic disease in other animals (494). This parasite is majorly transmitted through female phlebotomine sandflies that were infected (495). This disease usually known to affect some of the poorest populations worldwide and is associated with several socio-economical factors including poor housing, malnutrition, population displacements and lack of financial sources. There are 3 main forms of this disease observed to occur in humans, including visceral leishmaniasis (VL), cutaneous leishmaniasis (CL), and mucocutaneous leishmaniasis (MCL) (491, 493). Till date around 98 countries worldwide are discovered to be endemic to the leishmaniasis disease. Leishmaniasis is one of the major neglected tropical diseases (NTDs) and the second leading cause of deaths due to parasitic diseases. By 2017 reports of WHO, there are 700,000 to 1,000,000 new leishmaniasis cases occur every year in around 98 disease endemic countries worldwide and they likely leads to 20,000 to 30,000 deaths.

1.4.1. Visceral leishmaniasis (VL):

VL is also known as kala-azar and this is the most serious form of the leishmaniasis disease. VL is mainly caused by *L. donovani* and *L. infantum* species. This form of disease affects the visceral organs also, including spleen and liver, hence popularly described as visceral leishmaniasis (496-498). Clinical symptoms of VL include intermittent and irregular bouts of fever, progressive body weight loss (known as cachexia), anaemia and enlargements of the affected visceral organs liver and spleen, known as hepatomegaly and splenomegaly respectively. Other symptoms including lymphadenopathy and persistent diarrhoea are also frequently observed in leishmaniasis patients (499-503). VL is fatal, if left untreated, as observed in over 95% of cases. According to world health organization (WHO) disease statistics reports, approximately 50000 – 90000 new VL cases occur each year worldwide, among which major proportion observed in South-East Asia, Brazil and East Africa. India, Brazil, Ethiopia, Kenya, Somalia, Sudan and South Sudan are the 7 countries from where more than 90% of new VL cases were reported to WHO in 2015 (504-506).

1.4.2. Cutaneous leishmaniasis (CL):

CL is the most common form of leishmaniasis among all its 3 forms. Its clinical symptoms include skin lesions, majorly in the form of ulcers, on parasite exposed parts of the body. These skin lesions also leave life-long scars and disability, even after successful treatment (507-511). According to the WHO disease statistics reports, about 95% of CL cases are observed in the Central Asia, Middle East, Americas and Mediterranean basin; while Brazil, Colombia, Afghanistan, Algeria, Iran and Syrian Arab Republic are the 6 countries from where more than 70% of new CL cases were reported to WHO in 2015. Its occurrence is very frequent in several parts of the world with 600000 to 1 million new CL cases observed annually worldwide (504-505).

1.4.3. Mucocutaneous leishmaniasis (MCL) and tegumentary leishmaniasis (TL):

MCL is an infrequent non-lethal form of leishmaniasis and more than 90% of its cases usually occur in Brazil, Ethiopia, Bolivia and Peru. Its clinical symptoms include partial or complete destruction of the mucous membranes of the mouth, nose and throat (512-516). Several species of *Leishmania* also cause the infection known as tegumentary leishmaniasis (TL) which is a disease of the skin and mucosal tissues. The TL is also observed to occur with the co-infection of several pathogens other than HIV and including helminths or *Trypanosoma cruzi* (the parasite that causes Chagas disease) (517).

1.4.4. Post-kala-azar dermal leishmaniasis (PKDL):

In several cases of visceral leishmaniasis, recurrence of the disease is observed, usually 6 months to 1 or more years after the successful treatment and cure of kala-azar, which is popularly named as post-kala-azar dermal leishmaniasis (PKDL) due to its clinical manifestations which include papular or macular rashes and/or nodular spots that usually occur on face, upper arms, trunks and other parts of the body (518-521). PKDL is observed to occur mainly in the Indian subcontinent and East Africa where 5-10% of kala-azar patients usually develop the recurrent disease condition, while 50% of the properly treated VL cases in Sudan are observed to develop PKDL (522-527).

1.4.5. *Leishmania donovani* co-infection with HIV viruses:

In few cases of leishmaniasis disease, it's diagnosed that there is concomitant infection of the patients with HIV retroviruses, which is confirming the co-infection of *L. donovani* and HIV viruses (528-534). Usually high mortality rates, high relapse and chances of developing full-blown clinical symptoms of the leishmaniasis disease are observed to be associated with the

Leishmania-HIV coinfected people (535-539). High rates of this protozoan parasite-retrovirus coinfection are reported from India, especially the Bihar state, Brazil and Ethiopia countries. Treatment of the coinfected patients with antileishmanial and antiretroviral drugs together is observed with reduced symptoms of the leishmaniasis disease, delayed relapses and increased survival rates of the patients (540-542).

1.4.6. Reservoirs and vectors of transmission for *Leishmania* parasites, and canine visceral leishmaniasis (CVL):

Humans and their common domestic animals, including dogs, are the primary reservoirs of this deadly protozoan parasitic pathogen *L. donovani* (494, 543-544). The disease forms of leishmaniases that occur in canines are usually called as canine leishmaniases and the major form of canine leishmaniases is the canine visceral leishmaniasis (CVL) (543-546). Approximately 70 different animal species are found to be the natural reservoir hosts of *Leishmania* parasites, including *L. donovani*, and this parasite also causing the similar diseases in many of those animal reservoirs (545-546). People suffering from PKDL are also recognized as a potential source of this parasite that can readily spread among human populations and their dwellings (522-527).

Female phlebotomine sandflies are the common vectors of transmission for *L. donovani* parasites, while the sandflies of *Lutzomyia* genera also responsible for this parasite transmission among hosts (547-552). Several different species of sandflies are responsible for the trasnsmission of zoonotic and anthroponotic visceral leishmaniasis and cutaneous leishmaniasis, including *Phlebotomus argentipes*, *P. papatasi*, *P. sergenti*, *P. kandelakii*, *P. neglectus*, *P. perfiliewi*, *P. keshishiani* and *P. alexandri*, among many others. It transmits the parasite through its blood meal that it collects usually by biting the reservoir animals that are carrying the parasite in their blood circulation after its release from the human phagocytic cells which are intra-cellularly harboring that parasite (553-557).

1.4.7. *Leishmania donovani* life cycle and pathogenesis of leishmaniasis:

L. donovani spends a digenetic life cycle comprising the flagellated and motile promastigote form of *L. donovani* that is transferrable, through the vectors, between different hosts/reservoirs, and non-flagellated and non-motile amastigote form that spends intracellular life within the host (558-561). The promastigotes are morphologically distinct to amastigotes and are subclassified into five types: procyclic, nectomonad, leptomonad, haptomonad and metacyclic promastigotes. The metacyclic promastigotes are regarded as the infective stage and

have high adaptability for successful transmission within the human host. When an infected female phlebotomine sandfly bites human body to have its blood meal, it may concomitantly release/transmit the promastigotes, the infective form of *L. donovani* parasite in humans, from its proboscis into the human's bloodstream. Those newly entered promastigotes are phagocytized by human macrophages and other types of mononuclear phagocytic cells, and subsequently transform into amastigotes, the tissue stage and proliferative-form of *L. donovani* parasite in humans, within those phagocytic cells (560-564). Amastigotes live an intracellular life and proliferate by simple cell division inside the parasitophorous vacuoles of the macrophages until they are destroyed, and eventually infect the neighbor phagocytic cells. During this phase of infection, the symptoms of the leishmaniasis disease may develop depending on the human body and parasite conditions and several other factors, which gradually transforms the infection into symptomatic that results in either visceral or cutaneous leishmaniasis (565-569).

During the proliferative phase, in humans, the burst of phagocytic cells occur that leads to release of the amastigotes into the blood stream. These amastigotes may be ingested by the sandfly during its human bite for blood meal and subsequently transform into promastigotes within the sandfly gut epithelial cells (568-572). These promastigotes proliferate in the sandfly gut and eventually migrate to its proboscis to start its next stage of life cycle in human hosts.

The promatigote and amastigote forms of *L. donovani* parasite possess lipophosphoglycan (LPG) on their surface which helps them to manipulate the host immune system and to get protection from the host defence mechanisms. LPG helps the promastigotes from the host complement-mediated lysis and promotes parasite phagocytosis by parallelly inducing the complement activation (573-576). LPG layer also protects the amastigote form the actions of reactive oxygen species (ROS) and reactive nitrogen species (RNS), which are generated as part of host defence system, by delaying the assembly of NOX2 at the surface of the phago-lysosome. After phagocytosis, the *L. donovani* parasite itself secretes the arginase enzyme, which initiates the biosysnthesis of polyamines that are crucial for parasite metabolism, within the host macrophages or induces those macrophages to produce it (560, 564-569, 575).

1.4.8. Treatments against leishmaniases:

Traditionally the leishmaniasis had been treated by chemotherapy using the pentavalent antimonials, including sodium stibogluconate (SSG (Pentostam)) and meglumine antimoniate (Glucantime), as the standard first line of treatment (577-601). Due to emergence of resistance

towards pentavalent antimonials, the treatment strategies shifted towards alternative therapeutics including the second-line anti-leishmanial drugs miltefosine (MF, hexadecylphosphocholine), paromomycin (PM (aminosidine), an aminoglycoside-aminocyclitol antibiotic), amphotericin B (AmB, a polyene antibiotic) and their lipid formulations (602-624). The current day treatments for the visceral, cutaneous and mucocutaneous leishmaniases include the drugs like AmBisome (liposomal amphotericin B), pentamidine (aromatic diamidines), imiquimod (the active ingredient in a topical cream called Aldar), tamoxifen, PDT, ketoconazole, itraconazole, fluconazole (the antimycotic azoles), sitamaquine (a 4-methyl-6-methoxy-8-aminoquinolone (lepidine)), pentamidine structural analogs and nucleoside analogs (including allopurinol, a pyrazolopyrimidine), as these drugs offer better efficacy, easier administration and lower toxicity (625-634, 664). In children also, many of the common antiparasitic drugs are being used for the treatment of leishmaniases (591, 595, 604). With the emergence of resistance towards many classes of anti-leishmanial drugs, alternative strategies, including combination therapies, new delivery methods of drugs and new formulations of drugs, are in implementation (599-601, 603, 606, 617, 623, 633). In the case of co-infection of *Leishmania* parasites with other pathogens, including HIV retroviruses, helminthes and other trypanosomatids like *Trypanosoma*, the combination of anti-parasitic and anti-retroviral drugs are being used after proper diagnosis of the individual symptoms (517, 629). Several natural and plant derived products/extracts are reported to be exhibiting anti-leishmanial/leishmanicidal activities as part of phytotherapies, and many of them are characterized for their further analysis and applications (635-645, 664). Few peptide based therapies and immunotherapies are also discovered, along with the designing of nanotherapeutics with the help of nanothechnology (646-647). The antimicrobial Peptides (AMPs) are also being tested for the anti-leishmanial activities (664).

1.4.9. Vaccines against *Leishmania* parasites:

Several types of vaccine candidates, including killed or live attenuated whole parasite vaccines, wild-type/recombinant/synthetic whole/fragmented protein antigens, non-protein antigens and DNA vaccines, are characterized, experimented and tested against all forms of human and canine leishmaniases (648-651). Leishmanisation, the inoculation of live virulent *Leishmania*, had been the method practiced and used for immunization against *Leishmania* parasites for over a century in the past, and gradually several kinds of vaccine preparations are made including killed parasite vaccines (whole-cell, killed vaccines), live-attenuated vaccines,

subunit vaccines, polyprotein vaccines, single antigen vaccines, cocktail vaccines, prophylactic and therapeutic vaccines (652-654).

The several different antigenic/immunogenic molecules from different *Leishmania* species, that have been tested as anti-leishmanial vaccine candidates so far, include surface expressed glycoprotein leishmaniolysin (gp63), GPI-anchored membrane protein gp46, prasite surface antigen 2 (PSA-2), native polypeptides derived from promastigotes, Leishmania homologue for receptors of activated C kinase (LACK), amastigote cysteine proteases (CP), cysteine proteinase A2, amastigote membrane proteins P4 and P8, kinetoplastid membrane protein-11 (KMP-11), amastigote LCR1, hydrophilic acylated surface protein B1 (HASPB1), leishmanial antigen ORFF, acidic ribosomal protein P0, paraflagellar rod protein 2 (PRP-2), NH36 (a main component of the fucose-mannose ligand), proteophosphoglycan (PPG), ATP synthase alpha chain, beta-tubulin, heat shock 70-related protein 1 precursor, anti-sandfly saliva components (652-665). The adjuvants tested and used in the anti-leishmanial vaccine preparations include ODN containing immunostimulatory CG motifs, unmethylated CpG dinucleotides in bacterial DNA or synthetic oligonucleotides (ODN), CpG-containing immunostimulatory oligodeoxynucleotides (CpG ODNs), Bacille Calmette-Guerrin (BCG), monophosphoryl lipid A (MPL, a detoxified form of lipid A derived from the lipopolysaccharide of Salmonella minnesota R595) (648-665).

The various anti-leishmanial vaccine preparations tested in animal models include (1) two killed *Leishmania Major* vaccines - killed either by autoclave (ALM), or thimerosal plus freeze-thawing (KLM), with or without BCG as adjuvant, (2) DNA vaccine including *L. donovani* p36 (LACK) (3) live promastigotes, (4) killed promastigotes, (5) killed promastigotes with BCG, (6) killed promastigotes with IL-12, (7) irradiated promastigotes, (8) live attenuated promastigotes, (9) recombinant or native gp63 and synthetic peptides, (10) recombinant or native gp46/M2/PSA-2, (11) recombinant LACK, (12) A2, P4, and P8, (13) Flagellar antigen LCR1, (14) Naked DNA gp63, PSA-2, and LACK, (15) live parasites coinjected with CpG-containing immunostimulatory oligodeoxynucleotides (CpG ODNs) alone or in combination with whole-cell lysates of heat-killed *L. major* promastigotes bound to alum (ALM), (16) recombinant ORFF (rORFF) leishmanial antigen with or without CpG-ODNs as adjuvants, (17) Autoclaved *L. donovani* (ALD), (18) stimulatory soluble antigenic proteins, including F2 sub fraction and rF14, from *L. donovani*, (19) Th1-stimulatory polyproteins of soluble *L. donovani* promastigotes, which majorly include the subfractions elongation factor-2, p45, heat shock protein-70/83, aldolase, enolase, triosephosphate isomerase, disulfideisomerase and calreticulin

among the 19 identified immunostimulatory proteins (648-681). Many of those vaccines are proved to be exhibiting potent antigenic and immunogenic properties against *Leishmania* parasites, and found to be successful in eliciting immune responses in the experimental model organisms and human volunteers.

An 'ideal' anti-leishmanial vaccine is to be effective against more than one *Leishmania* species in order to protect individuals in areas where several forms of leishmaniasis coexist and thus should provide cross-protection. Hence, any anti-leishmanial vaccine preparation has to be checked whether it will work against both forms of the disease, and provides cross-immunity between different leishmania species (658-671). The ultimate anti-leishmanial vaccine would most likely be a cocktail of several well-defined immunogens rather than a single molecule to overcome genetic restriction of hosts and cover a wider diversity of parasites (648-663). Currently, there are no vaccines available with promising actions in preventing this parasitic pathogen and no vaccine against Leishmania in routine use anywhere in the world. Several vaccine preparations are in more or less advanced stages of testing, and many vaccines are clinical trials and have to reach the market (648-681). Animal vaccination is also very much necessary to control and prevent the spread of *Leishmania* parasites across the domestic animals and humans.

1.4.10. Drug-resistance in *Leishmania* parasites and insecticide-resistance in sandfly vectors:

The ineffectiveness of the pentavalent antimonial compounds (Sb^v), which have been the mainstay of anti-leishmanial therapy for more than 50 years, was reported and gradually emerged during the early 1980s in India. The important reasons for the rapid increase in the Sb^v refractoriness include the rampant use of sub-therapeutic doses, incomplete duration of treatment and substandard drugs, and the anthroponotic transmission of *Leishmania* parasites in India (682-683, 687, 690). Subsequently, resistance is observed for all the first-line drugs including antimonial compounds and amphotericin B, the second-line drugs including miltefosine, paromomycin, pentamidine, and many other drugs, which are at various stages of their development process, including imiquimod, tamoxifen, PDT, ketoconazole, itraconazole, fluconazole (the antimycotic azoles), sitamaquine, pentamidine structural analogs and nucleoside analogs (including allopurinol) (683-696). The resistance of *Leishmania* parasites towards the anti-leishmanial drugs is categorized broadly into "species variation", the intrinsic variation in the sensitivity of *Leishmania* species, and "acquired drug resistance". The mechanisms of intrinsic and acquired drug resistance, as well as clinical and *in vitro* resistance,

are being investigated with intense focus of research for the last few decades and yet obtained apparently contradictory results (683, 686).

The monitoring of anti-leishmanial drug resistance is crucial in understanding the resistance pattern and further development of the novel and efficient drugs. The factors like amastigote-macrophage culture assay, which is used to correlate clinical and *in vitro* resistance, and a lack of knowledge about the molecular and biochemical mechanisms of resistance to antileishmanial drugs, make the monitoring of anti-leishmanial drug resistance a difficult process (683-686, 688, 692-693). Hence, improved methods that determine either the (i) phenotypic sensitivity of parasite isolates or (ii) molecular changes that indicate alterations in either the drug target or mechanisms that alter the intraparasite level of active drug are required to monitor the drug resistance. It is also important to determine the factors involved in the spread of drug resistance (683, 686).

The resistance of sandflies, the vectors of *Leishmania* parasites, to insecticides had been reported from several parts of the world. Insecticide resistance in *P. argentipes*, the vector of kala-azar in the Indian subcontinent, was first reported in 1987 in Bihar, India. The sandflies were known to be susceptible to insecticides until 1978, but resistance to dichlorodiphenyltrichloroethane (DDT) in *P. papatasi* and *P. argentipes* was reported in 1979 and 1990 (697-699). In the kala-azar endemic areas of Bihar and West Bengal in India, the resistance of *P. argentipes* to DDT was reported, while in non-endemic areas it was reported to be susceptible. In areas of Nepal bordering India, resistance to DDT is emerging, while biochemical resistance was reported in Sri Lanka. However, the sandfly vector was reported to be still susceptible to pyrethroids in all kala-azar endemic areas in the aforementioned countries (553-555, 697-701). In 2003, it was reported that *P. papatasi* was tolerant to DDT, methoxychlor and dieldrin in Egypt, the Islamic Republic of Iran and Israel; *Lutzomyia youngi* were tolerant to malathion and fenthion while resistant to propoxur and deltamethrin. *L. longipalpis* was reported to be tolerant to fenitrothion and pirimiphos-methyl, while high resistance in *P. papatasi* against malathion and propoxur was reported in Sudan (555, 700, 702). The insecticide resistance and tolerance in phlebotomine sandflies was reported from different parts in the Southeast Asia region, including India, Bangladesh, Nepal and Sri Lanka. In India, *P. argentipes* and *P. papatasi* were reported to be resistant and tolerant to the insecticides DDT, dieldrin, malathion, propoxur, BHC, deltamethrin and permethrin from several states that are endemic to the disease (553-555, 699, 701, 703). The pyrethroid tolerance was also observed from the VL hotspot of Bihar, India.

The mechanism of insecticide resistance and tolerance exhibited by the sandflies was also studied in detail, and it was found that the *Vgsc* mutations detected in the para voltage-gated sodium channel (VGSC), which is the shared target site of DDT and pyrethroids, appear to be a primary mechanism underlying DDT resistance in *P. argentipes* and a contributory factor in reduced pyrethroid susceptibility, suggesting a potential impact if *P. argentipes* are subjected to suboptimal levels of pyrethroid exposure, or additional resistance mechanisms evolve (703) . There are four enzyme systems reported to be involved in insecticide resistance, including acetylcholinesterase, non-specific carboxylesterases, glutathione-S-transferases and cytochrome p450 monooxygenases, the first report of these resistance mechanisms in sand flies, which probably arose from the malathion-based spraying regimes of the anti-malarial campaign (698).

1.4.11. Prevention, control, elimination and eradication of Leishmaniases in Indian subcontinent and worldwide:

The prevention of Leishmaniases is chiefly dependent on control of the spread of *Leishmania* parasites, among the human and canine host reservoirs, through the sandfly vectors. There are several vector control strategies are in current implementation to combat leishmaniasis including indoor residual spraying (IRS), application of chemicals in rodent burrows, impregnation of bed nets and curtains with insecticides, the use of insect repellents, impregnation of dog collars; among which three different interventions are widely popular for VL vector management: indoor residual spraying (IRS); long-lasting insecticide treated nets (LLIN); and environmental modification (EVM) through plastering of walls with lime or mud (697-703). The main strategy for vector control of VL is to conduct two rounds of indoor residual spraying with DDT/pyrethroids in human dwellings and cattle sheds up to a height of 6 ft; the first round is usually undertaken from February to March and the second round during May to June but may vary from state to state. In accordance with the roadmap for elimination of kala-azar (www.nvbdcp.gov.in), micro-planning for vector control was instituted in 2014 whereby any village or hamlet reporting KA cases in the past 3 years qualifies for 100 % coverage by spraying. IRS results in significant sand fly reductions in all sites independent of type of walls or dwelling or type of insecticide (DDT or pyrethroids) (555, 697-699). Several insecticides are in current use to control the sandflies, including DDT, pyrethroids, synthetic pyrethroids, alpha-cypermethrine, deltamethrin, permethrin, dieldrin, malathion, fenthion, fenitrothion, lambda-cyhalothrin, propoxur, BHC, bendiocarb, methoxychlor, pirimiphos-methyl and few others (555, 697-707). Collateral benefits of anti-malaria programme are

noticed in VL control, as it was observed that the apparent disappearance of VL between 1960 and 1970 may partly be as a collateral benefit of DDT spraying under the National Malaria Eradication Programme, in Southeast Asia.

With the emergence of insecticide resistance, it was observed that indoor residual spraying and use of treated nets have low effectiveness, which warrants improvement in the quality of spraying, and research on alternative, integrated vector control methods to achieve VL elimination. Evaluation of insecticide resistance, subsequent monitoring through sentinel surveillance and capacity strengthening is required not only in India where kala-azar has yet to be eliminated but also in the neighbouring endemic countries of Bangladesh, Bhutan, Nepal and Sri Lanka as part of vector surveillance within an integrated vector management approach (699-711). The insecticide resistance in the Indian subcontinent is wide spreading and hence high IRS coverage, frequency of sprays and choice of insecticide will be important factors in achieving an impact on the vector population and reducing the spread of resistance; and new approaches including the investigation of the behavioral patterns of the adults of different sand fly species, introduction of biological insecticide agents, the use of insecticidal plants and other novel strategies for the control of sand fly populations should be recommended and improved since they provide optimistic results (555, 704-713). The eradication of the vector can be achieved through the use of insecticides, elimination of stagnant water, use of insect repellents, and prophylaxis; along with the use of thick clothes with long sleeves that can be impregnated with insecticides and long pants and by avoiding night walks in jungle areas (704-716).

The control and elimination of leishmaniases requires proper diagnosis of all forms of the human and canine leishmaniases, including VL, CL, MCL and TL; followed by precise treatment of the diagnosed disease form (704-714, 717-725). The diagnosis of the leishmaniases symptoms is very crucial during the co-infection of humans with *Leishmania* parasites along with the other pathogens including HIV retroviruses, helminth parasites or any other trypanosomatids like Trypanosoma (717-731).

There are several organizations in India and worldwide, including Leishmaniasis Research Society (India), Indialeish, World Health Organization (WHO), Worldleish, Drugs for Neglected Diseases initiative (DNDi), Centers for Disease Control and Prevention (CDC, USA), Uniting to Combat NTDs and many others, work together to implement many programmes for leishmaniases control/prevention/elimination/eradication and evaluate the subsequent progress/success (732-748). They also exercise on the necessary actions to be taken for the further control and eradication of leishmaniases diseases after completion of the earlier

implemented leishmaniases elimination programmes. These organizations also act together to help the poor populations being affected by these parasitic diseases in the developing countries. WHO is the leading organization which majorly contributes in executing the leishmaniases control/prevention/elimination/eradication programmes worldwide and helps the poor societies/countries by offering them the required medicine/vaccines (733, 738, 741-747). These organizations continuously monitor the spread of human and canine leishmaniases cases throughout the world, and keep the emergence and spread of anti-leishmanial drug resistance in *Leishmania* parasites and insecticide resistance in sandfly vectors under tight surveillance/vigilance. They also keep updating the new challenges in eliminating/eradicating the leishmaniases, educating the human populations in efficiently using the currently available anti-leishmanial drugs and insecticides and offering them with newly developed strategies for the prevention of the spread of the leishmaniases diseases (733-750). In January 2012, the WHO released a plan to control, eliminate, or eradicate 17 NTDs by 2020, and the global NTD community including pharmaceutical companies, donor and endemic countries, private foundations, civil society organizations, and others responded, with each committing to do its part to reach those goals for 10 of these diseases. This informal group was called Uniting to Combat NTDs (748). Leishmaniases, along with other NTDs and HIV/AIDS, tuberculosis, malaria and hepatitis, are widely focused by many of the worldwide health organizations for its control, prevention, elimination and eradication by 2030, according to the new agenda released for 2016-2030, by WHO (741).

1.4.12. Drug development and drug targets in *Leishmania* parasites:

Due to lack of vaccines, the current treatment of leishmaniases solely dependent on chemotherapy, but there certain challenges in the present-day antileishmanial chemotherapy including the availability of very few drugs, emergence of resistance to the existing drugs, their toxicity and lack of cost-effectiveness; and therefore, it is of utmost importance to look for effective drugs and new drug targets for the treatment of leishmaniasis (577-681). The emergence and gradual development of anti-leishmanial drug resistance in *Leishmania* parasites, as well as insecticide resistance in sandflies, which has been observed over the past few years, are raising the alarms for the development of novel anti-leishmanial drugs and insecticides (682-703). Hence, humans are continuously striving for the discovery of novel inhibitors against *Leishmania* parasites and insecticides for the sandflies. The human efforts include the discovery of new drug targets, finding new inhibitors with improved efficacies or novel modes of inhibition mechanisms, testing the synergistic effects of the existing anti-

leishmanial drugs for checking their fitness for combined therapy, exploring the alternative drug regimens, exercising the dosage pattern of the existing drugs and discovering the new formulations of the drugs for their better delivery and improved working efficiency (697-755). The prodrug approach, which is an effective way of improving the oral bioavailability of poorly soluble drugs by chemical derivatization to more water soluble compounds and topical drug delivery, is also exploited efficiently in the anti-leishmanial drug development. Human efforts also include implementation of new vector prevention methods/strategies; the pattern of IRS, the choice of insecticide for IRS, introduction of biological insecticide agents, the use of insecticidal plants and other novel strategies (697-768). Efforts for identifying and characterizing novel vaccine candidates and developing potent vaccines against *Leishmania* parasites are also underway (648-681). A welcome change is also observed in terms of flow of funds for antiparasitic drug discovery, as some of the organizations like Institute of One World Health (IOWH), DNDi, Bill and Melinda Gates foundation have had a significant impact on working towards the drug development for tropical diseases including leishmaniases (732-768).

Discovering new potent drug targets is a continuous human effort and revealed several metabolic pathways and their component enzymes, and the regulatory pathways of cellular functional machinery to be promising anti-leishmanial drug targets (769-778). These novel drug target pathways in the *Leishmania* parasites include the polyamine biosynthesis pathway, sterol biosynthetic pathway, isoprenoid pathway, glycolytic pathway, purine salvage pathway, glycosylphosphatidylinositol (GPI) glycolipids biosynthetic pathway, protein kinases (including cyclin dependent kinases ((CDKs), including CRK3 and GSK-3) and mitogen-activated protein kinases (MAP kinases, including LmxMPK1 (*Leishmania mexicana* mitogen-activated protein kinase 1) and LmxMPK2)), proteinases (proteases (peptidases), including cysteine proteinases (CPs)), folate biosynthesis pathway, glyoxalase system, trypanothione pathway, topoisomerases, ubiquitin conjugation system and hypusine biosynthesis pathway, among many others. The squalene synthase (SQS), $D^{24,25}$-sterol methyltransferase (SMT), glyceraldehyde-3-phosphate dehydrogenase (GAPDH), nucleoside transporters, hypoxanthine-guanine phosphoribosyl transferase (HGPRT), mannosyl transferases (MT), thymidylate synthase (TS), dihydrofolate reductase (DHFR), trypanothione reductase (TR), tryparedoxin peroxidase (TP), ornithine decarboxylase (ODC), arginase, topoisomerase I, topoisomerase II, deoxyhypusine synthase (DHS) and deoxyhypusine hydroxylase (DOHH) are few of the well characterized potential and promising drug targets from the *Leishmania* parasites and other trypanosomatids (769-786).

Several new anti-leishmanial drugs, targeting the aforementioned drug targets, are discovered in the last few years, and many inhibitors are designed, synthesized and tested (577-647, 697-716, 778, 782-784). Few of these targeted drugs and inhibitors with proven anti-leishmanial effects include zaragozic acids, quinuclidines, ER-119884, E5700, terbinafine (an allylamine), ketoconazole, bisphosphonates, azasterols, azoles, adenosine analogs (including N^6-(1-naphthalenemethyl)-2'-(3-methoxybenzamido) adenosine), indirubin class of chemicals (including 6-bromo substituted indirubins), 2, 6, 9-trisubstituted purines, paullones, derivatives of staurosporine (the non-specific kinase inhibitor), allopurinol, pthalic anhydride derivatives (structural analogs of purine bases, including TF1), phthalimide derivatives (including TF2), GlcNAc-PI analogs (including GlcNCONH2-b-PI and GlcNCONH2-(2-O-octyl)-PI), amphomycin (lipopeptide antibiotic), metal chelators (like EDTA), GlcN-PI analogs (including GlcN-(2-O-hexadecyl)PI), phenylmethylsulphonyl fluoride (PMSF, a serine esterase inhibitor), carbobenzoxy-phenylalanyl-alaninediazomethyl ketone (Z-Phe-Ala-CHN2), 9-anilinoacridine (used as anti-tumor agent) and other acridine derivatives, dihydrobetulinic acid (DHBA, a derivative of betulinic acid (which is a pentacyclic triterpenoid)), isoflavanoids (including 8-prenylmucronulatol, lyasperin H and smiranicin) and spermidine analogs (697-716, 778, 782-784).

The anti-leishmanial, anti-trypanosomatid, anti-parasitic drug development is in good progress, and several structure-based and mechanism-based inhibitors are discovered in the last few years which are in several stages of their development. The drugs which are in clinical trials include sitamaquine ((WR6026, lepidine), an 8-aminoquinolone), the antimycotic azoles (including ketoconazole, itraconazole, fluconazole, posaconazole and imiquimod), and few others (577-647, 697-716, 751-768). The experimental agents and lead compounds with antileishmanial activities, that are in preclinical stages (translation phase) or research phases (lead optimisation), include 2-substituted quinolines (alkaloids), 8-Aminoquinolines (including NPC1161 and tafenoquine), buparvaquone (a hydroxynaphtoquinone) [and its topical formulations, prodrugs, and derivatives (including the phosphate prodrug 3-phosphono-oxymethyl-buparvaquone)], new amphotericin B formulations (including solid nanoparticles of amphotericin B deoxycholate, novel lipid based amphotericin B formulations, N-(2-hydroxypropyl)-methacrylamide-GFLG-amphotericin B copolymer conjugates and poly(HPMA)-GFLG-amphotericin B-alendronic acid conjugates), new formulations of antimonial drugs (including the antimonial drugs entrapped into phosphatidylserine liposomes like the liposome-encapsulated meglumine antimoniate), nitroimidazooxazine (DNDi-

0690), oxaboroles (DNDi-5421, DNDi-5610 and DNDi-6148), aminothiazoles, aminopyrazoles, CGH VL series 1, CpG D35, 8-nitroquinolin-2(1H)-one series, PS-203 (4-(4,4,8-trimethyl-7-oxo-3-oxabicyclo[3.3.1]non-2-yl)-benzoic acid methyl ester), new 2,9-bis[(substituted-aminomethyl)phenyl]-1,10-phenanthroline derivatives, benzimidazole derivatives (including 2-(long chain)alkyl benzimidazoles, and 2-benzyl and 2-phenyl benzimidazoles (like (2-(4-chlorobenzyl)-1-lupinyl-5-trifluoromethylbenzimidazole))), bombinin H4 (an antimicrobial peptide) and bombinin H2, doxorubicin and its pegylated liposomal formulation (doxil, caelyx), sulphonamide nanoemulsions, benzoxaboroles (including a series of 6-substituted ureido- and thioureido-benzoxaboroles), trifluoromethyl-substituted benzo[b][1,8]naphthyridin-4(1H)-ones, 2-benzyl-5-nitroindazole-derived amines, 4-aryloxy-7-chloroquinoline derivatives, substituted 1,5-naphthyridine derivatives, triazolyl quinoline derivatives, voacamine (an indole alkaloid) and many other natural products (including plant extracts) (577-647, 697-716, 751-768, 778, 782-784, 787-801).

Many of the newly developed/discovered antileishmanial drugs/inhibitors/agents are also tested in combinations with old or new drug molecules and showed promising results. Few of these combinations include PS-203 with miltefosine, tamoxifen with meglumine antimoniate, and 4-aryloxy-7-chloroquinoline derivatives in combined therapy (756, 788, 798).

1.4.13. Hypusine biosynthesis pathway:

Hypusine (N6-(4-amino-2-hydroxybutyl)lysine) is a modified amino acid residue of specific lysine observed in the eukaryotic initiation factor 5A (eIF5A). Hypusine biosynthesis is the result of a post-translational modification occurring exclusively in the cellular protein eIF5A, by the transfer of the 4-aminobutyl moiety from spermidine to its lysine residue (802-803). Hypusine formation occurs mainly in two enzymatic steps and is studied in detail in mammals (including *Homo sapiens*), invertebrates (*C. elegans* and *D. melanogaster*), yeasts (including *S. cerevisiae*) and protists (including *L. donovani*, *Trypanosoma*, and *Plasmodium*) (804-813). The first step is catalyzed by the enzyme deoxyhypusine synthase (DHS), which catalyzes the NAD-dependent transfer of the 4-aminobutyl moiety of spermidine to a specific lysine residue of the eIF5A precursor protein to form an intermediate, deoxyhypusine (Figure 1.4). This intermediate is subsequently hydroxylated by the enzyme deoxyhypusine hydroxylase (DOHH), which completes the synthesis of hypusine and maturation of eIF5A. Biosynthesis of hypusine represents a novel, unique, and the most specific post-translational modification known in literature (802-813). Direct evidence showing the essential nature of eIF5A and DHS comes from gene disruption studies in *S. cerevisisae*; the disruption of the two eIF5A genes

(TIF51A and TIF51B) and the DHS gene produces a lethal phenotype. Although the hypusine biosynthesis pathway exists in humans and many of the protozoan parasites as well, many differences among the component enzymes of this pathway are noticed and hence validated as a drug target from these parasitic pathogens (807-816). Several antiparasitic drugs and inhibitors have been discovered based on the mechanistic and structural features of the component enzymes of this pathway, including bis- and mono-guanylated diamines and polyamines (including N-mono- and N,N'-bisguanyl derivatives of 1,6-diaminohexane, 1,7-diaminoheptane, and l,8-diaminooctane, like N^1-guanyl-1,7-diaminoheptane (GC7)), diamine and triamine analogs, difluoromethyl ornithine (DFMO), branched-chain and unsaturated 1,7-diaminoheptane derivatives (like 1,7-diamino-trans-hept-3-ene) and guanylhydrazone CNI-1493 (817-826). In mammalian cells, inhibitors of spermidine biosynthesis and hypusine biosynthetic enzymes, DHS and DOHH, exert anti-proliferative effects, including in cancer cell lines, and cause arrest of cell cycle progression (818, 820-823, 826).

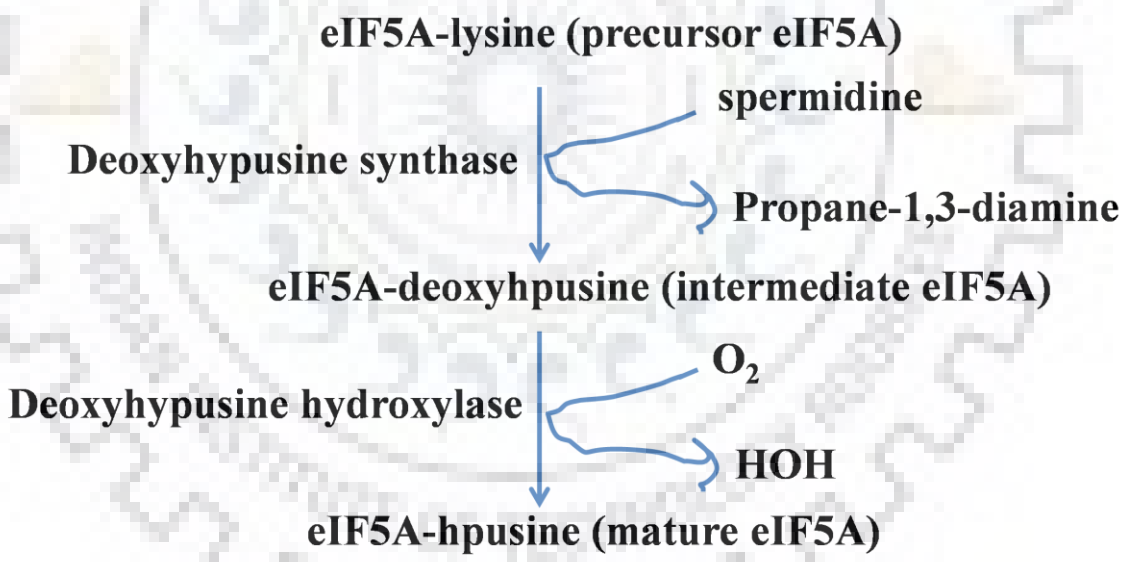

Figure 1.4. the hypusine biosynthesis pathway and its component enzymes, along with the reactions they are catalyzing.

1.4.14. Deoxyhypusine hydroxylase:

The first step in the modification of lysine to deoxyhypusine is reported to occur in all archaea. However, no orthologs of the second enzyme, DOHH have yet been reported in the archaeal genomes or proteomes. Interestingly, despite the lack of evidence for DOHH, archaeal species have been found to contain either hypusine or deoxyhypusine or both. On the contrary, there is no evidence for the occurrence of deoxyhypusine or hypusine in eubacteria (827-831). The DOHH gene is found to be essential in *C. elegans* and *D. melanogaster* but not in *S. cerevisiae*. DOHH seems to be functionally more significant in the yeast, *S. pombe*, in comparison to *S. cerevisiae*, where a mutation in the gene caused a temperature sensitive growth and abnormal distribution and morphology of mitochondria (830-833). DOHH was identified, characterized and studied in detail from several different eukaryotic organisms, including yeast, protists and mammals (including *H. sapiens*) (827-837). The structure of DOHH from humans (*Hs*DOHH) was elucidated by X-ray crystallography and is the only DOHH structure available till date (837). DOHH from several human pathogens, including the trypanosomatid protozoa *L. donovani*, *Trypanosoma*, and *Plasmodium*, was proved as a promising drug target due to its structural differences with its human homolog; and many structural and mechanistic inhibitors of parasitic DOHH were discovered for treating the parasitic diseases (838-848).

The hypusine pathway and DOHH protein from *L. donovani* (*Ld*DOHH) also proven to be promising drug targets and hence we are currently focusing in elucidating its molecular features including active site structural elements that may be helpful in antiparasitic and anti-leishmanial drug discovery using structure-based drug designing tools (813, 836). The *dohh* gene from *L. donovani* is 981 bp long and encodes a putative polypeptide of 326 amino acids. DOHH is a HEAT-repeat protein with eight tandem repeats of α-helical pairs. Four conserved histidine-glutamate sequences (HE motifs) have been identified that may act as metal coordination sites. It is a metalloenzyme and requires a di-iron active center for its activity. Alignment of the *Ld*DOHH sequence with the human homolog (*Hs*DOHH) showed two insertions in the former and one of the insertions were found to be crucial for its activity (836). Superposition of the modeled DOHH structures from human and *L. donovani* showed differences in the C-terminal His-Glu motifs and other stereo-chemical features.

1.5. Sex, gender and age differences in human resistance to infectious diseases:

Pathogens affect males and females, but the sex, gender and age differences in the host resistance and susceptibilities to infectious diseases, including the *M. catarrhalis* and *M.*

tuberculosis infections as well, are very well established in humans (849-856). Their root causes, other than the differences in the hormonal content, hormonal regulation of the host immune system, and the host responses to vaccination, remain unanswered till date.

1.5. Antimicrobial properties of estradiol and triclosan:

Triclosan (TCS), which is being used as a broad-spectrum antimicrobial for more than the past 40 years, is reported to be exhibiting endocrine-disruption and several other toxic properties due to its structural and functional similarities with many estrogen-like endocrine disrupting chemicals (EEDCs), including PCBs, BPA, PBDEs, DDT and dioxins. It also mimics the physiological activities of true estrogens, including estradiol, and hence is classified as a potential non-steroidal xenoestrogen (857-864). Triclosan and estradiol bind to several common protein targets in the biological systems including mammalian steroid hormone receptors (857-858, 860-862, 865-866), components of the steroid hormonal regulatory pathways (867-868), enzymes of steroid hormone biosynthesis/metabolic pathways (860, 869-871), and the bacterial/fungal oxidoreductase enzymes (872-874). They are also shown to exhibit antimicrobial properties against several bacterial, fungal and viral pathogens (857-858, 874-878). Triclosan exerts its antimicrobial activities by inhibiting the ENR enzyme from the type II fatty acid biosynthesis pathway and the mechanism has been elucidated at the molecular level (148-149). While few mechanisms are known for the antimicrobial actions of estradiol *in vitro* (879-880), it exerts *in vivo* antimicrobial activities through an indirect mechanism by regulating the mucosal and non-mucosal humoral immune responses, and the uterine epithelial cells (UECs) (876-878). The antimicrobial roles of estradiol, through the regulation of immune responses and polarized epithelial cells of the FRT, are crucial for the host innate immune defenses, fetal survival and perpetuation of the species (877). And they also majorly contribute to the well-established fact that females are immune-privileged and more resistant to the microbial infections than the males (850-852, 874-878).

Our current study is attempting to decipher the mechanism for the direct antimicrobial actions of 17β-estradiol which might also be contributing to the sex differences in the resistance to microbial infections in humans. In this study, it is also attempted to derive the possible similarities between the mechanisms of antimicrobial actions of triclosan, a non-steroidal xenoestrogen, and estradiol, a true steroidal estrogen.

CHAPTER 2

Biochemical and structural studies on Enoyl-ACP Reductase (ENR) from *M. catarrhalis* (*Mc*FabI) elucidating structural elements helpful in broad-spectrum drug design and identifying the target-specific antimicrobial activities of the steroid hormone 17β-estradiol

2.1. Introduction:

Moraxella catarrhalis is an opportunistic human respiratory tract pathogen and is one of the causative agents of bacterial otitis media in children, a leading cause of conductive hearing loss in children, and the exacerbations of chronic obstructive pulmonary diseases (COPD) in adults, the fourth leading cause of death worldwide (42-44). It also infects immuno-compromised patients and causes many severe pathological conditions, including bacterial sinusitis, bacterial meningitis, pneumonia and septicemia (45-57). The emergence of multi-drug resistant strains of *M. catarrhalis* over the last decade (35, 67-74, 99-118) and the current availability of very limited drugs (82-93) and no well-established vaccines against its infections (94-98), are together driving the need to develop antimicrobials with novel mechanisms of action. Therefore, it is also necessary to explore new drug targets for discovering novel antimicrobials and vaccine candidates against *M. catarrhalis* infections (121-147). Type2 fatty acid biosynthesis pathway (FASII) from pathogenic bacteria has been reported as an attractive drug target and members of this pathway including FabB, FabF, FabH, FabZ and ENR are known drug targets (148-170).

Enoyl-acyl carrier protein (ACP) reductases (ENRs) catalyze the ultimate and rate limiting step in the FAS II pathway and are the members of the short-chain alcohol dehydrogenase/reductase (SDR) superfamily. These reductases utilize the cofactor NAD(H) or NADP(H) for the reduction reaction and share a highly conserved catalytic dyad motif of Tyr-$(Xaa)_6$-Lys. FabI is the highly conserved among all known ENR isoforms; FabI, FabK, FabL, and FabV (175-221); and a proven target for few of the known antimicrobials including diazaborines, isoniazid and triclosan. Its functional, structural characterization and crystal structures are reported from various bacterial, plant and protozoan species and extensively studied from *Escherichia coli* (175-176, 187-190), *Mycobacterium tuberculosis* (191-197), *Staphylococcus aureus* (198-202), *Bacillus subtilis* (204), *Bacillus cereus* (205), *Bacillus anthracis* (206-207), *Burkholderia pseudomallei* (184), *Brassica napus* (177, 215-216), and *Plasmodium falciparum* (217-219).

Our current study is also attempting to decipher the mechanisms for the direct antimicrobial actions of 17β-estradiol which may also contribute to the sex differences in the resistance to microbial infections in humans. The sex, age and gender differences in the resistance and susceptibilities to infectious diseases, including the infections caused by *M. catarrhalis* as well, are very well established in humans (849-856) while their root causes, other than the differences in the hormonal content and their regulation of the host immune system and the host responses to vaccination, remain unanswered till date. TCS, which is being used as a broad-spectrum antimicrobial for more than the past 40years, is reported to be exhibiting endocrine-disruption and several other toxic properties, and sharing functional and structural similarities with many EEDCs (including PCBs, BPA, PBDEs, DDT and dioxins) and the true steroidal estrogens (including E2) and hence is classified as a potential non-steroidal estrogen (857-864). TCS and E2 are known to bind several common protein targets in the biological systems including mammalian steroid hormone receptors (857-858, 860-862, 865-866), components of the steroid hormonal regulatory pathways (867-868), enzymes of steroid hormone biosynthesis and metabolic pathways (860, 869-871) and bacterial and fungal oxidoreductase enzymes (872-874) and are also shown to exhibit antimicrobial properties against several bacterial, fungal and viral pathogens (857-858, 874-878). In this study it's also attempted to derive the possible similarities between the mechanisms of antimicrobial actions of the non-steroidal xenoestrogenic (estrogen-like) endocrine disrupting chemical (EEDC) triclosan (TCS), and the true steroidal estrogen 17β-estradiol (E2). TCS exerts its antimicrobial activities by inhibiting the ENR enzyme from the type II fatty acid biosynthesis pathway and the mechanism is deciphered at molecular level (148-149). While there are very few mechanisms known for the direct and indirect antimicrobial actions of E2 *in vitro* (879-880), it is exerting it's *in vivo* antimicrobial and immune activities within the human body through an indirect mechanism by regulating the mucosal and non-mucosal humoral immune responses and also through the uterine epithelial cells (UECs), which are the polarized epithelial cells lining the female reproductive tract (FRT) (876-878). These antimicrobial roles of estradiol through the regulation of immune responses and polarized epithelial cells of the FRT, which are crucial for the host innate immune defenses, fetal survival and perpetuation of the species (877), are also majorly contributing to the well- established fact that human females are immune-privileged and more resistant to the microbial infections than the males (850-852, 874-878).

In our present study, we have done the cloning, expression, purification, enzyme activity and crystallization of the ENR from *M. catarrhalis* (*Mc*FabI) and obtained its crystal structures in apo and ternary complex forms, *Mc*FabI-NAD-TCL and *Mc*FabI-NAD-EST. These Crystal structures revealed the substrate binding loop (SBL) and two more loops which play essential roles in the catalysis. We have done pharmacophore based virtual screening and obtained estradiol cypionate as one of the hit compounds. We assessed the antimicrobial properties of the major female sex hormone 17β-estradiol (E2), the physiological form of estradiol cypionate, and observed that it inhibits ~60% of *M. catarrhalis* growth at 100 μM (27μg/mL) concentration. The binding kinetics analysis by SPR showed that E2 binds to *Mc*FabI with a kD value of 5 μM, while triclosan with 4 nM. Enzyme inhibition studies revealed that triclosan inhibits the oxidoreductase activity of *Mc*FabI with a Ki value 31 nM in presence of NAD+, while E2 inhibits with a Ki value 38.1 μM. We have also determined the crystal structure of estradiol bound in the active site of *Mc*FabI, along with the cofactor NAD. The *in vitro* inhibition of *Mc*FabI by E2 is pointing to a possible mechanism for its direct *in vivo* antimicrobial activities which may be contributing to the differences in the sex and age distribution of *M. catarrhalis* cases (849). These results altogether indicate that estradiol maybe exhibiting its direct antimicrobial actions by inhibiting the FabI enzyme from the pathogenic bacteria and also hinting that these direct antimicrobial actions of estradiol may contribute to the sex differences in the resistance to microbial infections in humans.

2.2. Materials and Methods:

2.2.1. Materials

Most of the chemicals used in this study were purchased either from Sigma, Merck-millipore, Fluka, Himedia, Bio-Rad or SRL. The chromatography media and columns were procured from GE Healthcare or Bio-Rad. The molecular biology enzymes, including Taq DNA polymerase, restriction endonucleses and T4 DNA ligase are purchased from New England Biolabs (NEB). *M. catarrhalis* strain was procured from MTCC, IMTECH, Chandigarh, India; while *E. coli* DH5α and BL21 (DE3) strains and cloning and expression plasmids from Novagen (USA). The bacterial growth media were purchased either from Merck-millipore or Himedia laboratories, while the platic ware and glass ware from Tarsons and Borosil respectively.

The pre-optimized crystallization screens, including Crystal Screen, PEG/Ion, Index, Salt and Crystal Screen Cryo were purchased from Hampton Research, USA; while JCSG-plus, MIDASplus, Morpheus and PACT premier were from Molecular Dimensions, UK. The CM5

sensor chip and amine coupling reagents (EDC, NHS, and ethanolamine HCl) for SPR experiments were purchased from Biacore (Uppsala, Sweden).

2.2.2. Methods

2.2.2.1. Transformation of the *Mcfabi* gene-carrying plasmid vector:

The full length coding region of *MCRH_1153* gene from *Moraxella catarrhalis* was cloned, earlier in our laboratory by our senior colleague Dr. Shivendra Pratap, into pET28C plasmid vector using forward and reverse primers: 5' GTG AGG GTC CAT ATG TTA CTA AAA GGT CAG CGT TTT G 3' (forward) and 5' GAT TTG AAC CTC GAG TTA TTG TTC GCC GTC GCC TG 3' (reverse), containing NdeI and XhoI restriction sites respectively. The gene was cloned into pET28C vector with an N-terminal 6xHIS affinity tag and TEV protease site. The recombinant plasmid with *Mcfabi* gene was transformed into *E. coli* DH5α and BL21 DE3 cells, the cloning and expression hosts respectively. The transformation was carried out by $CaCl_2$ chemical-heat shock transformation method.

Non-transformed *E. coli* DH5α and BL21 DE3 cells were inoculated separately into 10 mL Luria-Bertani (LB) culture tubes and kept for overnight incubation at 37°C and 200 rpm speed in a Kuhner made refrigerated orbital incubator shaker. The overnight culture was centrifuged at 5000 rpm speed and 4°C for 10 mins in an Eppendorf made refrigerated table top centrifuge. The supernatant was discarded and the cell pellet was washed thrice with 5 mL of 100 mM ice cold $CaCl_2$ in each wash and 30 mins incubation was given in the last wash step. The $CaCl_2$-washed cell pellet was added with 100 µL of ice cold $CaCl_2$ and suspended with gentle mix using pipette. A 2 µL of recombinant plasmid DNA carrying the *Mcfabi* gene was added individually to the above DH5α and BL21 DE3 competent cells, and kept for incubation on ice for 20 mins with intermittent gentle mixing. The incubated cells were given quick and gentle heat shock at 42°C for 90 mins in a pre-equilibrated water bath and kept back on ice. 200 µL of autoclaved LB broth was added to each of these tubes and kept for 1-2 hrs incubation at 37°C and 200 rpm speed. The incubated transformed cells were spread on LB-KAN agar plates prepared using autoclaved LB agar culture medium added with 50 µg/mL kanamycin. The culture spread plates were kept for around 12-24 hrs incubation at 37°C.

2.2.2.2. Protein over-expression confirmation:

Single bacterial colony from each of the recombinant *Mc*FabI-6xHis-TEV-pET28C plasmid-transformed DH5α and BL21 DE3 agar plates was inoculated separately into autoclaved LB broth tubes, and kept for overnight incubation at 37°C and 200 rpm speed. These cultures were used as primary inoculums. The transformed DH5α cells were used for plasmid isolation for future needs and the BL21 DE3 cells for protein over-expression checking. A 10 mL LB broth tube was inoculated with the primary culture of the *Mc*FabI-6xHis-TEV-pET28C plasmid-transformed BL21 DE3 cells and kept for incubation at 37°C and 200 rpm speed until its OD_{600} reaches to 0.6. At this time point, the culture was subject to induction with 0.5 mM isopropyl β-D-1-thiogalactopyranoside (IPTG). After IPTG addition, the culture was further incubated at 18°C and 200 rpm for around 15-20 hrs. The cells were harvested from that incubated culture by centrifugation at 6000 rpm and 4°C for 10 mins.

The cell pellet was re-suspended in suspension buffer containing 25 mM tris-Hcl buffer pH 7.4, 100 mM sodium chloride and 2% glycerol, and cell disruption was carried out at 20 KPSI working pressure using Constant systems LTD made one shot cell disruptor, with 5-7 mL cell suspension in each shot. The cell lysate obtained after cell disruption was centrifuged at 12000 rpm and 4°C for 60-70 mins. The supernatant was separated out from the pellet containing the cell debris and the debris was dissolved in suspension buffer. The supernatant and pellet were run on 12% sodium dodecyl sulfate–polyacrylamide gel electrophoresis (SDS-PAGE) to check the presence and status of over-expression of the *Mc*FabI protein. The pre-stained SDS-PAGE protein ladder was also run along with the samples in order to confirm the molecular weights of the separated protein bands.

2.2.2.3. SDS-PAGE to confirm the protein presence and purity:

The 5% stacking gel and 12% resolving gels are prepared according to the established protocol in the laboratory that was adopted from the Laemmli method, using the components 30% acrylamide, 10% sodium dodecyl sulfate (SDS), stacking gel buffer (1 M Tris-HCl pH 6.8), resolving gel buffer (1.5 M Tris-HCl pH 8.8), 10% ammonium persulfate (APS) and N, N, N', N'-tetramethylethylenediamine (TEMED). The sample loading dye was prepared by adding both the SDS detergent and the reducing agent β-mercaptoethanol (BME) to the bromophenol blue (BPB) dye compound, along with other additives glycerol, 1 M tris-HCl buffer pH 6.8 and distilled water. The tris-glycine-SDS gel electrophoresis running buffer was used in both the tank and cassette. The SDS-PAGE was run at 80 V for 2 hrs in a vertical gel electrophoresis apparatus connected to a power supply. After completion of the electrophoresis run, the gel was

stained by coomassie brilliant blue (CBB) in 1:4:5 acetic acid:methanol:distilled water mixture, followed by destaining to visualize the stained protein bands.

2.2.2.4. Purification of *Mc*FabI protein by affinity chromatography:

After confirming the *Mc*FabI protein over-expression from the recombinant *Mc*FabI-6xHis-TEV-pET28C plasmid-transformed BL21 DE3 cells, the primary culture was used to inoculate large volumes of LB broth. One litre of broth was added with kanamycin antibiotic and 10 mL of overnight grown primary inoculum, followed by incubation at 37°C and 200 rpm speed until its OD_{600} reaches to 0.6. The culture was induced for protein over-expression using 0.5 mM IPTG, followed by incubation at 18°C and 200 rpm for around 15-20 hrs. The cells from the incubated culture were harvested by centrifugation 6000 rpm and 4°C for 10 mins.

All the purification steps were carried out at 4°C, unless otherwise mentioned. The cell pellet was re-suspended in 20 mL of suspension buffer (25 mM Tris pH 7.4, 100 mM NaCl and 2% glycerol) and ell disruption was carried out at 20 KPSI working pressure. The cell lysate thus obtained was centrifuged 12000 rpm and 4°C for 60-70 mins, using high-speed sustainable oakridge falcon tubes and the supernatant was separated out from the pellet containing the cell debris. Meanwhile a manually packed Ni^{2+}-NTA agarose affinity column having 5 mL of matrix/bed was washed properly with imidazole followed by 20-30 column volumes of water, and subsequently equilibrated with upto 10 column volumes of binding buffer. The supernatant was applied onto that buffer-equilibrated Ni^{2+}-NTA agarose column and incubated for 40-50 mins for allowing the His6-affinity tagged *Mc*FabI protein binding to the affinity matrix in the column at 4°C. Now the flow through is collected from the incubated protein-affinity matrix mixture, followed by the matrix wash with low concentration imidazole step gradient to remove the loosely bound unwanted impure proteins. A 10 mL of each 10 mM, 20 mM, 50 mM and 100 mM imidazole concentrations, that were dissolved in the binding buffer, were used to wash the column and corresponding flow through were collected in separate falcon tubes. Finally the tightly matrix-bound over-expressed His6-affinity tagged *Mc*FabI protein was eluted using 30 mL of the highest 250 mM imidazole concentration and the corresponding flow through was collected into multiple collection tubes with 5-10 mL in each. The supernatant, flow through and elution fractions collected at each purification step, along with a protein ladder sample, were run on the SDS-PAGE electrophoresis using a 12% separating gel.

2.2.2.5. Purification of *Mc*FabI protein by size exclusion chromatography:

The presence and purity of the protein fractions collected in the affinity chromatography step were analyzed in the SDS-PAGE gel. The fractions containing partially purified *Mc*FabI protein were pooled and concentrated using 10 kDa molecular weight cutoff (MWCO) amicon centrifugal filters (Merck-Millipore made) of 15 mL volume. The protein was concentrated upto 5 mg/mL concentration, which was assessed by UV absorbance-molecular extinction coefficient method. Meanwhile, a 120 mL HiLoad 16/600 Superdex 200 pg gel filtration column (GE Healthcare made), connected with the AKTA purifier 10 (GE Healthcare made), which is a fast performance liquid chromatography (FPLC) system, was very well equilibrated with 2 column volumes of gel filtration purification buffer (25 mM Tris pH 7.4 and 100 mM NaCl). After completion of equilibration, 500 µL of concentrated protein sample was loaded and eluted protein fractions, 2 mL of each, were collected from the point of void volume of the column. The elution from the column was monitored by UV absorption at 280 nm, along with other parameters including conductivity, ionic strength and pH. The protein elution was observed by the 280 nm absorption peaks and all the elution fractions corresponding to all the peaks were run on 12% SDS-PAGE gel to check for the presence and purity of the protein.

The gel filtration fractions containing purified *Mc*FabI protein were pooled and concentrated using the 10 kDa MWCO amicon centrifugal filters. The protein was concentrated upto 20 mg/mL and used for crystallization and other experimental studies.

2.2.2.6. Protein concentration measurement:

The protein concentration was assessed by UV absorbance method. Protein absorbance was measured at 280 nm using UV-visible spectrophotometer (Agilent made). Then protein concentration was calculated using the molecular extinction coefficient and gram molecular weight of *Mc*FabI protein, those were obtained by submitting the protein aminoacid sequence to the ExPASy ProtParam tool. The following formula was used for this protein concentration measurement from the A_{280}.

$$\text{Concentration(mg/ml)} = \frac{\text{A280 x GMW x DF}}{\varepsilon \text{ x } l}$$

2.2.2.7. Crystallization:

*Mc*FabI protein concentration of 20 mg/mL, in 25 mM Tris pH 7.5 and 100 mM NaCl, was used for crystalization experiments. Crystallization trials were performed at 4°C and 20°C and hanging drop and sitting drop vapor diffusion methods were employed. For apo crystals, 1 µL

of this protein solution was mixed with 1 μL of reservoir well solution containing 0.2 M calcium chloride, 0.1 M HEPES buffer pH 7.0 and 22% PEG400. After setting the crystallization experiments, the crystal trays were incubated in vibration free crystallization chambers (Rumed make) set at the appropriate temperature. Protein was set for co-crystallzation with the cofactor NADH and inhibitor compounds triclosan (TCL) and estradiol (EST) as follows for obtaining crystals of *Mc*FabI-NADH binary complex and *Mc*FabI-NADH-TCL and *Mc*FabI-NADH-EST ternary complexes. For *Mc*FabI-NADH binary complex, 20 mg/mL concentration of protein was added with 10-fold concentration of NADH and incubated for 4-5 hrs at 20°C. In case of triclosan, 20 mg/mL concentration of protein was added with 10-fold concentration of NADH and TCL and incubated similarly for 4-5 hrs at 20°C. For EST ternary complex crystals also the sample was prepared by mixing protein and NADH in a concentration ratio of 1:10 which was then added with saturated concentration of EST and incubated similarly. Thus incubated apo, binary and ternary complex mixtures of protein, cofactor and inhibitors were used for crystallization experiments as described for the apo crystals. Crystallization reservoir solution was mixed with the incubated protein binary/ternary complex solution at 1:1 ratio and set for crystallization at two different temperatures 4°C and 20°C.

2.2.2.8. Data collection, processing and refinement:

The diffraction data for well grown crystals of *Mc*FabI apo protein and *Mc*FabI-NADH-TCL were collected at home source X-ray diffraction facility, MCU lab, IIT Roorkee, India. The data were collected at 100K temperature on MAR345dtb IP detector using a Bruker Microstar Cu rotating anode X-ray generator (CuKα wavelength = 1.54 Å). 15% glycerol in reservoir solution was used as cryo-protectant to improve the diffraction pattern quality. The data for *Mc*FabI-NADH-EST ternary complex were collected at the European Synchrotron Radiation Facility (ESRF, Grenoble) beamline ID30A-3, France, equipped with Eiger X 4M detector.

The data collected, at the home source, from apo crystals and *Mc*FabI-NADH-TCL ternary complex crystals were processed; indexed, integrated and scaled; using the HKL2000 suite (881), while the data collected, at the ESRF beamline, from *Mc*FabI-NADH-EST complex crystals were indexed, integrated and scaled using XDS and AIMLESS as implemented in autoPROC (882). The image files were autoindexed and the suitable spacegroup with highest possible symmetry group, was selected during the autoindexing step for further processing of the image files. All the possible parameters including detector parameters, crystal parameters,

crystal to detector distance, unit cell parameters, rotation angle, ice ring, spot size and mosaicity were properly inspected during this step. It was followed by integrating the full set data, which was monitored by examining the $\chi 2$ value, and subsequently scaling it using global refinement method during which the unit cell parameters were refined again for whole data set and crystal slippage and imperfect goniostat was opted. During scaling step of data processing, both merge and unmerge (using Macros option) output files were prepared and the log files of this step were carefully observed to know the goodness of the data, data completeness and the resolution of the data upto which it can be used for further structure solution of the crystallized protein.

The scalepack output file (.sca format) was converted to .mtz file format in order for the processed data to be used by CCP4i and PHENIX suites. The crystal unit cell contents were assessed by calculating the crystal's Mathews coefficient and the best suitable space group of the crystal was analysed by pointless program of CCP4i.

The initial phases for *Mc*FabI were obtained by molecular replacement with MOLREP (883) and BALBES pipeline (884) of the CCP4 suite (885-886) using the processed .mtz data file, *Mc*FabI protein primary sequence and the protein atomic coordinates of a single subunit of *A. baumannii* FabI crystal structure (PBD ID: 4ZJU) as a search template. The output from the MOLREP program was analysed in the molecular building and visualization tool COOT. REFMAC5 (887) program of CCP4i suite and phenix.refine program from PHENIX (888-889) suite were used for refinement of the initial coordinates obtained from molecular replacement. Initially rigid body refinement was carried out and restrained refinement in the subsequent cycles of refinement, along with TLS and NCS refinement parameters. After each round of refinement of the protein atomic coordinates, the model building of the coordinates was carried out in the COOT tool with proper real space refinement (RSRZ). Iterative cycles of model building and refinement were performed by COOT (890) and REFMAC5/PHENIX. The progress, correctness and goodness of the refinement and model building were monitored by refinement statistics including the values of R_{work} and R_{free}. Once the protein coordinates were fit and refined properly, the water (solvent) molecules were added in the Fo-Fc difference map at 2.5σ using the other modeling tools option in the COOT and subsequently refined. Protein atomic coordinates of a single monomer from the final refined model of apo *Mc*FabI protein were used as initial template for solving the X-ray diffraction data collected for the *Mc*FabI-NADH-TCL and *Mc*FabI-NADH-EST ternary complex crystals. Protein chains were fit and refined properly and then density for the NADH and TCL/EST ligands was searched in the Fo-

Fc difference map at 2.5σ and fit properly in the match density using other modeling tools and real space refinement options of COOT. The ligand coordinates were imported into COOT from its monomeric compound/ligand dictionary.

2.2.2.9. Validation of the refined PDB structures:

During manual model building in the COOT, real space refinement was done using real space refine zone (RSRZ) option after every fit and validation and analysis tools, including geometry analysis, rotamer analysis, density fit analysis, Ramachandran plot analysis, temperature factor analysis, incorrect chiral volumes, unmodelled blobs and peptide omega analysis, were used for initial validation of the atomic model during its development. The stereo-chemical attributes of refined models were validated by MOLPROBITY (891). Further validation of the completely refined models was carried out by the PDB validation tool of the wwPDB deposition suite.

The data collection and refinement statics were calculated using the information contained in the log files (.log), that were written and obtained after every step of data processing and refinement, and are given in table 2.1.

2.2.2.10. Sequence and structure analysis:

The *Mc*FabI protein sequence was compared with homologous proteins from other bacterial species by multiple sequence alignment using the ClustalΩ tool (892-894). The amino acid sequences of FabI proteins of *Escherichia coli* (*Ec*FabI), *Pseudomonas aeruginosa* (*Pa*FabI), *Acinetobacter baumannii* (*Ab*FabI), *Francisella tularensis* (*Ft*FabI), *Burkholderia pseudomallei* (*Bp*FabI), *Neisseria meningitides* (*Nm*FabI), *Bacillus subtilis* (*Bs*FabI), *Bartonella henselae* (*Bh*FabI), *Helicobacter pylori* (*Hp*FabI), *Staphylococcus aureus* (*Sa*FabI) and *Mycobacterium tuberculosis* (*Mtb*FabI), were collected from the NCBI protein database in the FASTA format. All these sequences were submitted together to the ClustalΩ tool and the output options were chosen to be clustal file with numbering and percent identity matrix (PIM). The multiple sequence alignment file was analysed manually for the homology and conserved amino acid sequence regions and the presence of insertions or deletions. The evolutionary relationships of the FabI, FabK, FabL, FabV, FabG, all isoforms of the mammalian 17β-hydroxysteroid dehydrogenases, and fungal and bacterial OYE family oxidoreductases were also analysed by phylogenetic tree construction using the MEGA7 program (929).

The secondary structural features of these aligned sequences were comparatively analysed by ESPript (895), using the *Mc*FabI structure as template. The multiple sequence alignment file, obtained from the ClustalΩ tool, along with a single polymeric protein chain from the refined and validated final PBD format *Mc*FabI-NADH-TCL protein model, as a template PDB structure, was submitted to the ESPript server for calculating the conserved and homology secondary structural features among the FabI structures from various pathogenic bacteria.

2.2.2.11. Tertiary and quaternary structure analysis:

The secondary, tertiary and quaternary structural features of the final refined and validated apo *Mc*FabI, *Mc*FabI-NADH-TCL and *Mc*FabI-NADH-EST ternary complex structures were initially analysed and compared manually using the 3-D visualization tools like PyMOL (896), Discovery Studio Visualizer (897), Chimera (898) and COOT. This initial analysis include the type and amount of secondary structural elements (α-helices, β-sheets and random loops), number and type of domains present in each protein polymeric chain, number of protein chains present in the entire protein model and their arrangement in 3-D space. The protein-ligand interactions were also analysed using the same tools. The protein volume and volumes of all the cavities, active sites and ligand binding pockets were calculated using the tool.

The PDB structures of FabI from other bacterial species were downloaded from the RCSB PDB database and used for comparative analysis with the *Mc*FabI protein, which was carried out manually in the 3-D visualization tools like PyMOL, Discovery Studio Visualizer, Chimera and COOT. The distant structural homologues of *Mc*FabI protein were searched by the DaliLite server (899-900). A single polymeric protein chain from the *Mc*FabI-NADH-TCL structure was submitted to the DaliLite server and the output structures were analysed and inspected for homology by monitoring the Z-score and RMSD values.

2.2.2.12. Protein subunit and ligand interface analysis:

Subunit interface analysis was carried out by PDBe PISA server (901). The final refined quaternary structures of apo *Mc*FabI, *Mc*FabI-NADH-TCL and *Mc*FabI-NADH-EST complex structures, containing the crystal symmetry operators, were submitted individually to the PISA server. Different aspects of the interfaces were analysed including total surface area (solvent exposed area), buried area and interface area. Subunit-subunit interface interactions were analysed for salt bridges, hydrogen bonds, covalent bonds and disulfide bonds. The subunit-ligand and ligand-ligand interface areas and interactions were also analysed in the similar way.

The structural figures for all the structural analyses, including quaternary structure poses, subunit arrangements, secondary structural arrangements, domain organization, 3-D structural comparisons and subunit-subunit and subunit-ligand interface interactions, were prepared using PyMOL.

2.2.2.13. Pharmacophore modelling and virtual screening:

After obtaining the fully refined *Mc*FabI structure, the polypeptide chain containing all the structural elements of the full length protein was extracted, along with the bound NAD cofactor molecule, from the *Mc*FabI-NADH-TCL ternary complex for pharmacophore-based virtual screening. The FabI inhibitor compound AFN-1252 was chosen and docked into *Mc*FabI monomeric structure, using AutoDock (902) and Autodock Vina (903). The *Mc*FabI-AFN-1252 docked structure was used for pharmacophore model generation by Receptor-Ligand Pharmacophore Generation (RLPG) protocol (904-906), available in the Discovery Studio suite (BIOVIA) (897). The RLPG protocol was applied by defining the parameters: (i) the minimum and the maximum number of selected features were set at 5 and 6, respectively, (ii) the maximum number of excluded volumes (EV) at 5, and (iii) energy threshold value set at 20. Ten pharmacophore models were generated on the basis of protein-ligand interactions and they were ranked on the basis of fit value, sensitivity and specificity. The best pharmacophore model was selected for further screening of the small molecule drug database. The L1300-Selleck-FDA-Approved-Drug-Library (Selleckchem), a commercially available small molecule library (5.22), having 1443 compounds was used for virtual screening. All this processing was done using the DS suite.

2.2.2.14. Molecular docking:

The top hit compounds obtained from the virtual screening were docked into the template *Mc*FabI protein using AutoDock and Autodock Vina (902-903) in order to calculate the binding energies of those compounds at the active site of *Mc*FabI. Protein and ligand files were prepared by using AutoDock tools (902) according to the standard protocol. Protein file was prepared by removing any bound ligand molecules except for NAD and water; and adding Kollman charges and hydrogen atoms. Final hits were docked in the active site using the Lamarckian genetic algorithm (LGA) and the Grid centred at (29.58, 11.972, 17.167) 24×22×36 dimension with the default spacing (0.375 Å). The lowest energy conformation of the docked ligand was interpreted as the best pose. Results were analysed using PyMol and

Discovery studio visualizer. We also docked estradiol into the active site of InhA using the same protocol.

2.2.2.15. *Mc*FabI enzyme activity studies:

The purified *Mc*FabI protein was checked whether it's enzymatically active by measuring it's substrate catalytic activity. Although its real substrate *in vivo* is an acyl-ACP, i.e. an ACP-bound fatty acyl molecule, we have alternatively used crotonoyl-CoA (CCA), a Coenzyme-A bound crotonic acid (2-butenoic acid) which is a well established alternative substrate for enoyl-ACP reductase enzymes, to measure *Mc*FabI enzyme activity. The *Mc*FabI enzyme activity was measured by two methods: (i) Monitoring the consumption of NADH by spectrophotometrically measuring the decrease of UV absorbance at 340 nm (176) using an UV-visible spectrophotometer and (ii) Monitoring the consumption of NADH, during the course of enzymatic reaction, by measuring the decrease of fluorescence emission at 460 nm upon excitation at 340 nm (211, 907-908) using a fluoresecence measurement equipped micro-plate reader. All the enzyme activity measurements were carried out at 25°C. The enzyme was purified as described in the previous sections and the CCA substarte, NADH cofactor and buffer solutions were prepared before start of the measurements. The enzyme reactions were optimized for suitable protein and cofactor concentrations and buffer type also. Finally, the enzyme activity was measured using an optimized 100 µL of final standard reaction mixture containing 50 mM sodium phosphate buffer pH 7.5, 200 µM NADH, 5 µM of purified *Mc*Fabi protein, and variable concentrations of CCA between 100 µM and 1600 µM in order to measure the effect of the substrate on efficiency of the enzyme and its affinity towards enzyme. Enzyme kinetics reaction was monitored for initial 40 mins and absorbance/fluorescence data were recorded.

After collecting the absorbance/fluorescence data, the absorbance change or relative fluorescence change was plotted against time and initial enzyme velocity, corresponding to each substrate concentration, was measured from it. The initial enzyme velocities, calculated for all substrate concentrations, were plotted against substrate concentrations used in the experiment. Subsequently the data were fitted to Michaelis-Menten equation by linear regression, followed by plotting the reciprocals of initial enzyme velocities and corresponding substrate concentrations to generate Lineweaver-Burk double reciprocal plot in order to calculate the enzyme kinetic constants K_M, V_{max}, K_{cat} and K_{cat}/K_M.

2.2.2.16. Enzyme inhibition studies:

The enzyme inhibition studies were carried out for the inhibitors triclosan and estradiol to check their effect on *Mc*Fabi activity by varying the substrate concentration at different fixed concentrations of inhibitors; triclosan at 50, 100, 150 and 200 nM concentrations, while E2 at 12.5, 25, 50 and 100 µM concentrations. For inhibition studies, the enzyme, NADH and inhibitor mixtures were incubated for 5h at 4°C in the presence of 100 µM NAD^+ before adding the substrate at the time of kinetic data collection. The data collected for *Mc*Fabi activity in presence of the two inhibitors were analysed by plotting the enzyme velocities in presence of the inhibitors versus the substrate concentrations used. Subsequently the inhibition constant (Ki) values for the inhibitors were calculated from the secondary plots of the Y-intercepts from the LB plots versus inhibitor concentration. The corresponding graphs were prepared using the Microsoft Excel program.

2.2.2.17. MIC determination:

Bacterial growth inhibition studies were carried out by measuring the minimum inhibitory concentrations (MIC) of the inhibitors TCL and EST. The MIC values were determined by the microbroth dilution assay according to the Clinical and Laboratory Standards Institute (CLSI) methods for antimicrobial susceptibility tests for aerobically growing bacteria (909-910). *M. catarrhalis* was grown in Mueller–Hinton (MH) broth to mid-log phase till its OD at 550 nm reaches to 0.2 and diluted in MH broth to 1000-fold which is expected to contain 4×10^5 CFU/mL, for its usage as seed inoculum in bacterial growth inhibition studies. Serial dilutions of the inhibitor compounds were made in MH broth and used at concentration range 0.25 µg/mL-58 µg/mL for TCL and 0.1 µg/mL-27.2 µg/mL for estradiol, in 96-well microtiter plates. DMSO controls were also used at appropriate concentrations in MH broth to check its effect on bacterial growth. After making proper dilutions of the inhibitors and all the controls in 96-well plate, the *M. catarrhalis* bacterial inoculum was added to compound dilutions at 1:1 proportion and plates were incubated at 37°C for 12-24 hrs. The MH plain broth without inhibitor but added bacterial inoculum was used as positive control and MH plain broth with neither inhibitor nor bacterial inoculums as negative control. The bacterial growth was visually inspected and also measured spectrophotometrically at 600 nm.

2.2.2.18. Binding kinetics studies by SPR:

The protein-ligand binding interactions were analysed by surface plasmon resonance (SPR) technique by using Biacore T200 (GE Healthcare) instrument. *Mc*FabI that was purified to highest homogeneity was immobilized at ~4,000 RU level on active flow cell (Fc2) of CM5

sensor chip by standard amine-coupling procedure using the immobilization reagents EDC, NHS, and ethanolamine HCl, and 10 mM sodium acetate buffer pH 4.0 and HBS (HEPES-buffered saline: 20 mM HEPES, 150 mM sodium chloride, pH 7.4) as the immobilization buffer and running buffer respectively. But the reference flow cell (Fc1) was simply activated by EDC and NHS, followed by deactivation with ethanolamine HCl, using the same protocol. The binding of cofactor and inhibitors was assessed by binding analysis carried using the appropriate analyte concentration series. The sequence of estradiol concentrations used for binding kinetics and affinity analysis include 0.39, 0.78, 1.56, 3.125, 6.25, 1.56 and 12.5 µM, with an additional repeat of 1.56 µM concentration. The binding kinetics studies were performed by collecting the data at 25°C by injecting the concentration series of anlytes over reference and active flow cells with injection parameters: 30 µL/min flow rate and 30 s association and dissociation phases. Each concentration of analyte was analysed in triplicate injections in random order, with buffer blanks injected periodically for double referencing (911), which includes two references: (i) analyte response over reference cell and (ii) zero (0) concentration analyte sample response over both active and reference flow cells. The binding kinetics data were analysed by the Biacore evaluation software using the "surface bound" kinetics evaluation module.

2.2.2.19. SAR (Structure-activity relationship) studies:

These studies were carried out by analyzing the *Mc*FabI-NADH-TCL and *Mc*FabI-NADH-EST ternary complex structures and comparing the inhibitor interaction pattern in the enzyme's active site with the enzyme's catalytic mechanism, with special attention on the inhibitors' interactions with the enzyme's residues participating in the mechanism of catalysis. Crotonoyl Co-A, the alternative substrate of FabI enzymes, was also docked into the active site of *Mc*FabI-NADH protein binary complex, extracted from the *Mc*FabI-NADH-TCL ternary complex, using the same protocol described in the previous sections. The interactions of 2-butenoyl moiety of the docked Crotonoyl Co-A with the catalytic residues were compared with that of inhibitors.

2.2.2.20. CD spectroscopy studies:

The *Mc*FabI protein was analysed for its various biochemical properties, including thermal stability, resistance to denaturants, pH stability and ionic strength sustainability. These studies were carried out using JASCO circular dichroism spectroscopy. 10 µM *Mc*FabI protein, purified to its highest homogeneity, in 20 mM sodium phosphate buffer (without any salt) was

used for spectroscopy analysis and the experiment was carried out using 200 µL sample in 0.1 mm cuvette. The far UV spectral scan was recorded from 260-190 nm, at 1 nm band width. (i) The thermal stability of the protein was studied in the temperature range 25°C - 100°C; (ii) the resistance to denaturants was assessed by using 0.1 M – 8 M concentration range of urea and guanidine hydrochloride (GnHcl); (iii) the pH stability was analysed by using different buffers in the range 4.0 – 9.0; and (iv) the ionic strength sustainability was checked by using 0.1 M - 1 M salt strength. Before the start of sample analysis, the buffer was used to take the blank readings in the same scan range. The results were analysed in the Microsoft Excel and Origin softwares.

2.2.2.21. Intrinsic fluorescence studies:

The protein *Mc*FabI is having 3 tryptophan residues (Trp21, 81 and 241) and 5 tyrosine residues (Tyr38, 126, 151, 161 and 177) which can exhibit protein intrinsic fluorescence. This property of *Mc*FabI was analysed by Fluorolog 3 fluorescence spectroscopy (Fluorolog 3 spectrofluorometer) (HORIBA scientific). The protein's intrinsic fluorophores were excited at 280 nm and 295 nm to analyse the protein's overall fluorescence properties and exclusively tryptophan fluorescence respectively. The emission spectrum was collected in the range 300 nm - 500 nm, at both the excitation wavelengths. 1 mL of 0.25 µM protein solution in 20 mM sodium phosphate buffer was used for spectral analysis and the experiment was carried out at 25°C using 1mm quartz cuvette. Before the start of sample analysis, the buffer was used to take the blank readings in the same scan range. The results were analysed in the Microsoft Excel and Origin softwares.

2.2.2.22. Biophysical characterization by Differential scanning calorimetry:

The thermodynamic properties of *Mc*FabI protein were assessed by differential scanning calorimetry (DSC) analysis using the VP-DSC instrument (GE Healthcare made). The thermal denaturation analysis was carried out for apo *Mc*FabI, *Mc*FabI-NADH binary complex, and *Mc*FabI-NADH-TCL and *Mc*FabI-NADH-EST ternary complex structures. The thermal scan was carried out from 10°C to 90°C at 1°C per minute scan rate, with 10-minutes long pre-thermostat scan at 10°C, and 10 µM *Mc*FabI protein was used for the thermal scanning experiments in DSC. A 10 µM *Mc*FabI was added with 10-fold concentration of NADH, TCL and NADH, and EST and NADH compounds, in order to make *Mc*FabI-NADH binary complex form, and *Mc*FabI-NADH-TCL and *Mc*FabI-NADH-EST ternary complex forms respectively, and incubated at 20°C for 5-6 hrs before using for DSC analysis. The suitable

references were chosen for each experiment and 500 μL of sample and reference solutions each were loaded into sample and reference cells respectively. Reference solution, in all the cases, contains all the components that of the sample, except for the protein. Proper pressure was maintained throughout all the scans. The reference baseline was obtained in the initial 3-4 scans using the reference solution in both the cells (sample and reference) and then the sample was loaded to scan for the sample. The results were analysed using the Origin software provided with the instrument.

2.2.2.23. Binding studies using Isothermal titration calorimetry:

The *Mc*FabI protein-ligand binding interactions were assessed by isothermal titration calorimetry (ITC) using the Microcal ITC200 instrument (GE Healthcare made). The two interacting partners include protein (macromolecule/receptor) and ligand (small molecule) that were loaded into cell and syringe of the instrument respectively, while distilled water was loaded into the reference cell. The ligand component was used in higher concentrations than that of the protein component, starting from 10-folds to several. 10 μM *Mc*FabI was used in the experiments while NADH cofactor and/or inhibitors were used at 20 μM concentration for interaction studies. In case of the *Mc*FabI-NADH-TCL and *Mc*FabI-NADH-EST ternary complex interaction analyses, protein was incubated with the cofactor in advance and the equal amount of cofactor NADH was added in both the protein and ligand solutions. The experiments were carried out in highest quality mode at 25°C analysis temperature with the paramer settings including 18 injections, 2 μL injection volume, 180 s spacing and 1000 rpm stirring speed, while the initial injection was only 0.5 μL to monitor the system aberrations before collecting the data. All the solutions used in the ITC experiments including the reference solution, protein and ligand solutions were filtered and degassed thoroughly before usage. 200 μL of reference and protein macromolecule sample solutions were loaded manually into the reference and sample cells respectively, while 40 μL of ligand small molecule solution was loaded by automated mode into the syringe. Buffer-buffer, buffer-protein and buffer-ligand interaction scans were also recorded using the same experimental settings. The results were analysed using the Origin software provided with the instrument.

2.2.2.24. Inhibitor binding and protein oligomeric state analysis by Native-PAGE:

Native-PAGE analysis was carried out to check the *Mc*FabI protein's oligomeric state in its apo form, *Mc*FabI-NADH binary complex form, and *Mc*FabI-NADH-TCL and *Mc*FabI-NADH-EST ternary complex forms. The 12% native PAGE gel was prepared by using the same

protocol explained for the SDS-PAGE, except for the differences including (i) all the gel preparations are done without use of SDS detergent (ii) gel electrophoresis running buffer was made without SDS (iii) the sample loading dye was prepared without the reducing agent(s) β-mercaptoethanol (BME) and detergent SDS (iv) protein samples were not boiled after addition of the native PAGE dye (v) the electrophoresis run was carried out at 4°C inside a freezer chamber to maintain the temperature of the buffer during run. Low voltage and current were used during this run. In case of binary and ternary complexes, the *Mc*FabI protein was incubated with its ligand partners for 5-6 hrs before native PAGE run. A 35 µM (1 mg/mL) *Mc*FabI protein was added with 10-fold concentration of NADH, TCL and NADH, and EST and NADH compounds, in order to make *Mc*FabI-NADH binary complex form, and *Mc*FabI-NADH-TCL and *Mc*FabI-NADH-EST ternary complex forms respectively, and incubated at 20°C for 5-6 hrs before native PAGE run. A 15 µM (1 mg/mL) bovine serum albumin (BSA) protein was prepared and loaded into native PAGE along with our test samples, as a protein marker/reference. After run, the gel was stained and destained in the same way as done for the SDS-PAGE gel.

2.2.2.25. MD simulations:

The crystal structures obtained for the *Mc*FabI protein were subjected to molecular dynamics simulations to check their conformational stability. GROningen MAchine for Chemical Simulations (GROMACS) version 5.1.4 installed on a graphical processing unit (GPU) was used for the simulation studies (912). The topology for the protein polypeptide chains was prepared by the GROMOS43a1ff (Gromos43a1 force field) of GROMACS software, while the topology files for the cofactor (NADH) and inhibitor compounds (TCL and EST) were prepared by PRODRG server (939-940). Simple point charge (Spc) water model was used to solvate the protein in a cubic box. The "protein in water" system was neutralized by adding Na^+ and Cl^- ions and also the system was added with 150 µM extra amount of salt to mimic the biological buffering system. The xyz 3-D periodic boundary condition (pbc) was used to eliminate the surface effects and to maintain minimum image convention. A solute-box distance of 1.0 nm was used to maintain at least 2.0 nm between any two periodic images of a protein. The solvated, electro-neutral system was energy minimized to ensure that the system has no steric clashes or inappropriate geometry and it is relaxed properly. Vacuum minimization was done by steepest descent minimization algorithm and 50000 number of minimization steps. During the energy minimization step, the Verlet cutoff-scheme was used for neighbor searching, the simple grid method was used to determine the neighbor list,

treatment of long range electrostatic interactions was done by particle mesh Ewald (PME) electrostatics algorithm, maximum force to be achieved was set to < 1000.0 kJ/mol/nm and both short-range electrostatic and van der Waals cut-off were set to 1.0. Standard cut-off of 1.0 nm was used for both the neighbour list generation and the coulomb and Lennard–Jones interactions.

The position restrained parameters prepared for the protein, cofactor and inhibitors were used to apply a position restraining force on the heavy atoms of the protein (anything that is not a hydrogen), to avoid unnecessary distortion of the protein–ligand complex. The energy minimized system was equilibrated in 2 methods for 50 ns each: (i) NVT (constant Number of particles, Volume and Temperature) equilibration, which is also referred to as "isothermal-isochoric" or "canonical" ensemble, at 300 K reference temperature and (ii) NPT (constant Number of particles, Pressure and Temperature) equilibration, which is also referred to as "isothermal-isobaric" ensemble, at 1.0 bar reference pressure. Both the equilibration steps include two temperature coupling groups (tc_groups) comprising (i) the protein group: *Mc*FabI, *Mc*FabI_NADH, *Mc*FabI_NADH_TCL and *Mc*FabI_NADH_EST, in case of apo, binary and ternary complex forms respectively, and (ii) non-protein group: water_ions, in case of all the four simulations. During NVT equilibration, only temperature coupling (V-rescale modified Berendsen thermostat algorithm) was on, while both temperature coupling (V-rescale modified Berendsen thermostat) and pressure coupling (Parrinello-Rahman barostat) were on during the NPT equilibration.

The system that was well-equilibrated at the desired 300 K temperature and 1.0 bar pressure was used for production MD run. 50-ns MD run was executed with 25000000 steps and data were collected with 2 fs step size. During production MD run both the temperature and pressure coupling were on and the elctro-statistics were using PME algorithm. The production MD data were analysed for the stability of the polypeptide structure and complex stability by calculating the root-mean-square displacement (RMSD) of all the protein heavy atoms, i.e. non-hydrogen atoms, with respect to the starting structures. The time-dependent potential energy of the system and the root mean square fluctuation (RMSF) of all the protein residues were calculated, and the hydrogen bond pattern analysis between protein and the ligands was also carried out.

2.3. Results

2.3.1. Cloning, Expression and Protein purification:

The recombinant pET28C-6xHis-TEVP-*fabi* plasmid carrying the *MCRH_1153* gene from *M. catarrhalis* was successfully transformed into *E. coli* DH5α and BL21 (DE3) cells. IPTG induction of *E. coli* BL21 (DE3) cells harboring pET-28a(+)-*Mc*FabI vector resulted in over-expression of *Mc*FabI protein. Purification by Ni-NTA affinity chromatography resulted in homogeneous protein in the high imidazole concentration elutions (figure 2.1).

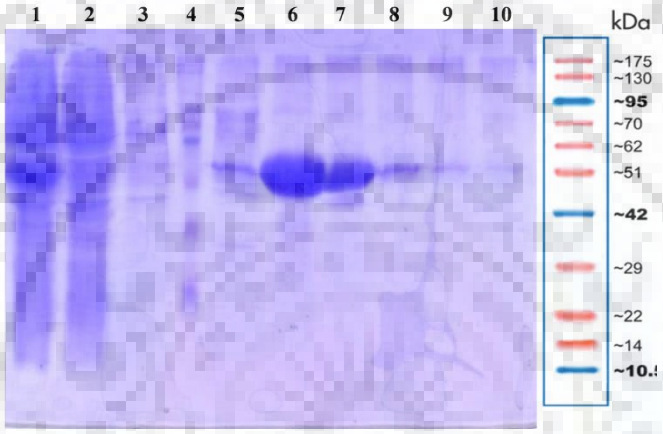

Figure 2.1: SDS-PAGE profile of the *Mc*FabI purification by Ni-NTA chromatography. Lane 1: supernatant, lane 2: supernatant flow through, lanes 3: eltion with purification buffer, lane 4: pre-stained protein ladder, lanes 5-10: elutions with imidazole concentrations.

When the apo protein was loaded onto superdex 200 pg column, we observed a chromatogram with two small UV 280 absorbance peaks at 45 mL and 55 mL, while a major peak at 72 mL with a shoulder edge at 80 mL elution volume (figure 2.2). These peak positions correspond to the different oligomeric states of the protein, monomer, dimer, tetramer and higher order oligomers, which were observed by the native PAGE. As a result, it is confirmed that *Mc*FabI protein exists majorly in tetrameric form in solution. The gel filtration separation also resulted in purified protein without any impurities (figure 2.3).

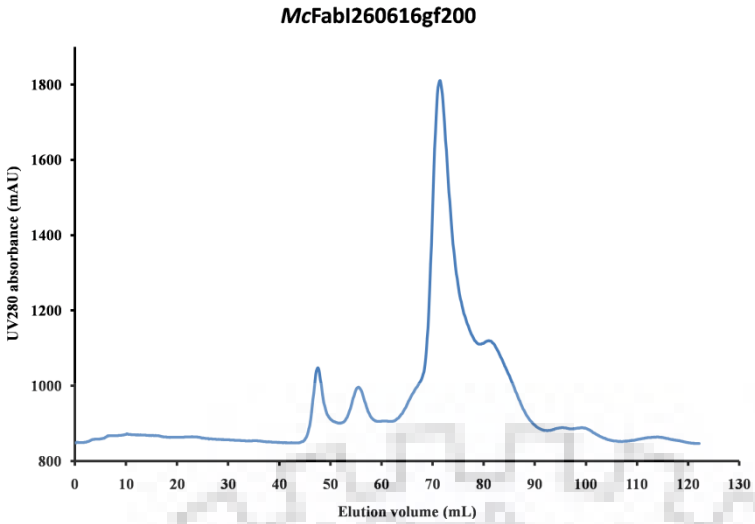

Figure 2.2: The size exclusion chromatography profile of the wild-type apo *Mc*FabI protein purification by Superdex 200 pg gel filtration column.

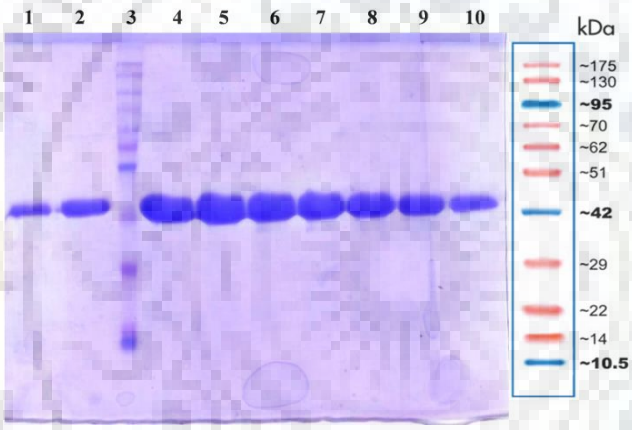

Figure 2.3: SDS-PAGE profile of the elutions obtained from the size exclusion chromatography of the wild-type apo *Mc*FabI protein purification by Superdex 200 pg gel filtration column.

2.3.2. Crystal structures:

The crystal structures of *Mc*FabI in apo form and *Mc*FabI-NAD-TCL and *Mc*FabI-NAD-EST ternary complex forms were determined at 2.4, 2.3 and 2.2 Å resolutions respectively. The corresponding crystallographic data and refinement statistics are presented in table 2.1. Crystals of apo *Mc*FabI belong to $P\ 4_2\ 2_1\ 2$ space group and refined to final R_{work} and R_{free} of 21.3% and 25.9% respectively, with one monomer in the asymmetric unit; whereas the crystals of TCL ternary complex belong to $P\ 2_1$ space group and refined to final R_{work} and R_{free} of 16% and 22.2% respectively, with one tetramer in the asymmetric unit; while the crystals of EST ternary complex belong to $P\ 2_1$ space group and refined to final R_{work} and R_{free} of 19.2% and 27.6% respectively, with one tetramer in the asymmetric unit (Figure 2.4). Electron density is missing

for 3 loop regions in the apo structure; Phe98-Thr112 (substrate binding loop 2, SBL2), Gly153-Tyr161 (active site loop, ASL) and Ser203-Phe208, the substrate binding loop (SBL); while present with full occupancy in both the ternary complex structures (Figure 2.4 and 2.5), indicating that these loop regions are disordered/flexible in the absence of cofactor and inhibitor binding. There is no interpretable density observed for few residues at the C-terminus in all the three *Mc*FabI structures solved.

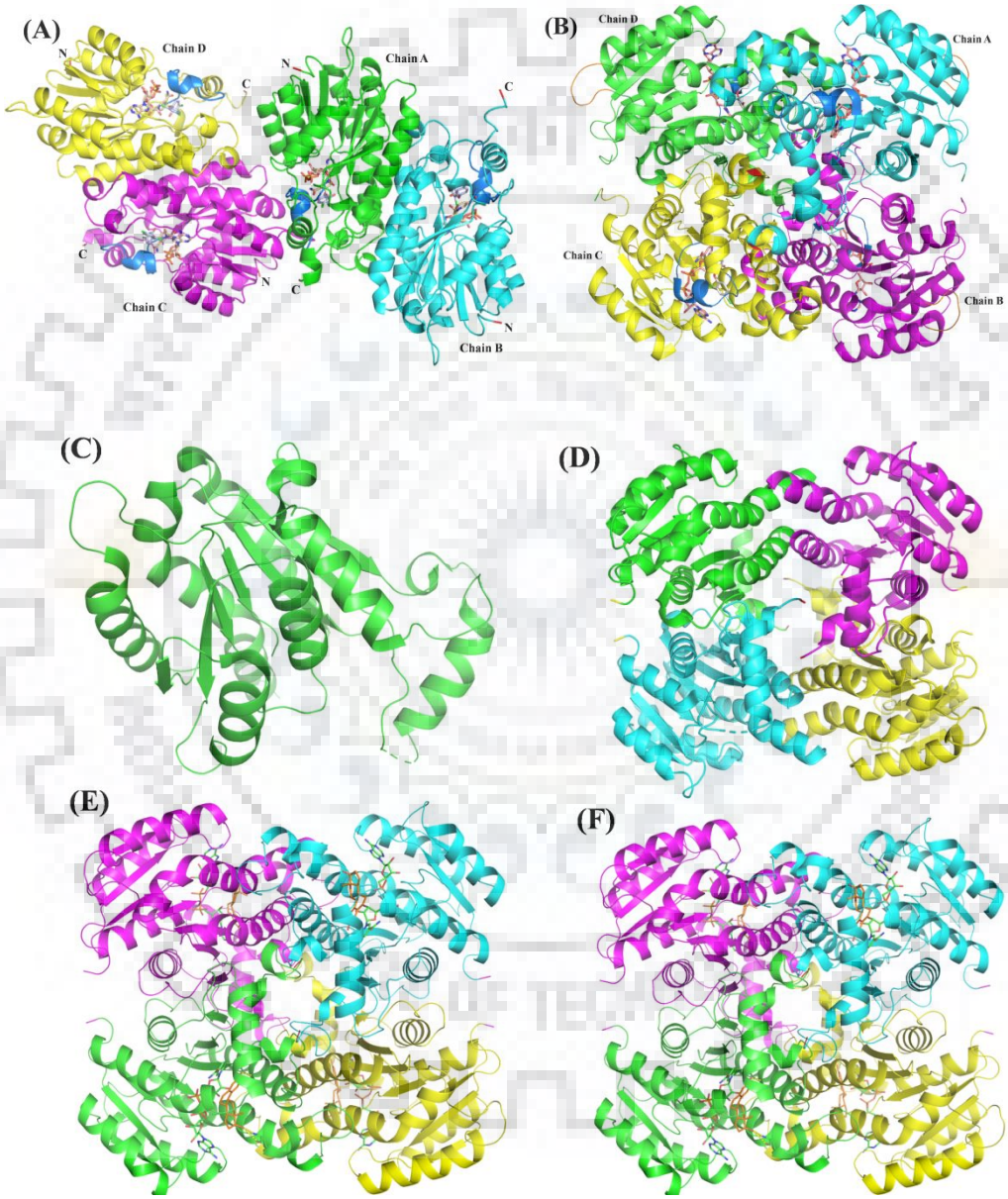

Figure 2.4: The crystallographic asymmetric unit and biological assembly states of the *Mc*FabI protein in its apo form, and *Mc*FabI-NAD-TCL and *Mc*FabI-NAD-EST ternary complex forms. **(A)**, **(C)** and **(E)** are the asymmetric unit states of the TCL ternary complex, apo, and EST ternary complex forms respectively, while **(B)**, **(D)** and **(F)** are their biological assembly states respectively.

Table 2.1: Data collection and refinement statistics

	*Mc*FabI-apo	*Mc*FabI-NAD-TCL ternary complex	*Mc*FabI-NAD-EST ternary complex
Wavelength (A°)	1.54	1.54	0.967
Resolution range	31.84 - 2.38 (2.465 - 2.38)	34.77 - 2.224 (2.303 - 2.224)	35.71 – 2.121 (2.196 - 2.121)
Space group	$P\ 4_2\ 2_1\ 2$	$P\ 2_1$	$P\ 2_1$
Unit cell	74.9 74.9 101.4 90 90 90	78.5 75.5 89.2 90 90 90	76.5 76.5 99.7 90 90 90
Total reflections	123196 (9936)	100664 (7133)	192954 (19088)
Unique reflections	12145 (1171)	48274 (4678)	49378 (4582)
Multiplicity	10.1 (8.4)	2.1 (1.6)	11.1 (11.3)
Completeness (%)	99.69 (98.57)	98.90 (92.03)	99.20 (93.27)
Mean I/sigma(I)	30.47 (4.86)	8.80 (1.64)	22.32 (0.82)
Wilson B-factor	50.03	33.53	63.39
R-merge	0.065 (0.496)	0.111 (0.502)	0.048 (2.728)
R-meas	0.068 (0.528)	0.143 (0.670)	0.051 (2.859)
CC1/2	0.999 (0.904)	0.991 (0.555)	1 (0.441)
CC*	1 (0.975)	0.998 (0.845)	1 (0.782)
Reflections used in refinement	12140 (1171)	51009 (4677)	57267 (4581)
Reflections used for R-free	600 (65)	2595 (217)	2857 (273)
R-work	0.213 (0.258)	0.1600 (0.2999)	0.1923 (0.3697)
R-free	0.259 (0.278)	0.2219 (0.2908)	0.2760 (0.3810)
CC(work)	0.940 (0.861)	0.945 (0.659)	0.960 (0.583)
CC(free)	0.916 (0.904)	0.910 (0.609)	0.894 (0.554)
Number of non-hydrogen atoms	1763	8630	8618
Macromolecules	1722	8056	8197
Ligands	1	258	364
Solvent	40	316	347

Protein residues	230	1077	1127
RMS(bonds)	0.011	0.022	0.021
RMS(angles)	1.41	2.01	1.91
Ramachandran favored (%)	96.85	96.07	93.21
Ramachandran allowed (%)	3.15	3.84	6.42
Ramachandran outliers (%)	0.00	0.09	0.38
Rotamer outliers (%)	3.95	4.04	3.85
Clashscore	1.73	2.89	5.82
Average B-factor	60.40	37.71	73.83
Macromolecules	60.50	37.83	72.85
Ligands	83.24	32.97	105.71
Solvent	55.42	38.61	72.29
Number of TLS groups	1	4	4

Statistics for the highest-resolution shell are shown in parentheses.

The monomeric *Mc*FabI apo structure is similar to all the 4 individual monomers of the both ternary complex structures, except for the 3 missing loops, the α-helical content, the conformation of the cofactor binding loop (CBL) and the bound ligands. The monomer of apo *Mc*FabI consists of 8 α-helices and 7 β-sheets, while that of the TCL ternary complex consists of 13 α-helices and 7 β-sheets and EST ternary complex containing 11 α-helices and 7 β-sheets (**Table 2.2**).

Table 2.2: The list of secondary structural elements of *Mc*FabI structures. The α-helix and β-strand are labeled with the Hn and Bn identifiers respectively.

Apo *Mc*FabI		*Mc*FabI-NAD-TCL		*Mc*FabI-NAD-EST	
Secondary structure	Residue range	Secondary structure	Residue range	Secondary structure	Residue range
B1	7-11	B1	6-10	B1	6-10
H1	19-30	H1	19-30	H1	19-30
B2	33-38	B2	33-38	B2	33-38
H2	44-55	H2	41-54	H2	43-54
B3	58-61	B3	59-61	B3	58-61
H3	66-82	H3	67-81	H3	67-81
B4	91-94	B4	91-94	B4	91-94
H4	Missing	H4	101-104	H4	101-104
H5	Missing	H5	108-111	H5	Loop
H6	114-142	H6	114-142	H6	114-142
B5	145-151	B5	145-150	B5	145-150
H7	Missing	H7	152-155	H7	152-155
H8	165-186	H8	163-183	H8	163-183
B6	188-194	B6	188-194	B6	188-194
H9	Missing	H9	200-204	H9	200-205
H10	207-219	H10	208-218	H10	210-218
H11	226-243	H11	227-238	H11	227-238
B7	249-252	B7	248-252	B7	248-252
H12	255-259	H12	256-258	H12	256-258
		H13	263-266		

In all the 3 structures, a seven-stranded parallel β-sheet is flanked by three α-helices on either side, a reminiscent of Rossmann fold (Figure 2.5A). The tetrameric *Mc*FabI-NAD-TCL and ternary complexes consists of four active sites corresponding to its 4 subunits and are identical in being occupied by NAD and triclosan; while the 4 subunits of *Mc*FabI-NAD-EST ternary complex are also identical and occupied by NAD and estradiol. The SBL, Arg198-Phe208,

adopts a two-turn α-helix in both the ternary complex structures, but with different conformations which differ at 6.8Å RMSD (Figure 2.6).

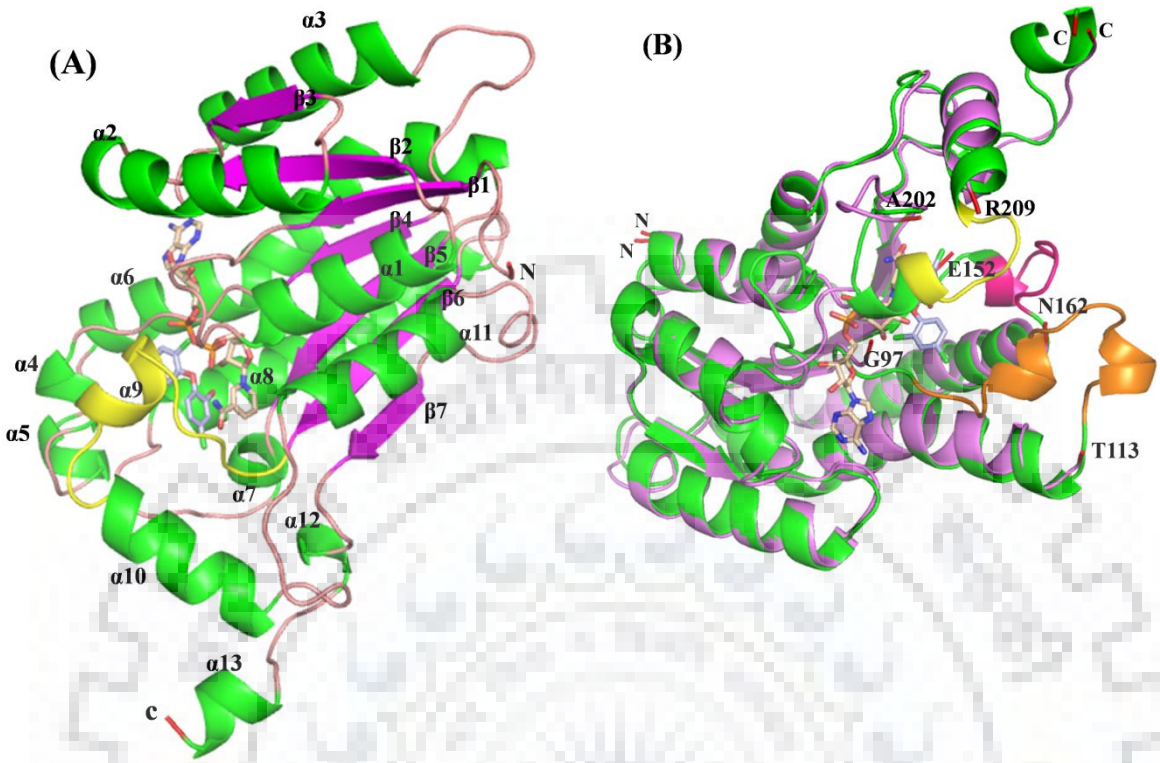

Figure 2.5: Structural organization of an intact monomer and comparison of apo *Mc*FabI monomer with the one having all the loops. **(A)**. The monomeric structure of the ternary complex of *Mc*FabI is presented as a ribbon diagram with secondary structures labeled. The α-helices, β-strands and loops are colored as cyan, magenta and gray respectively. NAD+ and triclosan are shown as stick models and colored as hot pink and lime green, respectively. The substrate binding loop (SBL) is colored in yellow. Both N- and C-termini are labeled in red. **(B)**. Comparison of *Mc*FabI apo structure with one of the four subunits of the tetrameric *Mc*FabI ternary complex.The 3 loops missing in apo structure are color coded in the counterpart of ternary complex.

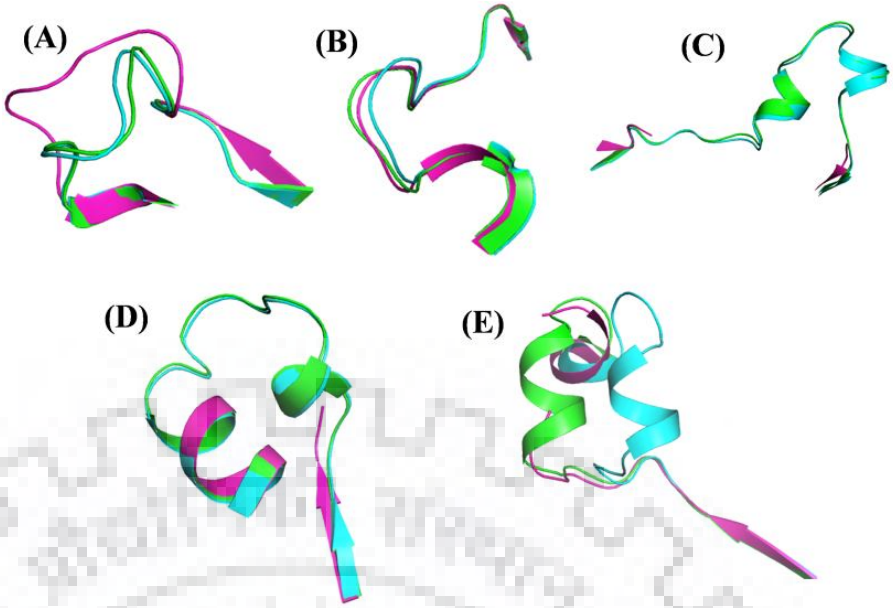

Figure 2.6: Differences in the loop structures among the 3 crystal structures of *Mc*FabI. The structural features of Apo, TCL and EST ternary complex structures are colored as magenta, cyan and green respectively. **(A).** CBL (Cofactor-binding loop) **(B).** IL (Insertion loop) **(C).** SBL2 (Substrate-binding loop 2) **(D).** ASL (Active site loop) **(E).** SBL (SBL1) (Substrate-binding loop 1).

2.3.3. Cofactor Binding site:

The NAD cofactor is present in the active site of *Mc*FabI. The sequence "GxxxxxSxA", a cofactor-binding motif conserved among the members of divergent subfamily of the SDR domain superfamily, is present in the *Mc*FabI indicating that it is also a member of the divergent subfamily. The conserved residues of this motif in *Mc*FabI include Gly12, Ser18, and Ala20 (Figure 2.7 and 2.8). The backbone carbonyl oxygen atom of Gly12 forms a hydrogen bond with the O3B atom of adenine ribose of NAD, while the OG atom of Ser18 with the O2A of NAD and the main chain amide nitrogen of Ile19 with O2N of NAD. The cofactor binding motif, which is also referred as the cofactor binding loop (CBL), is displaced at around 4.2Å RMSD in both the ternary complexes when compared to the apo structure (Figure 2.6). This positional displacement of CBL facilitates the binding of cofactor NAD.

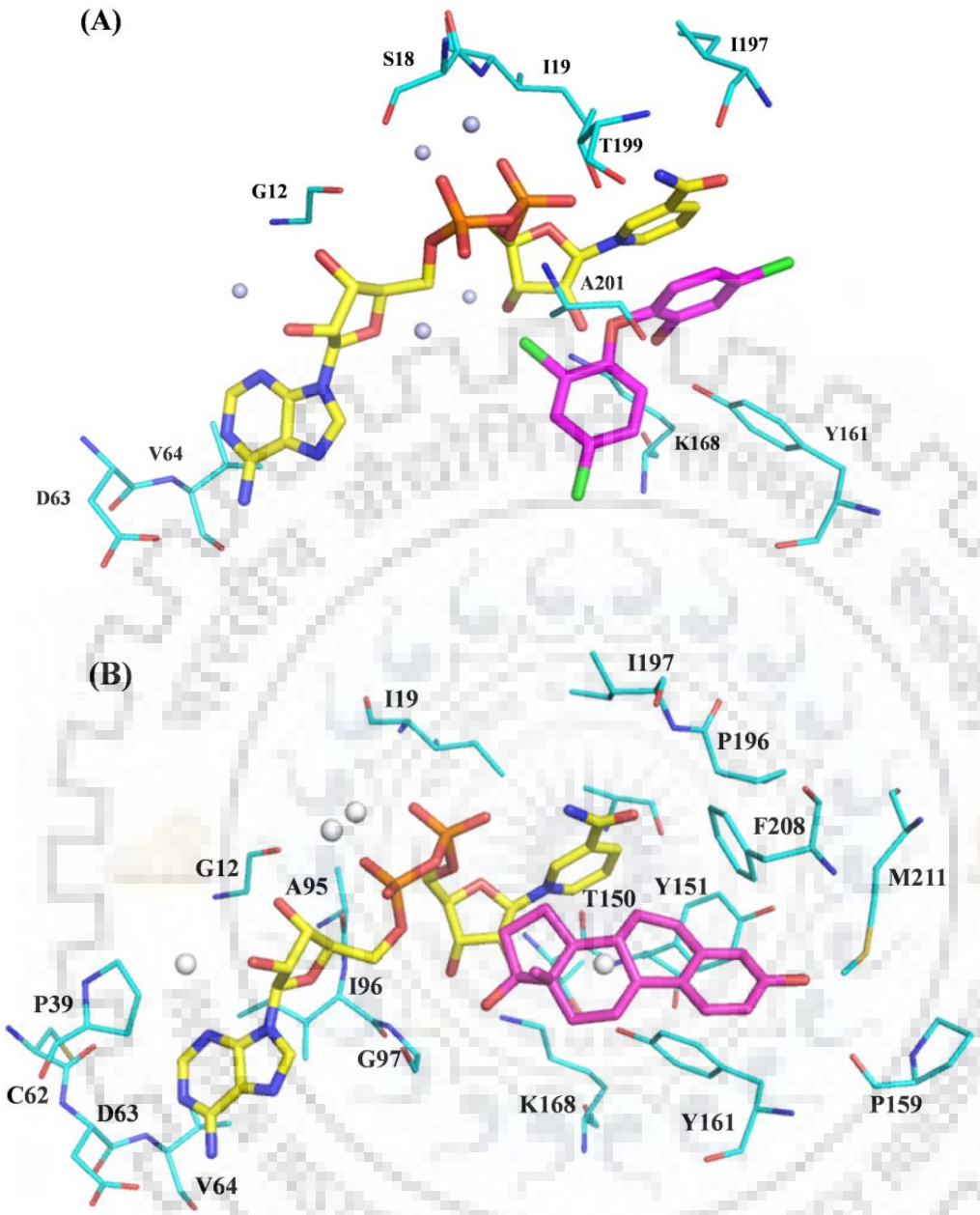

Figure 2.7: The active site architecture of *Mc*FabI. **(A)** TCL ternary complex showing the structural positions and arrangement of the protein residues (cyan) and water molecules (gray) that are interacting with the cofactor NAD (yellow) and inhibitor TCL (magenta). **(B)** EST ternary complex showing the structural positions and arrangement of the protein residues (cyan) and water molecules (gray) that are interacting with the cofactor NAD (yellow) and ligand EST (magenta).

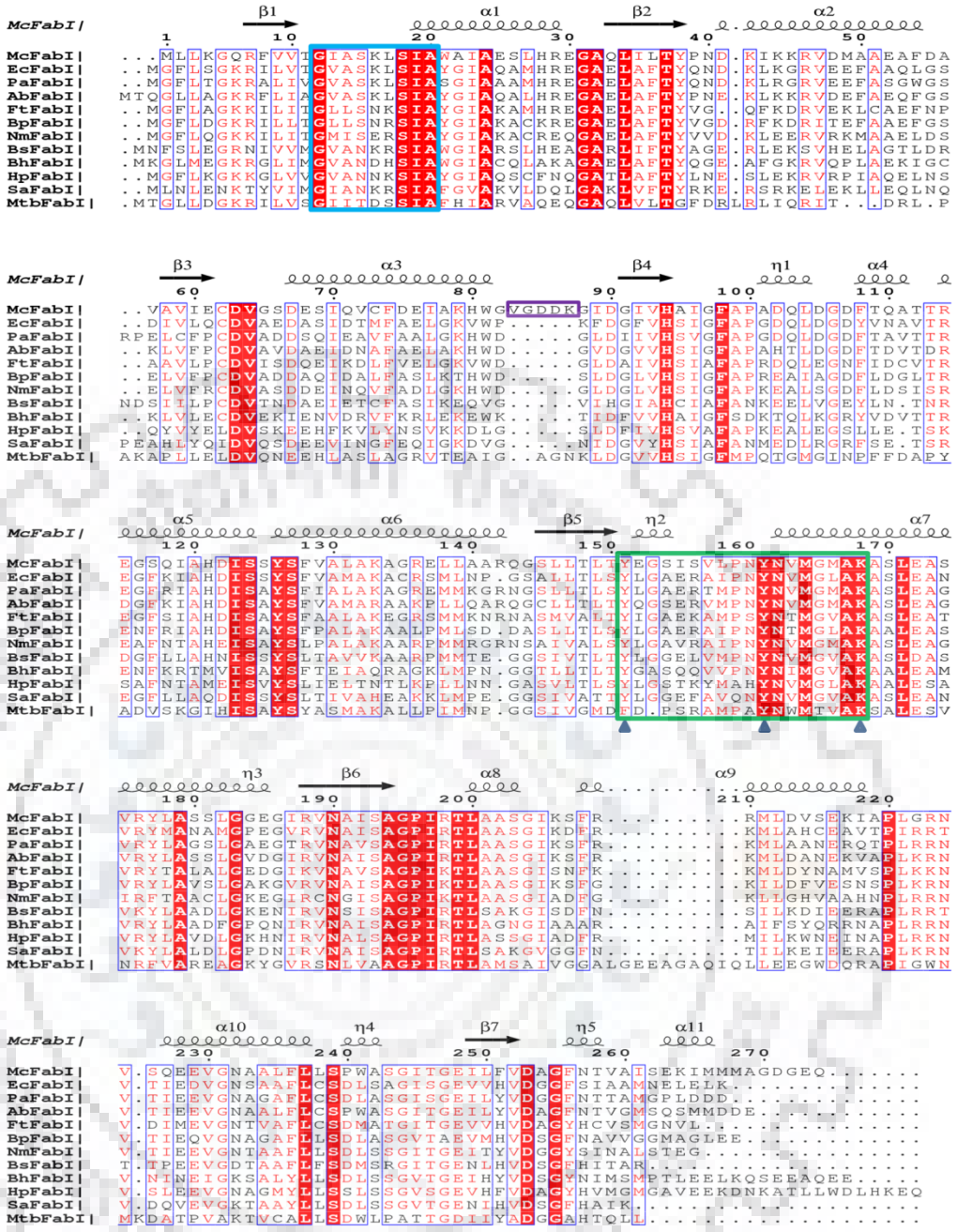

Figure 2.8: Multiple sequence alignment of FabI sequences from *M. catarrhalis* and other species. Completely conserved residues are shown in red boxes with white characters, while the residues in the white boxes with red characters are relatively conserved. The cofactor binding motif, active site motif and insertion are highlighted by the light blue, green and purple colored boxes respectively. The catalytic residues are pointed by blue coloured solid triangles. Secondary structure elements of *Mc*FabI are labeled above the sequences. FabI from different bacterial species were collected as explained in the methods section.

The NAD binding site of *Mc*FabI mostly consists of hydrophobic residues (Figure 2.7). In detail, the nicotinamide ring is surrounded by Ile19, Ala194, Gly195 and Ile197, and the pyrophosphate is surrounded by Leu200 and Ala201. The residues Ile13, Ala14, Val64, Ile96,

and Gly97 form a hydrophobic pocket for the adenine ring of NAD. In addition, there are 6 residues hydrogen-bonded with NAD: the OD2 atom of Asp63 is hydrogen-bonded with the N6A atom of NAD, while the NZ of Lys168 with the O2D and O3D atoms of NAD, the OG1 of Thr199 with O1N of NAD, the main chain backbone carbonyl oxygen of Gly195 with the N7N of NAD and the main chain backbone amide nitrogens of Val64 and Ala201 with the N1A and O1A atoms of NAD, respectively. Asp63 and Lys168 are the conserved residues among FabIs. There are 5 water molecules involving in the conventional hydrogen bonding network within the co-factor binding site, including HOH15, 32, 104, 117 and 132 that are hydrogen bonded with the O2N, O1A, O3D, O2A and N3A of NAD respectively.

There are few differences exist in the position and binding pattern of NAD between the TCL and EST ternary complexes. The positions of PA, O5B and C5B are differing at 1.07, 1.95 and 1.11 Å respectively, while the overall RMSD for NAD is 0.66 Å. Because of this positional shift of the NAD, it is unable to make few potential hydrogen bonds with the protein residues including Ser18, Thr199 and Ala201 in the EST complex when compared to the TCL complex.

2.3.4. Triclosan Binding pocket:

The electron density map clearly revealed the position of the triclosan in the ternary complex structure of *Mc*FabI (Figure 2.9). Triclosan is surrounded by the hydrophobic side chains of Tyr151, Tyr161, Pro196 and Phe208 (Figure 2.7A). The hydroxylchlorophenyl ring of triclosan occupied a position that is parallel to the nicotinamide ring of NAD with an interplanar stacking distance of 4.04 Å, making a π–π stacking interaction. Notably, the O17 of triclosan forms a tight hydrogen bond with OH of Tyr161, which is a highly conserved residue among FabI structures from other species. The O17 and O7 of triclosan are also making stable hydrogen bonds with the O2D of nicotinamide ribose of the NAD cofactor.

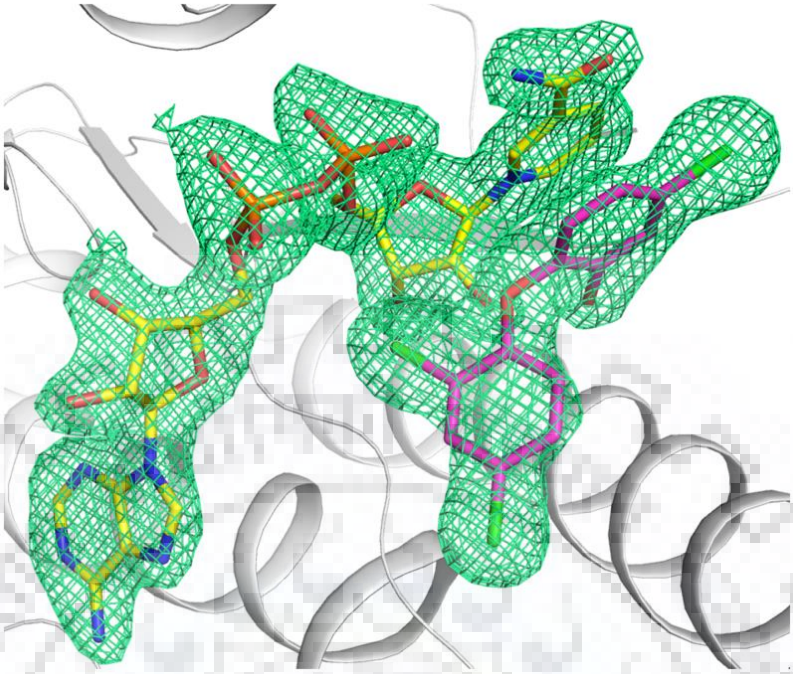

Figure 2.9: The electron density map for the ligands in the *Mc*FabI-NAD-TCL ternary complex structure. The 2|Fo| − |Fc| map of TCL and NAD were contoured at 1.0σ level. TCL and NAD are colored by element in magenta and yellow respectively.

2.3.5. Estradiol binding site:

We have obtained a partial density for the ligand EST, with the C ring having poor electron density (Figure 2.10). Most of the interactions that EST is making with the surrounding protein residues are hydrophobic in nature, while the O3 and O17 hydroxyl groups of EST are making strong hydrogen bonding. O3 is making 2.84 and 3.11 Å hydrogen bonds with SD of Met211 and peptidyl oxygen of Pro159 respectively, while O17 of D ring is making a 3.29 Å H-bond with the peptidyl oxygen of Gly159. The A ring of EST is making Π-Π T-shaped interactions with the side chain aromatic rings of Tyr161 and Phe208, while it is making the Π-alkyl interactions with the side chain of Met211. The B ring of EST is making Π-alkyl interactions with the side chains of Tyr151, Tyr161 and Phe208, while the C ring is making similar interactions with Tyr161.

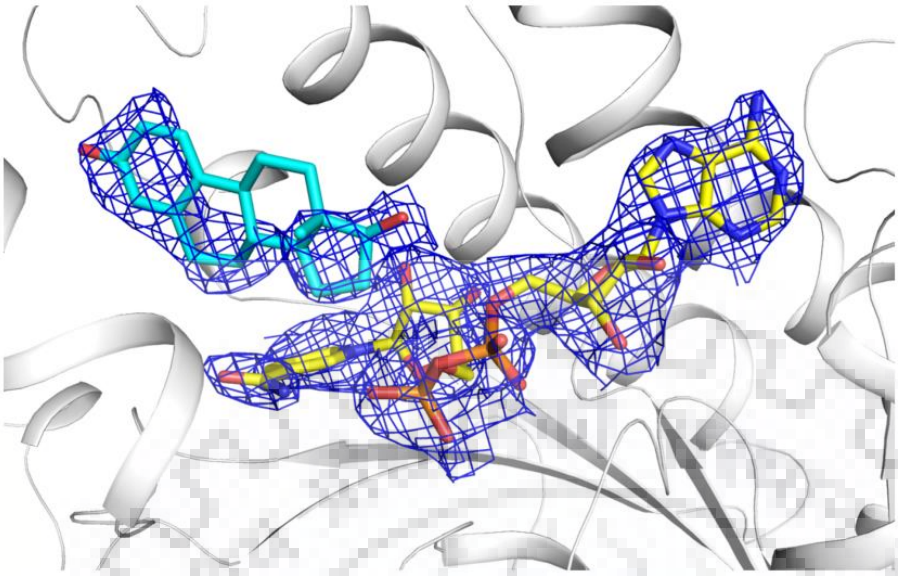

Figure 2.10: The electron density map for the ligands in the *Mc*FabI-NAD-EST ternary complex structure. The 2|Fo| − |Fc| map of EST and NAD were contoured at 0.8σ level. EST and NAD are colored by element in cyan and yellow respectively.

2.3.6. Oligomer interface analysis:

The monomer interfaces and tetramer interfaces are analysed, using the PISA server, for the residues participating in the oligomer formation and its stability. There are 22 residues are participating in the A:B and C:D monomer-monomer interface interactions, while 10 residues are participating in the A:D and B:C dimer-dimer interfaces and 7 residues in the A:C and B:D tetramer interfaces (Table 2.3). The five residues that are involving in strong monomer-monomer interface interactions include Asp67, Asp107, Arg114, Asp122 and Arg136, which are making strong hydrogen bonds and salt bridge interactions as well. The tetramer interfaces are stabilized mainly by the C-terminal residues including Thr258, Ala260, Ile261, Ile265 and Met266. The surface area of each of the monomers was calculated to be ~13000 $Å^2$. The A:B or C:D monomer interface area was estimated as ~1650 $Å^2$, while the A:D or B:C dimer interface area was calculated at ~1300 $Å^2$ and the A:C or B:D tetramer interface was ~900 $Å^2$.

Table 2.3: Protein residues involving in the *Mc*FabI protein interface interactions. The residues are listed according to the surface and the type of interactions they are involving in.

Residues participating in H-bonds				Residues participating in salt bridges
A:B interface and C:D interface		A:D interface and B:C interface	A:C interface and B:D interface	A:B interface and C:D interface
Val64	Tyr126	Gly184	Val157	Asp67
Gly65	Lys133	Pro220	Arg210	Asp107
Asp67	Arg136	Arg223	Thr258	Arg114
Asp107	Gly153	Glu229	Ala260	Asp122
Phe108	Ser154	Ser243	Ile261	Arg136
Thr109	Ser156	Gly244	Ile265	
Gln110	Leu158	Glu248	Met266	
Thr112	Ser170	Phe251		
Arg114	Arg176	Asp253		
His121	Tyr177	Ala254		
Asp122	Ser181			

2.3.7. Comparison of FabI structures from different bacterial species:

Structural comparison of *Mc*FabI with the FabI crystal structures reported from several bacterial species revealed that the monomer structures from all these FabI structures are almost similar, with root-mean-square deviations (RMSD) ranging from 0.8 to 2.0 Å for the main chain atoms (Figure 2.11). Comparison of the active site architecure indicates that the *Mc*FabI TCL ternary complex structure adopts a closed lid conformation of its active site upon ligand binding. It revealed the structural conservation of the catalytic residues Tyr161 and Lys168 and also the cofactor binding motif, which participate in the stabilization of protein-substarte and protein-cofactor interactions. The contacts that O17 of triclosan making with the O2D of NAD cofactor, OH of Tyr161 alcohol and NZ of Lys168 base at 2.5, 2.5 and 4.4 Å respectively in the *Mc*FabI active site, are similar to those it is making in the active sites of ENR enzymes from other species (913), indicating the similar fashion of tight binding of TCL and its recognition mechanism by the protein and cofactor residues (figure 2.17). It is also observed that there is a

5-amino acid long insertion (83V-87K) in the sequence of *Mc*FabI in comparison to ENR enzymes from other species, except for the InhA from *M. tuberculosis* which has a 3-aa long insertion at the corresponding position. It forms part of the loop 7 (L7: 82G-90D) between helix 3 (H3: 67D-81W) and β-sheet 4 (BS4: 91G-94H), and present at the surface of the monomer making hydrogen bond contacts at the tetramer-tetramer interface. The residue Gly84 of this insertion from one of the monomers of a tetramer makes a 3.1 Å hydrogen bond with Gly204 of one of the monomers of the neighbour tetramer.

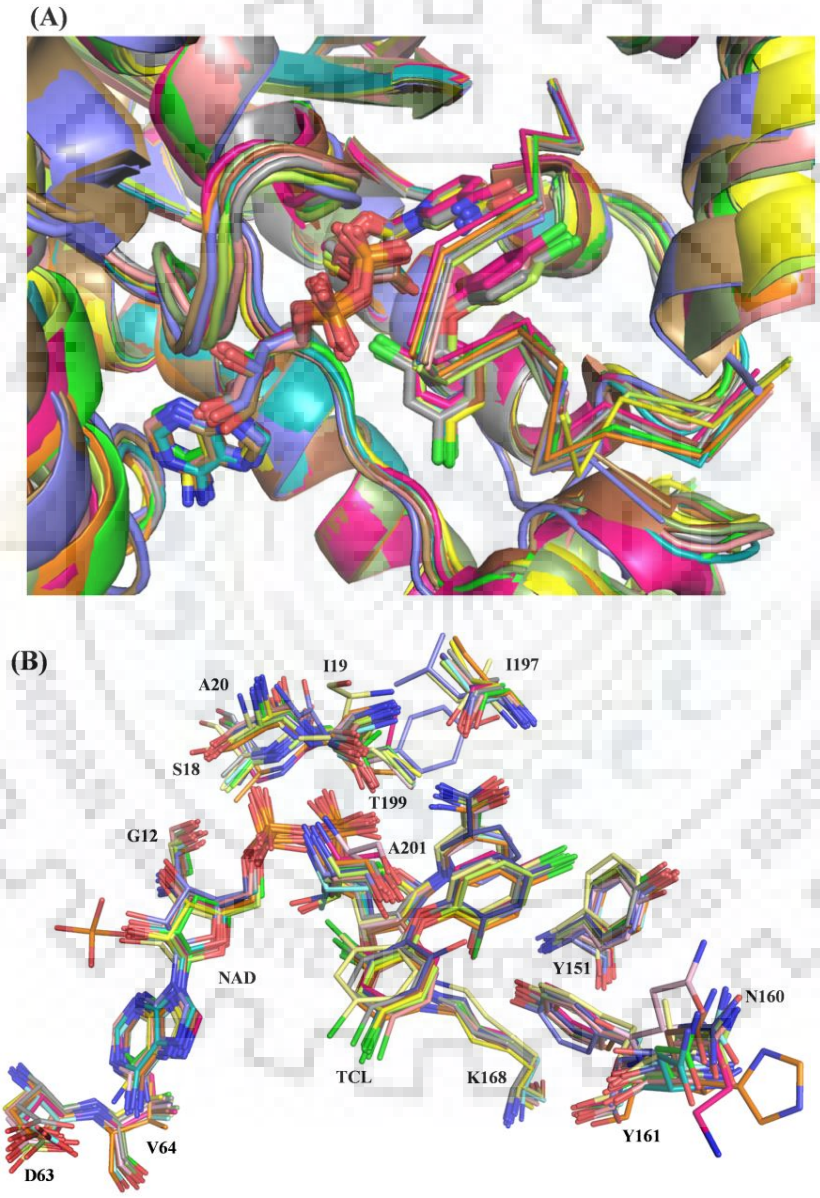

Figure 2.11: Superimposition of FabI-NAD-TCL ternary complex structures from different bacterial species. **(A)** NAD, TCL and SBL are shown superimposed. NAD and TCL are shown with stick representation, and the SBL in line representation, while rest of the protein in cartoon representation. **(B)** Active site residues are superimposed along with the ligands NAD and TCL.

Variations in the SBL conformation in FabI structures:

The SBL obtained in the TCL ternary complex of *Mc*FabI is of typical closed conformation in comparison to many similar complex structures from other bacteria, while the SBL observed in the EST complex structure adopted a conformation which is different and distant in position at an RMSD of 6.8 Å from the closed conformation of the TCL ternary complexes and 8.4 Å from the open conformation reported in few FabI structures, including 1ENO, 1ENP, 1D7O and 5YCV (Figure 2.12; Table 2.4). So the SBL obtained in the EST complex is observed as an intermediary conformation, which is similar to few FabI structures including 5TRT, 3GAF and 3K2E (Table 2.5). This intermediary conformation of SBL in EST complex is in acceptable agreement to the shifted positions of the cofactor NAD and the ligand EST, and their interaction pattern within the active site. This difference in the conformation of the SBL between TCL and EST ternary complexes may be due to the mechanism of enzyme inhibition or may also be resulted from crystallization conditions. The differences in structural ordering and conformation of SBL were addressed by similar explanations in case of the FabI structures from other species (195, 913).

Table 2.4: The conformational differences in the catalytically essential structural loops among the *Mc*FabI structures. CBL: cofactor binding loop, SBL: substrate binding loop.

Structural element	Structure 1	Structure 2	Cα RMSD (Å)
CBL	Apo *Mc*FabI	*Mc*FabI-NAD-TCL	4.2
CBL	Apo *Mc*FabI	*Mc*FabI-NAD-EST	4.2
CBL	*Mc*FabI-NAD-TCL	*Mc*FabI-NAD-EST	0.43
SBL	*Mc*FabI-NAD-TCL	*Mc*FabI-NAD-EST	6.8
SBL	*Mc*FabI-NAD-TCL	1ENO, 1ENP, 1D7O, 5YCV	13.6
SBL	*Mc*FabI-NAD-EST	1ENO, 1ENP, 1D7O, 5YCV	8.4
NAD	*Mc*FabI-NAD-TCL	*Mc*FabI-NAD-EST	0.66

Figure 2.12: Superimposition of the SBL among the FabI structures. The SBL from *Mc*FabI-NAD-TCL and *Mc*FabI-NAD-EST ternary complex structures, and *Bn*FabI are colored in cyan, green and yellow respectively indicating the closed, and are indicating the intermediary and open conformational states of SBL respectively.

Table 2.5: The structural conformation of substrate binding loop of FabI proteins from different pathogenic bacteria.

Structure	Organism	Molecule	Substrate binding loop	
			Structure	conformation
	M. catarrhalis	Apo	Absent	
3EK2	*B. pseudomallei*	Apo	Absent	
3GRK	*B. melitensis*	Apo	Absent	
2YW9 (A-G)	*T. thermophiles*	Apo	Absent	
1ULU	*T. thermophiles*	Apo	Absent	
5CFZ	*E. coli*	Apo	Absent	
4NQZ	*P. aeruginosa*	Apo	Absent	
5YCV (A & C)	*B. anthracis*	Apo	Loop	Open (wider)
3K2E (A)	*A. phagocytophil*	Apo	Loop	Open
3OIC (D)	*B. subtilis*	Apo	Loop	Open
5I7E	*B. pseudomallei*	Apo	Loop	Intermediary
3GAF	*B. melitensis*	Apo	α-helical	Open
4NK4	*C. liberibacter*	Apo	α-helical	Intermediary
5TRT (B-D)	*B. pseudomallei*	NAD	Absent	
2JJY	*F. tularensis*	NAD	Absent	
2YW9 (H)	*T. thermophiles*	NAP	Absent	
1DFI	*E. coli*	NAD	Absent	
5TRT (A)	*B. pseudomallei*	NAD	α-helical	Open
5KOI	*B. melitensis*	NAD	α-helical	Closed
4ZJU	*A. baumannii*	NAD	α-helical	Closed

1ENO	*B. napus*	NAD	Loop	Open (wider)
1ENP	*B. napus*	NAD	Loop	Open (wider)
	M. catarrhalis	NAD-TCL	α-helical	Closed
5IFL (and 8)	*B. pseudomallei*	NAD-TCL	α-helical	Closed
2PD3	*H. pylori*	NAD-TCL	α-helical	Closed
1QSG (and 1)	*E. coli*	NAD-TCL	α-helical	Closed
3PJD (and 2)	*E. coli*	NAD-TCL	α-helical	Closed
4NR0	*P. aeruginosa*	NAD-TCL	α-helical	Closed
3NRC	*F. tularensis*	NAD-TCL	α-helical	Closed
4M89	*N. meningitidis*	NAD-TCL	α-helical	Closed
2O2Y	*P. falciparum*	NAD-TCL	α-helical (res.mis)	Closed
3OID (FabL)	*B. subtilis*	NDP-TCL	α-helical	Closed
3OIF (A)	*B. subtilis*	NAD-TCL	Loop	Closed
3OIF (D)	*B. subtilis*	NAD-TCL	Loop (res.mis)	Closed
1D7O	*B. napus*	NAD-TCL	Loop	Open (wider)
	M. catarrhalis	NAD-EST	α-helical	Open
4RLH	*B. pseudomallei*	AFN1252	Absent	
4JQC	*E. coli*	NAD-AFN1252	α-helical	Closed
4Q9N	*C. trachomatis*	NAD-AFN1252	α-helical	Closed
5CG1	*E. coli*	NAD-BBN	Absent	
5CG2	*E. coli*	NAD-CJ3	Absent	
4CV2	*E. coli*	NAI-CG400549	Absent	
4CV3	*E. coli*	NAI-PT166	Absent	
1DFG	*E. coli*	NAD-NDT	Loop	Intermediary
1DFH	*E. coli*	NAD-TDB	Loop	Intermediary
4BKU	*B. pseudomallei*	NAI-PT155	Loop	Intermediary
3OIG	*B. subtilis*	NAD-INH	α-helical	Closed
3OJF	*B. cereus*	NDP-IMJ	α-helical	Closed
1CWU	*B. napus*	NAD-TDB	α-helical	Closed

2.3.8. Comparison of *Mc*FabI structures and sequences with rest of the ENR isoforms FabK, FabL, and FabV from different bacterial species:

All of the ENR isoforms including FabI, FabL and FabV, along with *Mc*FabI are sharing the highly conserved catalytic residues Tyr161 and Lys168 (*Mc*FabI numbering) in the identical positions, which are also conserved structurally and funactionally, except for the FabK isoform which is a flavoprotein belonging to AKR superfamily (Figure 2.13). The CA atoms of TCL and EST ternary complex structures of *Mc*FabI are superimposing at 1.1 to 2.2 Å and 1.6 to 2.6

Å RMSDs respectively, with overall structures of FabL isoforms. The better superposition of TCL complex is due to similarities in the SBL conformation with that of FabL structures. The CA atoms of TCL and EST ternary complex structures of *Mc*FabI are superimposing at 3.9 to 4.8 Å RMSDs with the dinucleotide binding domains of FabV isoforms. The *Mc*FabI structures are differing greatly from the FabK isoforms due to differences in their cofactor preferences and catalytic mechanisms, where FabK is a flavoprotein containing a flavor-mononucleotide binding site which horbors the cofactor FMN while the FabI isoform is a non-favoprotein which contains a dinucleotide binding site.

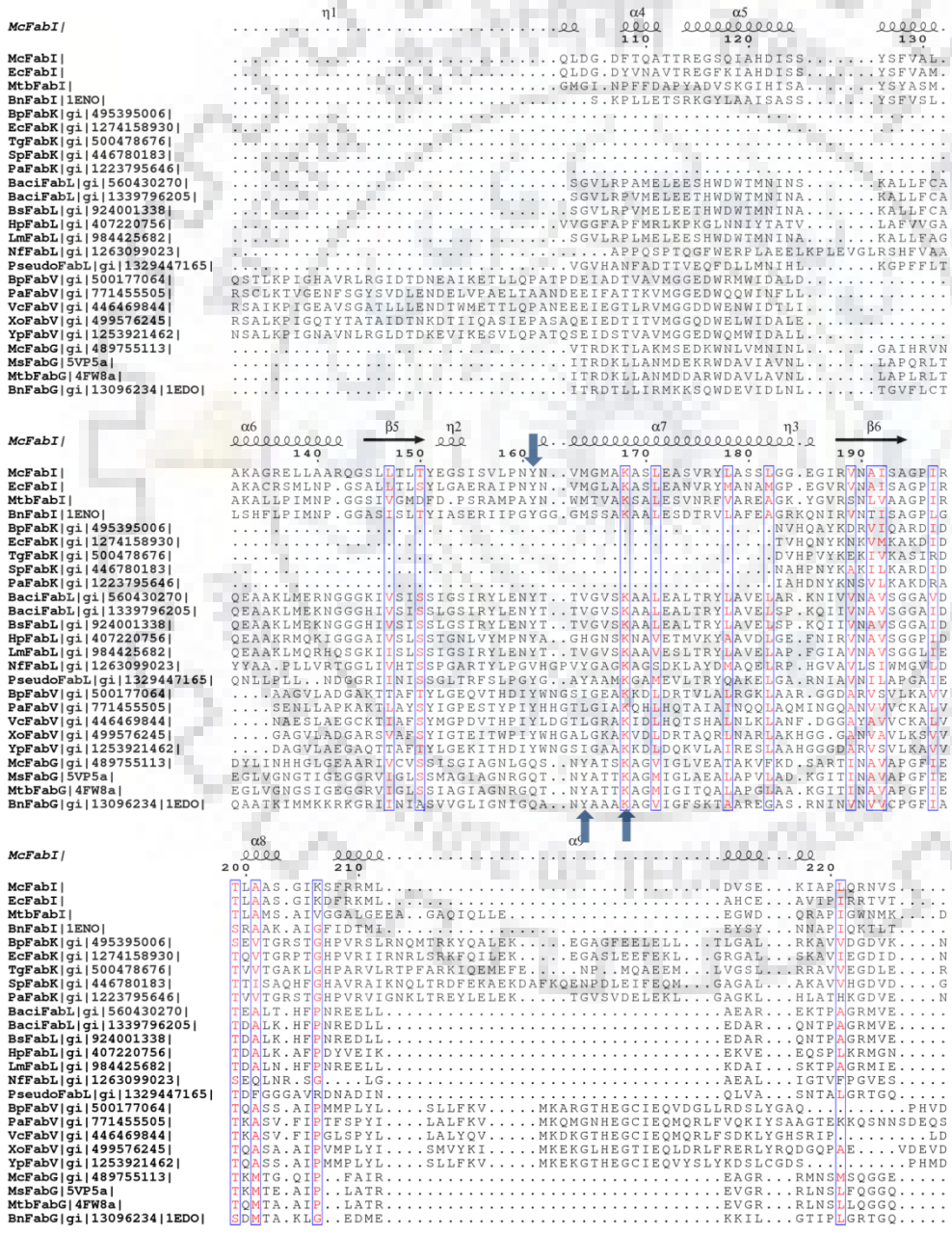

Figure 2.13: Alignment of the *Mc*FabI amino acid sequence with that of all different ENR isoforms, FabI, FabK, FabL and FabV, along with FabG. The color code of the residues is same

as explained in the figure 8. The conserved catalytic residues are indicated by blue colored solid arrows.

2.3.9. Comparison with BKR (FabG) enzymes and other oxidoreductases having significant similarity with *Mc*FabI structures:

A DALI search of McFabI final model resulted in several matches with significant Z-score values of more than 41 among which the ENR-NAD+-TCL ternary complex from *Pseudomonas aeroginosa* (PDB ID: 4NR0) is topping the list. This search revealed that several members from SDR superfamily are showing very good structural similarity with Z-scores around 30 and RMSD around 2 Å, which also include the human 17-β hydroxysteroid dehydrogenase 14 (PDB ID: 5EN4 and 5JS6) and estradiol 17-β dehydrogenase 8 (PDB ID: 4CQL) (figure 2.14).

The TCL and EST ternary complex structures of *Mc*FabI are superimposing very well with the dinculeotide binding domains of the FabG (BKR) structures reported from other bacterial species. They are also superimposing well at 2.3, 2.4 and 3.0 Å RMSDs respectively, with the overall structures of the human 17-β hydroxysteroid dehydrogenase isoforms 14, 8 and 10. The amino acid sequences from all these proteins were compared and analysed for their conserved structural and functional aspects (figure 2.15).

764:	4aln-C	31.5	1.4	222	225	47	PDB	MOLECULE: ENOYL-[ACYL-CARRIER-PROTEIN] REDUCTASE [NADPH];
765:	5en4-A	31.4	1.9	245	251	24	PDB	MOLECULE: 17-BETA-HYDROXYSTEROID DEHYDROGENASE 14;
766:	4aln-B	31.3	1.2	218	220	47	PDB	MOLECULE: ENOYL-[ACYL-CARRIER-PROTEIN] REDUCTASE [NADPH];
767:	5fff-B	31.0	2.0	244	257	25	PDB	MOLECULE: NOROXOMARITIDINE/NORCRAUGSODINE REDUCTASE;
778:	2wqz-D	30.7	1.9	240	254	27	PDB	MOLECULE: SHORT-CHAIN DEHYDROGENASE/REDUCTASE;
779:	3qvc-D	30.7	1.8	242	249	25	PDB	MOLECULE: PROBABLE SHORT-CHAIN TYPE DEHYDROGENASE/REDUCTA
780:	5is6-A	30.6	2.0	246	268	24	PDB	MOLECULE: 17-BETA-HYDROXYSTEROID DEHYDROGENASE 14;
781:	2wdz-A	30.6	1.9	240	254	27	PDB	MOLECULE: SHORT-CHAIN DEHYDROGENASE/REDUCTASE;
782:	2uvd-A	30.6	2.0	241	246	22	PDB	MOLECULE: 3-OXOACYL-(ACYL-CARRIER-PROTEIN) REDUCTASE;
794:	4cql-I	30.2	1.9	242	251	19	PDB	MOLECULE: ESTRADIOL 17-BETA-DEHYDROGENASE 8;
795:	5t2u-A	30.2	2.0	238	241	30	PDB	MOLECULE: OXIDOREDUCTASE, SHORT CHAIN DEHYDROGENASE/REDUC
796:	3r1i-A	30.2	1.8	240	254	24	PDB	MOLECULE: SHORT-CHAIN TYPE DEHYDROGENASE/REDUCTASE;
797:	1ahi-A	30.1	1.9	239	255	25	PDB	MOLECULE: 7 ALPHA-HYDROXYSTEROID DEHYDROGENASE;
798:	3icc-A	30.1	2.3	245	255	21	PDB	MOLECULE: PUTATIVE 3-OXOACYL-(ACYL CARRIER PROTEIN) REDUC
799:	2ewm-B	30.1	1.9	240	247	29	PDB	MOLECULE: (S)-1-PHENYLETHANOL DEHYDROGENASE;

Figure 2.14: DALI database search for the distant structural homologs of *Mc*FabI protein. The homologs of our interest are highlighted in yellow color.

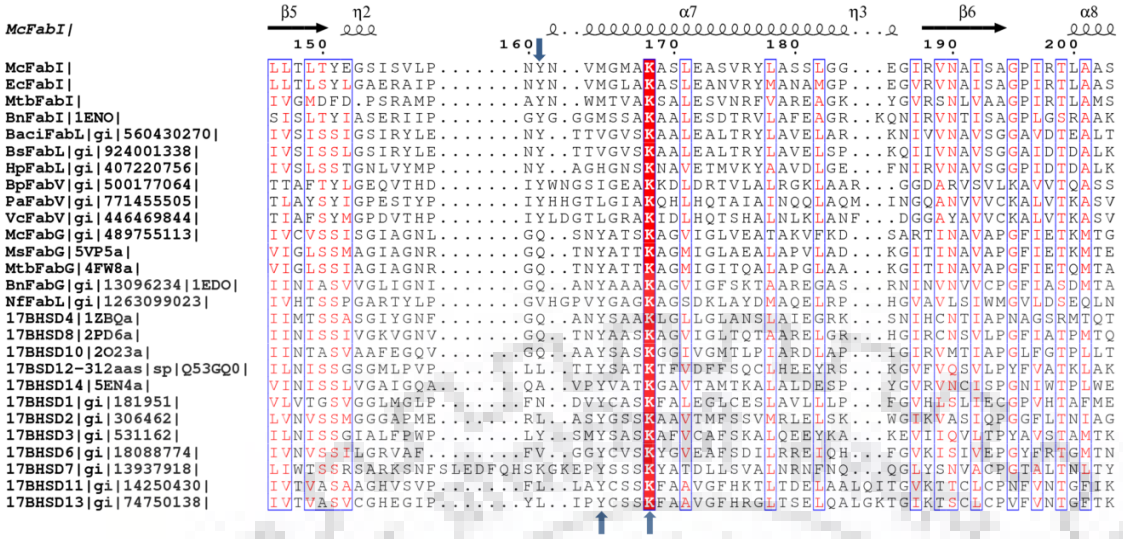

Figure 2.15: Alignment of the sequences of the ENR isoforms belonging to the SDR superfamily including FabI, FabL and FabV, with sequences of other oxidoreductase enzymes including FabG enzymes and 17-β HSD isoforms. Colour coding of the residues is same as explained in the figure 8. The catalytic residues conserved in these sequences are indicated by blue coloured solid arrows.

2.3.10. Substrate and inhibitor recognition by *Mc*FabI enzyme:

The mechanisms of substrate and inhibitor recoginition by *Mc*FabI enzyme are similar to that of FabI enzymes from other bacterial species. The substrate crotonyl coenzyme A (CCA) was docked in the active site of *Mc*FabI and analysed for its contacts with the protein residues and recognition mechanism. The C2 and O17 atoms of triclosan are contacting the C4N and side chain OH groups of NAD cofactor and the enzyme's Tyr161 catalytic residue respectively in the similar fashion of the C3 and the side chain carbonyl oxygen atoms of CCA (figure 2.16). In presence of both TCL and CCA, the NZ atom of Lys168 catalytic residue is making strong hydrogen bonds with the O2D and O3D atoms of the nicotinamide ribose of the NAD cofactor. Hence the mechanism of recognition and binding is similar for the substrate CCA and the inhibitor TCL.

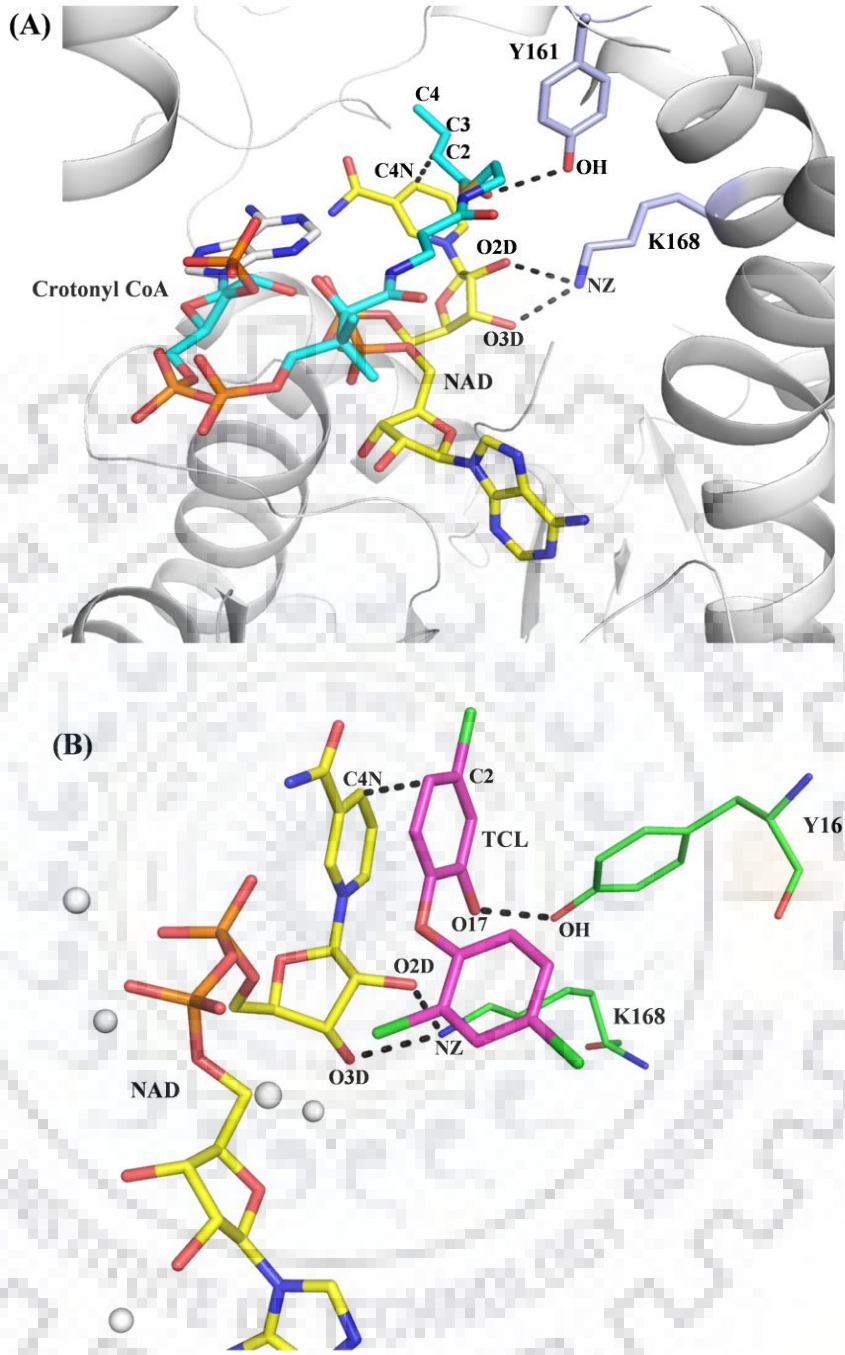

Figure 2.16: Recognition mechanism of the substrate crotonyl CoA (CCA) and the inhibitor triclosan (TCL). **(A)** All the atoms of the substrate CCA, cofactor NAD and the catalytic residues Y161 and K168 are labeled. CCA, NAD and catalytic residues are colored cyan, yellow and light blue respectively. **(B)** Atoms from the inhibitor TCL, cofactor NAD and the catalytic residues Y161 and K168 are labeled. TCL, NAD and catalytic residues are colored magenta, yellow and green respectively.

The different substrate binding loop conformations observed in the *Mc*FabI-NAD-TCL and *Mc*FabI-NAD-EST ternary complexes maybe correspond to the SBL movements during the

substrate or inhibitor binding. The SBL may attain closed conformation upon the tight binding of the substrate or/and inhibitor, in presence of the cofactor NAD, while an intermediary conformation when the substrate or inhibitor bound transiently/loosely during their travelling/approach towards the catalytic residues in the active site (figure 2.17). This hypothesis is in support of the fact that we observed the intact density for the tightly bound triclosan within the *Mc*FabI active site with the closed conformation of the SBL, while partial density is observed for the loosely and transiently bound estradiol within the active site with an intermediary conformation of the SBL. In the absence of substrate or/and inhibitor binding, the SBL remains flexible/disordered.

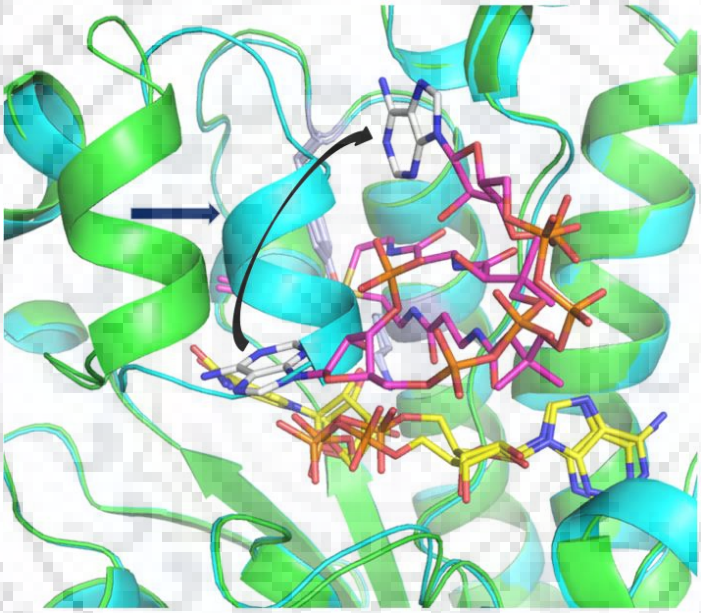

Figure 2.17: The SBL movements and conformations during the binding of substrate. The SBL movement is shown by blue colored solid right arrow and the corresponding movement in the substrate CCA is shown by the black colored solid curved down arrow.

2.3.18. Pharmacophore modeling, virtual screening and molecular docking:

RLPG protocol generated 10 pharmacophore models by using the defined strategies and features of all these models are listed in the Table 2.6. Because of its high selectivity score, model no1 afn_01.chm is used for screening the L1300-Selleck-FDA-Approved-Drug-Library and obtained 21 compounds with a fit value more than one. All these compounds are showing good binding scores when docked in the active site of the enzyme using AutoDock Vina and estradiol cypionate, the commercially available drug form of the major female sex hormone 17β-estradiol (E2), is found binding to *Mc*FabI with highest binding energy (Table 2.7).

Table 2.6: The pharmacophore models, with their selectivity score, that were generated during pharmacophore modeling.

Pharmacophore	No. of features	Feature set	Selectivity Score
afn_01.chm	6	AADHHH	10.65305
afn_02.chm	6	AADHHR	10.65305
afn_03.chm	5	ADHHH	9.13825
afn_04.chm	5	ADHHR	9.13825
afn_05.chm	5	ADHHH	9.13825
afn_06.chm	5	ADHHR	9.13825
afn_07.chm	5	AADHH	9.13825
afn_08.chm	5	AADHH	9.13825
afn_09.chm	5	AADHR	9.13825
afn_10.chm	5	AADHR	9.13825

Table 2.7: Docking scores of the top hit compounds obtained from the virtual screening.

S.No.	Ligand	energy
1.	Estradiol cypionate	-9.9
2.	Alibendol	-6.7
3.	Azactam	-7.3
4.	Bufexamac	-6.9
5.	butylparaben	-6.8
6.	caverject	-7.6
7.	Clorsulon	-6.8
8.	Compound 22	-7.4
9.	Depocyt	-6.0
10.	Doxrcalciferol	-8.6
11.	Ezetimibe	-8.2
12.	Furosemide	-7.6
13.	Lenalidomide	-7.8
14.	Levobetaxolol	-7.2
15.	Lm-3572	-7.0

16.	L-thyroxine	-6.1
17.	Nafamostat	-9.7
18.	Nelarabine	-7.0
19.	Nimesulide	-7.0
20.	Pci-24781	-7.3
21.	Silibinin	-8.3
22.	Sulisobenzone	-7.7
23.	Enteretinib	-10.1
24.	Nateglinide	-8.4
25.	Cytarabine	-6.0
26.	Tazobactam	-6.7
27.	Afn1252	-8.5

2.3.12. *Mc*FabI enzyme activity and inhibition studies:

*Mc*FabI is catalytically active in the presence of the substrate crotonyl CoA with K_M value of 358 μM, Vmax of 106.4 μM.min^{-1} and Kcat of 0.36 S^{-1}. The corresponding kinetics data were shown in the form of double reciprocal plots (Lineweaver-Burk plots) in figure 2.18. These kinetic parameters are in the ranges comparable to those of FabI enzymes from other species. Triclosan is inhibiting the *Mc*FabI catalytic activity with an inhibition constant (Ki) of 31 nM in an uncompetitive fashion (Figure 2.18 A and B). While, we observed upto 70.5% of enzyme inhibition in presence of 100 μM estradiol concentration and enzyme inhibition experiments couldn't be possible above this concentration due to limitations of the compound solubility. With this data it is calculated that estradiol may be inhibiting the *Mc*FabI catalytic activity with an inhibition constant (Ki) 0f 38.1 μM in an uncompetitive fashion (Figure 2.18 C and D). TCS and E2 are behaving as uncompetitive inhibitors with respect to the substrate CCA, indicating that they are binding to the enzyme via the conformationally altered enzyme-cofactor (*Mc*FabI-NAD) complex, rather than directly to the enzyme alone.

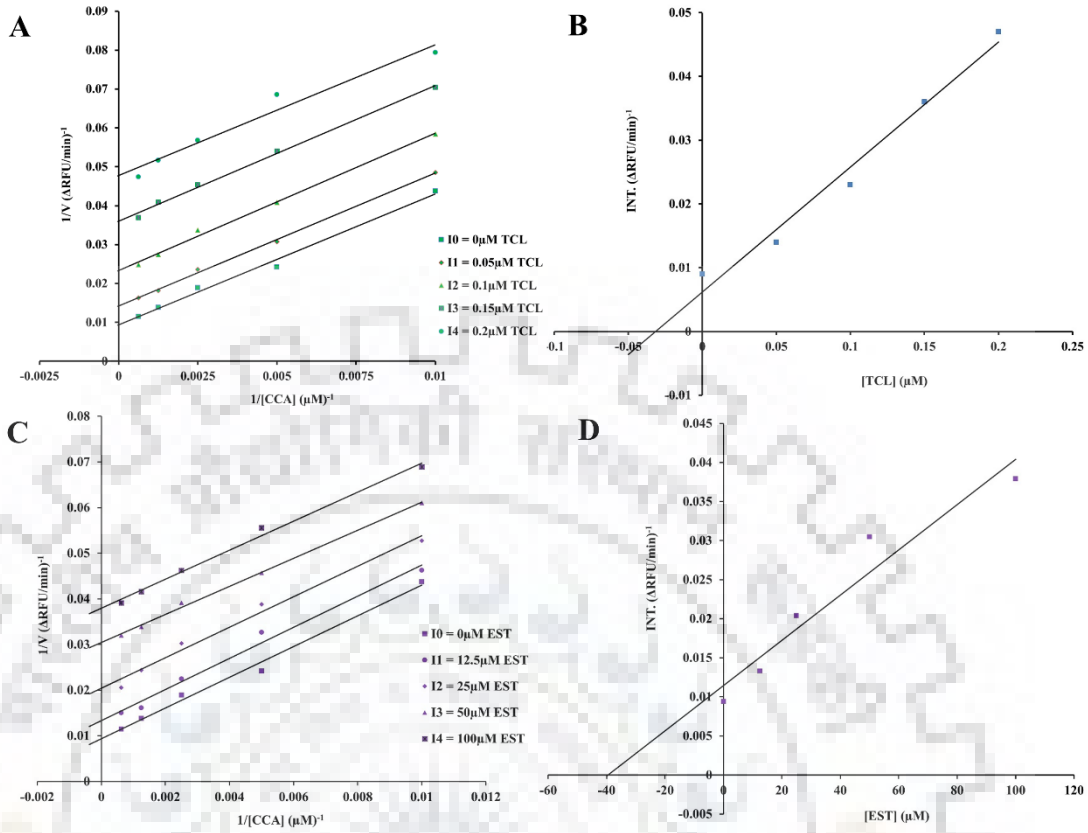

Figure 2.18: *Mc*FabI enzyme activity assay and the mechanism of *Mc*FabI inhibition by triclosan and estradiol compounds. **(A)** and **(C)** Lineweaver-Burk plots, the double reciprocal plots, representing the kinetic data showing the uncompetitive inhibition of *Mc*FabI binding to crotonyl coenzyme A by triclosan and estradiol respectively. The Michaelis-Menten constant (Km) and maximum velocity (Vmax) were calculated from the LB plot obtained for the enzyme kinetic data collected in the absence of the inhibitor (I0). **(B)** and **(D)** The secondary plots of the Y-intercept values of the lines from the (A) and (C) plots versus the inhibitor concentrations of TCL and EST respectively. The corresponding inhibition constant (Ki) values for both the inhibitors were calculated from these secondary plots.

2.3.13. Antimicrobial activities of the inhibitors:

The triclosan compound is inhibiting the growth of *M. catarrhalis* at a minimum inhibitory value of ≤0.5 μg/mL (1.7 μM), while estradiol is observed to be exhibiting antimicrobial actions by inhibiting 60% of the pathogen growth at ~27 μg/mL (100 μM) concentration (Table 2.8). Because of the solubility limitations, we couldn't able to use higher concentrations of the estradiol compound to find its MIC at which it can inhibit complete growth of the pathogen.

Table 2.8: The inhibitory properties of triclosan and estradiol.

Inhibitor	Ki (*Mc*FabI)	MIC (*M. catarrhalis*)
Triclosan	31 nM	≤0.5 µg/mL (1.7 µM)
Estradiol	38.1 µM	~27 µg/mL (100 µM) [inhibits 60% of the pathogen growth]*

2.3.14. Estradiol-*Mc*FabI interaction studies by SPR and ITC:

In the case of estradiol, the binding kinetics data were fit to 1:1 binding model with a χ^2 value of 0.04 RU^2 and U-value of 9, indicating that the experimental data fit with high confidence and the rate constants can be uniquely determined. The ka and kd kinetic constant values obtained for the *Mc*FabI-EST interactions are 9035 $M^{-1}S^{-1}$ and 0.0045 S^{-1} respectively, while the affinity constant kD observed for this interaction is 0.5 µM from the binding kinetics analysis, while it is 5 µM from the affinity fit analysis (Figure 2.19). All the kinetic parameters analysed are given in table 2.9. The kD value obtained for the binding interaction of triclosan to *Mc*FabI is 4 nM.

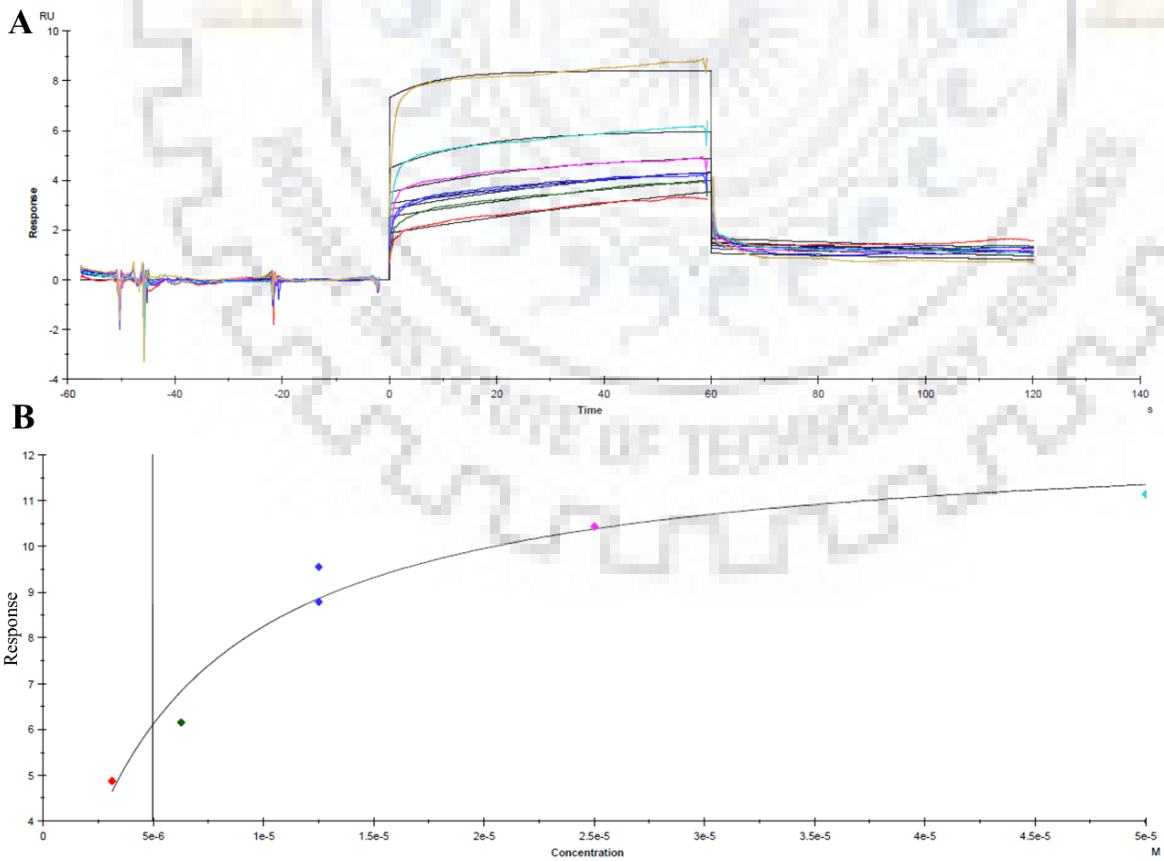

Figure 2.19: Binding studies of *Mc*FabI to 17β-estradiol by SPR. **(A)** Kinetics analysis of 17β-estradiol binding to *Mc*FabI. The binding kinetics data were fitted to 1:1 binding model and the corresponding sensograms, the plots of binding response (RU) versus time (S), are depicted here. The processed sensograms were color labeled according to the analyte concentration. **(B)** The binding kinetics data processed by affinity evaluation. Here in this case, the response (RU) was plotted against the analyte molar concentration (M) in order to find whether the binding interaction reached to saturation. The X-intercept of the vertical line intersecting the sensogram indicates the analyte concentration corresponding to its affinity constant (kD) value for the ligand.

Table 2.9. The report point table explaining all the kinetic parameters corresponding to the 1:1 binding model analysis of the *Mc*FabI to 17β-estradiol binding kinetics, studied by SPR.

Report table

Curve	ka (1/Ms)	kd (1/s)	KD (M)	Rmax (RU)	Conc (M)	tc	Flow (ul/min)	kt (RU/Ms)	RI (RU)	Chi² (RU²)	U-value
	9035	0.004528	5.011E-7			5.139E+6				0.0379	9
Cycle: 5 0.39 µM				9.973	3.900E-7		30.00	1.597E+7	1.875		
Cycle: 6 0.78 µM				4.856	7.800E-7		30.00	1.597E+7	2.537		
Cycle: 7 1.56 µM				2.961	1.560E-6		30.00	1.597E+7	2.827		
Cycle: 8 3.125 µM				1.861	3.125E-6		30.00	1.597E+7	3.519		
Cycle: 9 6.25 µM				1.625	6.250E-6		30.00	1.597E+7	4.487		
Cycle: 10 1.56 µM				2.476	1.560E-6		30.00	1.597E+7	3.063		
Cycle: 11 12.5 µM				1.106	1.250E-5		30.00	1.597E+7	7.332		

The interactions of *Mc*FabI with 17β-estradiol and triclosan are also analysed by isothermal titration calorimetry. The data were analysed by 1:1 single binding sites model and the corresponding isothermograms were shown in the figure 2.20. The thermodynamic properties of these interactions were also analysed, interpreted and found that the stoichiometric ratio (N) of triclosan and estradiol binding to *Mc*FabI is 1. The isothermograms obtained for these interactions haven't reached saturation and as a result the kD values obtained for the interactions of triclosan and estradiol with *Mc*FabI are 200 µM and 800 µM respectively, and further optimization needed.

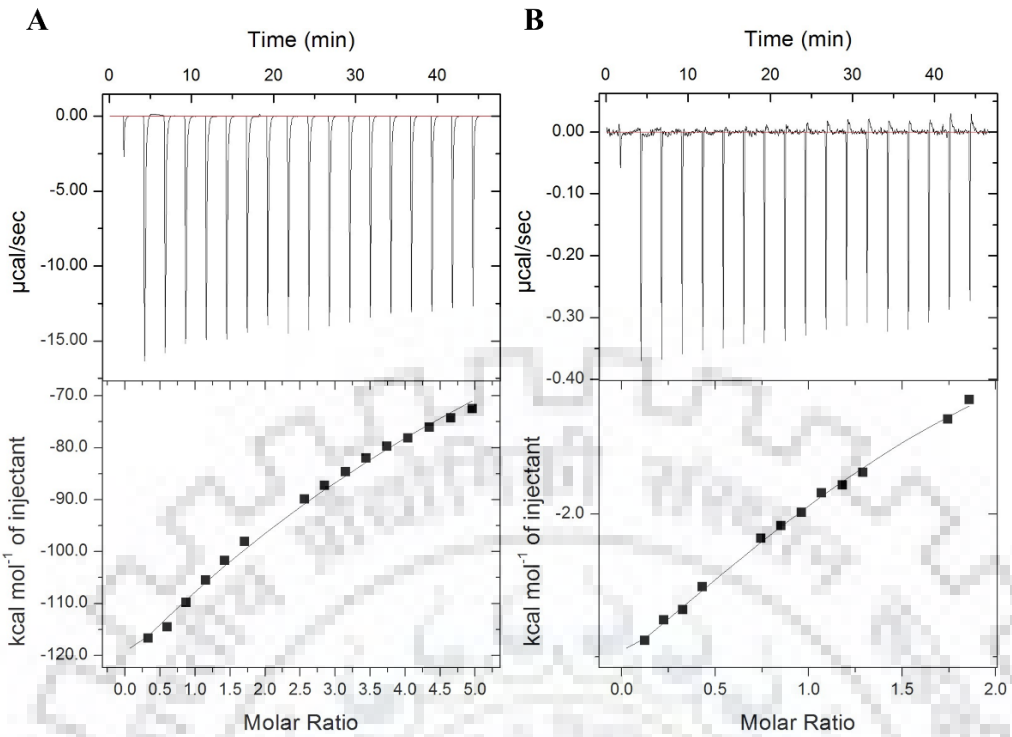

Figure 2.20: The *Mc*FabI-inhibitor interactions studied by ITC. **(A)** and **(B)** The isothermograms shown for the interactions of *Mc*FabI with EST and TCL respectively. The top panels in both **(A)** and **(B)** represent the raw data showing the heat changes (µcal/sec) during the sequential injections with time (min), while the bottom panels are the plots of the heat evolved (kcal/mol of injectant) upon binding of the injectant to the macromolecule within the cell.

2.3.15. DSC analysis of the thermal properties of *Mc*FabI and its interactions with estradiol and triclosan:

The *Mc*FabI protein was subjected to analysis by differential scanning calorimetry under different conditions including apo protein, the protein incubated with the cofactor NAD alone (*Mc*FabI-NAD binary complex), and the protein incubated with cofactor and inhibitor together (*Mc*FabI-NAD-TCL and *Mc*FabI-NAD-EST ternary complexes). These results revealed that the apo protein is exhibiting a Tm value of 52°C, and it is not affected by the binding of the cofactor alone as we obtained the same Tm value for the *Mc*FabI-NAD binary complex also (Figure 2.21). But the binding of the both inhibitors equally affected this thermodynamic property of the protein as we observed the Tm value of 65.1°C and 65.8°C for the *Mc*FabI-NAD-EST and *Mc*FabI-NAD-TCL ternary complexes respectively. The enthalpies of the corresponding thermal transitions were also calculated from these data. It can be understood

from these results that the inhibitors EST and TCL are equally stabilizing the thermal denaturation properties of the *Mc*FabI protein.

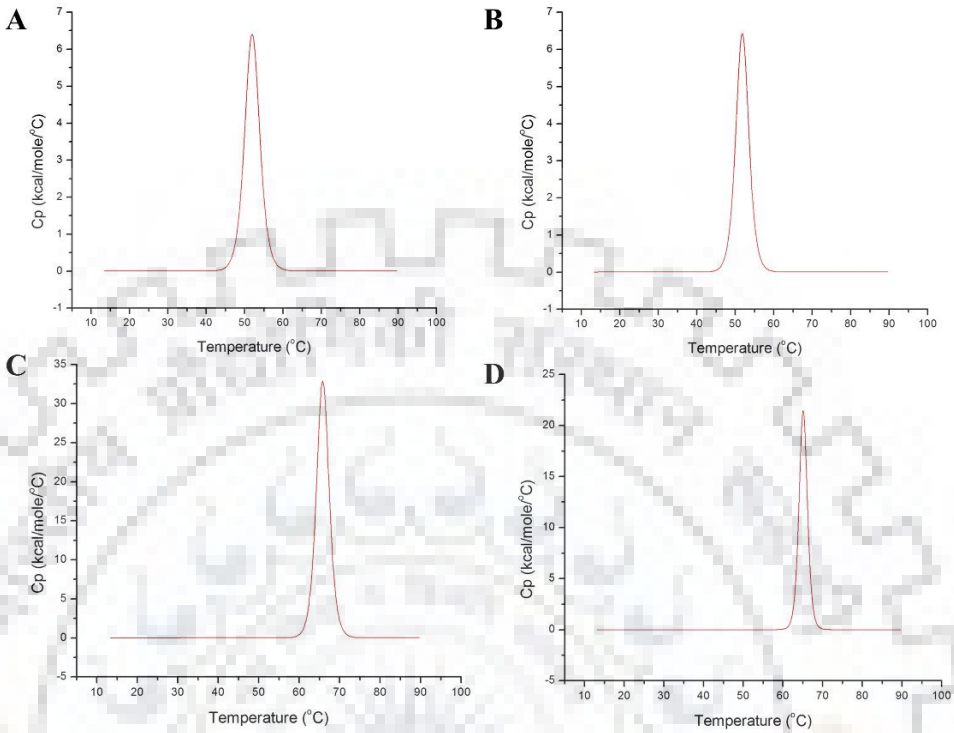

Figure 2.21: The thermal analysis of the *Mc*FabI protein and its interactions with the cofactor and inhibitors by DSC. **(A)**, **(B)**, **(C)** and **(D)** are showing the thermal analyses of the apo protein, the *Mc*FabI-NAD binary complex), and the *Mc*FabI-NAD-TCL and *M*FabI-NAD-EST ternary complexes respectively. The data were processed and plotted the heat capacity (Cp) (kcal/mole/°C) of the analyte sample versus the temperature (°C).

2.3.16. CD and fluorescence spectroscopic studies of the *Mc*FabI protein to unravel its biochemical attributes:

The circular dicroism spectroscopy studies were carried using the protocols explained in the methods section. The temperature stability of the protein was checked and from the analysis of the spectroscopy results, it was found that the protein is starting thermally denaturing at around 55°C temperature (Figure 2.22A), and it was also supported by the DSC experiments which showed the Tm of the apo protein as 52°C (Figure 2.21A). The denaturant resistance of the protein was also assessed by analyzing its structural stability in presence of the linear concentration gradient of the well-established protein denaturant urea. These results showed that the protein is stable upto 2 M urea and thereafter started getting denatured gradually with the increasing concentrations of urea (Figure 2.22B).

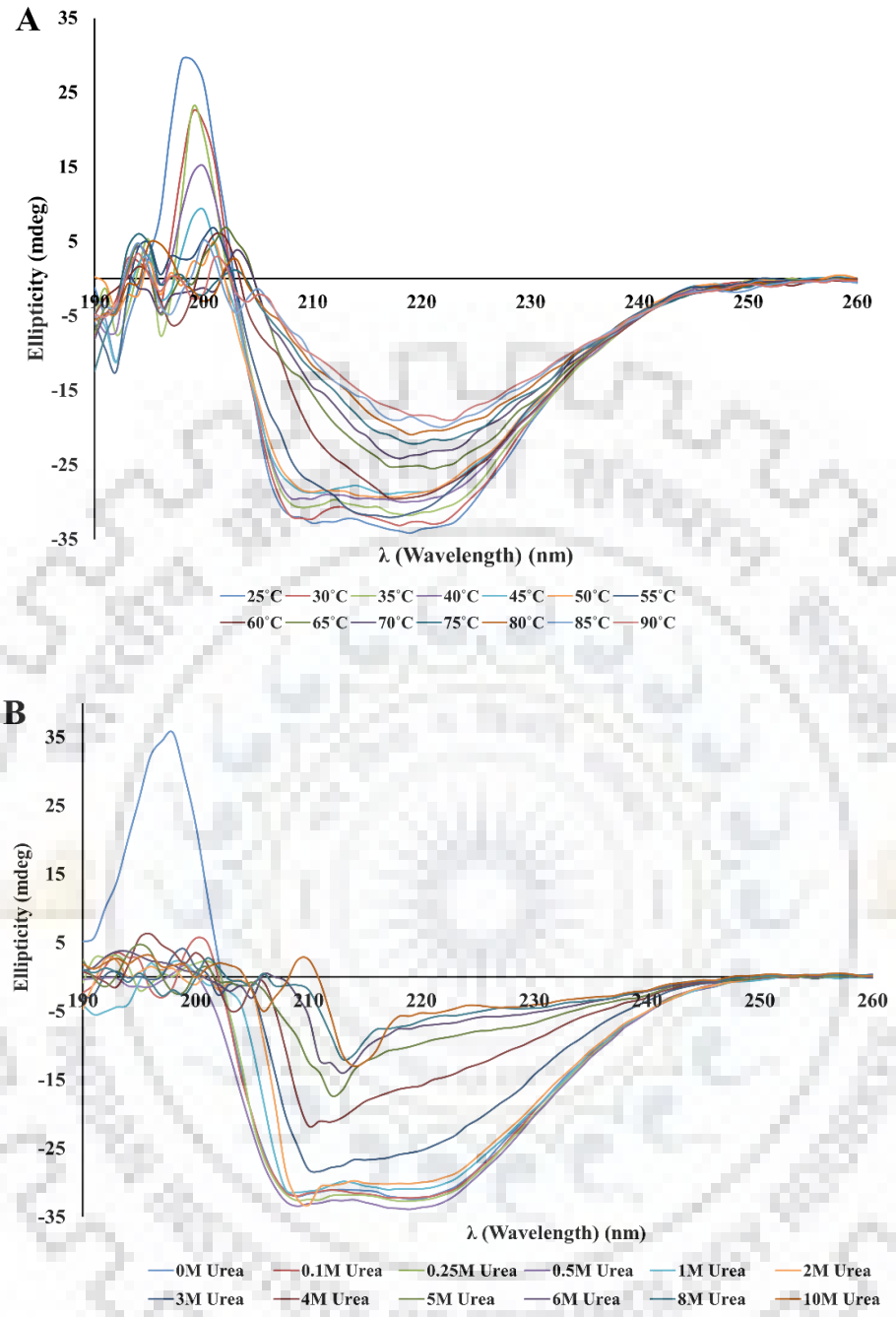

Figure 2.22: The biochemical attributes of *Mc*FabI revealed by CD spectroscopy studies. **(A).** Studying the temperature stability of the structural features of the protein. The far UV absorption spectrum was collected for the protein within the temperature range of 25°C to 90°C, at an interval of 5°C. **(B).** Stability of the protein in presence of the protein denaturant urea. The *Mc*FabI protein stability was analysed from 0.1 M urea concentration to 10 M. The data were processed by Microsoft excel as explained in the methods.

The fluorescence properties of the *Mc*FabI protein were also analysed by fluorescence spectroscopy as explained in the methods section. The protein was checked for fluorescence

emission at two different excitation wavelengths 280 nm and 295 nm to check its properties with respect to all of its intrinsic fluorophores and exclusively tryptophan, respectively. The results showed that protein is exhibiting maximum emission wavelength ($\lambda_{max(Em)}$) of 341 nm and 347 nm when excited at 280 nm and 295 nm respectively (Figure 2.23A and 2.23B). The binding of NAD cofactor shifted the $\lambda_{max(Em)}$ to 345 nm at λ_{Ex} of 280 nm, but didn't influence the $\lambda_{max(Em)}$ of *Mc*FabI at λ_{Ex} of 295 nm, while in the presence of triclosan inhibitor binding, *Mc*FabI protein is exhibiting $\lambda_{max(Em)}$ of 345 nm and 364 nm at λ_{Ex} of 280 nm and 295 nm respectively (Figure 2.23C and 2.23D, and Table 2.10). These results are indicating that the binding of NAD and triclosan are bringing certain conformational changes within the protein structure including the regions containing the intrinsic fluorophores tyrosines and tryptophanes. These results are supporting the conformational changes of the CBL, SBLs and ASL and few other structural elements, observed in the *Mc*FabI-NAD-TCL ternary complex in comparison to the apo structure.

The conformational and structural stability of the *Mc*FabI protein were also analysed by using its intrinsic fluorescence properties. The fluorescence emission pattern of *Mc*FabI was assessed in the presence of increasing concentrations of the protein denaturant urea. The results showed that the fluorescence intensity is gradually increased with the ΔRFU of 30000, and the corresponding $\lambda_{max(Em)}$ increased from 341 nm to 360 nm, with the increasing urea concentration at λ_{Ex} of 280 nm (Figure 2.24A). The similar results were also observed at λ_{Ex} of 295 nm, where the fluorescence intensity is gradually increased with the ΔRFU of 55000, and the corresponding $\lambda_{max(Em)}$ increased from 347 nm to 360 nm, with the increasing urea concentration (Figure 2.24B). These results are indicating the gradual denaturation of the protein with the increasing denaturant urea concentration, leading to gradual exposure of the intrinsic fluorophore amino acid residues.

Table 2.10. The fluorescence spectral parameters of the *Mc*FabI protein in various conditions including the presence of ligands and protein denaturing agents.

Sample	λ_{Ex}	$\lambda_{Em(max)}$	FI (fluorescence intensity)	Shift in $\lambda_{Em(max)}$
*Mc*FabI	280 nm	341 nm	-	-
*Mc*FabI	295 nm	347 nm	-	-
*Mc*FabI-NAD	280 nm	345 nm	Decreased	Red shift
*Mc*FabI-NAD	295 nm	347 nm	Increased	Red shift

*Mc*FabI-NAD-TCL	280 nm	345 nm	Decreased	Red shift
*Mc*FabI-NAD-TCL	295 nm	364 nm	Increased	Red shift
*Mc*FabI-urea	280 nm	360 nm	Increased	Red shift
*Mc*FabI-urea	295 nm	360 nm	Increased	Red shift

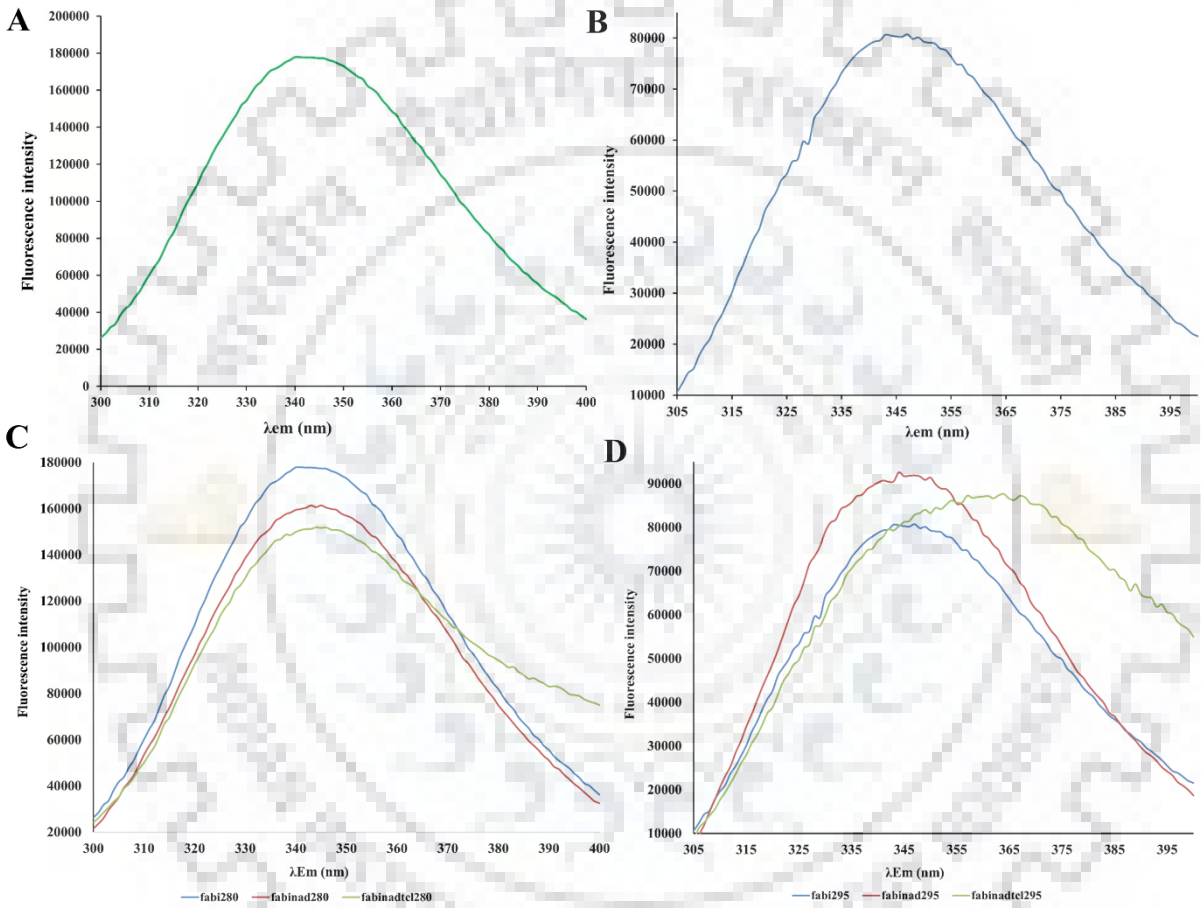

Figure 2.23: The intrinsic fluorescence properties of *Mc*FabI in its apo, *Mc*FabI-NAD binary complex and *Mc*FabI-NAD-TCL ternary complex forms studied by fluorescence spectroscopy. **(A)** and **(B)** are the fluorescence emission spectra of apo *Mc*FabI protein, in 300-400 nm range, at λ_{Ex} of 280 nm and 295 nm respectively. **(C)** and **(D)** are comparatively showing the fluorescence emission spectra of the apo protein, the *Mc*FabI-NAD binary complex and the *Mc*FabI-NAD-TCL ternary complex, in 300-400 nm range, at λ_{Ex} of 280 nm and 295 nm respectively.

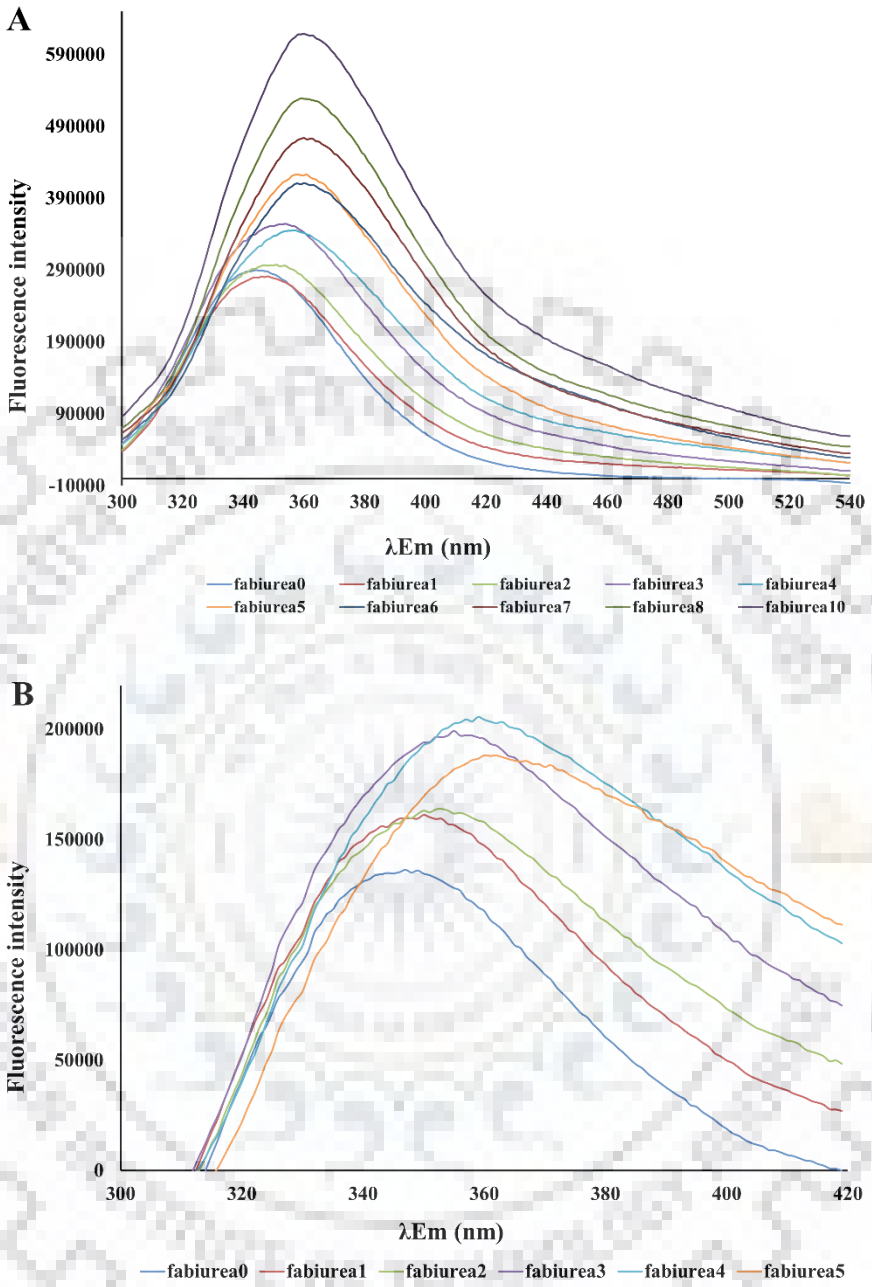

Figure 2.24: The conformational stability analysis of *Mc*FabI under urea denaturation conditions. The intrinsic fluorescence properties of apo *Mc*FabI were studied, by fluorescence spectroscopy, in presence of 1-10 M urea concentration. **(A)** The fluorescence emission spectrum of *Mc*FabI under increasing concentrations of urea, in 300-400 nm range, at λ_{Ex} of 280 nm. **(B)** The fluorescence emission spectrum under similar conditions at λ_{Ex} of 295 nm.

2.3.17. Native-PAGE analysis of inhibitor binding and protein oligomeric states:

The *Mc*FabI protein, in its apo, *Mc*FabI-NAD binary complex and *Mc*FabI-NAD-TCL and *Mc*FabI-NAD-TCL ternary complex forms, was analysed, by the Native-PAGE, for its oligomeric status and the influence of the cofactor and inhibitors on it. The results showed that the protein predominantly exists in monomer, dimer and tetramer states in its apo form in the solution and the binding of the inhibitors in presence of NAD cofactor led to the formation of tetramer species in major proportions, which is the biological assembly form of *Mc*FabI protein, while the cofactor alone didn't affect the oligomeric status significantly (Figure 2.25).

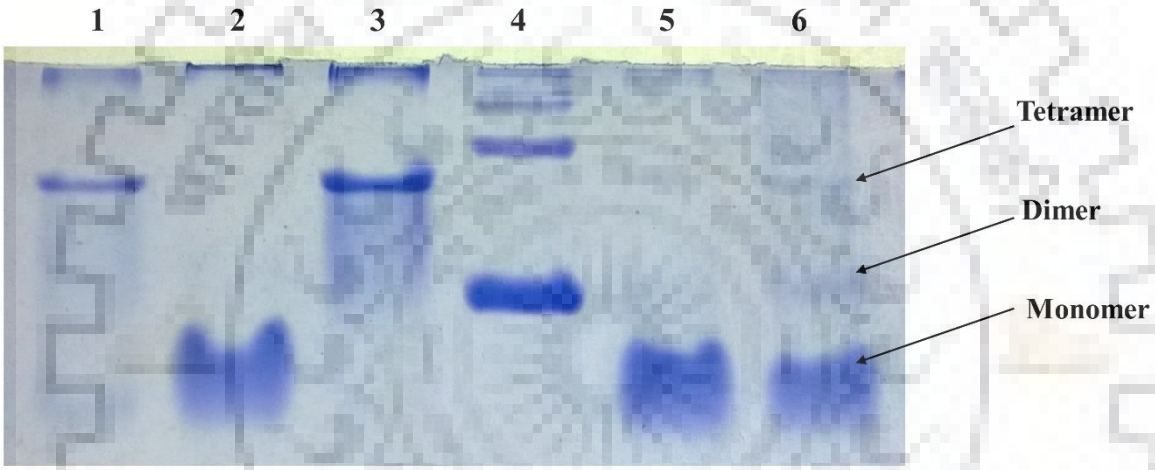

Figure 2.25: The Native-PAGE profile of *Mc*FabI protein in its apo, *Mc*FabI-NAD binary complex and *Mc*FabI-NAD-TCL and *Mc*FabI-NAD-EST ternary complex forms. Lane 1, 2 and 3: *Mc*FabI incubated with NAD-EST (*Mc*FabI-NAD-EST ternary complex form), NAD cofactor alone (*Mc*FabI-NAD binary complex), and NAD-TCL (*Mc*FabI-NAD-TCL ternary complex) respectively. Lane 4: Bovine serum albumin (BSA); Lanes 5 and 6 *Mc*FabI apo protein.

2.3.18. MD simulations of the *Mc*FabI-inhibitor complexes:

The *Mc*FabI apo protein and the *Mc*FabI-NAD binary complex structures extracted from the *Mc*FabI-NAD-TCL ternary complex crystal structure, along with the *Mc*FabI-NAD-TCL and *M*FabI-NAD-EST ternary complexes, were subjected to molecular dynamics simulations using GROMACS program and the protocols explained in the methods section. The results showed that the apo and the *Mc*FabI-NAD-TCL and *Mc*FabI-NAD-EST ternary complex structures are conformationally stable after 15 ns of MD simulation with an RMSD of ~0.35 – 0.4 Å (Figure 2.26A). The crotonyl coenzyme A (CCA) and estradiol docked in the *Mc*FabI and *Mtb*FabI

(InhA) active sites, respectively, were also analysed for their conformational stability by MD simulations.

The binding of CCA substrate in the *Mc*FabI active site is highly stabilized at 0.4 Å RMSD within 15 ns after the simulation start. While the estradiol binding in the InhA active site was unstable for longer time and stabilized with ~0.4 – 0.45 Å RMSD at around 25 ns.

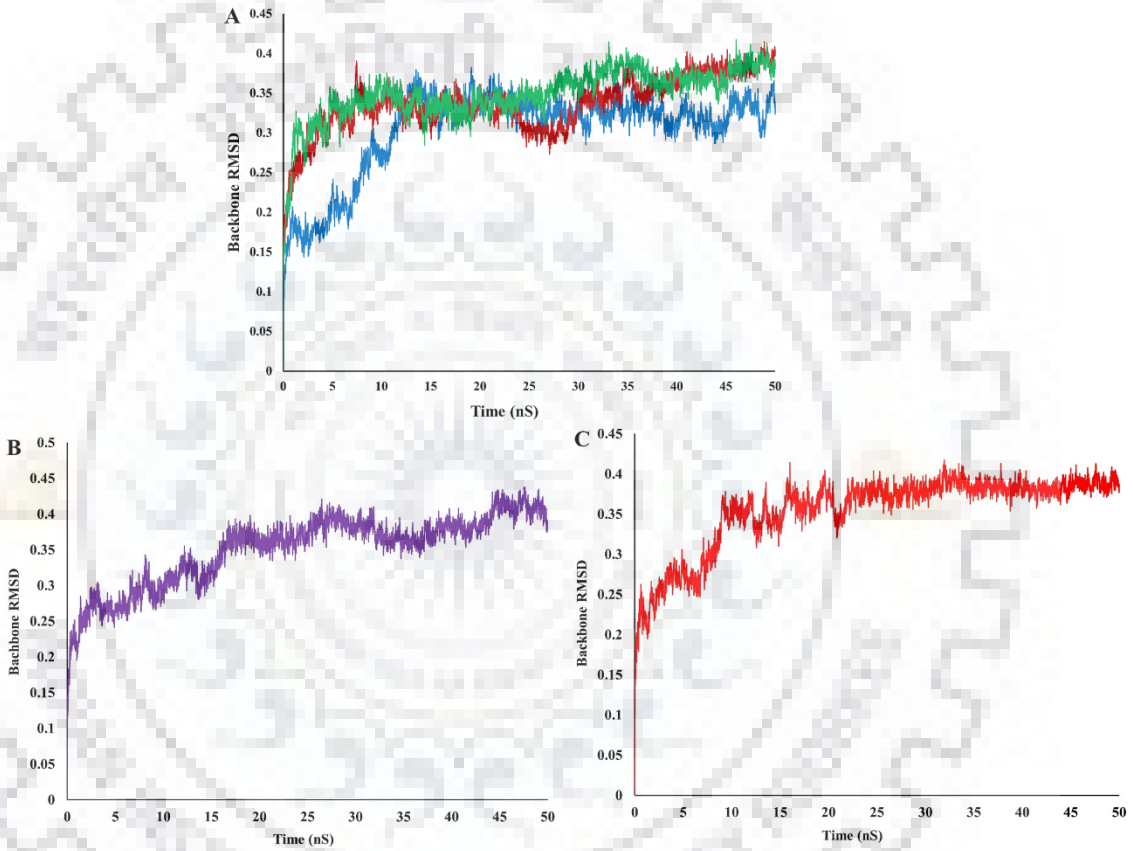

Figure 2.26: The MD simulations of the *Mc*FabI and InhA protein complexes with triclosan and estradiol inhibitors and CCA substrate. **(A).** The RMSD graphs corresponding to *Mc*FabI apo protein, and the *Mc*FabI-NAD-TCL and *Mc*FabI-NAD-EST ternary complex structures are shown colored by blue, red and green respectively. **(B).** and **(C).** The RMSD graphs of the InhA-NAD-EST and *Mc*FabI-NAD-CCA ternary complex structures respectively.

2.4. Discussion

The *Mc*FabI enzyme, the only isoform of ENR from *Moraxella catarrhalis* (914), was characterized, for the first time, biochemically and structurally in our current study. *Mc*FabI exists in homo-tetramer state in solution as well as in crystal, and this feature is in resemblance with many FabI proteins characterized from other bacterial species, except for *Sa*FabI, *Bc*FabI

and *Ba*FabI (198-199, 204-205, 207) (Table 2.11). The substrate binding loop (SBL) in the TCL ternary complex structure of *Mc*FabI is observed as a closed state conformation, as in the case of FabI structures characterized from many bacteria except for few (Table 2.5). Surprisingly the SBL is observed with an intermediary conformation in the EST ternary complex structure when compared with that of the closed and open conformations. This SBL, along with substrate binding loop 2 (SBL2) and active site loop (ASL), is found missing or highly disordered in case of apo structure and obtaining a stable ordered structure upon interaction with the cofactor and inhibitor molecules within the active site of ternary complexes. The cofactor binding loop (CBL) is present in all 3 structures, but shifted positionally at 4.2 Å RMSD in the two ternary complexes to accommodate and interact with the cofactor.

Table 2.11: The biological assemblies of FabI proteins from different pathogenic bacteria. ADBU: author determined biological unit, SDQS: software determined quaternary structure.

Organism	PDB	Molecule	Biological assembly		Asymmetric unit
			1 (ADBU)	2 (SDQS)	
M. catarrhalis		Apo	Tetramer	Tetramer	Monomer
M. catarrhalis		NAD-TCL	Tetramer	Tetramer	Tetramer
M. catarrhalis		NAD-EST	Tetramer	Tetramer	Tetramer
B. cereus	3OJE	Apo	Dimer	Dimer	Monomer
B. cereus	3OJF	NDP-IMJ	Tetramer	Tetramer	Tetramer
B. anthracis	5YCX	Apo (His-tag)	Dimer	Dimer	Monomer
B. anthracis	5YCV	Apo (no-tag)	Tetramer	Tetramer	Tetramer
B. anthracis	5YCR	NAD		Tetramer	Tetramer
B. anthracis	5YCS	NAD-TCL	Tetramer	Tetramer	Tetramer
S. aureus	3GNT	Apo	Tetramer	Dimer	Dimer
S. aureus	3GNS	Apo	Tetramer	Dimer	Monomer
S. aureus	3GR6	NAP-TCL	Tetramer	Tetramer	Tetramer
A. baumannii	4ZJU	NAD	Tetramer	Tetramer	Monomer

The disordered loops, missing in the apo structure, are found to be stabilized by the interactions of many protein residues with the cofactor and inhibitor molecules in both the ternary complex structures. The protein residues Ala14-Ile19, which constitute the CBL, and the side chains of Ala95, Gly97, Leu149, Tyr151, Glu152, Ala194 and Arg209, the component residues of

ASL/SBL2/SBL, are showing significant positional rearrangements and shifts to accommodate the entering cofactor and inhibitor molecules into the binding pocket. We have observed that the Asn160 of ASL is playing a crucial role in the stabilization of the 3 disordered loops by making hydrogen bonding with Gly106 of SBL2 and Lys206 of SBL1, in the case of both ternary complex structures. It is making a 3.2 Å hydrogen bond with the peptidyl oxygen of Lys206 of SBL, in case of TCL complex which has the closed state conformation of SBL, while a 3.9 Å hydrogen bond with the side chain oxygen OG atom of Ser207 of SBL, in case of the EST complex which has the intermediary conformation. This residue is conserved among many bacterial species and play the similar role (Table 2.12).

Table 2.12: Protein residues involving in the inter-loop interactions in FabI structures. SBL2: substrate binding loop2, CBL: cofactor binding loop, SBL: substrate binding loop.

Structure	Organism	SBL2 range	ASL range	SBL range	Residues participating in inter-loop interactions*
TCLcomp	McFabI	95-115	150-165	195-210	106G, 160N, 206K
1QSG	EcFabI	91-111	145-160	190-205	102G, 155N, 201K
5IFL	BpFabI	91-111	145-160	190-205	102G, 155N, 201K
4M89	NmFabI	91-111	146-161	191-206	102G, 156N, 202A
3NRC	FtFabI	90-110	145-160	190-205	99L, 155S, 201S
5TF4	BhFabI	92-112	146-161	191-206	104L, 158N, 204G
2PD3	HpFabI	91-110	144-159	189-204	100L, 154H, 201D
3GR6	SaFabI	93-112	146-161	191-206	103R, 156N, 202G
3OIF	BsFabI	94-113	147-162	192-207	105G, 157N, 203S
4NR0	PaFabI	93-113	148-163	193-208	104G, 158N, 205S
4ZJU	AbFabI	93-113	148-163	193-208	102L, 158N, 205S
1CWU	BnFabI	136-153	187-203	234-249	

The active site architectures of both the ternary complexes are showing significant differences with respect to the SBL conformation, NAD position and the interaction pattern of the protein residues with the ligand and the cofactor molecules. The SBL, CBL and NAD positions in the EST and TCL ternary complexes are differing at 6.8, 0.43 and 0.66 Å RMSD respectively (Table 2.4). The SBL conformation of TCL complex is evident and found in most of the FabI protein comolexes reported, while that observed in the EST complex is a rare conformation. These two conformations of the SBL in *Mc*FabI are proving that the enzyme is having an active

site with flexible loops surrounding it and can obtain different active site pocket volumes that can accommodate ligands of different sizes and shapes. Although EST and TCL are sharing few structural similarities, they differ in their size, shape and electrochemical features, which might have affected the SBL conformations.

Structural analysis, comparisons and sequence alignment of *Mc*FabI structures with that from other bacterial pathogens revealed the conservation of many structural elements including the cofactor binding motif and active site motif, that participate in stabilizing the cofactor and substrate binding, and many active site elements including the catalytic diad Tyr161 and Lys168. The active site architecture of *Mc*FabI is sharing considerable similarity with that of FabI structures from many pathogenic species. This will make the *Mc*FabI structural features to be highly helpful in designing novel structure-based antimicrobials with broad-spectrum activity. This comparison also revealed a 5-amino acid long insertion (83V-87K) in the sequence of *Mc*FabI, which make hydrogen bonds at the tetramer-tetramer interface to stabilize the protein in solution and helps in its crystal packing process.

Structural comparisons also revealed the similarity of *Mc*FabI with the human hydroxy steroid dehydrogenases (HSDs), including 17β-hydroxysteroid dehydrogenase 14 (HSD17B14) and estradiol 17β-dehydrogenase 8 (HSD17B8). These oxidoreductases, which belong to the SDR superfamily, are sharing ≤24% similarity in their conserved sequence, structural and functional features, while differing in their substrate specificity and catalytic mechanism (188, figure 2.14, 2.15 and 2.16). Substrate preferences vary among these enzymes based on the stereochemistry and size of the active site, chemical nature of the bonds they are acting upon and species distribution of the enzyme (176, 188, 193). Most of the HSDs are known to exhibit remarkably broad substrate specificity; 17β-HSDs type 4, 8, 10, 12 and 14 act on fatty acyl-CoA derivatives and type 6, 9 and 15 act on retinoic acid metabolites along with the steroidic substrates (915-919). Whereas, the bacterial, fungal and plant ENR enzymes exhibit narrow substrate specificity with fatty acyl-CoA derivatives being the only substrates. The human 17β-HSDs, which belong to the EC 1.1 class oxidoreductases, catalyze the reduction of a keto group (C=O), whereas the ENR enzymes, belonging to the EC 1.3 class, do the reduction of a C=C double bond conjugated to a keto group. This difference in the chemistry of their reduction mechanisms resulted in two significant structural differences between ENRs and HSDs: (i) the relative positions of the catalytic residues (Tyr and Lys) are varying in these enzymes, YX_6K in ENRs and *Mc*FabI and YX_3K in HSDs and (ii) an approximately 2 Å shift is observed in the relative positions of the base tyrosine and cofactor NADH in ENRs and HSDs, as the distance

between phenolic oxygen of the base and C4N atom of the cofactor is around 6 Å and 4 Å respectively (176, 188). Although type 4, 8, 10, 12 and 14 17β-HSDs are acting on fatty acyl-CoA derivatives as substrates, their dehydrogenase domains act with high specificity towards the β-hydroxy/β-keto groups to only catalyze the reversible conversion of β-ketoacyl-CoA derivatives and β-hydroxyacyl-CoA derivatives, i.e. the 2nd and 3rd steps of fatty acid elongation cycle and the β-oxidation of fatty aicds respectively (915-919). These differences between ENRs and HSDs are supporting the hypothesis that the steroids do not necessarily act as substrates for ENRs too, even if they are similar to certain extent (≤24%), and may bind in the active site of ENRs to act as inhibitors.

The sequence and phylogenetic tree analyses are showing that HSDs are exhibiting higher sequence, structural and functional similarities with the FabG enzymes (BKRs) than the ENR enzymes of SDR family (figure 2.27). The evolutionary relationships of HSDs also showed that the 3-hydroxyacyl-CoA dehydrogenase and 3-ketoacyl-ACP reductase (BKR) enzymes, catalyzing the 3rd and 2nd steps of β-oxidation of fatty aicds and fatty acid elongation cycle respectively, are their deep ancestors (920-921). The ENRs, BKRs (FabG) and the dehydrogenase domains of HSDs which are acting on the fatty acyl derivatives as substrates, belong to the SDR family. And it's a well observed/understood fact that despite their highly diverse substrate specificities, the members of SDR family exhibit a close to identical structural architectures and a common catalytic mechanism (921-922) and that is how the ENRs and HSDs might be sharing few structural and mechanistic features, irrespective of their substrate and functional group specificity that they are acting upon. The bacterial HSDs, involving in the metabolism of host steroid hormones and steroid metabolites including the steroid antibiotics, also showing high similarity with 3-hydroxyacyl-CoA dehydrogenase and 3-ketoacyl-ACP reductase (BKR) enzymes of fatty acid degradation and synthesis pathways and mammalian HSDs than the ENR enzymes (920-923). While the mammalian HSDs exhibit broad substrate specificity towards compounds other than the steroids also, the bacterial HSDs are showing limited substrate specificity for steroids only (924-925). These all issues are hinting that mammalian and bacterial HSDs are more structural and functional homologues of BKRs than to ENRs; and the ENRs, being bacterial proteins, exhibit limited substrate specificity for fatty acyl derivatives only.

The interactions made by 17β-estradiol with the cofactor and residues lining the active site of *Mc*FabI, are almost similar to that of triclosan (figure 2.7). The few differences between the position and binding pattern of EST and TCL within the active site are due to the differences in

their size, shape and the electrochemical features which might have also affected the SBL conformation and position of the cofactor NAD. Estradiol and triclosan are also sharing similarities in binding to estrogen receptors (ER) (857-858, 860-862, 865-866) and HSDs (860, 867-871), in addition to the bacterial ENR enzymes.

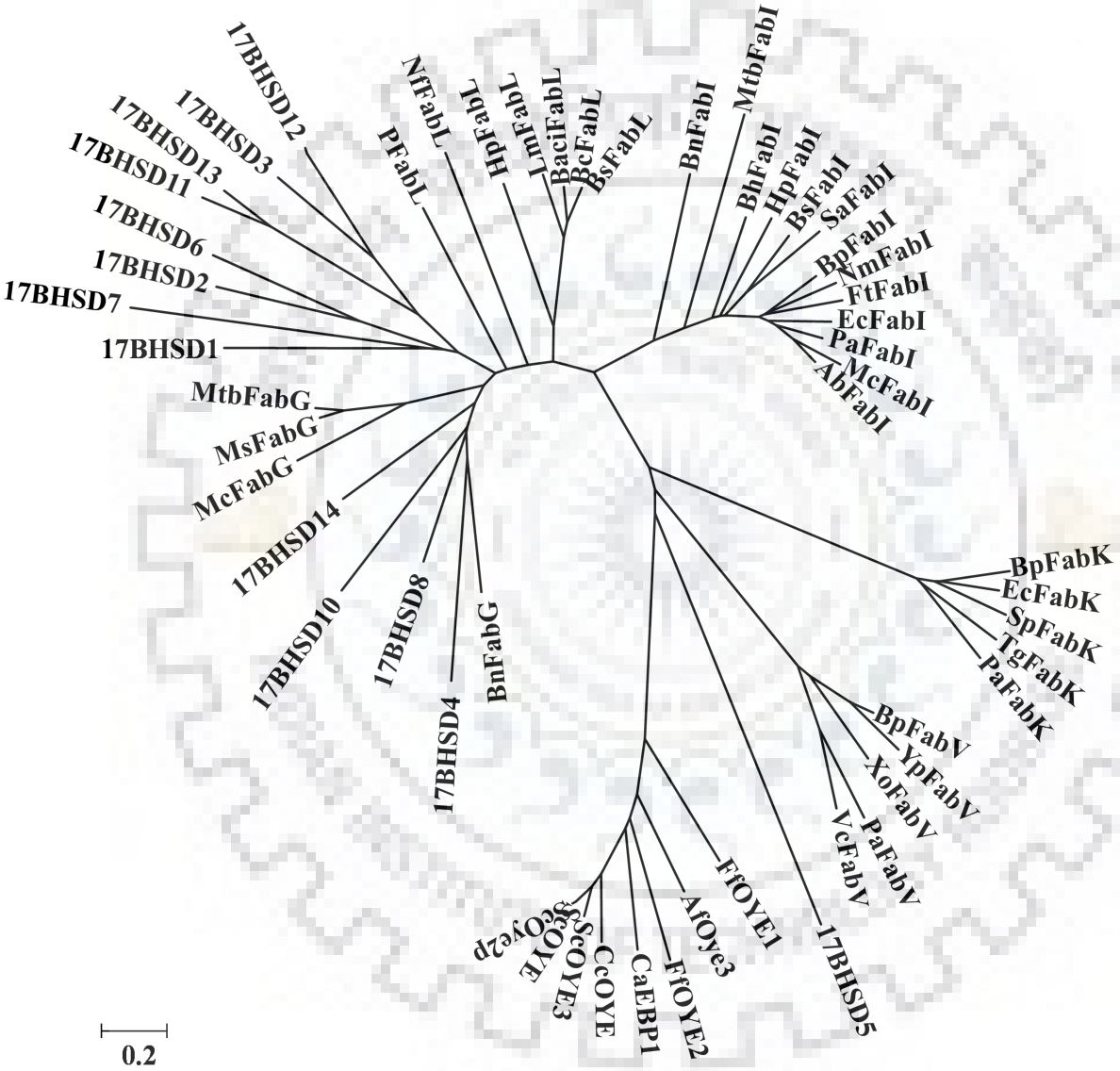

Figure 2.27: The phylogenetic tree analysis of the protein sequences of FabI, FabK, FabL, FabV, FabG, all isoforms of the mammalian 17β-hydroxysteroid dehydrogenases and fungal OYE family oxidoreductase enzymes. The tree is generated by using the MEGA7 program.

The binding kinetics studies by SPR and ITC revealed that estradiol is exhibiting very high binding affinity (0.5-5 μM) towards *Mc*FabI. The enzyme activity studies are showing that *Mc*FabI is able to utilize the crotonyl CoA as substrate, as in the case of ENR enzymes from many other bacteria, and the activity is not affected significantly by the presence of N-terminal His6-tag. TCL is inhibiting the activity with a ki value of 31 nM, in an uncompetitive fashion, in the presence of NAD+, indicating that it is binding to the enzyme-cofactor complex rather than the free enzyme. E2 is inhibiting the *Mc*FabI activity *in vitro* with a ki value 38.1 μM. E2 was reported to be exhibiting direct antimicrobial activities *in vitro* at concentrations higher than its *in vivo* levels (875), but not at its physiological levels (877). It was also reported that several endogenous antimicrobials in the human body are biologically active and exhibit *in vivo* antimicrobial activities, at their physiological concentrations, depending on their local environment; and there are several factors in the milieu which determine the biological activities of these antimicrobials (856, 874, 876). Hence more precise measurements would be required to determine whether E2 exhibits direct antimicrobial activities *in vivo* at its physiological concentrations.

The direct interactions of human estrogens with the bacterial, yeast and fungal oxidoreductase enzymes; other than the HSDs; including the estrogen binding proteins (EBPs) and old yellow enzyme (OYE) family proteins, and other proteinaceous molecules were also reported in the past (872-874, 879-880, 926). The oxidoreductase activity of these estrogen binding proteins from yeasts, fungi and bacteria was also reported to be inhibited by the estrogens (874, 926). Inhibition of this oxidoreductase activity of EBPs and OYEs by 17β-estradiol, in case of yeasts and fungi, is shown to be possibly a part of the signalling pathway which leads the dimorphic conversion of yeast to hyphal/mycelial form or vice versa depending on the surrounding hormonal milieu of the host, and thereby modifying their growth, morphogenesis and pathogenecity (856, 874, 879, 926). In the case of prokaryotic bacteria also it's been shown that the direct interactions of host steroid hormones, especially the estrogens, with the bacterial enzymes or steroid-binding proteins may affect the growth development and modulate the virulence of those pathogenic bacteria (856, 879, 927-928). But the inhibition of FabI by 17β-estradiol, shown in our current study, is possibly indicating a bacteriostatic mechanism of E2 to inhibit the growth of bacteria by inhibiting one of its essential enzymes and proposing a new mechanism for the direct antimicrobial actions of E2 *in vitro*. The comparison of sequences of

EBPs from bacteria and yeasts with ENRs, BKRs and HSDs showed that they are sharing no similarity with any of the ENR/BKR/HSD enzymes (figure 2.27).

The estrogen hormones were shown to exhibit concentration specific bi-functionality; they enhance the microbial growth and pathogenicity at one end and inhibit the microbial growth by direct or indirect mechanisms on the other end (879). In our current study also we observed the direct *in vitro* antimicrobial actions of E2 against *M. Catarrhalis* (table 2.8). The inhibition of the growth of several bacterial and fungal pathogens *in vitro* by estrogens was shown through several direct and indirect mechanisms, other than those involving direct inhibition of pathogen's essential enzymes (879-880, 867). E2 was proved to exhibit its *in vivo* antimicrobial and immune activities through an indirect mechanism by regulating the host mucosal and non-mucosal immune responses (876-878), while there is no direct mechanism known. These antimicrobial roles of E2 are also known to majorly contributing to the well established fact that human females are immune-privileged and more resistant to the microbial infections than their male counterparts. The root causes, other than the differences in the sex hormonal levels and their regulation of the host immune responses and influence on the host responses to vaccination, for sex differences in the resistance to infectious diseases remain to be uncovered till date. Our current results are suggesting that the direct antimicrobial actions of 17β-estradiol *in vitro* by inhibiting certain metabolically essential enzymes in bacteria and fungi, maybe pointing to a new mechanism for the direct antimicrobial actions and microbial inhibition by E2 *in vivo* which may also contribute to the sex differences in the resistance to microbial infections in humans.

Estradiol was shown to down-regulate a significant portion of genes involved in the fatty acid biosynthesis and nucleotide metabolism, as part of pathogen's survival responses, through genomic pathways (879, 927). But in our current study, we are showing that estradiol is inhibiting the bacterial ENR enzyme as part of host defence mechanisms, in a non-genomic style. Till date 3 types of steroid-protein interactions were shown to occur in the biological systems and now we may observe a 4th type of interaction in which the host steroids bind to bacterial or fungal essential enzymes to inhibit their catalytic activity followed by the inhibition of microbial growth. The interactions of host steroids with the bacterial ENR enzymes may be of 4th type interactions.

The biochemical studies, by DSC and CD spectroscopy, on *Mc*FabI protein revealed that the protein is structurally stable upto 55°C temperature, with a Tm value of 52°C which is

extended upto 65°C in presence of the inhibitors triclosan and estradiol. The CD and fluorescence spectroscopy studies also showed that the protein can withstand upto 2 M urea concentration and maintain its structural integrity. The crystal structures, and molecular docking and subsequent MD simulation studies also revealed that the complexes of *Mc*FabI and InhA with triclosan and estradiol are also conformationally stable with an RMSD of 0.35 – 0.4 Å. The binding of CCA in the active site of *Mc*FabI is conformationally stable as shown by the docking and MD simulation studies. The native PAGE studies showed that the *Mc*FabI protein exists in 3 different oligomeric states, including monomer, dimer and tetramer, in its native state in the solution. It was also revealed by these studies that the binding of inhibitors triclosan and estradiol further promotes the tetramer formation and hence in presence of these inhibitors, maximum proportion of *Mc*FabI exists in tetrameric form.

CHAPTER 3

Studies on OXA-58 from *Acinetobacter baumannii* to unfold the key structural elements essential for β-lactam substrate recognition and enzyme activity and helpful in the structure-based inhibitor design

3.1. Introduction:

Acinetobacter baumannii is an opportunistic nosocomial pathogen in humans and causes several bloodstream and ventilator-associated infections in the health-care facilities. It's one of the major causes of the hospital-derived nosocomial infections in humans, especially the people with compromised immune systems. While other species of the genus *Acinetobacter* are often found in soil samples (leading to the common misconception that *A. baumannii* is a soil organism and ubiquitous organism, too), it is almost exclusively isolated from hospital environments. The potential of this organism to respond swiftly to changes in selective environmental pressure (selective antibiotic pressure, for example) contributes to the rapid global emergence of *A. baumannii* strains resistant to all β-lactams, including carbapenems. It also has a potential to upregulate its innate resistance mechanisms and potential of acquisition of foreign determinants. The genetic complexity, genetic agility and broad resistance armamentarium of *A. baumannii* and its wide array of drug resistance determinants and its ability to effectively regulate these according to selective environmental pressures clearly demand respect. Much of the success of *A. baumannii* to be multidrug-resistant can be directly attributed to its plastic genome, which rapidly mutates when faced with adversity and stress. The WHO has included carbapenem-resistant *A. baumannii* in the critical group in the list of bacteria that pose the greatest threat to human health, prioritizing research and development efforts for new antimicrobial treatments. The molecular features that promote environmental persistence, including desiccation resistance, biofilm formation and motility, and the most recently identified virulence factors, such as secretion systems, surface glycoconjugates and micronutrient acquisition systems collectively enable these pathogens to successfully infect their hosts.

The most prevalent mechanism of β-lactam resistance in *A. baumannii* is enzymatic degradation by β-lactamases. However, in keeping with the complex nature of this organism, multiple mechanisms often work in concert to produce the same phenotype. The nonenzymatic mechanisms of β-Lactam resistance, including carbapenem resistance, include changes in outer

membrane proteins (OMPs), multidrug efflux pumps, and alterations in the affinity or expression of penicillin-binding proteins (PBPs). The resistance mechanisms toward other classes of antibiotics such as aminoglycosides, quinolones, tetracyclines and glycylcyclines, polymyxins and other antibiotics, include the aminoglycoside-modifying enzymes, ribosomal (16S rRNA) methylation, tetracycline-specific efflux, modification to target binding sites, ribosomal protection and multidrug efflux.

The emergence of MDR *A. baumannii* emphasizes the urgency of developing alternative treatment strategies. These anti-virulence strategies include phage-therapy, metabolic interference therapy, antimicrobial peptide therapy and vaccine strategies. Despite the absence of new therapeutic options for *A. baumannii* in clinical studies, the activity in the preclinical arena is notable. Such agents can be divided into those that inhibit a currently recognized mechanism of resistance or those that have a novel mechanism of action. With regard to the former, attention has been directed toward new β-lactamase inhibitors, especially those targeting the Ambler class D OXA type carbapenemases (serine oxacillinases) (CHDLs) and Ambler class B MBLs, as well as toward inhibitors of aminoglycoside-modifying enzymes and multidrug efflux pumps.

Carbapenem-hydrolyzing class D β-lactamases (CHDLs) are a subgroup of class D β-lactamases, which are the enzymes that hydrolyze carbapenem class of β-lactams. There are four gene clusters encoding the CHDLs reported, including the $bla_{\text{OXA-23}}$ gene cluster, the $bla_{\text{OXA-24}}$-like gene cluster and the $bla_{\text{OXA-58}}$-like gene cluster, which are acquired or native to *A. baumannii*, and the $bla_{\text{OXA-51}}$-like gene cluster which naturally occurs in *A. baumannii*.

3.2. Materials and Methods:

3.2.1. Materials

Many of the chemicals used in this study were purchased either from Sigma, Merck-millipore, Fluka, Himedia, Bio-Rad or SRL. The bacterial growth media were purchased either from Merck-millipore or Himedia laboratories, while the platic ware and glass ware from Tarsons and Borosil respectively. The chromatography media and columns were procured from GE Healthcare or Bio-Rad. *E. coli* DH5α and BL21 (DE3) strains were purchased from Novagen (USA). The pre-optimized crystallization screens, including Crystal Screen, PEG/Ion, Index, Salt and Crystal Screen Cryo were purchased from Hampton Research, USA; while JCSG-plus, MIDASplus, Morpheus and PACT premier were from Molecular Dimensions, UK. The pET24d(+)::*blaOXA-58SP* expression vector containing *blaOXA-58* gene from *Acinetobacter*

baumannii was provided by Dr. D. Golemi-Kotra, York University, Canada. We have been also provided with six different pET24d(+)::*blaOXA-58SP* expression vectors containing the *blaOXA-58* genes with point mutations K86A, M225A, F113Y, F114A, F113A, M225T and F114I individually. She also provided the compounds 6α-hydroxymethyl penicillin (6αHMP) or 6α-hydroxyoctyl penicillin (6αHOP) for crystallization studies.

3.2.2. Methods:

3.2.2.1. Transformation of the pET24d(+)::*blaOXA-58SP* expression vectors:

The recombinant pET24d(+)::*blaOXA-58SP* plasmid expression vector containing the coding region, with the truncated N-terminal signal peptide, of the wildtype *blaOXA-58* gene from *Acinetobacter baumannii* was transformed into *E. coli* DH5α and BL21 DE3 cells, the cloning and expression hosts respectively. The transformation was carried out by $CaCl_2$ chemical-heat shock transformation method, using the protocol explained in the previous chapter. The pET24d(+)::*blaOXA-58SP* expression vectors containing the *blaOXA-58* genes with point mutations K86A, M225A, F113Y, F114A, F113A, M225T and F114I individually, were also transformed into *E. coli* DH5α and BL21 DE3 cells in the similar way.

3.2.2.2. Protein over-expression:

Single bacterial colony from each of the recombinant pET24d(+)::*blaOXA-58SP* plasmid-transformed BL21 DE3 agar plates was inoculated separately into autoclaved LB broth tubes, and IPTG induction and protein over-expression checking were carried out using the same protocol explained in the previous chapter.

3.2.2.3. Purification of OXA-58 wild-type and its point mutation variant proteins:

The wild-type and all its point mutation variants were purified using the same protocol as follows. After confirming the protein over-expression from all the recombinant pET24d(+)::*blaOXA-58SP* plasmid-transformed BL21 DE3 cells, the primary cultures were used to inoculate large volumes of TB broth. 1 L of TB broth was added with 50 µg/mL kanamycin antibiotic and 10 mL of overnight grown primary inoculums, followed by incubation at 37°C and 200 rpm speed until its OD_{600} reaches to 0.6. The culture was induced for protein over-expression using 0.4 mM IPTG, followed by incubation at 18°C and 200 rpm for around 15-20 hrs. The cells from the incubated culture were harvested by centrifugation 6000 rpm and 4°C for 10 mins.

All the protein purification steps were carried out at 4°C, unless otherwise mentioned. The cell pellet was re-suspended in 30 ml of suspension buffer (10 mM potassium phosphate buffer, pH 6.5) and cell disruption was carried out at 20 KPSI working pressure using Constant systems LTD made one shot cell disruptor, with 5-7 mL cell suspension in each shot. The cell lysate thus obtained was centrifuged 12000 rpm and 4°C for 60-70 mins and the supernatant was separated out from the pellet containing the cell debris. Meanwhile a 5 mL pre-packed SP Sepharose cation exchange column having 5 mL of matrix/bed was connected to an AKTA purifier 10, an FPLC system, and washed properly with binding buffer containing high salt concentration followed by 20-30 column volumes of water, and subsequently equilibrated with upto 10 column volumes of binding buffer (10 mM potassium phosphate buffer, pH 6.5 (buffer A)). During equilibration phase, the column flow rate was maintained at 1.0 mL/min. The supernatant was applied onto that buffer-equilibrated SP sepharose column at very low flow rates, 0.2 mL/min, for allowing the protein binding to the ion exchange matrix in the column at 4°C, and the flow through was collected simultaneously from the outlet. A linear gradient of 0% to 100% of high-concentration 200 mM potassium phosphate buffer pH 6.5 (buffer B) was used to elute the matrix-bound protein. Elution from the column was monitored by the UV absorption at 280 nm and eluent conductivity, and the elution of desired protein was observed in the conductivity range of 8-12 milli-siemens/cm. The supernatant, flow through and elution fractions corresponding to the 280 nm UV absorption peaks, along with a protein ladder sample, were run on the SDS-PAGE electrophoresis using a 12% separating gel.

3.2.2.4. Size exclusion chromatography purification:

The presence and purity of the protein fractions collected in the ion exchange chromatography step were analyzed in the SDS-PAGE gel. The fractions containing partially purified OXA-58 or its point mutation variant, appropriately, protein were pooled and concentrated using 10 kDa molecular weight cutoff (MWCO) amicon centrifugal filters. The protein was concentrated upto 10 mg/mL. Meanwhile, a 120 mL HiLoad 16/600 Superdex 200 pg gel filtration column, connected with the AKTA purifier 10 FPLC system, was equilibrated with 2 column volumes of gel filtration purification buffer (10 mM potassium phosphate buffer, pH 7.0 and 100mM NaCl). 500 μL of concentrated protein sample was loaded onto the equilibrated column and elution was collected into 2 mL fractions, from the point of void volume of the column. The elution from the column was monitored by UV absorption at 280 nm, along with conductivity, ionic strength and pH. The protein elution was observed by the 280 nm absorption peaks and all the elution fractions corresponding to all the UV absorption peaks were run on 12% SDS-

PAGE gel to check for the presence and purity of the protein. The gel filtration fractions containing purified protein were pooled and concentrated upto 20 mg/mL, using the 10 kDa MWCO amicon centrifugal filters, and used for crystallization and other experimental studies.

3.2.2.5. Co-crystallization of wild-type OXA-58 protein:

The wild-type OXA-58 protein concentrated upto 20 mg/mL in 10 mM potassium phosphate buffer, pH 7.0 and 100mM NaCl was used for crystallization studies. Crystallization experiments were carried out by hanging drop and sitting drop vapor diffusion methods and at 4°C and 20°C. 96-well sitting drop plates and 24-well hanging drop plates were used and for initial trials the pre-optimized crystal screens were employed. Crystallization experiments were set up manually. In case of apo crystals, 1µL of the concentrated protein solution was mixed homogeneously with 1µL of reservoir well solution containing 2.2 M Sodium chloride, 0.1 M Tris buffer pH 8.0 and 28% w/v polyethylene glycol 3,350.

To obtain the co-crystals of wild-type OXA-58 protein with the carbapenem mimetic compounds 6αHMP and 6αHOP, the apo protein solution was added with 10-folds of these compounds independently and incubated for 2 hrs at 20°C and then set for crystallization using the same method explained for the apo protein. After long incubations also we haven't obtained any co-crystals for the wild-type OXA-58-6αHMP and OXA-58-6αHOP binary complexes and hence we followed the soaking experiments. We have grown the apo crystals and soaked them in a solution prepared by mixing the 10 mM 6αHMP or 6αHOP prepared in 0.1 M Tris-HCl (pH 8.0) buffer and 30% (wt/vol) PEG 3350 with the reservoir well solution corresponding to the apo crystal in 4:1 ratio and subsequently incubated for 15 min at room temperature. This solution also helped as cryo-protectant for the crystals and crystal soaking in the inhibitor solution was carried out before collecting the data.

3.2.2.6. Crystallization of point mutation variants of OXA-58 protein:

All the seven point mutation variants, including K86A, M225A, F113Y, F114A, F113A, M225T and F114I, of OXA-58 protein were purified to highest homogeneity and concentrated upto 20 mg/mL in 10 mM potassium phosphate buffer, pH 7.0 and 100mM NaCl was used for crystallization experiments. The mutant proteins were also given crystallization trials using the optimized crystallization condition of the wild-type apo protein and we have obtained crystals for few of the mutants but very much fragile and with poor structural strength, as they are collapsing at the moment they are coming in contact with the cryo-protectant solution. And the crystals are not diffracting well without cryo and sometimes diffracting but poorer with ice

rings and other errors. Then we extended our trials using other polyethylene glycol precipitant solutions and buffers. We obtained better quality mutant crystals with the reservoir solution containing 2.2 M Sodium chloride, 0.1 M HEPES buffer pH 7.0 and 22% w/v Polyethylene glycol 4000.

3.2.2.7. Data collection, processing and refinement:

The diffraction data for well grown crystals of wild-type OXA-58 apo, OXA-58-6αHMP and OXA-58-6αHOP binary complexes, and all the mutant OXA-58 proteins were collected at home source X-ray diffraction facility, MCU lab, IIT Roorkee, India. The data were collected at 100K temperature on MAR345dtb IP detector using a Bruker Microstar-H Cu rotating anode X-ray generator (Cu Kα wavelength = 1.54 Å) operated at 45 kV and 60 mA. The crystals were collected from the wells using cryo-loops (Hampton Research, USA) of appropriate size and 10% ethylene glycol in reservoir solution was used as cryo-protectant to improve the diffraction quality of the crystals. Prior to data collection, the apo crystals were soaked in the 10 mM 6αHMP or 6αHOP solution prepared in the reservoir equivalent solvent and incubated for 15 min at room temperature, in order to obtain the diffraction data for wild-type OXA-58-6αHMP and OXA-58-6αHOP binary complexes. The crystal to detector distance was kept 200 mm and images were collected with an X-ray exposure time of 5 min per frame and an oscillation width of 1° per image.

The data collected at the home source, from all the OXA-58 crystals were processed; indexed, integrated and scaled; using the HKL2000 suite (881) using the protocols explained in the previous chapter. The scalepack output files (.sca format) that were obtained from the HKL2000 program after data processing subsequently converted to .mtz file format for the processed data to be used for refinement by CCP4i (885-886) and PHENIX (888-889) suites. The crystal unit cell contents were assessed by calculating the crystal's Mathews coefficient and the best suitable space group of the crystal was analysed by pointless program of CCP4i.

The initial phases for the wild-type OXA-58-6αHMP and OXA-58-6αHOP binary complex structures were obtained by molecular replacement with MOLREP (883) of the CCP4i suite (885-886) using the processed .mtz data file, OXA-58 protein primary sequence and the protein atomic coordinates of a single subunit of *A. baumannii* wild-type apo OXA-58 crystal structure, solved in our laboratory, as a search template. REFMAC5 (887) program of CCP4i suite was used for the initial rigid body refinement of the initial coordinates obtained from molecular replacement. It was followed by the restrained refinement in the subsequent cycles of

refinement, along with TLS and NCS refinement parameters. After each round of refinement of the protein atomic coordinates, the model building of the coordinates was carried out in the COOT with proper real space refinement (RSR). Iterative cycles of model building and refinement were performed by COOT (890) and REFMAC5, until the refinement quality obtained at maximum possible, which was monitored by refinement statistics including the values of R_{work} and R_{free}. Once the protein atomic coordinates were fit and refined properly, the water (solvent) molecules were added in the Fo-Fc difference map at 2.5σ and refined. Density for the 6αHMP or 6αHOP ligands was searched in the Fo-Fc difference map at 2.5σ and fit properly in the match density using other modeling tools of COOT, and subsequently refined by REFMAC and PHENIX. The ligand PDB coordinates were prepared in the PHENIX program using their SMILES strings and imported into COOT for searching their density.

3.2.2.8. Validation of the refined PDB structures:

It was carried out during manual model building in the COOT and also during refinement by REFMAC. The stereo-chemical attributes of refined models were validated by MOLPROBITY (891) and further validation of the completely refined models was carried out by the PDB validation tool of the wwPDB deposition suite.

The data collection and refinement statics were calculated using the information contained in the log files (.log), that were written and obtained after every step of data processing and refinement, and are given in Table 3.1.

3.2.2.9. Sequence and structure analysis:

The *Ab*OXA-58 protein sequence from *A. baumannii* was compared with other oxacillinases including CHDLs from *A. baumannii* itself and other pathogenic bacteria producing similar enzymes, and other classes of homologous β-lactamase proteins, by multiple sequence alignment (MSA) using the ClustalΩ tool (892-894). The amino acid sequences of OXA-58, OXA-23, OXA-24, OXA-48, OXA-10, OXA-51, OXA-143, OXA-160, OXA-239, OXA-257, OXA-274 and OXA-296 from *A. baumannii*, and OXA-48 from *Klebsiella pneumoniae*, OXA-232 from *Escherichia coli*, OXA-45, 46 and 145 from *Pseudomonas aeruginosa*, OXA-163 from *Enterobacter cloacae*, OXA-405 from *Serratia marcescens*, Ybxl from *Bacillus subtilis*, BPu1 from *Bacillus pumilus* and OXA-2 from *Salmonella typhimurium*, were collected from the NCBI protein database in the FASTA format. All these sequences were submitted to the ClustalΩ tool to obtain multiple sequence alignment in the clustal file with numbering and percent identity matrix (PIM). The multiple sequence alignment file was analysed manually for

the homology and conserved amino acid sequence regions and the presence of insertions or deletions.

The conserved secondary structural features of these aligned sequences were comparatively analysed by ESPript server (895), using the *Ab*OXA-58 structure as template. The MSA file, obtained from the ClustalΩ tool, along with a single polymeric protein chain from the refined and validated final *Ab*OXA-58-6αHMP protein model, as a template PDB structure, was submitted to the ESPript server for calculating the conserved and homology secondary structural features among the CHDLs and other β-lactamase proteins from various pathogenic bacteria. The secondary, tertiary and quaternary structural features of the final refined and validated structures of transiently and non-covalently bound *Ab*OXA-58-6αHOP and covalently bound *Ab*OXA-58-6αHMP binary complexes were initially analysed and compared manually using the 3-D visualization tools like PyMOL (896), Discovery Studio Visualizer (897), Chimera (898) and COOT. These initial analyses include the type and amount of secondary structural elements (α-helices, β-sheets and random loops), number and type of domains present in each protein polymeric chain, number of protein chains present in the entire protein model and their arrangement in 3-D space. The protein-ligand interactions were also analysed using the same tools.

Subunit interface analysis was carried out by PDBe PISA server (901). The final refined binary structures of *Ab*OXA-58-6αHOP and *Ab*OXA-58-6αHMP complexes, containing the crystal symmetry operators, were submitted individually to the PISA server. Different aspects of the interfaces were analysed including total surface area (solvent exposed area), buried area and interface area. Subunit-subunit interface interactions were analysed for salt bridges, hydrogen bonds, covalent bonds and disulfide bonds. The subunit-ligand and ligand-ligand interface areas and interactions were also analysed in the similar way.

The PDB structures of CHDL oxacillinases and β-lactamases of other classes from *A. baumannii* and other bacterial species, including OXA-24-doripenem (PDB code 3PAE), OXA-24-avibactam (PDB code 4WM9), and OXA-23-meropenem (PDB code 4JF4) from *A. baumannii* itself, and TEM-1-6αHMP (PDB code 1TEM) from *E. coli*, OXA-48-avibactam (PDB code 4WMC) from *K. pneumoniae* and many other β-lactamases were downloaded from the RCSB PDB database and used for comparative analysis with the *Ab*OXA-58 protein, which was carried out manually in the analysis and visualization tools for 3-D protein structures including PyMOL.

The structural figures for all the structural analyses, including quaternary structure poses, subunit arrangements, secondary structural arrangements, domain organization, 3-D structural comparisons and subunit-subunit and subunit-ligand interface interactions, were prepared using PyMOL.

3.3. Results and discussion:

3.3.1. Transformation and protein over-expression studies:

The recombinant pET24d(+)::*blaOXA-58SP* plasmids containing the coding regions of the wild-type and the seven point mutation variants, including K86A, M225A, F113Y, F114A, F113A, M225T and F114I, of *OXA-58* gene from *A. baumannii* were transformed successfully into *E. coli* DH5α and BL21 DE3 cells. The plasmids were isolated from the transformed DH5α cells and confirmed their integrity (figure 3.1) and subsequently stored for future usage. The transformed BL21 DE3 cells were confirmed to be over-expressing their respective soluble OXA-58 or its point mutation variant protein, that were observed by thick ~29 kDa bands in the SDS-PAGE gel (figure 3.2).

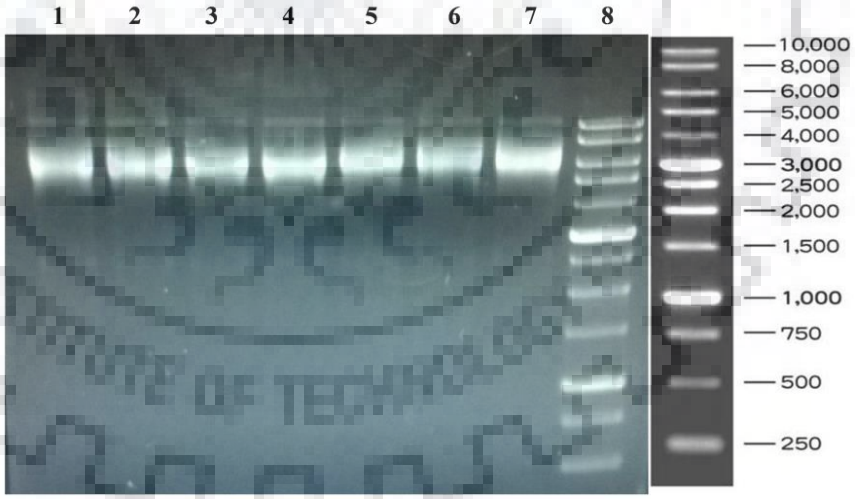

Figure 3.1: Plasmids of the point mutation variants of OXA-58 from *A. baumannii*, transformed into *E. coli* DH5α cells. Lanes 1-7: K86A, F113A, F113Y, F114A, F114I, M225A and M225T plasmids respectively, and Lane 8: 1 Kb DNA ladder.

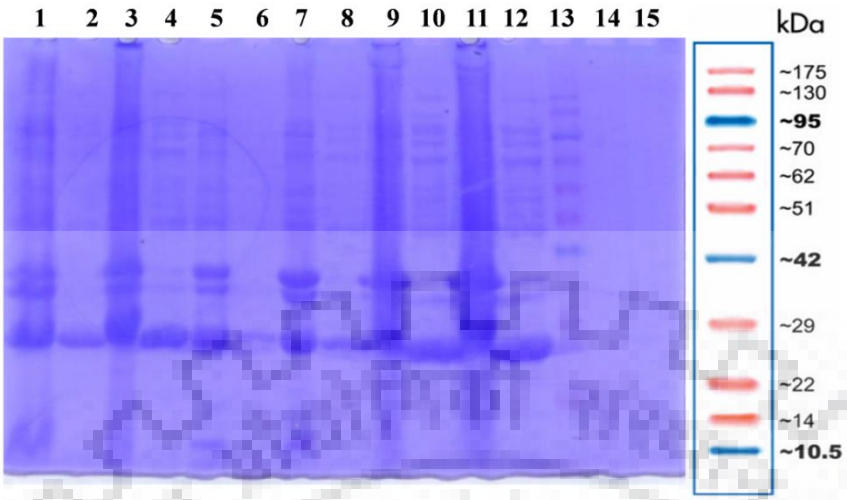

Figure 3.2: The protein over-expression studies for the *Ab*OXA-58 point mutation variants. The supernatant and pellet samples collected from different over-expression plasmids were run on 12% SDS-PAGE gel. Lane 1-2: pellet and supernatant samples of the over-expressed F114A mutant protein respectively. Lanes 3-12: similar samples from the over-expressed M225T, F114I, K86A, F113A and M225A mutant proteins respectively, and lane 10: pre-stained protein ladder.

3.3.2. Purification of OXA-58 wild-type and its point mutation variant proteins:

The wild-type OXA-58 protein was purified by cation exchange chromatography using 5 mL pre-packed SP sepharose column connected to an AKTA purifier 10 FPLC system and the corresponding chromatogram showed two UV280 absorption peaks, the first peak during the sample injection indicating the loading of the crude protein extract onto the column and its flow through from the column and the second peak at ~40% concentration of buffer B indicating the elution of the desired OXA-58 protein (figure 3.3A). Protein bands at molecular weight of ~29 kDa corresponding to OXA-58 protein were observed in the SDS-PAGE profile of the cation exchange chromatography purification shown in figure 3.3B. The elution fractions obtained from this purification step were further purified by size exclusion chromatography using a HiLoad 16/600 Superdex 200 pg column and the respective chromatogram showed a UV280 absorption peak at an elution volume of 85 mL corresponding to molecular weight of ~30 kDa indicating the elution of the OXA-58 protein as a monomer (figure 3.4A). The SDS-PAGE profile of the SEC purification of OXA-58 protein is shown in figure 3.4B. The purified protein from the ion exchange chromatography step was also loaded onto the HiLoad 16/600 Superdex 75 pg column and the chromatogram exhibited an absorption peak at 65 mL of

elution volume which corresponds to the molecular weight of ~30 kDa indicating the elution of the OXA-58 protein as a monomer (figure 3.5).

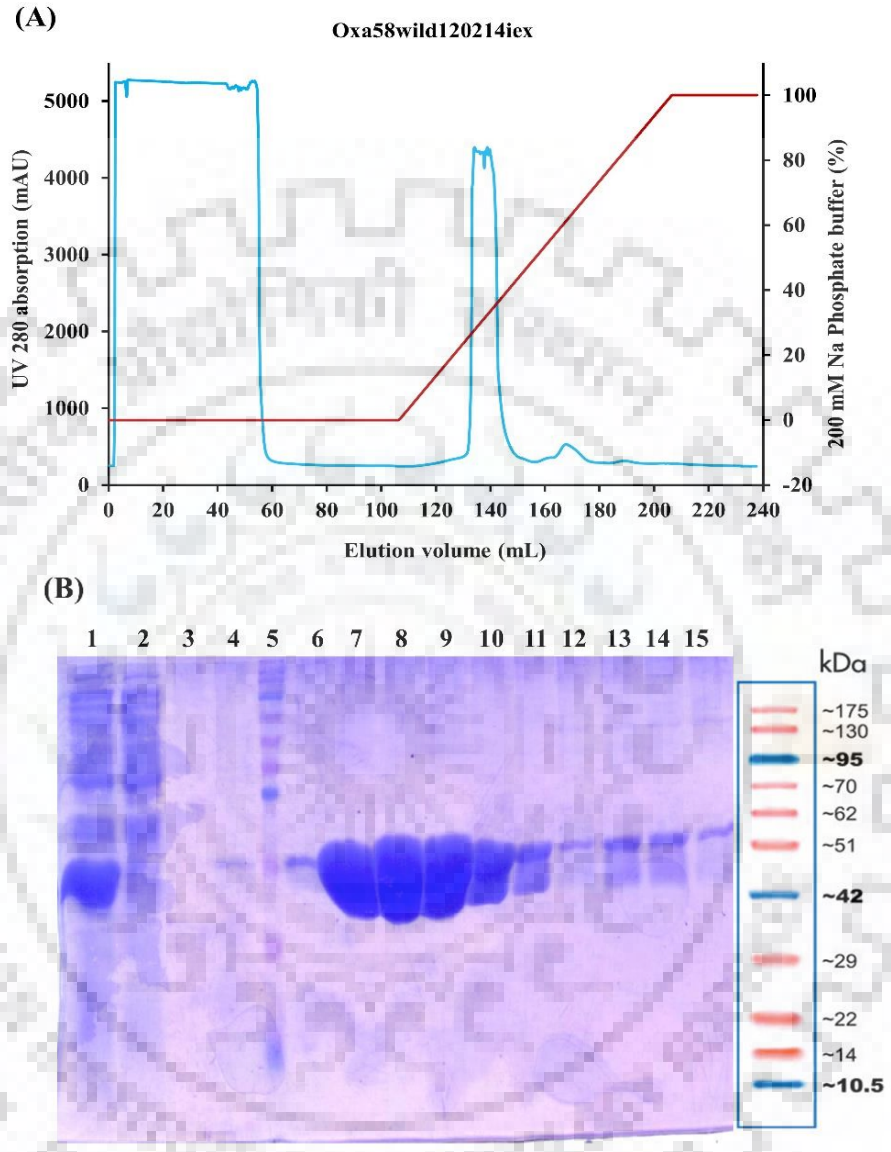

Figure 3.3: The ion exchange chromatography purification of wild type *Ab*OXA-58 protein by using a 5 mL pre-packed SP sepharose column. (A). Ion exchange chromatogram showing the 280 nm absorption peak (light blue color) of the desired protein at ~140 mL elution volume and 35-40% buffer B (dark red color). In the chromatogram the X-axis corresponds to the elution volume (mL), and the primary and secondary Y-axes to the 280 nm absorption and buffer B % concentration respectively. The light blue color graph is the 280 nm absorption graph and the dark red color graph is the buffer B % concentration graph. (B). The SDS-PAGE profile of the protein elutions collected from the ion exchange chromatography step. Lane 1: supernatant from the cell disrupted sample, Lane 2: column flow through, Lane 3 and 4: buffer A washes, Lane 5: protein ladder, and Lane 6-15: elution fractions from the buffer B liner gradient wash.

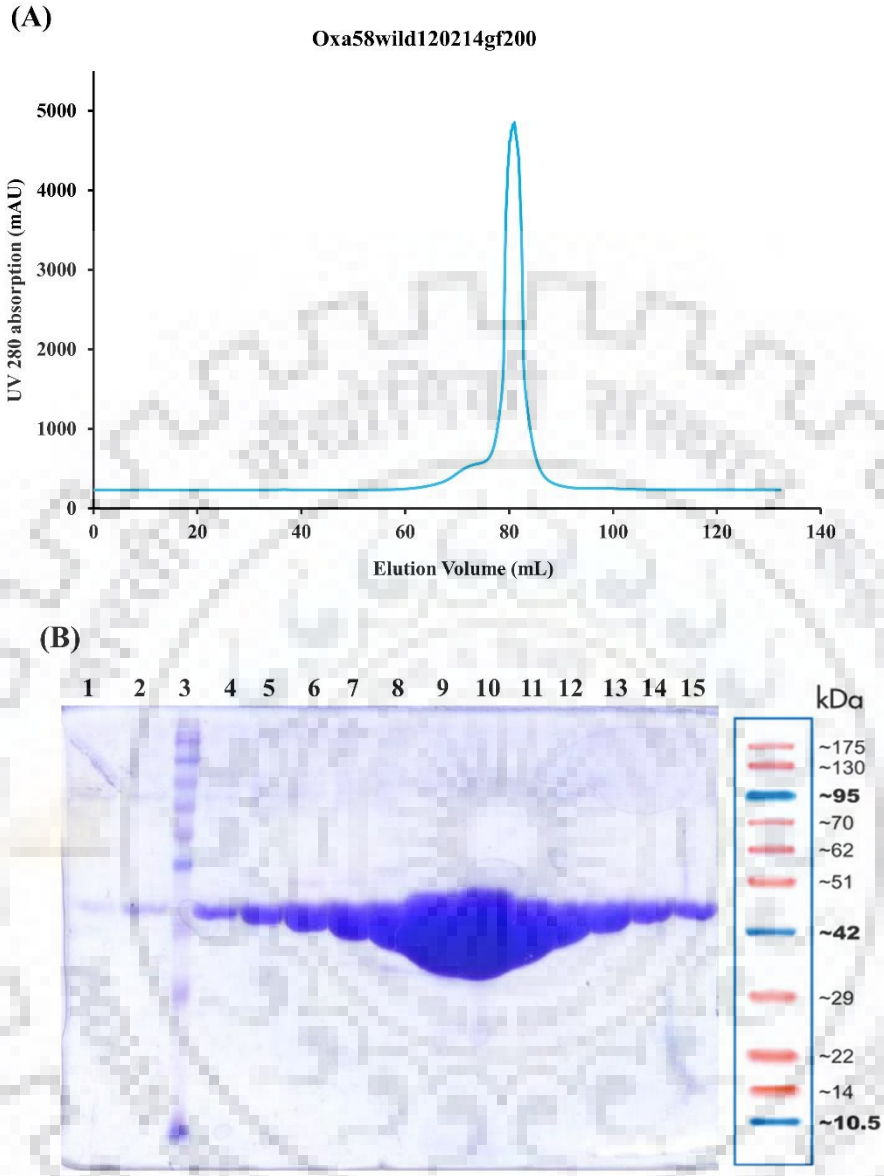

Figure 3.4: The size exclusion chromatography purification of wild type *Ab*OXA-58 protein by using the HiLoad 16/600 superdex 200 prep grade column. (A). Chromatogram showing the 280 nm absorption peak (light blue color) of the desired protein at ~85 mL elution volume. In the chromatogram the X-axis corresponds to the elution volume (mL) and the Y-axis to the 280 nm absorption. The light blue color graph is the 280 nm absorption graph. (B). The SDS-PAGE profile of the protein elutions collected from the gel filtration chromatography step. Lanes 1-2 and 4-15: protein elution fractions collected from different regions of the 280 nm absorption peak, and Lane 3: protein ladder.

The mutant proteins K86A, M225A, F113Y, F114A, F113A, M225T and F114I were also purified in the similar way and few of these purification profiles are shown in figure 3.5.

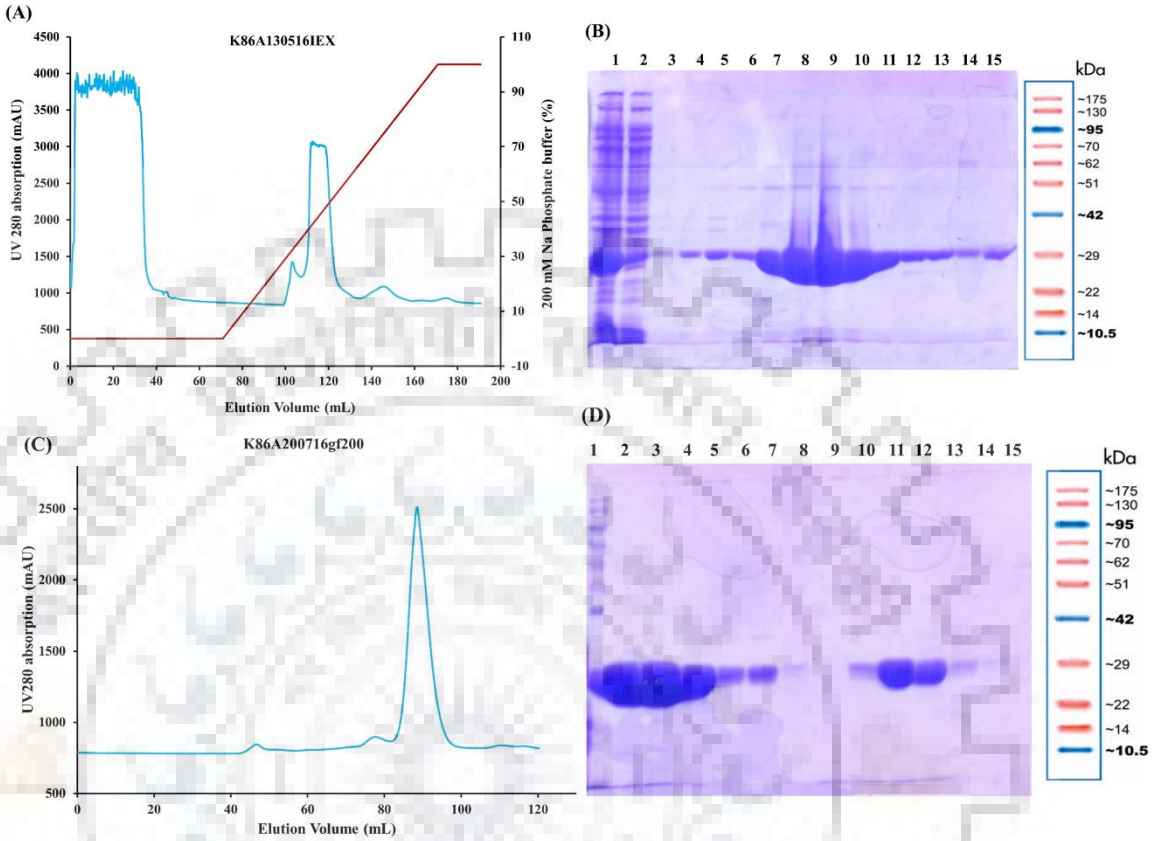

Figure 3.5: The purification profile of point mutation variants of *Ab*OXA-58 protein by using the similar protocol explained for the wild type protein. (A). Ion exchange chromatogram showing the 280 nm absorption peak (light blue color) of the desired protein at ~110 mL elution volume and 40-45% buffer B (dark red color). (B). The SDS-PAGE profile of the protein elutions collected from the ion exchange chromatography step. Lane 1: supernatant, Lane 2: column flow through, Lane 3 and 4: buffer A washes, and Lane 5-15: elution fractions from the buffer B liner gradient. (C). Size exclusion chromatogram showing the 280 nm absorption peak (light blue color) of the desired protein at ~85 mL elution volume. (D). The SDS-PAGE profile of the protein elutions collected from the gel filtration chromatography column. Lane 1: protein ladder and Lanes 2-15: protein elution fractions collected from different regions of the 280 nm absorption peak.

3.3.3. Crystal structures of wild-type OXA-58 protein in complex with 6α-alkyl penicillin derivatives:

We have soaked the native wild-type crystals of OXA-58 with the 6αHMP and 6αHOP compounds before mounting and collected the data at home source as explained in the methods section. The data were processed using HKL2000, CCP4i and PHENIX suits, and COOT tools and the corresponding procedures were detailed in the methods.

The wild-type OXA-58 crystals soaked with the 6αHOP compound diffracted to 2.3Å resolution and belong to $P2_1$ space group with unit cell parameters a, b, c = 37.02, 65.10, 191.96; and β = 91.28°. The data collected from these crystals were refined to final R_{work} and R_{free} of 19 and 24% respectively, with one tetramer in the asymmetric unit (figure 3.6), and we observed several conformational changes in the functionally significant loop elements and active site residues although didn't find any interpretable density for the ligand 6αHOP in any of the chains, and hence this structure hereafter will be considered as pseudoapo OXA-58 structure.

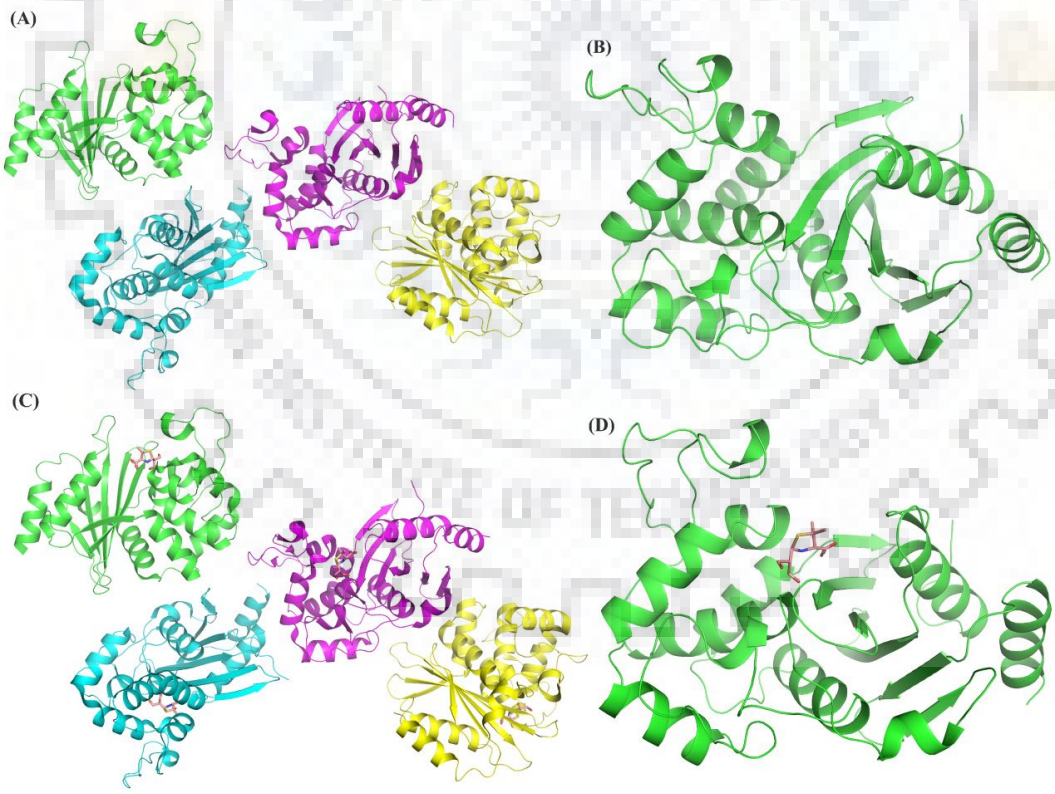

Figure 3.6: The crystallographic asymmetric unit and biological assembly states of the *Ab*OXA-58 protein in its *Ab*OXA-58-6αHOP and *Ab*OXA-58-6αHMP binary complex forms. **(A)** and **(C)** are the asymmetric unit states of the 6αHOP and 6αHMP binary complex forms respectively, while **(B)** and **(D)** are their biological assembly states respectively.

The crystals soaked with the 6αHMP compound diffracted up to 2.6Å resolution and belong to $P2_1$ space group with unit cell parameters a, b, c = 36.94, 65.65, 191.59; and β = 91.7°. The data collected from these crystals were refined to final R_{work} and R_{free} of 21 and 26% respectively, with one tetramer in the asymmetric unit (figure 3.6), and we found interpretable density for the ligand 6αHMP in all the four chains along with conformational changes in the functionally significant loop elements and active site residues, and hence this structure will be regarded as the OXA-58–6αHMP binary complex structure. The data collection statistics are given in table 3.1.

Table 3.1: Data collection and refinement statistics

	OXA-58-6αHMP Complex	**OXA-58 (pseudoapo structure)**
Wavelength (Å)	1.54	1.54
Resolution range (Å)	36.93 - 2.60 (2.69 - 2.60)*	34.79 - 2.29 (2.37 - 2.29)
Space group	*P* 21	*P* 21
Unit cell a, b, c (Å); β (°)	36.94, 65.65, 191.59; 91.7	37.02, 65.10, 191.96; 91.28
Total reflections	70515 (4578)	100971 (7493)
Unique reflections	21116 (1637)	37470 (2741)
Multiplicity	3.3 (2.8)	2.8 (2.7)
Completeness (%)	87.3 (69.3)	91.23 (74.8)
Mean I/sigma(I)	8.45 (2.30)	9.15 (2.65)
Wilson B-factor	39.21	33.11
R-merge	0.15 (0.43)	0.12 (0.42)
R-meas	0.15	0.14
CC1/2	0.97 (0.68)	0.99 (0.78)
CC*	0.99 (0.90)	0.99 (0.94)
R-work	0.21(0.31)	0.19 (0.30)
R-free	0.26 (0.36)	0.24 (0.36)
Number of non-hydrogen atoms	8126	8146
macromolecules	7784	7758
ligands	60	-

water	282	388
Protein residues	975	968
RMS(bonds)	0.019	0.016
RMS(angles)	1.80	1.65
Ramachandran favored (%)	96	99
Ramachandran outliers (%)	0.41	0
Clashscore	0.38	1.29
Average B-factor A2	54.2	44.5
macromolecules	54.1	44.7
ligands	56.2	-
solvent	55.7	44.5

Statistics for the highest-resolution shell are shown in parentheses.

The overall structural organization of the monomers from pseudoapo OXA-58 and OXA-58–6αHMP binary complex structures is almost identical to the apo OXA-58 structure elucidated in our laboratory, except for few conformational changes observed in the active site elements and catalytically significant loops, and domain movements. The pseudoapo and OXA-58–6αHMP complex structures have two extra short β-strands β3 and β4, located on the α3/α5-loop and on either side of the α4 helix, which are not observed in the both apo structures (figure 3.7 and 3.9). The monomers from the pseudoapo OXA-58 and OXA-58–6αHMP structures are exhibiting typical α/β fold where the β-sheet core is surrounded by the solvent exposed α helices and the overall monomer structure consists of nine α-helices, eight β-strands and fifteen loops, and can be divided into two non-contiguous structural domains that can be distinguished by the distinct arrangement of secondary structure elements. The first domain showed a mixed α/β arrangement with six stranded central anti-parallel β-sheet (consisting of β1, β2 and β5 through β8) and two terminal helices (α1 and α9) located on one side of the central β sheet, while the second domain contained seven α helices (α2 through α8) and two short β-strands (β3 and β4), located on the α3/α5-loop, and arranged at the other side of the central β-sheet (Figure 3.7). The active site is situated at the junction of these two domains in the form of an extended cleft and formed predominantly by positive charged residues. The substrate binding and catalysis pocket was formed together by the NH2 terminal end of helix α3, strand β4 and connecting loop in between helix α4 and α5.

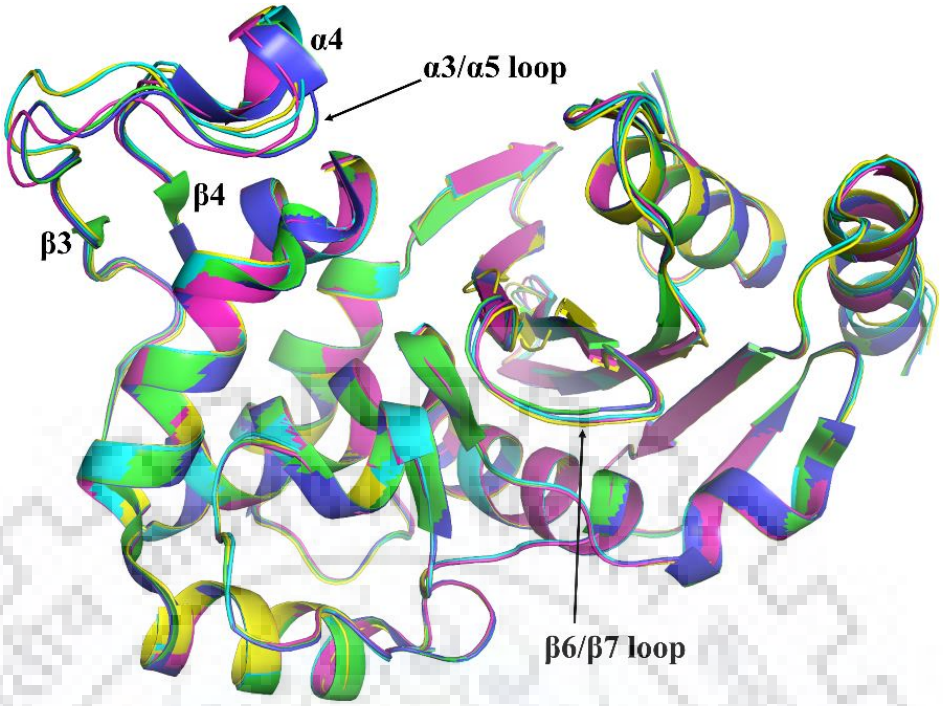

Figure 3.7: The monomers of OXA-58 from apo from our laboratory (4Y0O) (cyan), apo by Smith et al (4OH0) (yellow), pseudoapo (4Y0T) (magenta) and chain A (green) and chain B (blue) from the *Ab*OXA-58-6αHMP binary complex (4Y0U) structures are shown superimposed. The α3/α5-loop and β6/β7-loop are indicated by thick black colored arrows.

Analysis of the apo, pseudoapo and OXA-58–6αHMP complex structures by the DynDom server revealed that each monomer from these structures consists of two rigid domains that are connected through flexible hinge regions (figure 3.8). Domain-1 consists of 215 residues, in overall, located in regions from Gln42 to Glu103 and Gly124 to Val276 that are separated by the hinge regions and the domain-2; while the domain-2 containing 20 residues from Ile104 to Leu123. The hinge-1 is formed by the flexible residues Glu103 and Ile104, while the hinge-2 by Thr122 and Leu123. Domain-1 is containing the β6/β7-loop which is harboring the Met225 residue while domain-2 is containing the α3/α5-loop which is harboring the Phe113 and Phe114 residues, on its α4 helix, that are known to participate in the hydrophobic bridge formation over the active site-bound ligand.

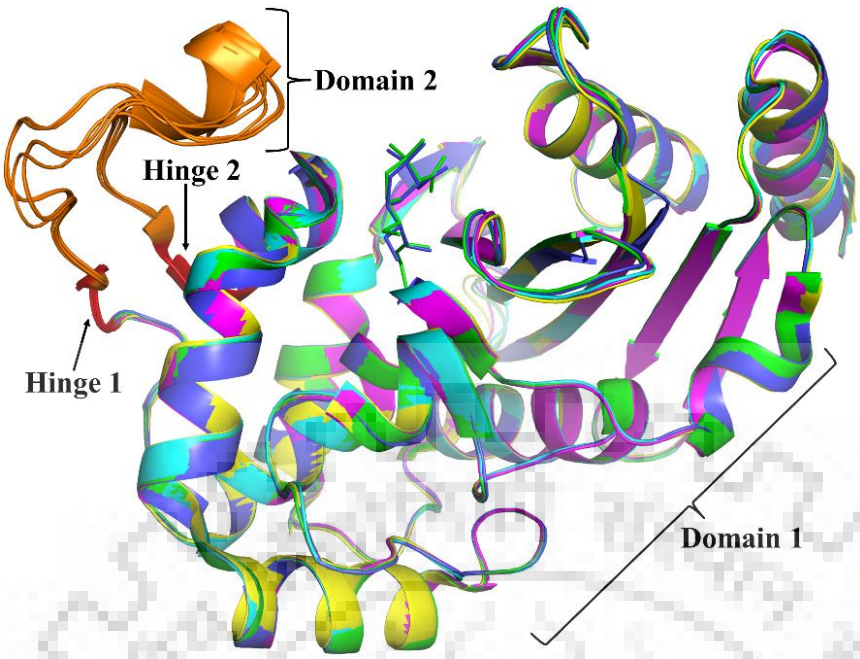

Figure 3.8: The structural domains revealed by the DynDom server. Domain 1 is shown with same color legend of the monomers from apo from our laboratory (4Y0O) (cyan), apo by Smith et al (4OH0) (yellow), pseudoapo (4Y0T) (magenta) and chain A (green) and chain B (blue) from the *Ab*OXA-58-6αHMP binary complex (4Y0U) structures as shown in figure 3.7, while the domain 2 from all the structures is highlighted in orange color. The hinge regions are shown in red color and pointed with the black colored arrows.

3.3.4. Ligand-induced changes in the overall OXA-58 structure:

It was observed that soaking of apo OXA-58 crystals with the 6αHOP compound led to its transient and non-covalent binding in the crystal which triggered few structural changes and the crystal space group symmetry reduction from $P2_12_12_1$ (observed for the apo crystals) to $P2_1$, but no interpretable density for the bound compound. In case of soaking with the 6αHMP compound, its covalent binding in the crystal induced formation of stable acyl-enzyme species with proper density for the bound compound, along with other structural changes and the crystal space group symmetry reduction to $P2_1$. The backbone of pseudoapo OXA-58 structure is superimposing with our apo, chain A and chain B of OXA-58–6αHMP binary complex structures, and the apo structure solved by Smith et al. (470) at RMSD values of 0.47, 0.30, 0.31 and 0.55 Å respectively, while the chains A of OXA-58–6αHMP structure is superimposing with our apo and of Smith et al. with RMSD values of 0.46 and 0.55 Å respectively, while its B chain with 0.48 and 0.58 respectively. The chain A and chain B of OXA-58–6αHMP structure are superimposing with each other at an RMSD of 0.12 Å.

The transient non-covalent binding of 6αHOP and covalent binding of 6αHMP induced the formation of two extra short β-strands β3 (Ile104-Phe105) and β4 (Phe121-Thr122), located on

the α3/α5-loop and on either side of the α4 helix, which are not observed in the both apo structures. These two β-strands β3 and β4 are arranged in antiparallel fashion, where β3 is observed to be entering the α4 helix and β4 is exiting it, and constituting a structural part of domain 2 of pseudoapo OXA-58 and OXA-58–6αHMP structures (figure 3.9). Because of this, we can observe secondary structural content differences among apo structures and the ligand-bound structures. According to the DynDom server domain analysis, the newly formed β3 and β4 strands, in pseudoapo and OXA-58–6αHMP structures, are forming parts of the hinge-1 and hinge-2 flexible regions that are connecting the two rigid domains 1 and 2 of the monomeric structures.

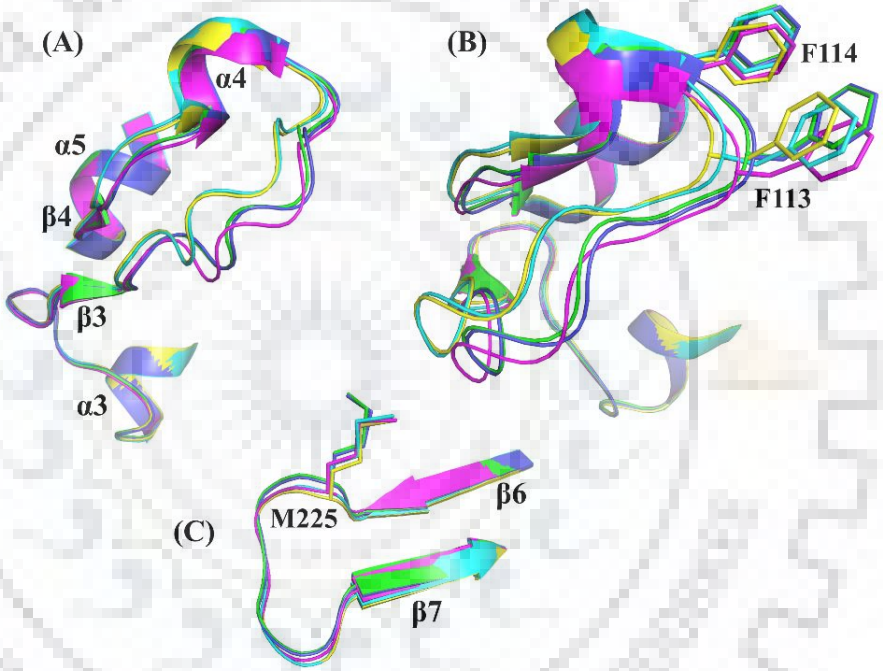

Figure 3.9: The α3/α5-loop and β6/β7-loop are shown in close up view. The colore legend for all the 5 different monomer structures is same as in figure 7. (A). The α3/α5-loop showing all its structural components including α3, β3, α4, β4 and α5, and the main chain deviations among the 5 different OXA-58 structures shown. (B). The α3/α5-loop harboring the hydrophobic residues F113 and F114 and depicting their structural poses with differences in their propensity for forming the hydrophobic bridge. (B). The β6/β7-loop showing the deviations of the main chain among the 5 structures and the differences among the M225 residue being harbored it.

The binding of 6αHOP or 6αHMP compound triggered major structural conformations in the α3/α4-loop and β6/β7-loop which are harboring the key catalytic residues including Phe113 and Phe114 and Met225 respectively. In fact, the clear positional shifts are observed in the Ile104-Thr122 amino acid range of α3/α5-loop, constituting the α4 helix, β3 and β4 strands and L6 and

L7 loops, as well as the Met225-Gln230 amino acid range of the β6/β7-loop. We observed ~1.5 Å shift of the α3/α5-loop towards the active site-bound ligand and this is an inward movement in both the pseudoapo and OXA-58–6αHMP complex structures in comparison to the apo structure. This α3/α5-loop movement brought significant shifts in the side chains of Phe113 and Phe114 at 1.23 and 0.8 Å respectively in the OXA-58–6αHMP complex in comparison to the apo structures, while at 0.86 and 0.89 Å respectively in the pseudoapo OXA-58 structure (figure 3.9 and 3.10) (table 3.2). The β6/β7-loop also showed an inward movement of 0.85 and 0.32 Å respectively in the OXA-58–6αHMP complex and pseudoapo structures respectively in comparison to the apo structures. Of note, the β6/β7-loop movement was observed to facilitate the reorientation of the side chain of Met225 towards the active site side, in the OXA-58–6αHMP complex structure, with an overall RMSD of 1.5 Å in comparison to the apo structures; while, only 0.26 Å shift of the side chain of Met225 is brought by the β6/β7-loop movement in case of the pseudo apo structure (figure 3.10).

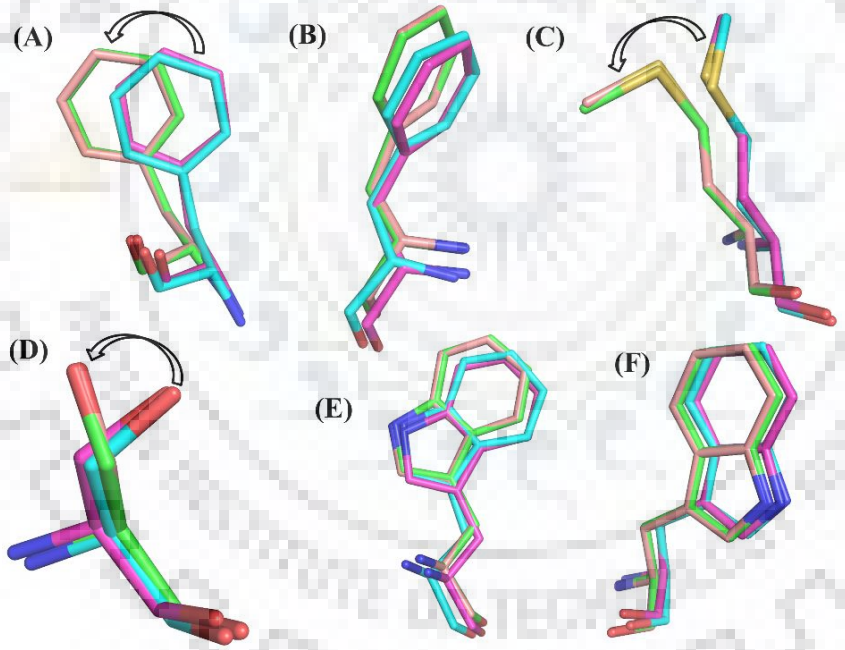

Figure 3.10: The major ligand-induced changes, by 6αHMP, in the backbone and side chain conformations of the OXA-58 protein. The five amino acid residues exhibiting major conformational changes are shown superimposed from the 4 different monomer structures with the same color legend as in figure 7, except for the chain B from the OXA-58–6αHMP complex which is in grey color. **(A)**, **(B)**, **(C)**, **(D)**, **(E)** and **(F)** are showing the Phe113, Phe114, Met225, Ser130, Trp117 and Trp223 respectively. Phe113, Phe114 and Met225 are exhibiting changes in their side chains as well as backbone conformations, while Ser130, Trp117 and Trp223 are showing changes mainly in their side chain conformations.

Table 3.2: Comparison of the differences in the α3/α5- and β6/β7-loops and their component residues among the apo, pseudoapo and OXA-58–6αHMP binary complex structures.

Structure1	Structure2	Alignment range	RMSD (Å^2)		
			Cα atoms	Backbone	Whole residue
α3/α5 loop					
4Y0O	4Y0T	106-122	1.358	1.398	1.499
4Y0O	4Y0U	106-122	1.264	1.294	1.357
4Y0O	4OH0	106-122	0.316	0.338	0.612
4Y0T	4Y0U	106-122	0.716	0.717	0.940
4Y0U (A)	4Y0U (B)	106-122	0.090	0.096	0.484
B6/β7 loop					
4Y0O	4Y0T	225-230	0.238		0.320
4Y0O	4Y0U	225-230	0.549		0.838
4Y0O	4OH0	225-230	0.224		0.315
4Y0T	4Y0U	225-230	0.562		0.842
4Y0U (A)	4Y0U (B)	225-230	0.151		0.185
4Y0O	4Y0U	Phe113	1.035	0.903	1.228
4Y0O	4Y0U	Phe114	0.662	0.798	0.703
4Y0O	4Y0U	Met225	0.566	0.706	1.510
4Y0O	4Y0T	Phe113	0.850	0.848	0.856
4Y0O	4Y0T	Phe114	0.798	0.894	0.683
4Y0O	4Y0T	Met225	0.207	0.260	0.260

The above conformational changes in the α3/α5- and β6/β7-loops led to an overall 1.5 Å decrease in the distance between the Cα atoms of the Phe113/Met225 and Phe114/Met225, from 13.6 and 14.9 Å respectively in the apo structures, to 12.1 and 13.7 Å respectively in the OXA-58–6αHMP complex structure (table 3.3). Whereas, only an overall 0.5 Å decrease is observed in the distance between the respective atoms from 13.6 and 14.9 Å respectively in the apo structures to 13.1 and 14.5 Å respectively in the pseudoapo structure. Overall, the extent of inward movements of the α3/α5- and β6/β7-loops are higher in case of the OXA-58–6αHMP complex than that of the pseudoapo structure in comparison to the apo structures. Of note, the side chains of Phe113 and Met225 are reoriented at overall RMSD of 1.23 and 1.5 Å towards each other in the OXA-58–6αHMP complex, which is significantly higher than the rearrangement of side chains of other residues of these loops including Phe114/Met225, and also very much higher in comparison to the pseudoapo and apo structures. The 12.1 and 13.7 Å distances between the Cα atoms of Phe113/Met225 and Phe114/Met225 can facilitate the hydrophobic interactions between the α3/α5- and β6/β7-loops, while the side chains of these residues can facilitate the van der Waals interactions between the same loops as these side chains are coming within the limits of van der Waals interactions with distances of 4.09 Å for Phe-113/Met-225 and 5.30 Å for Phe-114/Met-225 that are measured between the C-ζ of the phenyl ring and the sulfur atom of methionine (figure 3.9 and 3.10).

Table 3.3: Comparison of the Cα-Cα distances of the residues involving in hydrophobic bridge formation, among the apo, pseudoapo and OXA-58–6αHMP binary complex structures.

Structure	Residue 1	Residue 2	Cα-Cα distance (A˚)
4Y0O	Phe113	Met225	13.6
	Phe114	Met225	14.9
4Y0T	Phe113	Met225	13.1
	Phe114	Met225	14.6
4Y0U	Phe113	Met225	12.1
	Phe114	Met225	13.7

Analysis of the OXA-58–6αHMP complex structure by the DynDom server also revealed that the binding of 6αHMP compound induced an inter-domain closure movement of 8.3° around a rotation axis close to the flexible residues of both the hinge regions connecting the two rigid domains (figure 3.11). The inter-domain movement can be directly correlated with the fact that the inward movements of the α3/α5- and β6/β7-loops that are being harbored by the domain-2 and domain-1 respectively resulted from the binding of 6αHMP in the active site. In an overall view, the binding of 6αHMP compound in the active site of OXA-58 induced the inter-domain movement which triggered the inward movements of the α3/α5- and β6/β7-loops which further facilitated the inward movements of the Cα atoms and rearrangements of the side chains of Phe113/Phe114 and Met225 which resulted in the hydrophobic interactions as well as van der Waals interactions between the side chains and whole of these residues/loops/domains that finally led to the formation of hydrophobic bridge over the ligand-bound active site connecting the above mentioned residues from the corresponding loops harbored by the respective rigid domains. All these facts are exemplifying the plasticity of the OXA-58 active site and drawing the researchers' attention to the domain closure phenomenon that occurs upon covalent binding of the β-lactam in the active site.

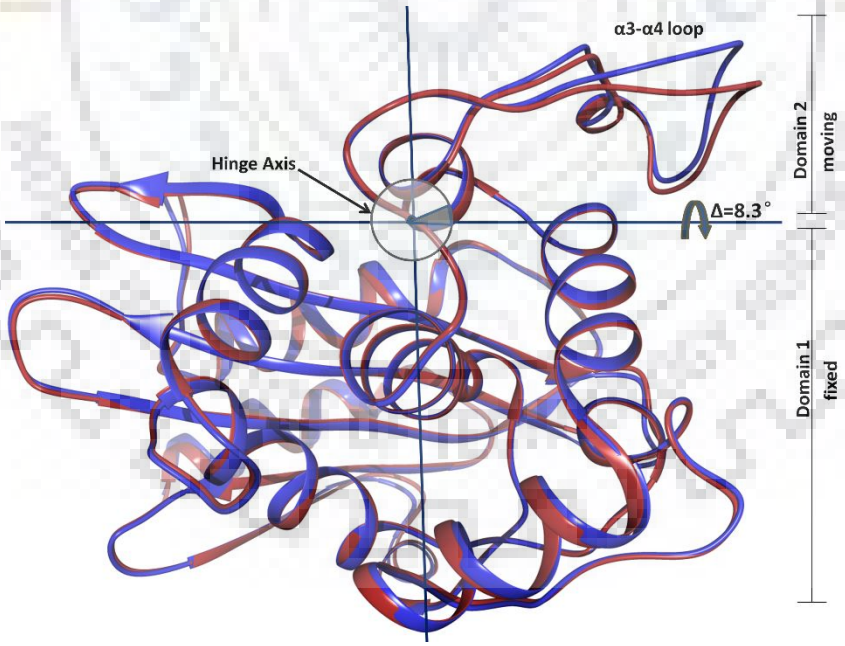

Figure 3.11: The interdomain movement in the monomer from OXA-58–6αHMP complex shown in comparison with the apo OXA-58 structure by the DynDom server, that are represented by brown and blue colors respectively. Movement of the domain 2 towards the rigid domain 1 is shown by the arrow and the rotational axis comprising the hinge region is shown by the black colored circle.

3.3.5. Active site of OXA-58 in its ligand-bound state:

The active site of ligand-bound OXA-58 is predominantly formed by the polar residues from all the conserved structural motifs including Ser83 and Lys86 (in its carboxylated state, i.e. KCX86) from the STFK motif, Ser130 from the STV motif and Lys220 and Ser221 from the KSG motif, that interact among each other through a strong hydrogen-bonding network in order to structurally stabilize each other and to facilitate the enzyme catalysis (figure 3.12). In the pseudoapo structure the carboxyl group of the caroxylysine86 (KCX86) is stabilized by its interactions with the Ser83, Trp169 and one water molecule. Here, OQ1 atom of KCX is forming 2.9 and 3.0 Å hydrogen bonds with the NE1 of Trp169 and HOH352 (referred to as W3 according to the naming assigned in the apo structure) respectively; and the OQ2 atom is forming 3.5 and 2.5 Å H-bonds with the NE1 of Trp169 and OG of Ser83 respectively; while the NZ atom is making 3.4 and 3.5 Å H-bonds with the OG of Ser83 and O (backbone oxygen atom) of Ser130 respectively. The OG atom of Ser83 is also making 3.2 and 2.7 Å H-bonds with the OG of Ser130 and HOH323 (which is positioned in the oxyanion hole and referred to as W1) respectively, while its backbone amide nitrogen is also forming a 2.8 Å H-bond with W1. The OG atom of Ser130 is further making 2.9 Å H-bond with the NZ of Lys220, which in turn making 3.0 and 3.3 Å H-bonds with the backbone carbonyl oxygen of Ser221 and HOH311 (referred to as W4) respectively.

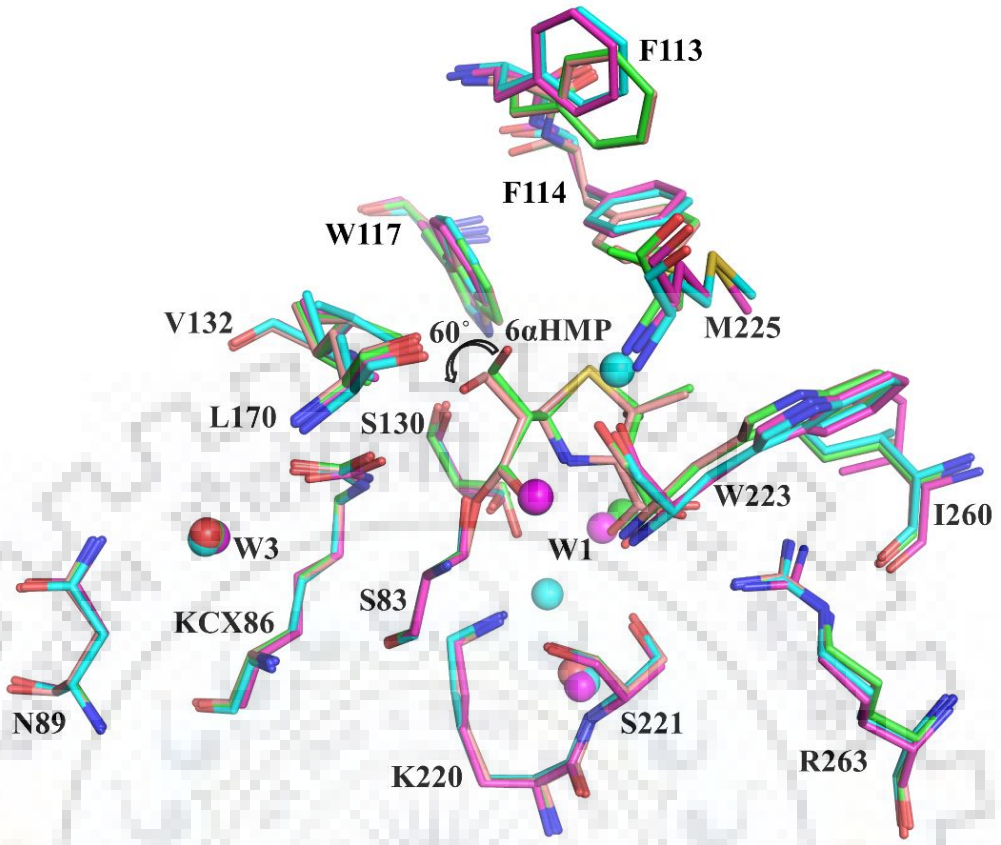

Figure 3.12: The active site architecture of OXA-58 protein from OXA-58–6αHMP complex in comparison with that from apo, pseudoapo and its own chain A monomers. The color legend of the residues is same as in figure 10. The active site water molecules are also shown in sphere with the corresponding colors of their protein chains. The bound 6αHMP ligand from chains A and B of OXA-58–6αHMP complex is shown in stick representation with the corresponding chain colors. The conformational difference of the hydroxyl moiety of the side chain hydroxymethyl group of 6αHMP is shown by its rotation of 60° which is denoted by arrow.

In the OXA-58–6αHMP complex also the active site residues are making an intricate hydrogen-bonding network with few differences from that of the apo and psudoapo structures, including the additional interactions made by KCX86, Ser83 and Ser 130 residues with the covalently bound 6αHMP compound (figure 3.12). The OQ1, OQ2 and NZ atoms of KCX86 are interacting with the OG of Ser83, NE1 of Trp169 and W3 water in the similar way explained for the pseudoapo structure. The OQ2 atom of KCX86 is making 3.5 Å H-bond with the O22 atom of the 6αHMP in the B chain, while these two atoms are at 4.8 Å distance in the rest A, C and D chains. The OG of Ser83 is interacting with the OQ2 and NZ atoms of KCX86 in the similar way, but it couldn't make hydrogen bond with the OG atom of Ser130 as the later moved away by 76° (in comparison to its position in the apo and pseudoapo structures) towards

the N7 atom of 6αHMP making the distance increased to 4.3 Å. The OG of Ser83 is interacting covalently with the C1 atom of 6αHMP with a covalent bond distance of 1.3 Å and its backbone amide nitrogen is also interacting with the O1 atom of 6αHMP with an H-bond distance of 2.7 Å. After making a rotation of 76°, the OG of Ser130 is interacting with the NZ of Lys220 at H-bond distance of 2.6 Å which is stronger in comparison to the 3.0 Å distance in the apo and pseudopao structures. It is also making 3.1 Å H-bond with the O82 atom of 6αHMP in the B chain, while it is interacting with O81 at 3.7 Å in the rest of the chains. The NZ atom of Lys220 is interacting with the backbone carbonyl oxygen of Ser221 and W4 water in the similar way explained for the apo and pseudoapo structures.

In overall, the W1 and W3 water molecules were observed in the active site of pseudoapo structure, while only W3 is found in the OXA-58–6αHMP complex. The transient binding of 6αHOP led to the displacement of the W2 which was reported to be bridging the KCX86 and Ser83 in the apo structure, while the covalent binding of 6αHMP displaced W1 (which is positioned in the oxyanion hole in the apo and pseudoapo structures) and W2 molecules as well. As a result, only W3 water molecule is found in all the three structures of OXA-58 reported from *A. baumannii*.

3.3.6. 6αHMP interactions and binding conformations in the OXA-58 active site:

The 6αHMP compound is thoroughly making several types of interactions with the protein residues lining the active site and binding pocket, and binding covalently within the active sites of all the four chains of OXA-58, but with two different conformations including conformation 1 in A, C and D chains and conformation 2 in B chain (figure 3.12 and 3.13A). These two different conformations are due to variations in the orientation of the hydroxyl group of the hydroxymethyl side chain of 6αHMP, which resulted in differences in its hydrogen bonding pattern with the surrounding active site residues. The C1 atom of the β-lactam ring of 6αHMP is forming a 1.3-Å covalent bond with the OG atom of Ser83 in all the four chains of OXA-58. The O1 atom of the carbonyl group of 6αHMP β-lactam ring, which is forming and persistently occupying the oxyanion hole, is making 2.7, 2.8 and 3.3 Å H-bonds with the backbone amide nitrogens of Ser83 and Trp223 and backbone carbonyl oxygen of Trp223 respectively. The hydroxyl group of the hydroxymethyl side chain at C2 position of β-lactam ring is observed to be rotated at 60° in the conformation 2 of 6αHMP in the chain B, in comparison to its positional orientation in its conformation 1 in the rest chains and due to these different orientations of the O22 atom, its bonding pattern varies in the different chains. The O22 of 6αHMP in its conformation 1 is making 3.4 Å H-bonds with the backbone carbonyl oxygen and

the central oxygen of Trp223 and HOH460 respectively, in chains A, C and D; while in its conformation 2, it is making a 3.5 Å H-bond with the OQ2 atom of KCX86 in chain B (figure 3.14). The O81 atom of the side chain carboxyl group at C6 position of thiazolidine ring of 6αHMP is making 2.7, 3.4 and 3.7 Å H-bonds with the OG and backbone oxygen of Ser221 and OG of Ser130 respectively in its conformation 1, while it is forming 2.7, 3.7 and 3.1 Å H-bonds with the corresponding atoms in its conformation 2 in chain B. The O82 atom of the same carboxyl group of 6αHMP is making 3.1 and 2.7 Å H-bonds with the NH1 and NH2 atoms of the side chain guanidine group of Arg263 in its conformation 1, while it is forming 2.8 and 2.9 Å H-bonds with the corresponding atoms in its conformation 2 in chain B.

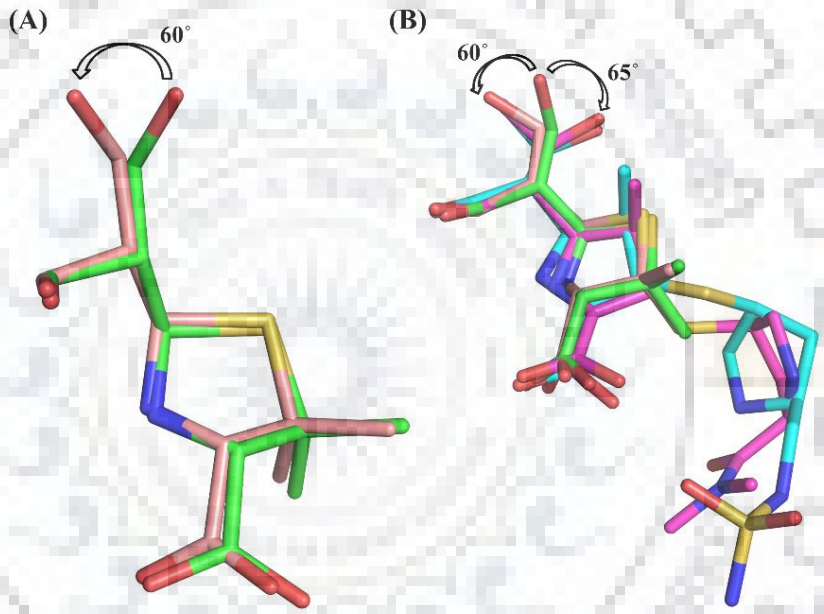

Figure 3.13: The conformations of the side chain hydroxyalkyl groups observed in different chains of OXA-58 structure. **(A)**. The two different conformations of the hydroxyl moiety of the side chain hydroxymethyl group of 6αHMP is shown by its rotation of 60° which is denoted by arrow. The 6αHMP from chains A and B are represented with the same colors used for their chains as shown in figure 10. **(B)**. The conformations of the hydroxyl moiety of the side chain hydroxyethyl groups of meropenem (magenta) and doripenem (cyan) from OXA-23 (4JF4) and OXA-24 (3PAE) are shown by ~65° of rotation, which is denoted by arrow, from the similar group in the OXA-58 chain A.

The formation of a stable covalent bond between OG atom of the catalytic serine Ser83 and C1 atom of the β-lactam ring resulted in the stable deacylation-deficient acyl-enzyme species of OXA58 enzyme. The H-bond network made by the carbonyl O1 atom, which is persistently

locked in the oxyanion hole, and its interacting protein residues in the OXA58-6αHMP complex are similar to the hydrogen bonding pattern made by the W1 water molecule in the apo and pseudoapo OXA-58 structures and hence it can be concluded that the O1 atom displaced W1 in the OXA58-6αHMP complex structure. Overall, the main differences between the two conformations of the bound 6αHMP in the OXA-58 active site include (i) the 60° counterclockwise rotation of the hydroxyl group of the side chain hydroxymethyl group at C2 position of the β-lactam ring (figure 3.13B) towards the back of the active site in its conformation 2 in chain B made it to interact with the carboxyl moiety of the catalytic KCX86 residue, and (ii) the small rotation of the side chain carboxyl moiety at the C6 position of the thiazolidine ring altered its bonding pattern with the Ser130 and Ser221 residues.

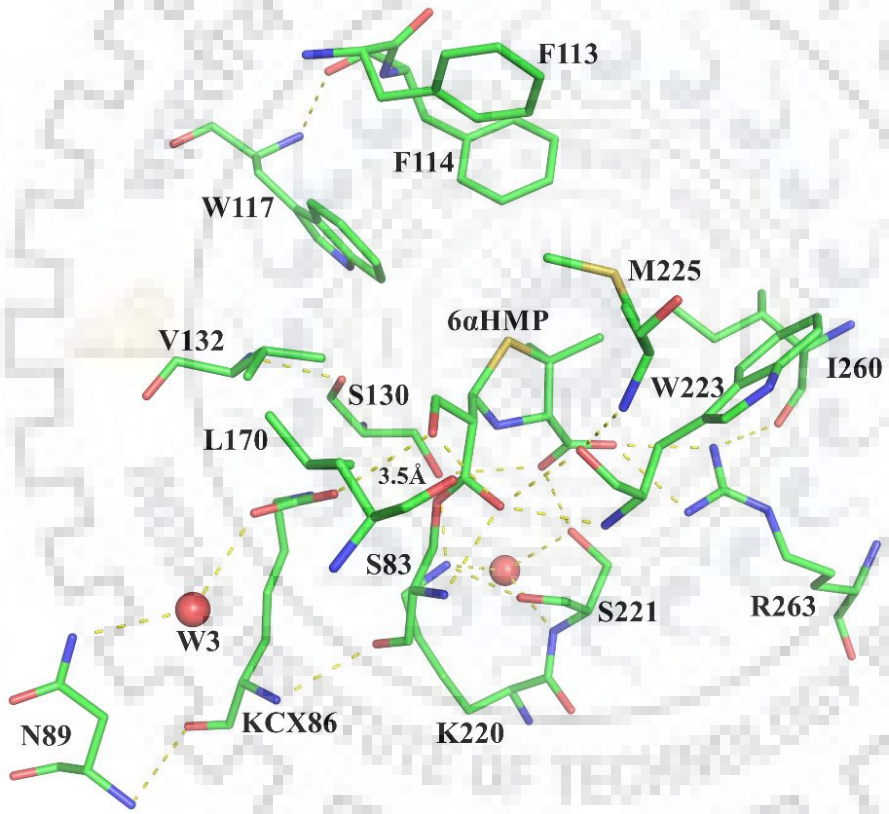

Figure 3.14: The interactions of 6αHMP within the active site of OXA-58 and are shown for the chain B. The W3 water molecule conserved in the active site of OXA-58–6αHMP complex is also shown in spheres representation. The 3.5 Å hydrogen bond made by the side chain hydroxyl group of 6αHMP in the chain B is labeled. All the hydrogen bonds that the 6αHMP ligand making with the protein residues are shown by yellow color dashed lines.

The methylene carbon of the side chain hydroxymethyl group of 6αHMP is also making hydrophobic interactions with the side chains of Val132 and Leu170 whose CG2 and CD2

atoms are at 3.4 and 3.8 Å distances from the C21 methylene carbon respectively (figure 3.14). The S4 atom of the thiazolidine ring is making Π-sulfur interactions at 5.4 Å distances with the Π-electron clouds of the side chain benzene rings of Phe114 and Trp117. The C51 methyl carbon connected at the C5 ring atom of the thiazolidine ring is also making Π-alkyl interactions at 5.2 Å distance with the side chain benzene ring of Phe114. The C52 methyl carbon is making Π-alkyl interactions with the side chain benzene ring of Trp223, and alkyl interaction with the alkyl side chains of Ile260 and Met225 at 5.1, 5.4 and 5.2 Å distances respectively. The C51 and C52 methyl groups and the thiazolidine ring plane are also making van der Waals contacts with the side chains of Ile260 and Trp117 at 3.9 and 4.1 distances respectively. The inward movements of the α3/α5- and β6/β7-loops facilitated the interactions of the thiazolidine ring with Phe114 and Trp117, and Met225 respectively.

3.3.7. Insights into the stability of the deacylation-deficient OXA58-6αHMP complex:

We have compared the deacylation-deficient OXA58-6αHMP complex, which is the stable acyl-enzyme species of OXA58 enzyme, with the similar deacylation-deficient species of other CHDLs including the structures of the OXA-24 variant (Lys84Asp) bound to doripenem (PDB code 3PAE) and the wild-type OXA-23 bound to meropenem (PDB code 4JF4), and ESBLs including the TEM-1 bound to 6αHMP (PDB code 1TEM), to gain insights into the factors stabilizing this deacylation-deficient acyl-enzyme species of OXA58 enzyme. Superposition of the two conformations of 6αHMP, conformation 1 and conformation 2, and meropenem and doripenem bound in the active sites of the chains A and B of OXA58 and OXA23 and OXA24 respectively revealed that the hydroxyl moiety of hydroxymethyl group of the meropenem and doripenem rotated clockwise at ~65° from the position of the hydroxymethyl group of 6αHMP in the chain A, while the hydroxyl moiety of hydroxymethyl group of 6αHMP in the chain B rotated counterclockwise at 60°. It is a noteworthy observation that the hydroxyl moiety of hydroxymethyl group of 6αHMP in the chain B of OXA58 is located away at 60°, 120° and 130° from the positions of the same group of 6αHMP, meropenem and doripenem in the chain A of OXA58, OXA23 and OXA24 respectively, and is positioned towards the back of the active site (figure 3.13B and 3.15A). This positional orientation of the hydroxyl moiety of hydroxymethyl group of 6αHMP in the chain B of OXA58 allows its O22 atom to make a 3.5 Å H-bond with the OQ1 atom of the side chain carboxyl moiety of KCX86, which may dampen the basicity of that catalytic carboxylated Lys86 towards the deacylating water molecule that is essential to accomplish the carbapenem hydrolysis by OXA58 enzyme; and this conformation of hydroxymethyl group of 6αHMP may also be acting as a physical barrier for the approach of

the deacylating water molecule. These experimental observations are concluding that the positional orientation of the hydroxyl moiety of hydroxymethyl group of 6αHMP may be responsible for the stability of the deacylation-deficient OXA58-6αHMP complex and the acyl-enzyme species of 6αHMP.

Further supporting the above said fact that the orientation/conformation of the hydroxymethyl group of 6αHMP may be responsible for the stability of the deacylation-deficient OXA58-6αHMP, it is also observed that the conformation of the hydroxyl moiety of hydroxymethyl group of 6αHMP in the chain A of OXA58 is similar to that observed in the TEM-1–6αHMP complex (figure 3.15A) which was also reported to be displacing the structurally conserved deacylating water molecule.

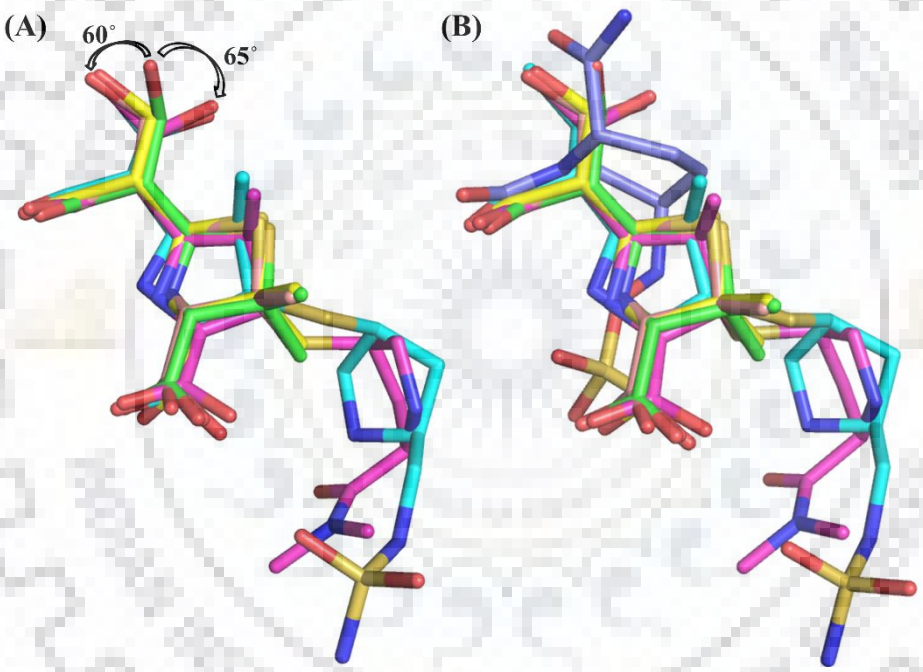

Figure 3.15: The conformations of the side chain hydroxyalkyl groups observed in the active sites of different classes of β-lactamases, including several CHDLs. **(A)**. The different conformations of the hydroxyl moiety of the side chain hydroxymethyl group of 6αHMP in the active sites of OXA-58 (4Y0U) chain A (green) and chain B (grey) and TEM1 (1TEM) (yellow), and the conformations of the hydroxyl moiety of the side chain hydroxyethyl group of meropenem (magenta) and doripenem (cyan) from OXA-23 (4JF4) and OXA-24 (3PAE) respectively are comparatively shown by superimposition. **(B)**. The conformation of the similar hydroxyl moiety of the side chain group of avibactam (light blue) from OXA-48 (4WM9) is also shown.

All the hydrophobic and van der Waals interactions made by the thiazolidine ring and its component atoms including S4, and side chain C51 and C52 methyl carbons with the side chains of Phe114, Trp117, Trp223, Met225 and Ile260 are collectively creating a sandwich effect with respect to 6αHMP and this, together with the hydrophobic bridge formed over the active site, may help preferentially stabilizing the Δ^2-tautomer of the β-lactam ring-opened 6αHMP (and similar carbapenems) within the active site of OXA-58. Stabilization of the Δ^2-tautomer keeps the side chain C51 and C52 methyl carbons at the C5 ring atom of 6αHMP (or any other side chains at the similar position in other carbapenems/β-lactams) away from the side chains of Phe113 and Phe114 of α3/α5-loop, which supposed to participate in the formation of hydrophobic bridge, in order to avoid steric hindrance/clashes among themselves which finally lead to a more stable acyl-enzyme species of 6αHMP and the deacylation-deficient OXA-58-6αHMP complex.

3.3.8. Comparison of OXA-58-6αHMP overall structure and its active site architecture with other CHDLs:

First of all, the amino acid sequence of OXA-58 from *A. baumannii* was compared with the sequences of other CHDL enzymes from *A. baumannii* itself and other pathogenic bacteria. It was found that the four functional motifs, including the STFK motif, the STV motif, the YGN motif and the KSG motif harboring the active site residues Ser83 and Lys86, Ser130 and Val132, and Lys220 and Ser221 respectively, are conserved among all these CHDLs (figure 3.16). The residues participating in forming the hydrophobic bridge are varying among these sequences and are observed to be not conserved among different classes of CHDLs. The residues with high propensity of involving in making the hydrophobic bridge are Phe110 and Met221 and Tyr112 and Met223 from OXA-23 and OXA-24 respectively, whose homologous residues are Phe114 and Met225 in *Ab*OXA-58. But after analyzing the crystal structures of the *Ab*OXA-58 acyl-enzyme species elucidated in our current study, it became evident that Phe113, rather than Phe114, is involving in making hydrophobic bridge with Met225 (figure 3.17). From the sequence and structure analysis its found that Phe113 of OXA-58 has no homologue in OXA-23, OXA-24 and OXA-48, and instead they are containing Ser109, Thr111 and Asp101 polar residues respectively (figure 3.16). It is also observed that the homologous residues including Asp101, Ile102 and Thr244 from OXA-48 are not forming any hydrophobic bridge. The Met225 residue in the apo and pseudoapo structures of OXA-58 is oriented toward the Phe114 residues as in the case of OXA-23 and OXA-24, and is repositioned towards Phe113 upon 6αHMP binding.

The superimposition of OXA-58 (4Y0U), OXA-23 (4JF4), OXA-24 (3PAE) and OXA-48 (4WM9) from *A. baumannii* showed that OXA-58 is superimposing at 1.03, 1.08 and 1.13 $Å^2$ RMSD with OXA-23, OXA-24 and OXA-48 structures respectively (figure 3.18). The active sites from the different CHDL enzymes were superimposed and their component residues were compared. The homologous residues of the OXA-58 active site residues in OXA-23, OXA-24 and OXA-48 (4WMC) are labeled and compared for their interactions (figure 3.19).

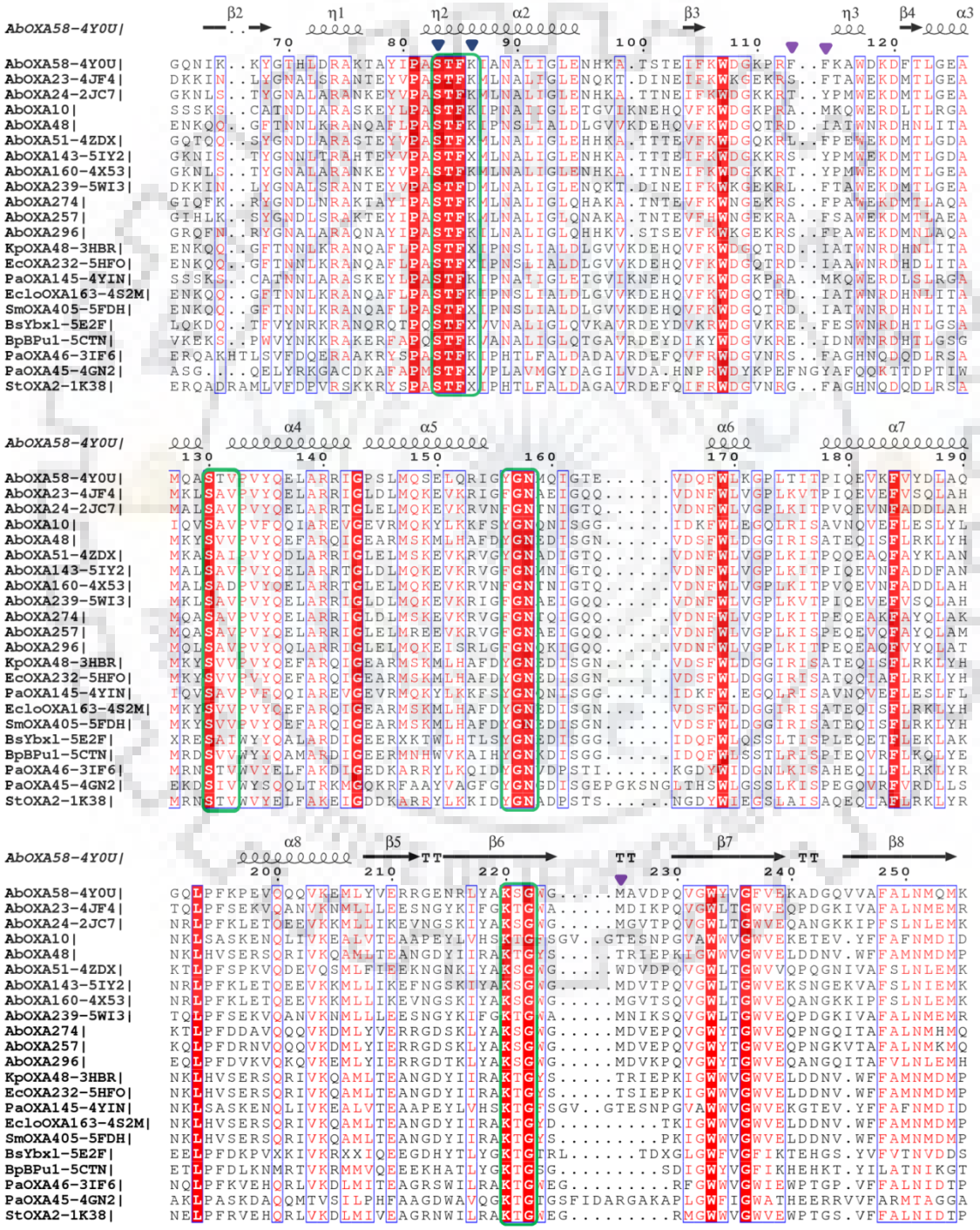

Figure 3.16: Comparison of the *Ab*OXA-58 amino acid sequence with CHDLs from other pathogenic bacteria, by multiple sequence alignment. Completely conserved residues are shown in red boxes with white characters, while the residues in the white boxes with red characters are relatively conserved. The conserved sequence motifs including STFK, STV, YGN and KSG are highlighted by the green colored boxes. The catalytic residues are pointed by blue coloured solid triangles, while the residues involving in forming the hydrophobic bridge are shown by the purple coloured solid triangles. Secondary structural elements of these aligned sequences are labeled above the sequences. The amino acid sequences of CHDLs from different bacterial species were collected as explained in the methods section.

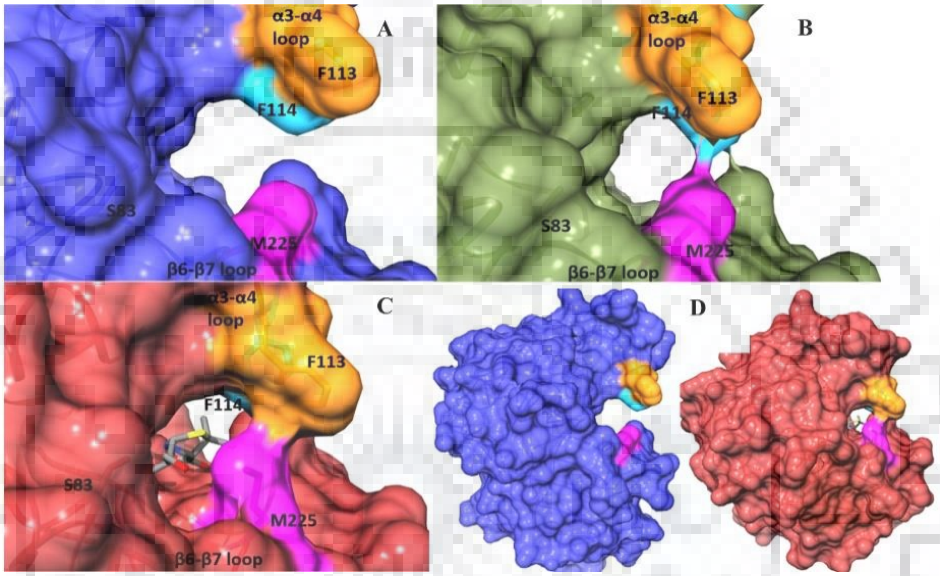

Figure 3.17: Snapshots of the active-site closure in OXA-58 induced by 6αHMP. The side chains of Phe113, Phe114, and Met225 implicated in the formation of the hydrophobic bridge over the active-site cleft are coloured orange, cyan, and magenta, respectively. (A), (B), and (C) are the surface diagrams depicting the active-site pocket of the apo, pseudoapo and the OXA-58–6αHMP binary complex respectively. (D) Side-by-side comparison of the overall structures of apo structure (left) and OXA-58–6αHMP complex (right), depicted in molecular surface diagrams.

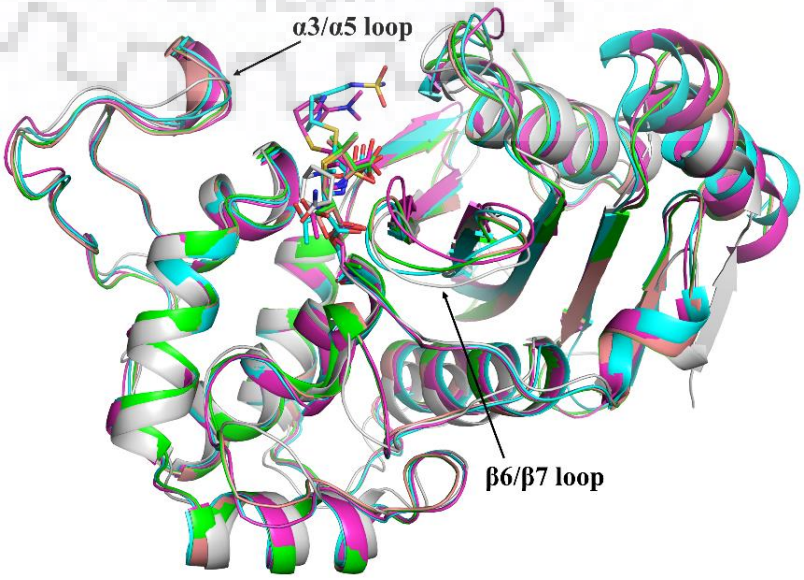

Figure 3.18: Superimposition of the CHDL enzymes including chain A (green) and chain B (grey) from OXA-58–6αHMP complex (4Y0U), OXA-23–meropenem (4JF4) (magenta), OXA-24–doripenem (3PAE) (cyan) and OXA-48–avibactam (4WMC) (white). The α3/α5- and β6/β7-loops corresponding to OXA-58 structure are labeled.

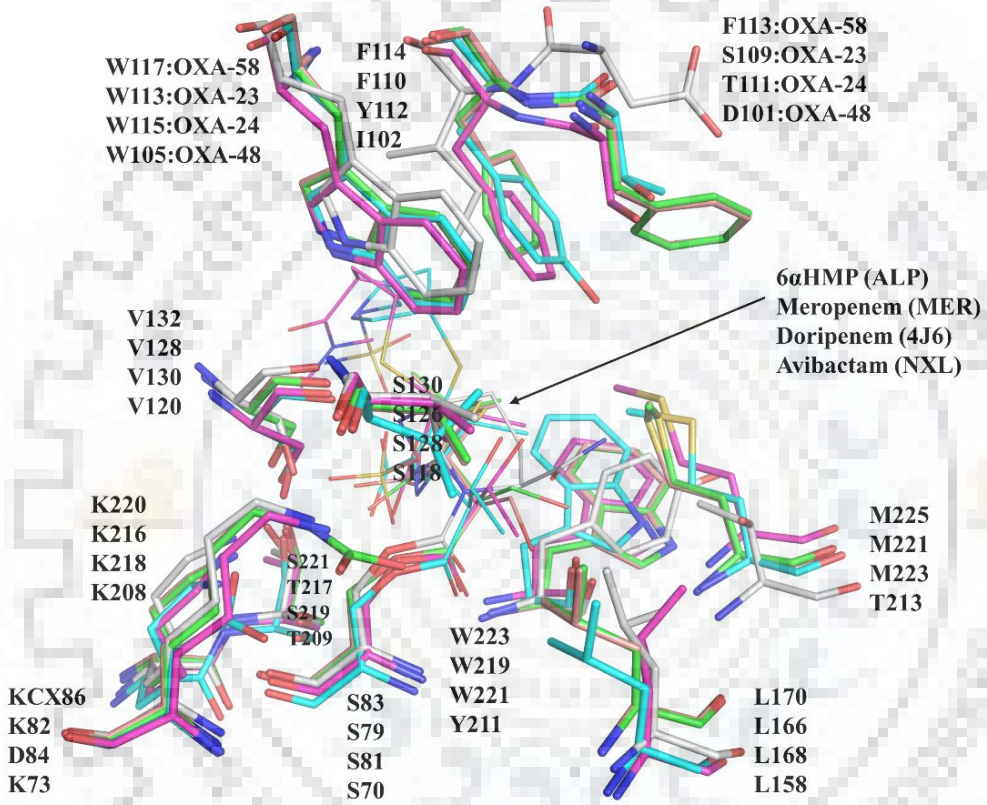

Figure 3.19: Comparison of the active site architecture and the component residues from the acyl-enzyme species of different CHDL enzymes with bound β-lactams including chain A (green) and chain B (grey) from OXA-58–6αHMP complex (4Y0U), OXA-23–meropenem (4JF4) (magenta), OXA-24–doripenem (3PAE) (cyan) and OXA-48–avibactam (4WMC) (white). The active site residues are shown in stick representation with colors corresponding to their polypeptide chains and are labeled with residue names and identifiers. The ligands bound covalently to the OG atoms of the respective catalytic serine residues of their corresponding protein chains are also shown in stick representation with lesser stick_radius and the corresponding chain color.

3.3.9. Crystal structures of the point mutation variants of OXA-58 protein from *A. baumannii*:

The structures of K86A, F113A, F114I, M225A and M225T were obtained and all were solved in the $P2_12_12_1$ space group. The data collection and refinement corresponding to all these mutant proteins are given in the table 3.4. All these were refined and validated in the similar way for the wild-type apo, paseudoapo and OXA-58–6αHMP complex structures. The refined structures were analysed for all the structural features and active site elements and compared among each other and also with the three OXA-58 wild-type structures obtained in our laboratory. We have observed all the structural elements in the five mutant structures except for the F114I structure in which we haven't obtained density for the α3/α5-loop region from Glu102 to Ser130.

Table 3.4: Data collection and refinement statistics for the crystal structures of the point mutation variants of *Ab*OXA-58.

	K86A	**M225T**	**M225A**	**F113A**	**F114I**
Wavelength (A°)	1.54	1.54	1.54	1.54	1.54
Resolution range	35.70 - 2.22	31.2- 2.20	44.6 – 2.6	47.77- 2.25	49.29- 2.24
Space group	$P2_12_12_1$	$P2_12_12_1$	$P2_12_12_1$	$P2_12_12_1$	$P2_12_12_1$
Unit cell	38.81 55.99 90.96 90 90 90	37.6 55.9 90.3 90 90 90	36.6 58.7 89.3 90 90 90	36.54 56.48 89.53 90 90 90	36.72 58.55 91.33 90 90 90
Total reflections	10254	10157	6321	9217	10012
Completeness (%)	93.0 (35.70-2.22)	92.0 (31.23-2.20)	86 (44.6 – 2.6)	71.5 (47.77-2.25)	84.3 (49.29-2.24)
Mean I/sigma(I)	1.75 (at 2.22Å)	2.14 (at 2.20Å)	1.68 (at 2.61Å)	1.26 (at 2.24Å)	1.43 (at 2.25Å)
Wilson B-factor	36.2	31.5	43.0	47.9	41.0

Reflections used in refinement	9070	8869	4839	6255	8004
R-work	0.217	0.253	0.216	0.222	0.228
R-free	0.275	0.328	0.314	0.343	0.303
Macromolecules	1911	1885	1877	1917	1925
Ligands	0	0	0	0	0
Solvent	0.34	0.34	0.33	0.33	0.34
Protein residues	239	236	236	240	241
Ramachandran favored (%)	97	95	95	93	96
Ramachandran allowed (%)	2	5	5	6	4
Ramachandran outliers (%)	1	0	0	1	0
Average B-factor	39.0	35.0	60	60	50

The comparative details of the conformational changes in the residues involving in hydrophobic bridge from K86A mutant with the wild-type apo protein are listed in the table 3.5. The distances between the Cα atoms of Phe113/Phe114 and Met225, harbored by the α3/α5- and β6/β7-loops respectively, in all the mutants are listed in the table 3.6. These results are showing that the hydrophobic bridge is formed in all the 4 mutant structures, including K86A, F113A, M225A and M225T (figure 3.20), except for the F114I in which the α3/α5-loop is missing. In F113A, the bridge is formed between Phe114 and Met225, while in case of K86A it is formed between Phe113 and Met225 from the α3/α5- and β6/β7-loops respectively. Of note, the hydrophobic bridge is formed in the M225A mutant also and in this case Ile260 is involved in bridge formation with the Phe114 residue; while, in case of M225T mutant, the

bridge is observed between the Phe113/Phe114 and Thr225/Ile260. In the structure of M225T, the Ile260 residue is partially involving in the bridge formation by making contacts with the Phe114 residue.

Table 3.5: Comparison of the differences in the α3/α5- and β6/β7-loops and their component residues among the wild-type and mutant OXA-58 structures.

Structure1	Structure2	Alignment range	RMSD (Å^2)		
			Cα atoms	Backbone	Whole residue
4Y0O	K86A	Met225	0.119	0.295	1.67
4Y0O	K86A	Phe113	1.8	1.7	1.8
4Y0O	K86A	Phe114	1.849	1.925	1.859
4Y0O	K86A	106-122	1.8	1.7	2
4Y0O	K86A	225-230	0.517	0.548	0.931
4Y0O	M225A	Met225			0.4
4Y0O	M225A	113			2.086
4Y0O	M225A	114			1.57
4Y0O	M225A	106-122			1.659
4Y0O	M225A	225-230			0.589

Table 3.6: Comparison of the Cα-Cα distances of the residues involving in hydrophobic bridge formation, among the mutant OXA-58 structures.

Structure	Residue 1	Residue 2	Cα-Cα distance (Å)
K86	Met225	Phe113	11.9
	Met225	Phe114	13.1
M225T	Met225	Phe113	12.3
	Met225	Phe114	13.9
M225A	Met225	Phe113	12.6
	Met225	Phe114	13.7
F113A	Met225	Phe113	11.1
	Met225	Phe114	13.0

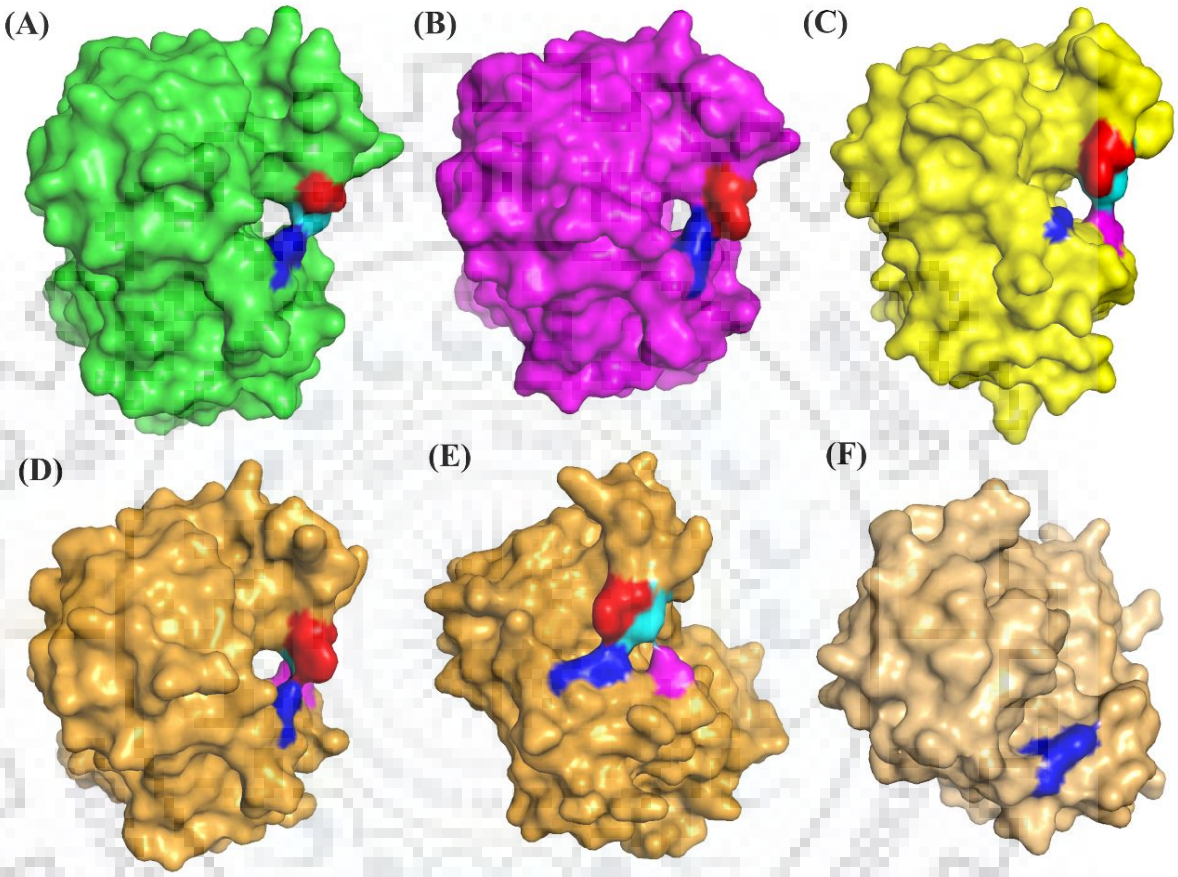

Figure 3.20: The pattern of hydrophobic bridge formation among the different mutant proteins of OXA-58 from *A. baumannii*. **(A)**, **(B)**, **(C)**, **(D)** and **(E)**, and **(F)** are representing the F113A, K86A, M225A, M225T and F114I respectively, and showing the hydrophobic bridges formed in these mutant structures. The mutants' polypeptide chains are color coded differently with green (F113A), magenta (K86A), yellow (M225A), orange (M225T) and grey (F114I). The residues involving in the hydrophobic bridge formation Phe113, Phe114, Met225, Thr225 and Ile260 are colored with red, cyan, blue, blue and magenta respectively. Two different views of the hydrophobic bridge are shown for M225T in (D) and (E) panels.

3.4. Conclusions:

We have observed the inward movements of α3/α5- and β6/β7-loops harboring the Phe113/Phe114 and Met225 residues, respectively, involving in the formation of a hydrophobic bridge over the active site upon binding of the carbapenem mimetic 6α-HMP. The loop movements trigger the realignment of the side chains of those residues and forms the hydrophobic bridge which plays roles in substrate recognition and subsequent catalysis. These features of the OXA-58-6α-HMP acyl-enzyme complex, are indicating that the plasticity of the active site elements is essential for the β-lactam recognition and its catalysis by the OXA-58 β-lactamase enzyme. The three different conformations observed for the side chain hydroxyl group of the hydroxyalkyl side chain of the carbapenem β-lactams and their structural mimetics play crucial roles in the substrate recognition by the β-lactamase enzymes. These three conformations (two rotamers of 6α-HMP and the virtually identical rotamers of meropenem and doripenem) are indicating the conformational sampling of the side chain hydroxyl group of the hydroxyalkyl moiety and also showing a sequence of key events that may take place during the carbapenem catalysis that is going to happen subsequently. The first rotamer (chain B of OXA-58-6α-HMP complex) may correspond to the acyl-enzyme complex formed from the Michaelis-Menten complex, while the second rotamer (chain A) may represent an intermediate conformation obtained while the hydroxyethyl sidechain samples the conformational space for optimal orientation for catalysis in the active site of CHDLs. The third rotamer (observed in OXA-23–meropenem and OXA-24–doripenem complexes) may show the optimal location of the hydroxyethyl side chain for the last step of catalysis, deacylation. A deacylation step in β-lactam catalysis by OXA β-lactamases requires that a water molecule be in hydrogen bond distance from the carboxylysine active-site residue (Lys-86) and the carbonyl moiety of the acyl-enzyme species. The proposed flow of catalytic events suggests that class D β-lactamases may have acquired carbapenemase activity by selecting a rotamer conformation that allows not simply retention of the deacylating water molecule but its retention in the position between the carboxylysine and the carbonyl of the acyl-enzyme complex, as required for catalytic deacylation.

The crystal structures obtained for the K86A, F113A, F114I, M225A and M225T point mutations of *Ab*OXA-58 are showing that the hydrophobic bridge is formed even in the absence of one of the phenyl alanine residues or the mutated methionine residues. And the hydrophobic bridge formation over the active sites of mutant proteins is supporting the results showing the catalytic activity of these proteins and concluding that these point mutant proteins of *Ab*OXA-58 are catalytically activity but with decreased catalytic efficiencies.

CHAPTER 4

Purification, crystallization and characterization of deoxyhypusine hydroxylase (DOHH) from *Leishmania donovani*

4.1. Introduction:

Parasitic diseases have an enormous health, social and economic impact and are a particular problem in tropical regions of the world. Major human parasitic protozoan diseases are such as malaria, trypanosomiasis, toxoplasmosis, cryptosporidiosis and leishmaniasis. *Leishmania donovani* is an intracellular parasitic protozon, belongs to the genus *Leishmania*, which causes the disease leishmaniasis. According to the recent reports on Leishmaniasis, it is being informed that over more than 90% cases of visceral leishmaniasis (VL) ensue in 5 countries: India, Bangladesh, Nepal, Sudan and Brazil. The global burden of these diseases is exacerbated by the lack of vaccines, making safe and effective drugs vital to their prevention and treatment.

Currently the treatment of visceral leishmaniasis is achieving by the use of single-dose liposomal amphotericin B (AmBisome; Gilead Sciences), which is adopted by the Indian subcontinent as a first-line drug few years back. Even though good progress is there in decreasing the disease incidence frequency after adopting this drug, amphotericin B, which is mainly an antifungal drug and targets by binding to sterols, is not a targeted drug against the *Leishmania* protozoan parasites. In addition to this, amphotericin B drug has several highly risky side-effects. And also the prevention of leishmaniasis transmission by using the insecticides to kill the sandflies, the vectors responsible for transmitting the disease and its widespread, is helping to some extent in controlling the epidemics of leishmaniasis. But there are many sand fly species are reported in recent times which are showing resistance to the currently using insecticides. Treatment of leishmaniasis by using amphotericin B is able to prevent the first appearance of visceral leishmaniasis, but recurrence of the disease is recorded at most cases and it's because of the post-treament survival of the Leishmania parasites. Also PKDL (Post-kala-azar dermal leishmaniasis), in addition to sand flies and few other animals, is acting as a main reservoir between the occurrence of successive leishmaniasis epidemics. Occurrence of leishmaniasis in HIV infected individuals is also main concern in the spread of this disease. Even though leishmaniasis is endemic to the Bihar state and its surrounding regions, leishmaniasis cases are being reported from many other parts of India also, including Rajasthan and Kerala, very recently. Leishmania parasites are showing resistance to the many

other available drugs and antibiotics; and also there are no efficient vaccines available till date. It menas that even though we are treating the disease by using currently available drugs like amphotericin, there is recurrence of disease in the drug-treated patients, and leishmaniasis epidemics and spread to new parts of the country is quite evident. Hence it came into the clear knowledge that there is a need for a parasite-specific targeted drug(s) or vaccine(s) to kill the parasite completely and to achieve the prevention of disease recurrence and its complete eradication/elimination from all the disease susceptible communities/societies worldwide.

Unfortunately, where drugs are available, their usefulness is being increasingly threatened by parasite drug resistance. The need for new drugs drives antiparasitic drug discovery research globally. As proteins are the driving horses of the cellular life of any living organism, it is a good idea to target the protein components of the pathogen(s) (causative agent(s)) of any disease/infection. There are different metabolic pathways essential for the survival of *Leishmania* pathogen. One of them is hypusine pathway which is essential for the post translational modification of the eukaryotic initiation factor 5A (eIF5A), which helps in initiation process of protein synthesis. To understand the hypusine biosynthetic pathway of *L. donovani*, we have chosen the enzyme deoxyhypusine hydroxylase (DOHH), which completes the synthesis of hypusine and maturation of eIF5A. An Inhibitor of DOHH has been shown to inhibit the protein synthesis in the pathogen (836). DOHH can be used as a potential drug target against *L. donovani*. Therefore, it is necessary to understand the structure-function relationship of this enzyme. The structural differences between the *L. donovani* DOHH and the human homolog may be exploited for structure-based design of selective inhibitors against the parasite.

4.2. Materials and Methods:

4.2.1. Materials:

The chemicals used in this study were purchased either from Sigma, Merck-millipore, Fluka, Himedia, Bio-Rad or SRL. The bacterial growth media were purchased either from Merck-millipore or Himedia laboratories. The enzymes required for gene cloning including Taq DNA polymerase, restriction endonucleases and T4 DNA ligase were procured from NEB, while the mini plasmid preparation kit, PCR purification kit and gel extraction kit from Qiagen. The DNA oligonucleotide primers, used for PCR amplification of all gene truncates made in this study, were synthesized by IDT technologies. *E. coli* DH5α and BL21 (DE3) strains were purchased from Novagen (USA). The chromatography media and columns were procured from

GE Healthcare or Bio-Rad; and the dialysis membranes from Thermo Fisher scientific. The pre-optimized crystallization screens, including Crystal Screen, PEG/Ion, Index, Salt and Crystal Screen Cryo were purchased from Hampton Research, USA; while JCSG-plus, MIDASplus, Morpheus and PACT premier were from Molecular Dimensions, UK. The genomic DNA from *Leishmania donovani* was provided by Prof. R. Madhubala, Jawaharlal Nehru University, New Delhi, India.

4.2.2. Methods:

4.2.2.1. *Ld*DOHH cloning:

The full length ORF of the 981-bp long wild-type *dohh* gene (hereafter designated as *lddohh*) from *L. donovani* was cloned into pET28c vector using the forward and reverse primers, containing NdeI and SalI restriction sites respectively. The N-terminal 6xHis-affinity tag was used along with the TEV protease digestion site, inserted in between the gene and the affinity tag.

4.2.2.2. Transformation of the *lddohh* gene-carrying plasmid vector:

The recombinant pET28C-6xHis-TEVP-*dohh* plasmid expression vector containing the coding region of the wild-type *dohh* gene from *L. donovani* was transformed into *E. coli* DH5α and BL21 DE3 cells, the cloning and expression hosts respectively. The transformation was carried out by $CaCl_2$ chemical-heat shock transformation method, using the protocol explained in the previous chapter.

4.2.2.3. Over-expression and purification of recombinant *Ld*DOHH:

Single bacterial colony from the agar plates of the recombinant pET28C-6xHis-TEVP-*dohh* plasmid-transformed BL21 DE3 cells was inoculated into autoclaved LB broth tubes, and IPTG induction and protein over-expression and solubility confirmation were carried out using the same protocol explained in the previous chapter. After confirming the *Ld*DOHH protein over-expression from the recombinant *Ld*DOHH-6xHis-TEV-pET28C plasmid-transformed BL21 DE3 cells, 1 L of LB broth was added with 50 μg/mL kanamycin antibiotic and 10 mL of overnight grown primary inoculum, followed by incubation at 37°C and 200 rpm speed until its OD_{600} reaches to 0.6. The culture was induced for protein over-expression using 0.4 mM IPTG, followed by incubation at 20°C and 200 rpm for around 18 hrs. The cells from the incubated culture were harvested by centrifugation 6000 rpm and 4°C for 10 mins.

All the purification steps were carried out at 4°C. The cell pellet was re-suspended in 20 mL of suspension buffer (25 mM Tris pH 7.4, 100 mM NaCl and 2% glycerol) and ell disruption was carried out at 20 KPSI working pressure. The cell lysate was centrifuged 12000 rpm and 4°C for 60-70 mins and the supernatant was separated out from the pellet containing the cell debris. Meanwhile a manually packed Ni2+-NTA agarose affinity column having 5 mL of matrix/bed was washed properly with imidazole followed by 20-30 column volumes of water, and subsequently equilibrated with 10 column volumes of binding buffer. The supernatant was applied onto that buffer-equilibrated Ni^{2+}-NTA agarose column and incubated at 4°C for 40-50 mins for allowing the His6-affinity tagged *Ld*DOHH protein binding to the affinity matrix in the column. Now the flow through is collected from the incubated protein-affinity matrix mixture, followed by the matrix wash with low concentration imidazole step gradient to remove the loosely bound unwanted impure proteins. 5 mL of each 10 mM, 20 mM, 50 mM and 100 mM imidazole concentrations, that were dissolved in the binding buffer, were used to wash the column and corresponding flow through were collected in separate tubes. The tightly bound over-expressed His6-affinity tagged *Ld*DOHH protein was eluted using 30 mL of the highest 250 mM imidazole concentration and the corresponding flow through was collected into multiple collection tubes with 5-10 mL in each. The supernatant, flow through and elution fractions collected at each purification step, along with a protein ladder sample, were run on the SDS-PAGE electrophoresis using a 12% separating gel.

The fractions, collected in the affinity chromatography step, containing partially purified *Ld*DOHH protein were pooled and concentrated using 10 kDa MWCO amicon centrifugal filters, upto 5 mg/mL concentration. Meanwhile, a 120 mL HiLoad 16/600 Superdex 200 pg gel filtration column, connected with the AKTA purifier 10 FPLC system, was equilibrated with 2 column volumes of gel filtration purification buffer (25 mM Tris pH 7.4 and 100 mM NaCl). After completion of equilibration, 500 µL of concentrated protein sample was loaded and eluted protein fractions, 2 mL of each, were collected from the point of void volume of the column. The elution from the column was monitored by UV absorption at 280 nm, along with conductivity, ionic strength and pH. The protein elution was observed by the 280 nm absorption peaks and all the elution fractions corresponding to all the peaks were run on 12% SDS-PAGE gel to check for the presence and purity of the protein. The gel filtration fractions containing purified *Ld*DOHH protein were pooled and concentrated upto 20 mg/mL or the needful concentration and used for crystallization and other experimental studies.

4.2.2.4. TEV protease protein purification:

The *E. coli* Rosetta cells harboring the recombinant plasmid carrying the wild-type TEV protease gene were grown in LB broth by adding ampicillin and chloramphenicol antibiotics. The protein over-expression induction was achieved by adding 0.5 mM IPTG to the appropriate bacterial culture and incubating at 30°C and 200 rpm for 6-7 hrs. TEV protease protein over-expression was confirmed using the same protocol explained in the previous sections. The over-expressed 6xHis-tagged TEV protease was purified by Ni-NTA agarose affinity chromatography using the similar protocol, with minor alterations, explained for *Ld*DOHH and *Mc*FabI proteins. Purification buffer composed of 20 mM Tris pH 8.0, 3% glycerol and 100 mM NaCl, and 20-250 mM imidazole (prepared in purification buffer) step gradient were used for this purification. The elution fractions containing purified TEV protein were pooled and kept for dialysis against the purification buffer, in order to remove the imidazole from the elutions. The reducing agents BME (during protein elution) and dithiothreitol (DTT) (during protein storage) were also used here in this case. 1 mg/mL of protein aliquots were made, flash-frozen in liquid nitrogen (LN2) and stored at -80°C for future usage.

4.2.2.5. Purification of non-tagged *Ld*DOHH protein after 6xHis-affinity-tag removal:

The 6xHis-affinity-tag removal was achieved by optimizing the digestion of purified 6xHis-tagged *Ld*DOHH protein by purified TEV protease protein, which included several variables (i) quantitative ratio of 6xHis-tagged *Ld*DOHH protein to TEV protease in the digestion mixture [1:5, 1:10 and 1:20] (ii) incubation temperature [4°C and 20°C] (iii) incubation duration [5 hrs, 10 hrs and 15 hrs] and (iv) stirring speed [0 rpm and 100 rpm].

After incubation of the 6xHis-tagged *Ld*DOHH protein with TEV protease to facilitate the affinity tag digestion and removal from the desired *Ld*DOHH protein, the digestion mixture was kept for dialysis in order to remove imidazole, reducing agents and many other unwanted solutes. Dialysis was carried out in prior-cold 2 L purification buffer at 4°C and 100 rpm for overnight.

The non-tagged *Ld*DOHH protein from the thoroughly dialysed 6xHis-tagged *Ld*DOHH - TEV protease protein digestion mixture was purified by Ni-NTA agarose affinity chromatography using the similar protocol explained for the 6xHis-tagged *Ld*DOHH protein purification, with little modifications including (i) the digestion mixture was not incubated with the equilibrated beads and (ii) less number of imidazole washes. All the flow through and elution fractions, along with the undigested 6xHis-tagged *Ld*DOHH and pure TEV protease protein control

samples, were run on 12% SDS-PAGE which was run for comparatively longer duration to achieve proper resolution of band separation to distinguish the non-tagged protein from the tagged one. The flow through samples containing the purified non-affinity-tagged *Ld*DOHH were pooled and concentrated using 10 kDa MWCO amicon centrifugal filters, upto 5 mg/mL, and subsequently loaded onto a buffer-equilibrated 120 mL HiLoad 16/600 Superdex 200 pg gel filtration column. The gel filtration fractions containing pure non-tagged *Ld*DOHH protein were concentrated upto 20 mg/mL and used for crystallization and other experimental studies.

4.2.2.6. Native-PAGE analysis of *Ld*DOHH protein conformational and oligomeric states:

Native-PAGE analysis was carried out to check the *Ld*DOHH protein's oligomeric state in its apo form. The 12% native PAGE gel was prepared and run by using the same protocol explained in the previous chapters. 27 μM (1 mg/mL) of wild-type apo *Ld*DOHH protein was used for native PAGE analysis and 15 μM (1 mg/mL) BSA was also loaded into native PAGE along with our test samples, as a protein marker/reference. After run, the gel was stained and destained in the same way as done for the SDS-PAGE gel.

4.2.2.7. Crystallization of wild-type *Ld*DOHH:

The wild-type 6xHis-tagged *Ld*DOHH protein that was purified to highest homogeneity and concentrated upto 20 mg/mL in 25 mM Tris pH 7.4 and 100 mM NaCl was used for crystallization studies at the start. The initial crystallization experiments were carried out by sitting drop vapor diffusion methods and incubation at 4°C, and the pre-optimized crystallization screens purchased from Hampton Research were used. Crystallization experiments were set up manually using 96-well sitting drop plates. The crystallization trials were carried out using the several combinations of different variables of crystallization parameters including (a) protein nature [apoenzyme and holoenzyme] (b) protein type [6xHis-affinity-tagged and non-affinity-tagged] (c) protein concentration [1 mg/mL to 80 mg/mL] (d) method of crystallization [hanging drop and sitting drop] (e) crystallization incubation temperature [4°C - 37°C] (f) type of pre-optimized commercial screen [Crystal Screen, PEG/Ion, Index, Salt and Crystal Screen Cryo from Hampton Research, and JCSG-plus, MIDASplus, Morpheus and PACT premier from Molecular dimensions]. Few crystals observed which turned out to be salt. Many of these crystallization trials also repeated by using Mosquito (TTP Labtech) and MICROLAB STARLET (Hamilton Robotics) at XRD Protein Crystallization Laboratory, AIRF Facility, JNU, New Delhi. Hanging drop crystallization was carried out in 96-well format using the crystallization robotics.

The subsequent crystallization trials included manually prepared crystal screens in different combinations with other variables of crystallization parameters. The manually prepared crystallization screens include the variable crystallization parameters (i) buffer type, its pH and its concentration (ii) salt type and its concentration (iii) precipitant type and its strength and (iv) additives. We have also carried out co-crystallization studies using protein's known inhibitor molecules and by adding external source of iron.

4.2.2.8. Protein disorder and crystallizability prediction and analysis:

The intrinsic structural disorderedness of *Ld*DOHH protein was assessed and analysed by different computational web servers including Protein DisOrder prediction System (PrDOS) (930), DisEMBL Intrinsic Protein Disorder Prediction 1.5 (931) and GlobPlot 2.3 predictor of intrinsic protein disorder and globularity (932). The amino acid sequence of the *Ld*DOHH protein was submitted to these servers individually and the analysis parameters were chosen respectively. The crystallizability of *Ld*DOHH protein was computed and analysed by the XtalPred web server.

4.2.2.9. Constructing the *Ld*DOHHΔ3, *Ld*DOHHΔ6 and *Ld*DOHHΔ9 protein truncates:

Based on the computational predictions of intrinsic disorder regions of *Ld*DOHH protein, 3 random truncations of the disordered regions from the C-terminus of the protein were made. These include *Ld*DOHHΔ3, *Ld*DOHHΔ6 and *Ld*DOHHΔ9 protein truncates that were constructed by truncation/removal of 3, 6 and 9 consecutive amino acid residues respectively from the C-terminus of the protein. The *dohhΔ3*, *dohhΔ6* and *dohhΔ9* gene truncations were made from the *Ld*DOHH-6xHis-TEV-pET28C vector plasmid template using a common forward primer 5'-CAGCCATATGATGTCTGCTTTGAACAGCCGCAC-3' containing the NdeI restriction endonuclease site, while individual reverse primers 5'-CATAGTCGACTCACTGCTGCTGATGAGCGAGG-3', 5'-CATAGTCGACTCAATGAGCGAGGCCGTTGAAGTTC-3' and 5'-CATAGTCGACTCAGCCGTTGAAGTTCGCCCAGTAC-3' respectively having the SalI restriction site. PCR amplification for all the 3 constructs was carried out using the *lddohh*-6xHis-TEV-pET28C vector plasmid template containing the wild-type dohh gene from *L. donovani*, respective forward and reverse primers, dNTPs, Taq DNA polymerase and Thermocycler (Eppendorf make). Amplification of the required construct band was confirmed by agarose gel electrophoresis (AGE) and the respective amplicons were purified from the PCR reaction mixtures using the PCR purification kit. Blank pET28C vector plasmid was isolated

and purified from pET28C-harboring *E. coli* DH5α-cells, using mini plasmid isolation kit. The amplicons of all the three *dohh*Δ*3*, *dohh*Δ*6* and *dohh*Δ*9* gene truncates and blank pET28C vector plasmid were subjected individually to double restriction endonuclease digestion using NdeI and SalI enzymes at 37°C for 2-3 hrs. The endonuclease digested amplicons and pET28C vector plasmid were run on 0.8% low melting agarose and subsequently purified from the gel by using gel extraction kit. The double-digested and gel purified *dohh*Δ*3*, *dohh*Δ*6* and *dohh*Δ*9* gene amplicons and pET28C vector plasmid were ligated using T4 DNA ligase enzyme at 16°C overnight.

The ligated *lddohh*Δ*3*-6xHis-TEV-pET28C, *lddohh*Δ*6*-6xHis-TEV-pET28C and *lddohh*Δ*9*-6xHis-TEV-pET28C constructs were transformed into *E. coli* DH5α-cells, cloning host, using the CaCl2 chemical-heat shock transformation method as explained in the previous chapters. The colonies from the transformation plates were inoculated into LB broth tubes and subsequently plasmids corresponding to all the three *dohh*Δ*3*, *dohh*Δ*6* and *dohh*Δ*9* gene truncation constructs were isolated and purified and the presence of the corresponding *dohh* gene truncation was confirmed by subjecting the respective plasmid construct to restriction endonuclease digestion. After confirming the truncation of corresponding nucleotide sequences, the *lddohh*Δ*3*-6xHis-TEV-pET28C, *lddohh*Δ*6*-6xHis-TEV-pET28C and *lddohh*Δ*9*-6xHis-TEV-pET28C plasmid constructs were individually transformed into *E. coli* BL21 DE3 cells in the similar way.

4.2.2.10. Agarose gel electrophoresis (AGE) to confirm DNA presence and quality:

The presence and quality/purity of the genes, plasmid vectors, recombinant plasmids and DNA oligonucleotides were known to be confirmed by the agarose gel electrophoresis (AGE) run. 0.8% agarose gel was made by boiling (at 90°C) the agarose added in 30 mL running buffer, followed by adding ethidium bromide (EtBr) dye after cooling (to 50°C) and just before pouring into the gel caster. DNA samples were mixed well with the gel loading dye before loading into the agarose gel along with a 1-kB DNA ladder. The Tris/Acetate/EDTA (TAE) buffer was used for gel preparation as well as an electrophoresis running buffer. The AGE was run at 60 V for 40 mins, in case plasmid samples, in a horizontal electrophoresis apparatus connected to a power supply. After completion of AGE run, the gel was observed under UV illumination to visualize the separated plasmid/amplicon DNA samples that in-gel stained by EtBr.

4.2.2.11. Over-expression and purification of the DOHH protein truncates:

Single bacterial colony from each of the BL21 DE3 agar plates transformed with the recombinant *lddohh*Δ*3*-6xHis-TEV-pET28C, *lddohh*Δ*6*-6xHis-TEV-pET28C and *lddohh*Δ*9*-6xHis-TEV-pET28C plasmid constructs was inoculated separately into autoclaved LB broth tubes, and IPTG induction and protein over-expression confirmation were carried out using the same protocol explained in the previous chapters.

Purification of the 6xHis-affinity-tagged *Ld*DOHHΔ3, *Ld*DOHHΔ6 and *Ld*DOHHΔ9 protein truncates was carried out by Ni-NTA affinity chromatography followed by size exclusion chromatography using the similar protocol explained for the wild-type *Ld*DOHH protein. The purified *Ld*DOHHΔ3, *Ld*DOHHΔ6 and *Ld*DOHHΔ9 protein truncates were concentrated upto 20 mg/mL and used for crystallization and other experimental studies.

The non-affinity-tagged *Ld*DOHHΔ3, *Ld*DOHHΔ6 and *Ld*DOHHΔ9 protein truncates were also using the similar protocol explained for the wild-type non-affinity-tagged *Ld*DOHH protein and used for crystallization and other experiments.

4.2.2.12. Crystallization of truncated proteins:

The 6xHis-affinity-tagged and non-affinity-tagged *Ld*DOHHΔ3, *Ld*DOHHΔ6 and *Ld*DOHHΔ9 protein truncates were also used for crystallization experiments in the similar way explained for the affinity-tagged and non-tagged wild-type *Ld*DOHH protein.

4.2.2.13. CD spectroscopy studies:

Various biochemical properties of the wild-type *Ld*DOHH protein were analysed by circular dichroism spectroscopy, including (i) protein's thermal stability [25°C - 100°C], (ii) resistance to protein denaturants [0.1 M – 8 M concentration range of urea and GnHcl], (iii) pH stability [pH 4.0 – pH 9.0] and (iv) ionic strength sustainability [0.1 M - 1 M salt strength]. 10 μM *Ld*DOHH protein in 20mM sodium phosphate buffer was used for spectroscopy analysis and the experiment was carried out using 200μL sample in 0.1 mm quartz cuvette. The far UV spectral scan was recorded from 260-190nm, at 1nm band width. The buffer was used to take the blank readings in the same scan range, before the start of sample analysis.

4.2.2.14. *Ld*DOHH sequence analysis:

The amino acid sequence of *Ld*DOHH protein was compared with homologous proteins from other trypanosomatids, protozoans, several members of animalia and plants by multiple sequence alignment using the ClustalΩ tool (892-894). The amino acid sequences of DOHH proteins from *Leishamani donovani* (*Ldo*DOH), *Homo sapiens* (*Hsa*DOH), *Trypanosoma cruzi* (*Tcr*DOH), *Mus musculus* (*Mmu*DOH), *Bos taurus* (*Bta*DOH), *Python bivittatus* (*Pbi*DOH), *Pteropus Alecto* (*Pal*DOH), *Xenopus laevis* (*Xla*DOH), *Drosophila obscura* (*Dob*DOH), *Trichinella pseudospiralis* (*Tps*DOH), *Brassica napus* (*Bna*DOH), *Zea mays* (*Zma*DOH), *Saccharomyces cerevisiae* (*Sce*DOH), and *Chlamydomonas reinhardtii* (*Cre*DOH) were collected from the NCBI protein database in the FASTA format. All these sequences were submitted together to the ClustalΩ tool with the output options chosen to be clustal file with numbering and percent identity matrix (PIM). The multiple sequence alignment file was analysed manually for the homology and conserved amino acid sequence regions and the presence of insertions or deletions. The *Ld*DOHH protein sequence was also analysed for several of its molecular properties using computational tools including ExPASy ProtParam (933).

4.2.2.15. *Ld*DOHH molecular modeling:

The wild-type *Ld*DOHH protein sequence was queried in the NCBI protein BLAST (892-894) against the PDB database and searched for the best homolog, having highest sequence identity with good query coverage, for which structure is elucidated and deposited in the database. After obtaining the 4D4Z structure as the best template, the *Ld*DOHH protein sequence was modeled using the MODELLER 9.19 program (934). The homology models obtained from the MODELLER were validated using PROCHECK (935), ERRAT (936), PROVE (937), VERIFY3D (938) programs of the SAVES server. The best model was selected after validation and used for further structural analysis and experiments.

4.2.2.16. *Ld*DOHH structure analysis:

The secondary structural features of the aligned DOHH protein sequences were comparatively analysed by ESPript (895), using the *Ld*DOHH protein modeled structure as template. The multiple sequence alignment file, obtained from the ClustalΩ tool, along with a single polymeric protein chain from the modeled and validated final PBD format *Ld*DOHH protein model, as a template PDB structure, was submitted to the ESPript server for calculating the conserved and homology secondary structural features among the DOHH structures from various pathogenic bacteria.

The secondary, tertiary and quaternary structural features of the final validated wild-type apo *Ld*DOHH were initially analysed by using the 3-D visualization tools like PyMOL (896), Discovery Studio Visualizer (897) and Chimera (898). These initial analyses include the type and amount of secondary structural elements (α-helices, β-sheets and random loops), number and type of domains present in each protein polymeric chain, number of protein chains present in the entire protein model and their arrangement in 3-D space.

The PDB structures of DOHH from other organisms were downloaded from the RCSB PDB database, if any available, and used for comparative analysis with the *Ld*DOHH protein, which was carried out manually in the 3-D visualization tools like PyMOL, Discovery Studio Visualizer and Chimera. The distant structural homologues of *Ld*DOHH protein were searched by the DaliLite server. The final structural model of *Ld*DOHH protein was submitted to the DaliLite server and the output structures were analysed and inspected for homology by monitoring the Z-score and RMSD values.

4.2.2.17. Pharmacophore modelling and virtual screening:

To construct pharmacophore models that are both sensitive and selective, all combinations of three to six features pharmacophores are enumerated and ranked by decreasing selectivity. Only the top 10 models are selected. Firstly, the RLPG protocol (904-906) identifies pharmacophore features of the ligand. Six standard pharmacophore features (HBA, hydrogen bond acceptor; HBD, hydrogen bond donor; HYD, hydrophobic; NI, negatively ionizable; PI, positively ionizable; RA, ring aromatic) are considered. ChEBI_lite_3star library of EBI databased with 46,125 molecules was screened through the first pharmacophore model because of its high selectivity score. 1125 molecule were able to cross the pharmacophore filter. Out of them, 523 molecules cross the Lipinski filter. And 16 molecule shows the docking score comparable to deoxyhypusine. The input site sphere values used for docking molecules in CDOCKER include -0.459209, 56.9617, 12.1817, 8.04679.

4.2.2.18. Molecular docking:

The top hit compounds obtained from the virtual screening were docked into the template *Ld*DOHH protein using AutoDock (902) and Autodock Vina (903) in order to calculate the binding energies of those compounds at the active site of *Ld*DOHH. Protein and ligand files were prepared by using AutoDock tools (902-903) according to the standard protocol. Protein file was prepared by removing any bound ligand molecules except for iron and water; and adding Kollman charges and hydrogen atoms. Final hits were docked in the active site using the

Lamarckian genetic algorithm (LGA) and the Grid centred at (29.58, 11.972, 17.167) 24×22×36 dimension with the default spacing (0.375 Å). The lowest energy conformation of the docked ligand was interpreted as the best pose. Results were analysed using PyMol and Discovery studio visualizer

4.2.2.19. MD simulations:

The *Ld*DOHH protein model and its docked complexes were subjected to molecular dynamics simulations to check their conformational stability. The topology for the protein polypeptide chains was prepared by the GROMOS43a1ff (Gromos43a1 force field) of GROMACS software (912), while the topology files for the inhibitor compounds were prepared by PRODRG server (939-940). Simple point charge (Spc) water model was used to solvate the protein in a cubic box. The "protein in water" system was neutralized by adding Na^+ and Cl^- ions and also the system was added with 150 μM extra amount of salt to mimic the biological buffering system. The xyz 3-D periodic boundary condition (pbc) was used to eliminate the surface effects and to maintain minimum image convention. A solute-box distance of 1.0 nm was used to maintain at least 2.0 nm between any two periodic images of a protein. The solvated, electro-neutral system was energy minimized to ensure that the system has no steric clashes or inappropriate geometry and it is relaxed properly. Vacuum minimization was done by steepest descent minimization algorithm and 50000 number of minimization steps. During the energy minimization step, the Verlet cutoff-scheme was used for neighbor searching, the simple grid method was used to determine the neighbor list, treatment of long range electrostatic interactions was done by particle mesh Ewald (PME) electrostatics algorithm, maximum force to be achieved was set to < 1000.0 kJ/mol/nm and both short-range electrostatic and van der Waals cut-off were set to 1.0. Standard cut-off of 1.0 nm was used for both the neighbour list generation and the coulomb and Lennard–Jones interactions.

The position restrained parameters prepared for the protein, cofactor and inhibitors were used to apply a position restraining force on the heavy atoms of the protein (anything that is not a hydrogen), to avoid unnecessary distortion of the protein–ligand complex. The energy minimized system was equilibrated in 2 methods for 50 ns each: (i) NVT (constant Number of particles, Volume and Temperature) equilibration, which is also referred to as "isothermal-isochoric" or "canonical" ensemble, at 300 K reference temperature and (ii) NPT (constant Number of particles, Pressure and Temperature) equilibration, which is also referred to as "isothermal-isobaric" ensemble, at 1.0 bar reference pressure. Both the equilibration steps include two temperature coupling groups (tc_groups) comprising (i) the protein group and (ii)

non-protein group: water_ions, in case of all the four simulations. During NVT equilibration, only temperature coupling (V-rescale modified Berendsen thermostat algorithm) was on, while both temperature coupling (V-rescale modified Berendsen thermostat) and pressure coupling (Parrinello-Rahman barostat) were on during the NPT equilibration.

The system that was well-equilibrated at the desired 300 K temperature and 1.0 bar pressure, was used for production MD run. 50-ns MD run was executed with 25000000 steps and data were collected with 2 fs step size. During production MD run both the temperature and pressure coupling were on and the elctro-statistics were using PME algorithm. The production MD data were analysed for the stability of the polypeptide structure and complex stability by calculating the root-mean-square displacement (RMSD) of all the protein heavy atoms, i.e. non-hydrogen atoms, with respect to the starting structures. The time-dependent potential energy of the system and the root mean square fluctuation (RMSF) of all the protein residues were calculated, and the hydrogen bond pattern analysis between protein and the ligands was also carried out.

4.3. Results and discussion:

4.3.1. *Ld*DOHH cloning, transformation and protein over-expression:

The wild-type *dohh* gene from *L. donovani* was successfully cloned into pET28c vector with an N-terminal 6xHis-tag and TEV protease digestion site (figure 4.1). The recombinant pET28C-6xHis-TEVP-*dohh* plasmid vector containing the coding region of the wild-type *lddohh* gene was transformed successfully into *E. coli* DH5α. The clone was confirmed by double restriction endonuclease digestion using both NdeI and SalI enzymes, and also by PCR amplification, where we have observed a DNA band of ~1Kb corresponding to the size of the *lddohh* gene (981-bp) (figure 4.2). And subsequently the nucleotide sequence of the cloned gene was also confirmed by gene sequencing.

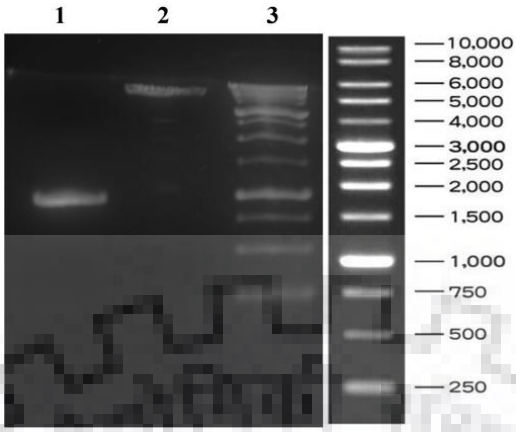

Figure 4.1: PCR amplification and subsequent restriction digestion of the *lddohh* gene amplicon and pET28C plasmid. Lane 1: *lddohh* gene amplicon after restriction endonuclease digestion, lane 1: pET28C plasmid after restriction endonuclease digestion, and lane 3: DNA ladder.

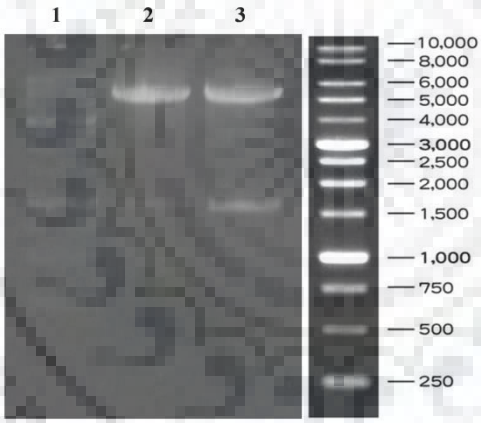

Figure 4.2: confirmation of the *lddohh* gene cloning by double restriction endonuclease digestion of the plasmid isolated from the pET28C-6xHis-TEVP-*dohh* plasmid vector transformed *E. coli* DH5α cells. Lane 1: DNA ladder, lane 2 and 3: the recombinant pET28C-6xHis-TEVP-*dohh* plasmids, isolated from different batch cultures, after restriction digestion.

The recombinant pET28C-6xHis-TEVP-*dohh* plasmid vector was then transformed successfully into *E. coli* BL21 DE3 cells, and the transformed *E. coli* BL21 DE3 cells were confirmed to be over-expressing a soluble wild-type 6xHis-tagged *Ld*DOHH protein, which was observed by a thick ~37 kDa band in the SDS-PAGE gel (figure 4.3).

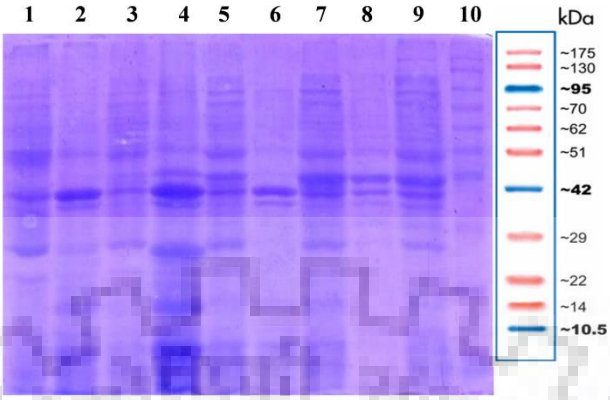

Figure 4.3: The wild-type 6xHis-tagged *Ld*DOHH protein over-expression studies. The supernatant and pellet samples collected under different over-expression conditions. Lane 1: control supernatant at 37°C, lanes 2 and 3: IPTG induced pellet and supernatant respectively at 37°C, lanes 4 and 5: IPTG induced pellet and supernatant respectively at 25°C, lanes 6 and 7: IPTG induced pellet and supernatant respectively at 20°C, lanes 8 and 9: IPTG induced pellet and supernatant respectively at 18°C, and lane 10: pre-stained protein ladder.

4.3.2. Purification of recombinant wild-type *Ld*DOHH protein:

The wild-type 6xHis-tagged *Ld*DOHH protein was purified by Ni-NTA agarose affinity chromatography and found over-expressed bands in almost all fractions corresponding to all the purification steps. The elutions corresponding to the 10 mM, 20 mM, 50 mM and 100 mM imidazole concentrations contained gradually decreasing amounts of impurities, with the increasing imidazole concentration, and we obtained pure form of *Ld*DOHH protein, with the 250 mM imidazole elution (figure 4.4). The elution fractions obtained from the 250 mM imidazole wash contained protein corresponding to a single band of 37 kDa size on the SDS-PAGE gel.

The purified wild-type 6xHis-tagged *Ld*DOHH protein was subjected to TEV protease digestion, followed by dialysis against purification buffer. From the 6xHis-tagged *Ld*DOHH-TEV protease protein digestion reaction mixture, the wild-type non-tagged *Ld*DOHH protein was purified by using the same Ni-NTA column as explained in the methods section. We have observed a protein band migrated little faster than the 6xHis-tagged protein, indicating the removal of 6xHis-tag from the protein and resulting in the recombinant wild-type non-tagged *Ld*DOHH protein (figure 4.5).

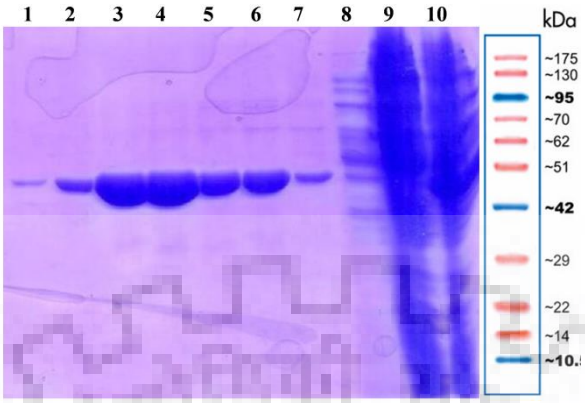

Figure 4.4: The SDS-PAGE profile of the wild-type 6xHis-tagged *Ld*DOHH protein purification carried out by Ni-NTA affinity chromatography. Lanes 1-7: elutions with imidazole concentrations, lane 8: lysis buffer wash, lane 9: crude flow through and lane 10: crude extract.

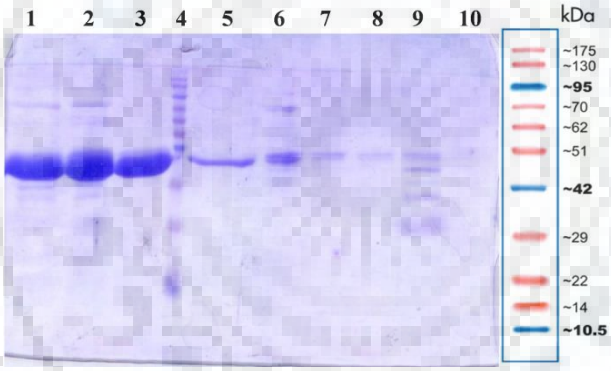

Figure 4.5: The SDS-PAGE profile of the wild-type non-tagged *Ld*DOHH protein purification carried out by Ni-NTA affinity chromatography after 6xHis-affinity tag cleavage from the affinity-tagged protein by the TEV protease. Lanes 1 and 2: undigested 6xHis-tagged *Ld*DOHH protein, lane 3: flow through sample containing the digested 6xHis-tag free *Ld*DOHH, lane 4: protein ladder, lane 5: wash with purification buffer, lanes 6-8: elution fractions collected from low imidazole concentration washes, and lanes 9-10: elution fractions collected from high-concentration imidazole washes.

The purified protein fractions from the affinity chromatography step, were concentrated and loaded onto 120 mL HiLoad 16/600 Superdex 200 pg gel filtration column, and we have observed a single major peak at ~82 mL elution volume (corresponding to a molecular weight of ~40 kDa) with a leading edge shoulder at ~75 mL column elution volume and expected to be the position for *Ld*DOHH monomer of 37-kDa molecular weight (figure 4.6). The elution fractions collected from the column contained purified protein bands of ~37 kDa size, without

any impurities, when checked by SDS-PAGE, while they displayed a different band separation profile when analysed by native gel electrophoresis (native PAGE).

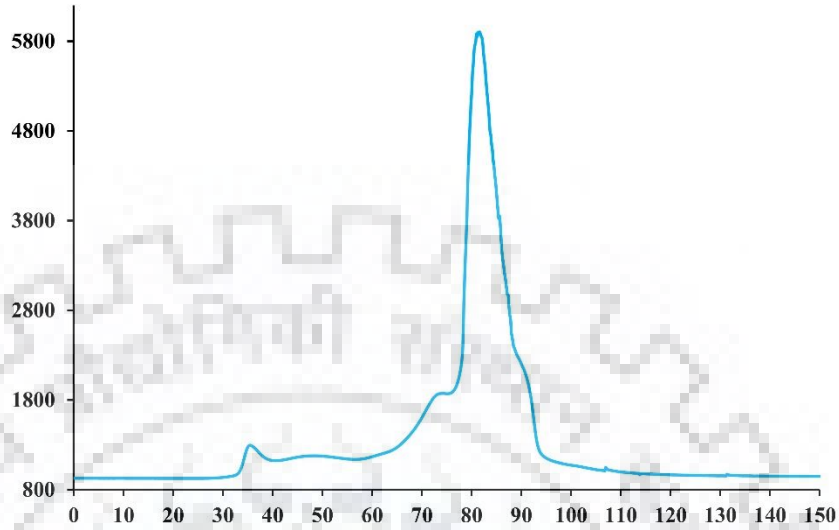

Figure 4.6: The size exclusion chromatography profile of the wild-type non-tagged *Ld*DOHH protein purification carried out by using Superdex 200 pg gel filtration column.

4.3.3. Separation of apoenzyme and holoenzyme forms of wild-type *Ld*DOHH protein:

When the purified protein fractions from the affinity chromatography step were analysed by the native PAGE, we have observed two major/predominant protein species/bands corresponding to two different conformations/states of the wild-type *Ld*DOHH protein. The more diffusive and slow-migrating band (hereafter it will be named as band 1) corresponding to the apoenzyme species, while the fast moving and sharp band (hereafter it will be named as band 2) belongs to the holoenzyme form/species of the protein (figure 4.7A). The apoenzyme form is the *Ld*DOHH protein without bound iron, while the holoenzyme form contains bound iron which confers a molecular conformation different from that of the apoenzyme. These two different conformational states of *Ld*DOHH protein were separated from each other by gel filtration purification. When the gel filtration elution fractions corresponding to the major peak were run on native PAGE we have observed band 2 in dominant form in most of the center fractions with negligible size band 1, while the elution fractions corresponding to the early shoulder exhibited band 1 in dominant size with negligible amounts of band 1 (figure 4.7B). The shoulder fractions were pooled and concentrated in order to obtain pure apoenzyme form,

while the centre fractions of the major peak were concentrated together to obtain pure form of holoenzyme.

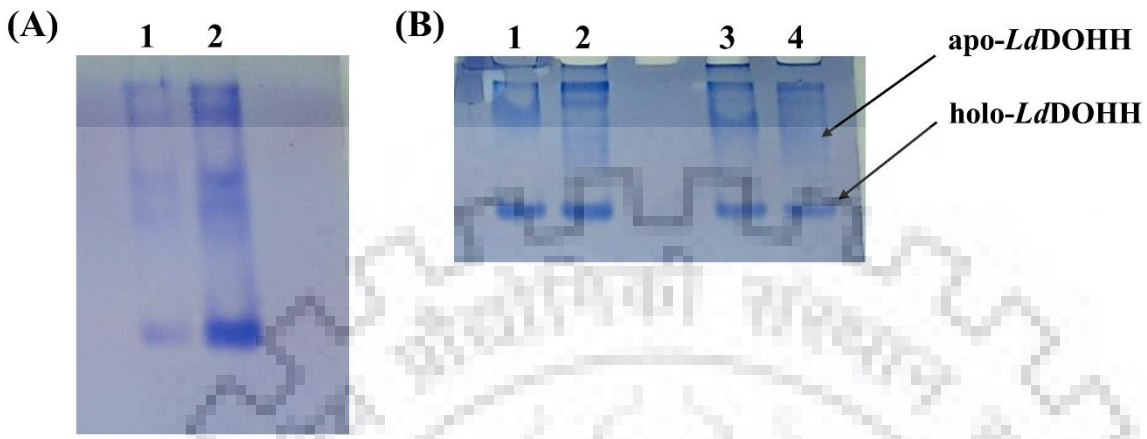

Figure 4.7: The native PAGE profile of the wild-type non-tagged *Ld*DOHH protein. **(A).** Protein samples from the Ni-NTA affinity chromatography. **(B).** The native PAGE profile of the *Ld*DOHH protein elution fractions obtained from the Superdex 200 pg gel filtration column.

4.3.4. Crystallization of wild-type *Ld*DOHH:

The *Ld*DOHH protein crystallization experiments were carried out by hanging and sitting drop vapor diffusion methods as explained in the methods section. We obtained very much irregular shaped tiny crystals (figure 4.8), in one of the manually prepared crystallization condition containing 50 mM tris buffer pH 7.4, 0.1 M calcium chloride, and PEG4000 precipitant. But these crystals were of very poor quality that diffracted only to 15 A˚ with very less number of reflection spots. Several cryo-protectants were used to improve the diffraction quality from those crystals, but no positive results gained. Many crystallization conditions and methods were also employed to improve the crystals' quality and size, and ended up with similar quality crystals.

Figure 4.8: The tiny crystals of poor quality obtained for wild-type non-tagged *Ld*DOHH protein.

4.3.5. Protein disorder and crystallizability prediction and analysis:

We have observed certain intrinsically disordered regions in the wild-type *Ld*DOHH protein, which were analysed by using different software tools as explained in the methods section. These regions mainly include the N-terminal and C-terminal regions of the protein, Met1 – Glu11 and Phe315 – Ala326 respectively, which are not participating in the stable secondary structural elements (α-helices or β-sheets), and forming only the flexible loops, while another major disordered region, Lys146 – Glu177, identified in the *Ld*DOHH protein includes the parts of inter-domain loop connecting the two structural domains of this protein (figure 4.9). These disordered regions forming loops at the both termini of the protein and inter-domain regions are found to be flexible and hence need to be truncated in order for the protein to be structurally stabilized and subsequently crystallized.

A

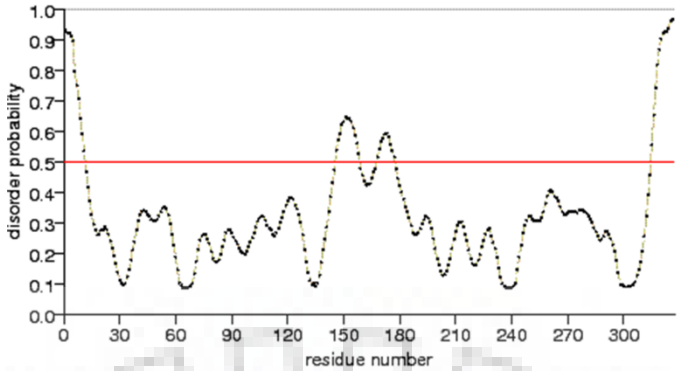

B

```
1   MSALNSRTVE EVRKDYAKLL DPQEPLDSRM RELYRLKEDC LKTAAGVTVI 50
51  LETIDTTDSV LLQHELAYNA GQSGREEAVP ELERILRTTS YDVVTRHEAA 100
101 EALGAIGSPL ALQVLEAHSD PTTEPEAPIR ETCELALARI AMKETKGDAA 150
151 VAPPSGCEFV SVDPSPAFSA LYSSTDEPVP HTVEELEAVL LDTSGRTRLF 200
201 RRYMAMFTLR NLATEAAVAA LCRGLREDNV SALFRHEVAF VLGQLERPSS 250
251 QPALIAALKD EEEAPMVRHE AAEALGAIAD PATLPVLESY ATHHEPIVRD 300
301 SCVVALEMHK YWANFNGLAH QQQQEA 326
```

Figure 4.9: PrDOS prediction of disorder regions in the wild-type *Ld*DOHH protein. **(A)** the disorder probabilities plot of *Ld*DOHH predicted by PrDOS web server. **(B)** the *Ld*DOHH protein sequence with the disordered protein regions highlighted by color coding.

The crystallizability of the wild-type *Ld*DOHH protein was also predicted by XtalPred web server and this protein was classified to be Expert pool (EP) crystallizability class 4 and Random forest (RF) crystallizability class 11 (figure 4.10). These crystallizability class analyses are indicating that the *Ld*DOHH protein belongs to a least promising crystallizable class with overall combined class score of 5.

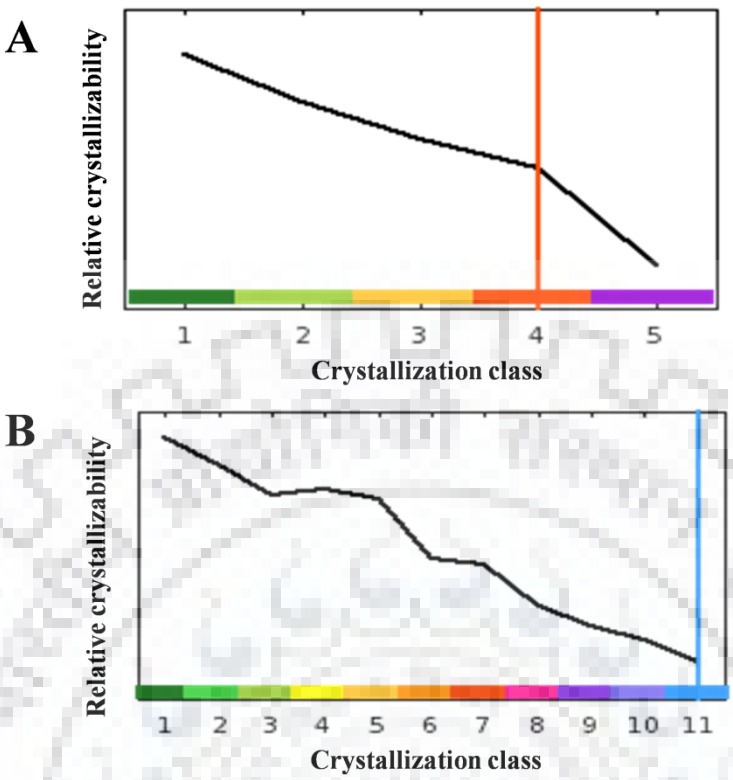

Figure 4.10: Crystallizability prediction for the wild-type *Ld*DOHH protein by Xtalpred web server. **(A)** the relative crystallizability of *Ld*DOHH protein by EP class prediction **(B)** the relative crystallizability of *Ld*DOHH protein by RF class prediction.

4.3.6. Constructing the *Ld*DOHHΔ3, *Ld*DOHHΔ6 and *Ld*DOHHΔ9 protein truncates:

The DNA oligo primers were designed for *Ld*DOHHΔ3, *Ld*DOHHΔ6 and *Ld*DOHHΔ9 protein truncates and PCR amplied using the wild-type full length *lddohh* gene carrying pET28C-6xHis-TEVP-*dohh* plasmid as template. The PCR amplicons were ligated with the empty pET28C vector, after double restriction endonuclease digestion, keeping the N-terminal 6xHis-affinity tag with the TEV protease digestion site. The ligated products were successfully transformed into *E. coli* DH5α cells, followed by confirmation of the clones by restriction digestion using the respective endonuclease enzymes, and also by PCR amplification, where we have observed a DNA band of ~1Kb corresponding to the size of the truncated gene amplicons (figure 4.11). The nucleotide sequences of the truncated genes were also confirmed by gene sequencing.

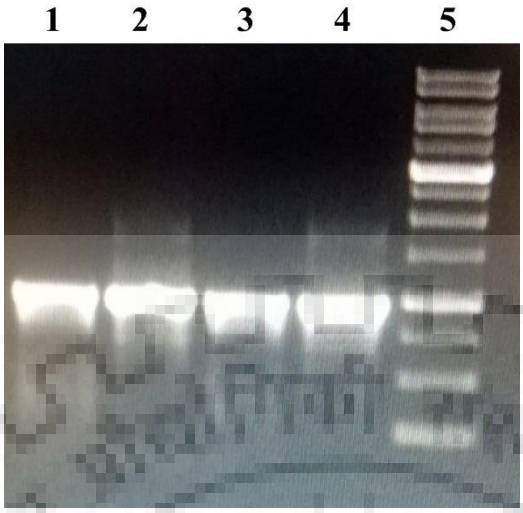

Figure 4.11: PCR amplification of the truncated *lddohh* genes. Lanes 1-4: the gene amplicons of *lddohh*Δ*3*, *lddohh*Δ*6*, *lddohh*Δ*9* and wild-type *lddohh* genes respectively. Lane 5: 1 kb DNA ladder.

4.3.7. Over-expression and purification of the DOHH protein truncates:

The recombinant *lddohh*Δ*3*-6xHis-TEV-pET28C, *lddohh*Δ*6*-6xHis-TEV-pET28C and *lddohh*Δ*9*-6xHis-TEV-pET28C plasmid constructs containing the *dohh*Δ*3*, *dohh*Δ*6* and *dohh*Δ*9* gene truncations respectively were transformed successfully into *E. coli* BL21 DE3 cells, and the transformed *E. coli* BL21 DE3 cells were confirmed to be over-expressing a soluble 6xHis-affinity-tagged *Ld*DOHHΔ3, *Ld*DOHHΔ6 and *Ld*DOHHΔ9 protein truncates respectively, which was observed by the ~37 kDa bands in the SDS-PAGE gel.

The recombinant 6xHis-affinity-tagged *Ld*DOHHΔ3, *Ld*DOHHΔ6 and *Ld*DOHHΔ9 proteins were purified by Ni-NTA agarose affinity chromatography followed by the size exclusion chromatography and obtained homogeneous proteins that were concentrated and used for crystallization studies. The non-tagged truncated proteins were also purified in the similar way explained for the wild-type full length protein and separated from each other by same method.

4.3.8. Crystallization of truncated proteins:

All the three truncated *Ld*DOHHΔ3, *Ld*DOHHΔ6 and *Ld*DOHHΔ9 proteins were used for crystallization by the different protocols explained in the methods section. The crystallization trials are still underway and I haven't obtained any hit condition for the growth of *Ld*DOHH crystals.

4.3.9. CD spectroscopy studies:

The wild-type *Ld*DOHH protein was analysed for its biochemical attributes, including thermal stability, resistance towards the protein denaturants, and buffer and ionic strength sustainability, by the circular dicroism spectroscopy. The CD spectrogram of the wild-type protein was showing that the protein is exclusively containing α-helices and loops only, and it doesn't contain β-sheets or any other protein secondary structural elements. The thermal analysis results are showing that the protein is structurally stable upto 45°C temperature and above which it is losing its structural integrity, and the Tm value of the protein was calculated to be 43°C (figure 4.12).

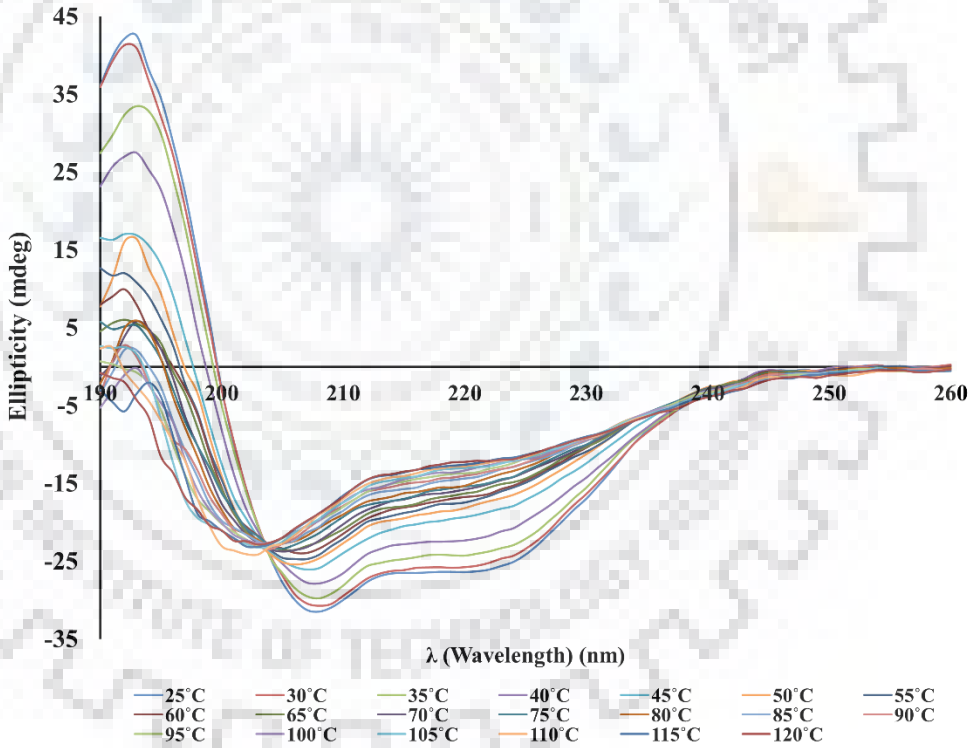

Figure 4.12: Thermal analysis studies of the wild-type *Ld*DOHH protein by CD spectroscopy. The analysis was carried in the temperature range of 25°C till 120°C, at an interval of 5°C. The spectrographs corresponding to each temperature are color labeled and indicated at the bottom of the graphs.

The results from the spectroscopic analysis of the protein's stability to denaturants are showing that the protein can withstand up to 1 M urea and 1 M guanidinium hydrochloride (GnHCl) concentrations, and its losing its secondary and tertiary structural features upon increasing their concentrations further (figure 4.13A and 4.13B). The affect of pH on the protein structural stability was also assessed in the range of 4.0 to 9.0 and the corresponding results are showing that the pH 4.0 is harmful for the protein as its getting denatured and losing structural features (figure 4.13C). The protein is structurally stable in the pH range of 5.0 to 9.0. The sustainability of the protein to ionic strength was also analysed by using the increasing concentrations of the sodium phosphate buffer pH 7.4 from 0.02 M to 1.0 M. Results from these studies are showing

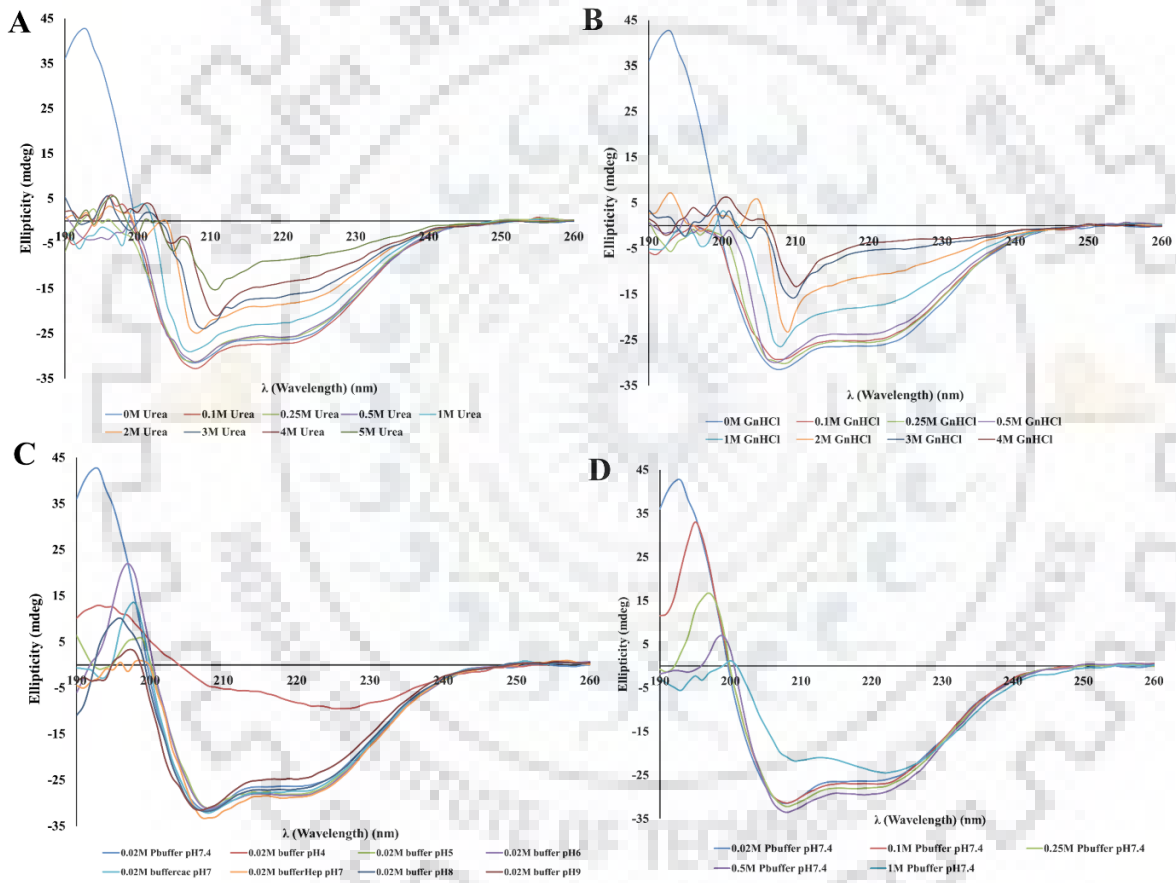

that the protein is structurally behaving well in the ionic strength range of 0.02 M to 0.5 M, but becoming unstable at the buffer concentration of 1.0 M (figure 4.13D).

Figure 4.13: The CD spectroscopic analysis of the different biochemical attributes of *Ld*DOHH protein. **(A).** and **(B).** are showing the denaturant stability of the protein in presence of the increasing concentrations of urea and GnHCl respectively. **(C).** and **(D).** are showing the pH stability analysis and the ionic strength sustainability of the protein respectively.

4.3.10. *Ld*DOHH sequence analysis:

The sequences from different protozoans (including few trypanosomatids), human, fungal, plant and animal species were compared and analysed for their characteristic features. It was found that *Ld*DOHH protein sequence has few insertions when compared to human counterpart, which were found in few other protozoans also, especially other trypanosomatids (figure 4.14). One of these insertions, which is 9-amino acid long from Tyr172 to Pro180, was found to be playing functional roles in the enzyme activity of the protein, proved by earlier research.

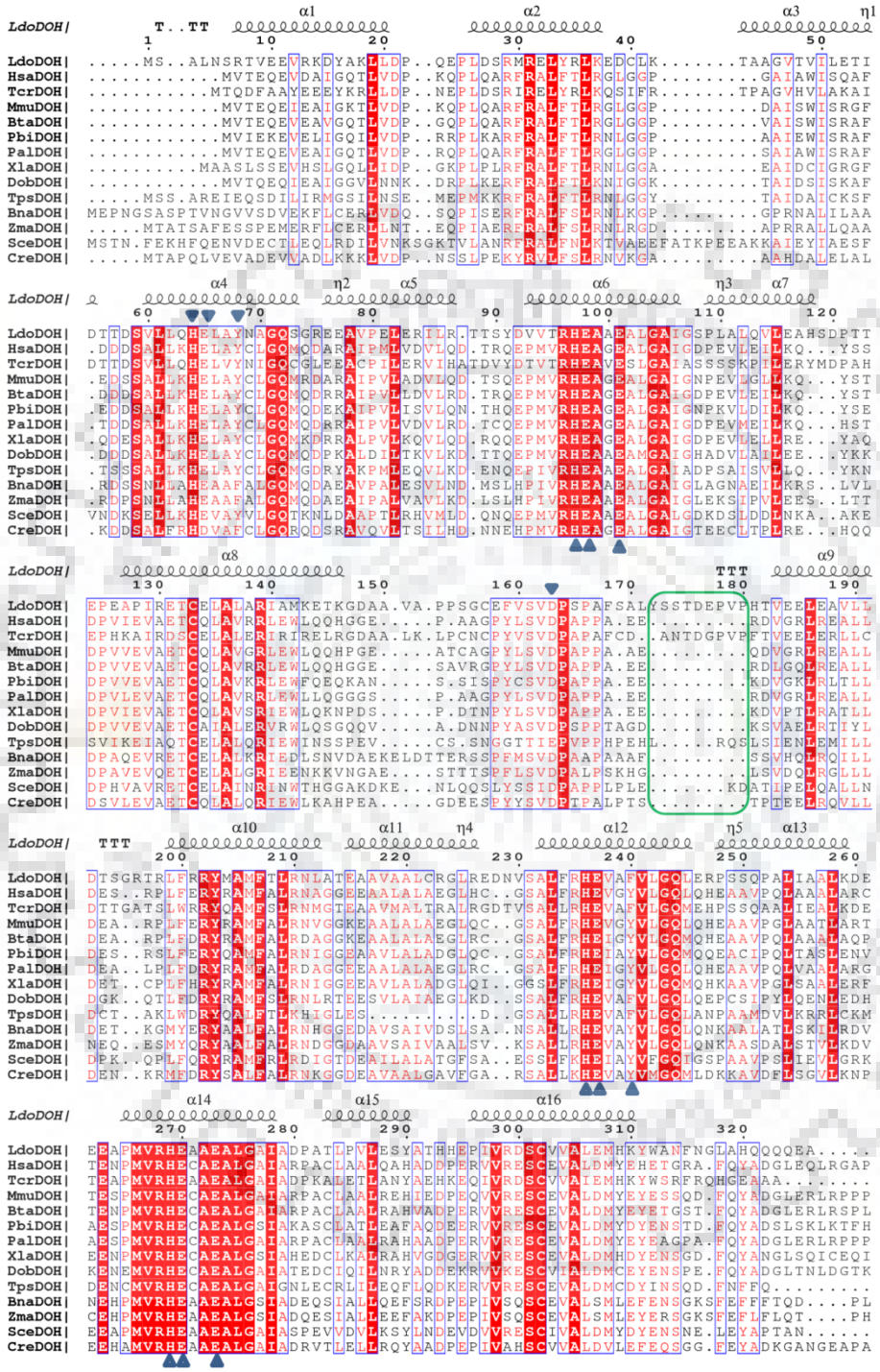

Figure 4.14: multiple sequence alignment of the *Ld*DOHH protein. Completely conserved residues are shown in red boxes with white characters, while the residues in the white boxes with red characters are relatively conserved. The amino acid sequence corresponding to the major insertion is highlighted by the green colored box. The His-Glu motifs (HE motifs) and the catalytic residues are pointed by blue coloured solid triangles. Secondary structural

elements of DOHH protein are labeled above the sequences. The amino acid sequences of DOHH protein from different protozoan, human, plant and animal species were collected as explained in the methods section.

4.3.11. *Ld*DOHH molecular modeling:

The amino acid sequence of wild-type *Ld*DOHH protein was modeled using the crystal structure of human DOHH protein (PDB ID: 4D4Z) as template and by using the autodock tools and autodock vina as explained in the methods section. We have obtained 10 models and validated all of them by SAVES server to choose the best model. The overall structure of the *Ld*DOHH protein is depicted in figure 15 and its validation reports are in figure 16. The *Ld*DOHH protein model chosen for structural analyses has more than 91% of residues in the most favored regions, according to the Ramachandran plot statistics obtained from the PROCHECK program and has an overall quality factor of 71 which was assessed by the ERRAT2 program. These validation parameters are indicating that the model is of enough quality that can be used for further structural studies. I have also modeled the *Ld*DOHH sequence using other molecular modeling tools including Phyre2, but models of poor quality were obtained from these programs.

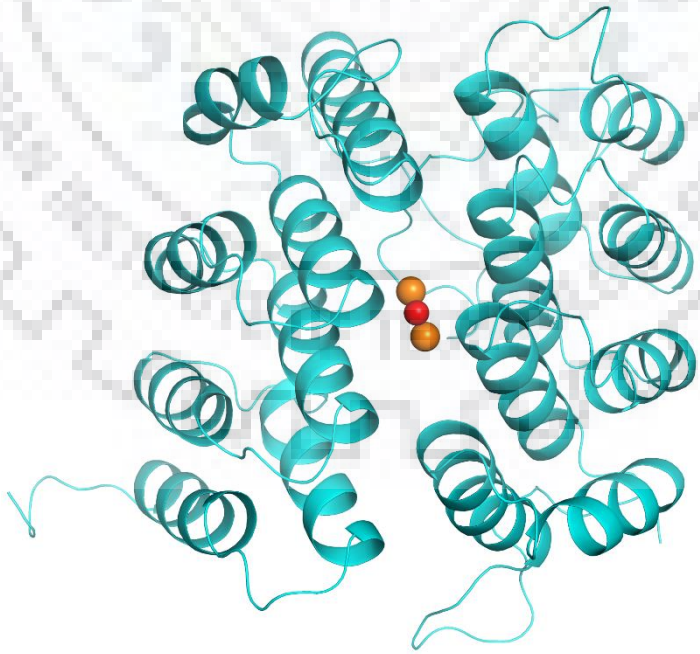

Figure 4.15: The 3-D structural model of wild-type *Ld*DOHH protein. The polypeptide chain is colored in cyan, and the iron atoms and active site oxygen are labeled orange and red respectively.

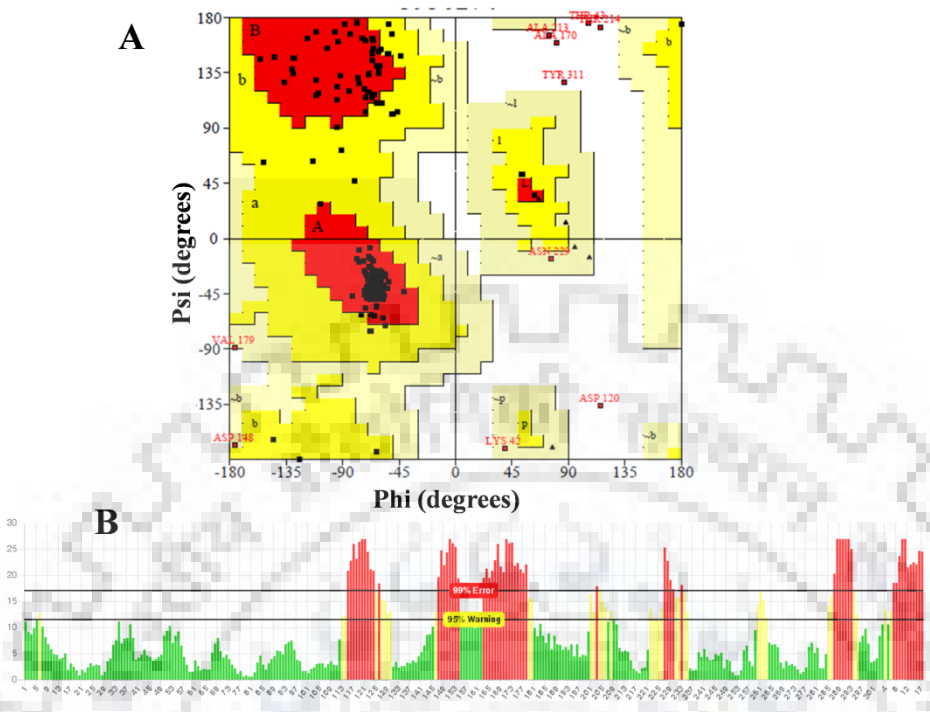

Figure 4.16: Validation of the 3-D structural model of wild-type *Ld*DOHH protein by the SAVES server tools. **(A).** and **(B).** are showing the Ramachandran plot analysis and the ERRAT plot analysis of the protein model.

4.3.12. *Ld*DOHH structure analysis:

The *Ld*DOHH protein structure was analysed for all its structural elements and their arrangement in the 3-D space. The structure was found to contain majorly the α-helical secondary structural elements that are arranged in hairpins, which in turn arranged into two identical structural domains connected by a flexible long loop. Each domain is having 4 pairs of α-helices, i.e four α-helical hairpins, and hence the overall structure has eight α-helical hairpins (eight α-helical pairs) (figure 4.17) (table 4.1). This structural arrangement of the α-helical pairs in the *Ld*DOHH protein resembles the α-helical tandem repeats of the HEAT-repeat protein and hence was classified as a member of this protein family.

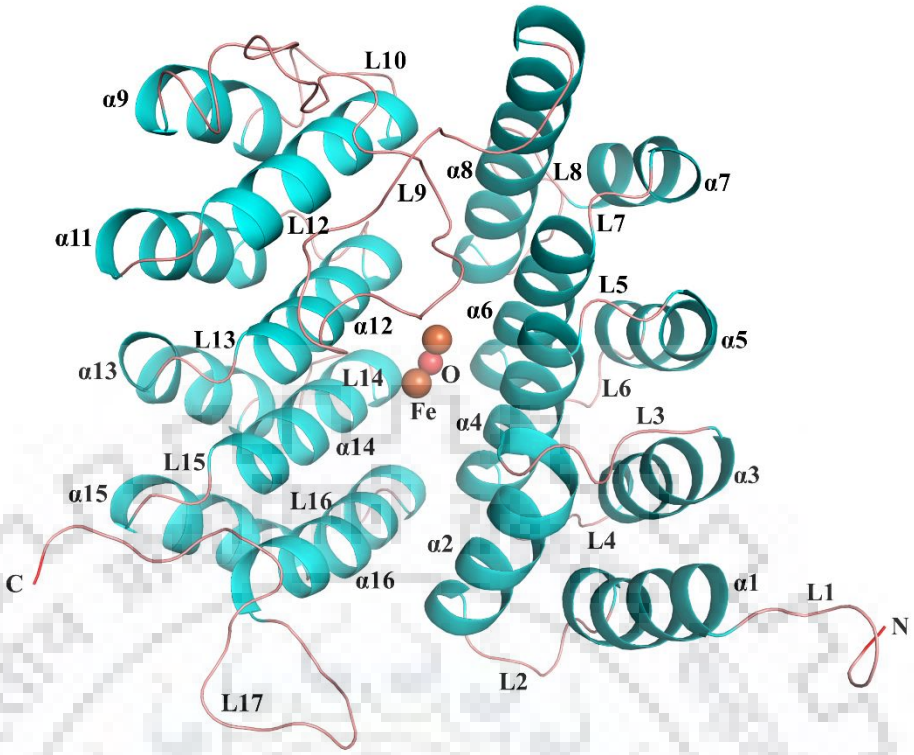

Figure 4.17: The secondary structural elements of *Ld*DOHH protein model. The helices and loops are color labeled by cyan and grey respectively. The bound iron and oxygen atoms are also shown in the diagram in the spheres.

Table 4.1: The list of secondary structural elements of *Ld*DOHH protein. The loop and helices are labeled with the Ln and Hn identifiers respectively.

Loops		Helices	
Loop Identifier	Residue Range	Helix Identifier	Residue Range
L1	Met1 - Ser6	H1	Arg7 – Leu20
L2	Asp21 – Phe25	H2	Leu26 – Glu38
L3	Asp39 – Thr43	H3	Ala44 – Asp55
L4	Thr56 – Ser59	H4	Val60 – Ser73
L5	Gly74 – Arg75	H5	Glu76 – Arg87
L6	Thr88 – Asp92	H6	Val93 – Ile106
L7	Gly107 – Ser108	H7	Phe109 – His118
L8	Ser119 – Glu126	H8	Ala127 – Lys146

L9	Gly147 – Thr182	H9	Val183 – Leu191
L10	Asp192 – Arg198	H10	Leu199 – Leu212
L11	Ala213 – Thr214	H11	Glu215 – Arg226
L12	Glu227 – Ser231	H12	Ala232 – Leu245
L13	Glu246 – Arg247	H13	Phe248 – Lys259
L14	Asp260 – Ala264	H14	Phe265 – Ile278
L15	Ala279 – Asp280	H15	Phe281 – Ala291
L16	Thr292 – Glu295	H16	Phe296 - Lys310
L17	Tyr311 – Ala326		

The *Ld*DOHH protein is compared with the human counterpart, *Hs*DOHH, and analysed for the active site architecture and catalytic residues. The His-Glu motifs are structurally aligned along with the other active site residues (figure 4.18). The differences in the length of the inter-domain loop, which is also called as connecting loop, are highleted in these structures.

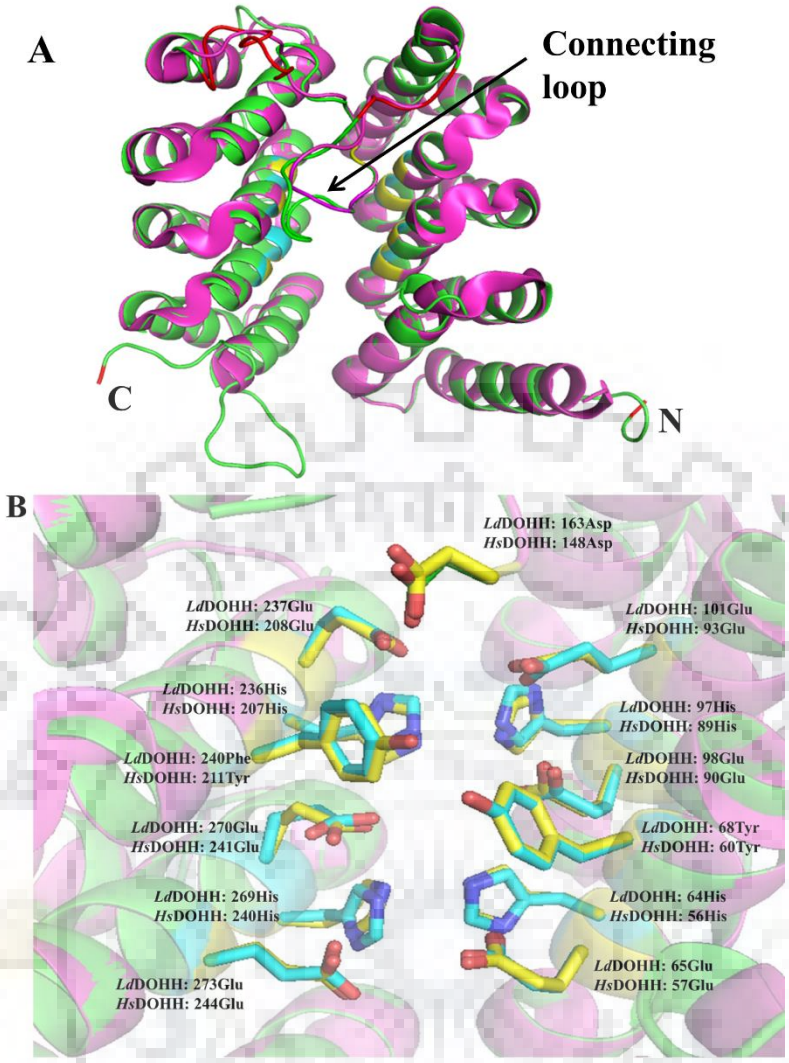

Figure 4.18: Comparison of the active site architecture of *Ld*DOHH and *Hs*DOHH. **(A).** Superposition of *Ld*DOHH model (Green) and *Hs*DOHH crystal (4D4Z: chainA) (Magenta) structures. The two insertion loops, D148-V151 and L171-P180, present in the connecting loop, are color coded (Red). **(B).** Structural superposition of His-Glu motifs and other key residues from *Ld*DOHH model (Green) and *Hs*DOHH crystal (4D4Z: chainA) (Magenta) structures. Residues are color coded: Cyan – *Ld*DOHH and yellow – *Hs*DOHH.

The coordination of the iron atoms within the active site of the protein was analysed and found that each iron atom is making three coordination bonds with the NE2 nitrogen atoms of the two histidine residues from two HE motifs and OE1 oxygen atom of one glutamate residue of one of the HE motifs at 2.4 Å distances (figure 4.19A). The deoxyhypusine binding within the active site and its interactions were analysed and depicted in the figure 4.19B.

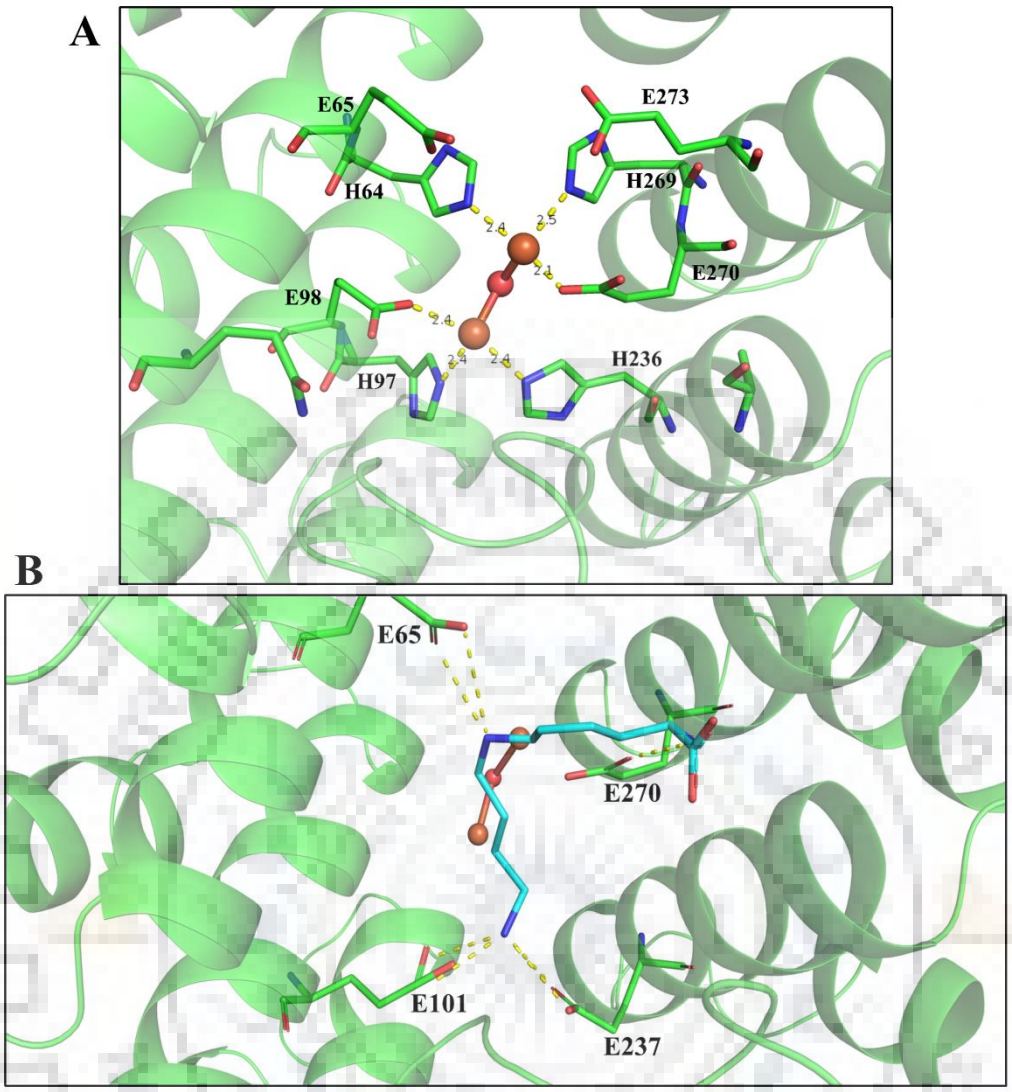

Figure 4.19: Iron coordination and the substrate deoxyhypusine interactions in the active site pocket of *Ld*DOHH. **(A).** Iron coordination by the HE motifs and other residues of *Ld*DOHH protein. The iron atoms are orange color labeled in sphere representation. **(B).** Substrate deoxyhypusine interactions in the active site pocket with the catalytic residues, diiron center, oxygen molecule, HE motifs, residues of inter-domain loop and insertion loop.

4.3.13. Pharmacophore modeling, virtual screening and molecular docking:

RLPG protocol generated 9 pharmacophore models by using the defined strategies and features of all these models are listed in the Table 4.2. ChEBI_lite_3star library of EBI databased with 46,125 molecules was screened through the first pharmacophore model because of it's high selectivity score. 1125 molecule were able to cross the pharmacophore filter. Out of them, 523 molecules cross the Lipinski filter. And 16 molecule shows the docking score comparable to hypusine. The list of molecules and their details are given in the table 4.3.

Table 4.2: The pharmacophore models, with their selectivity score, that were generated during pharmacophore modeling.

Phamacophore	No. of features	Feature set	Selectivity score
Pharmacophore_01	4	DPPP	10.912
Pharmacophore_02	4	APPP	9.9987
Pharmacophore_03	3	PPP	8.4839
Pharmacophore_04	3	DPP	8.0040
Pharmacophore_05	3	DPP	8.0040
Pharmacophore_06	3	DPP	8.0040
Pharmacophore_07	3	APP	7.0904
Pharmacophore_08	3	APP	7.0904
Pharmacophore_09	3	APP	7.0904

Table 4.3: The details of the compounds obtained with best docking scores from the virtual screening.

1	Compound 43 (CHEBI: 59621)	L-lysyl-D-alanine	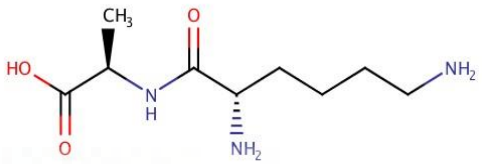
2	Compound 470 (CHEBI: 64339)	N(1)-aminoaminopropylagmatine	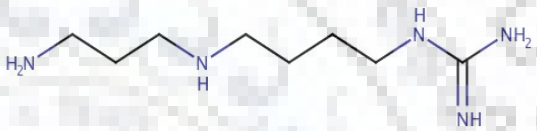
3	Compound 68 (CHEBI :61869)	N(6)-L-homocysteinyl-L-lysine	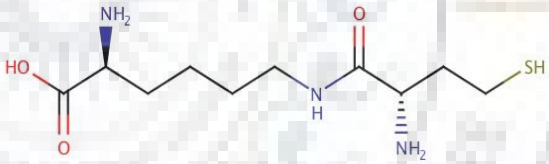
4	Compound Chebi (CHEBI: 17312)	N(1)-acetylspermine	
5	Compound 1071 (CHEBI: 63333)	L-arginyl-L-glutamic acid monoacetate	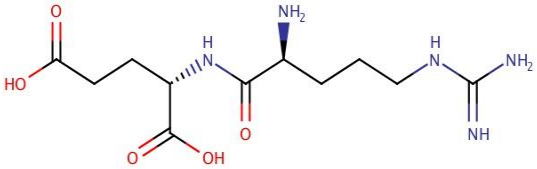

6	Compound 1157 (CHEBI: 57825)	L-lombricine dizwitterion	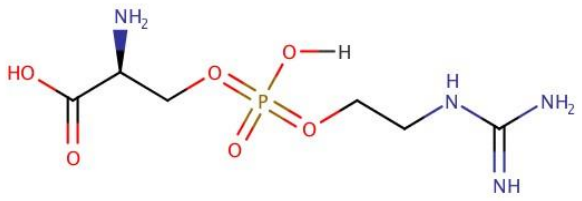
7	Compound 1366 (CHEBI: 58074)	D-nopalinate(1-)	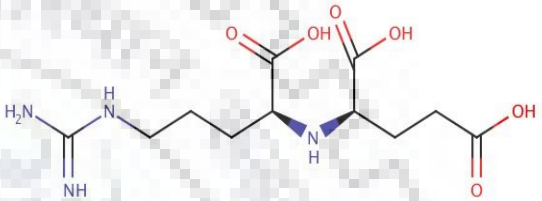
8	Compound 1827 (CHEBI: 47819)	N(5)-[amino(hydroxyimino)methyl]-L-ornithine	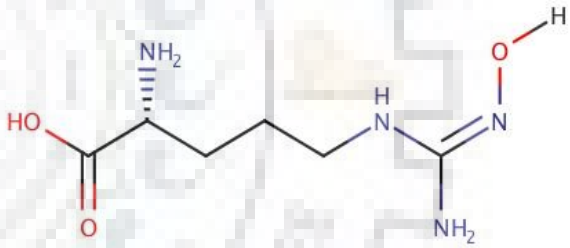
9	Compound 1911 (CHEBI: 48005)	gamma-L-glutamylputrescine	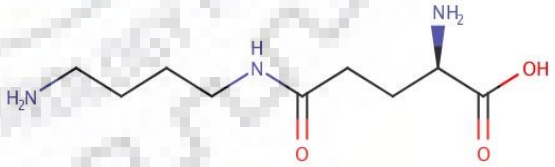

10	Compound 751 (CHEBI: 15949)	diphthamide	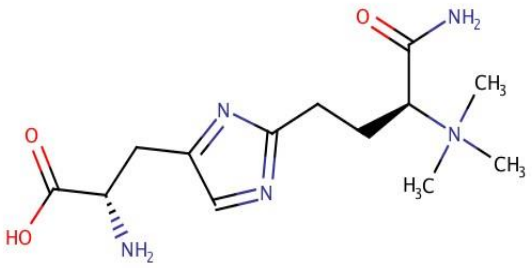
11	Compound 937 (CHEBI: 137738)	Val-Ala-Lys	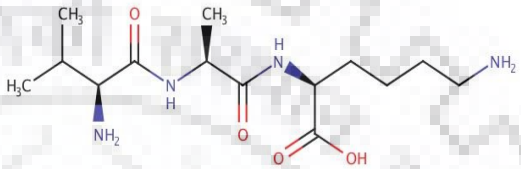
12	Compound 515 (CHEBI: 38153)	(R,R,R)-avenic acid A	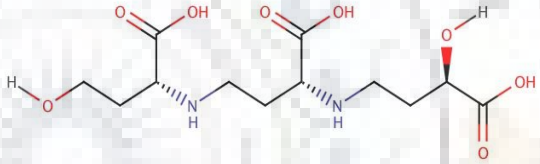
13	Compound 712 (CHEBI: 57304)	N(2)-(2-carboxyethyl)-L-arginine dizwitterion	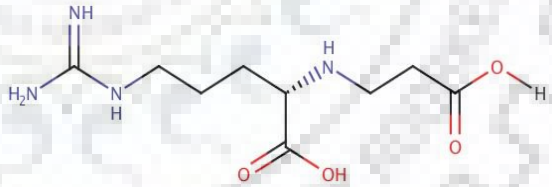
14	Compound 601 (CHEBI: 15746)	spermine	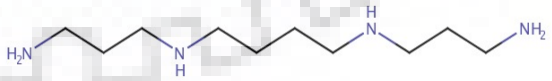

The molecules obtained from the virtual screening were subsequently docked in the active site of *Ld*DOHH model and analysed for their interactions. The interactions of these compunds are depicted in the following panels of figure 4.20. Maximum of the inhibitor interactions are observed with the active site histidine and glutamate (from the HE motifs), and tyrosine residues.

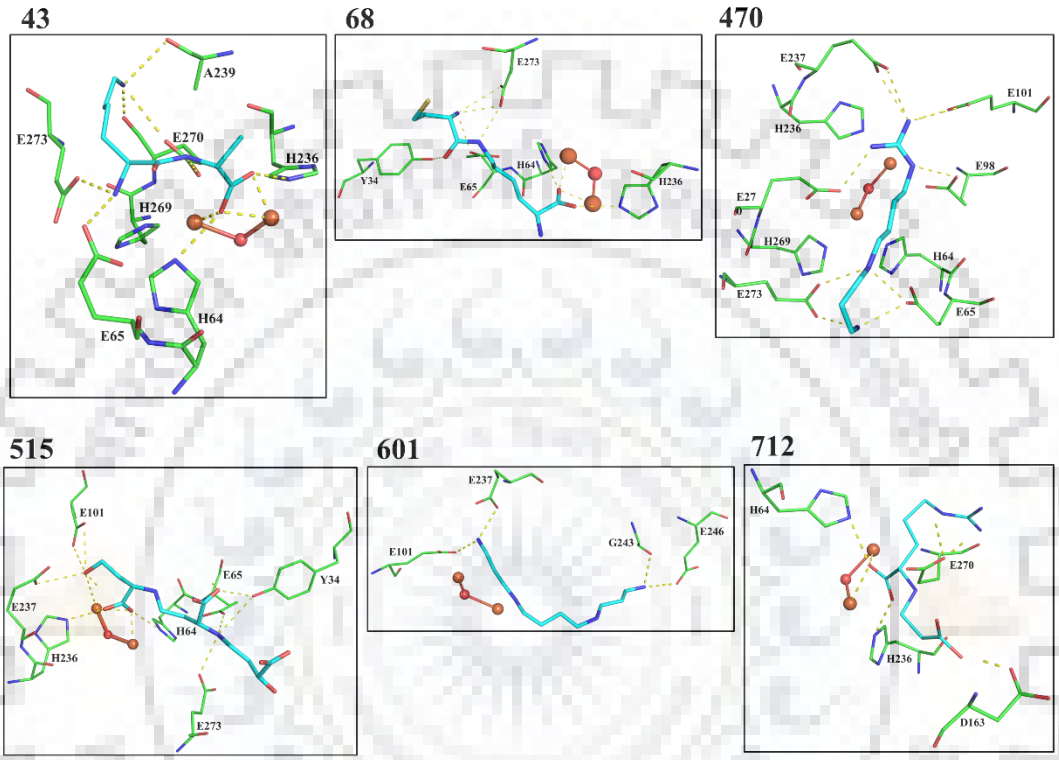

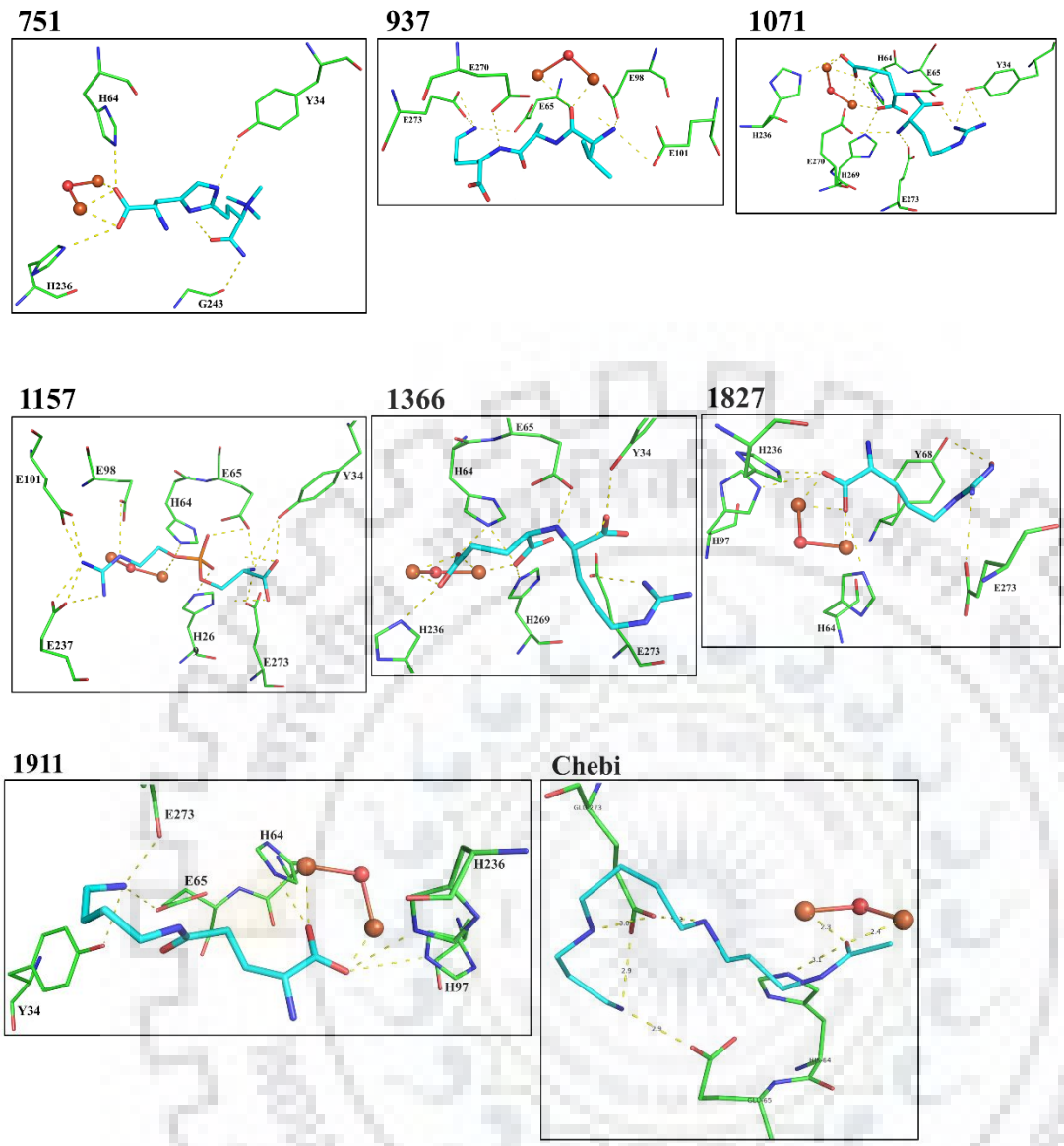

Figure 4.20: The protein-inhibitor interactions in the docked complexes. The panels of the *Ld*DOHH-inhibitor complexes are labeled by the inhibitor compound ID, on top of the panel. The inhibitor and protein residues are shown in stick representations with cyan and green colored respectively. The iron molecules are colored orange and shown with stick representation.

4.3.14. MD simulations:

The apo *Ld*DOHH, holo *Ld*DOHH and the complexes of the *Ld*DOHH protein model with the substrate deoxyhypusine and the inhibitor hit compounds, obtained from the virtual screening, were also analysed by molecular dynamics simulations for their binding and conformational stability. The results obtained from these studies are showing that iron atoms are stabilizing the structure of the holo *Ld*DOHH and without which the apo *Ld*DOHH protein is very much

unstable (figure 4.21). Simulations of the holo *Ld*DOHH are showing that the binding of iron atoms is stabilizing the structure with an RMSD of 0.45 $Å^2$.

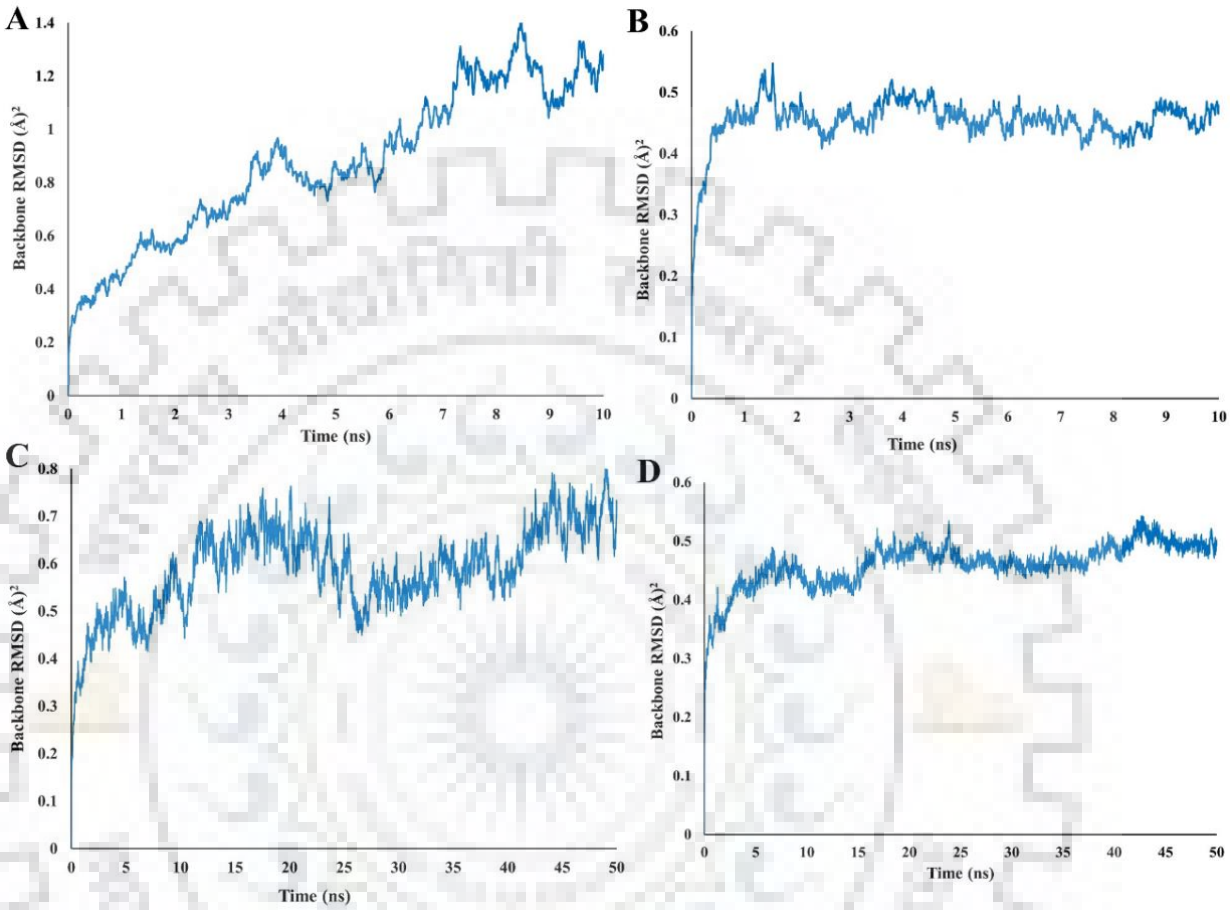

Figure 4.21: The MD simulations of the apo, holo, substrate-bound and inhibitor docked *Ld*DOHH complexes. **(A)**, **(B)**, **(C)** and **(D)** are showing the RMSD graphs of the simulations of the apo *Ld*DOHH protein, holo *Ld*DOHH, *Ld*DOHH-deoxyhypusine and *Ld*DOHH-43 complexes respectively.

The molecular docking analyses and MD simulation studies are showing that the binding of the inhibitor compounds 43 (figure 4.21D), 712 (figure 4.22C) and 1366 (figure 4.23A) within the active site of holo *Ld*DOHH protein are conformationally and structurally stabilizing the protein (figure 4.20). These compounds are also making extensive hydrogen bonding network in the active site of the protein.

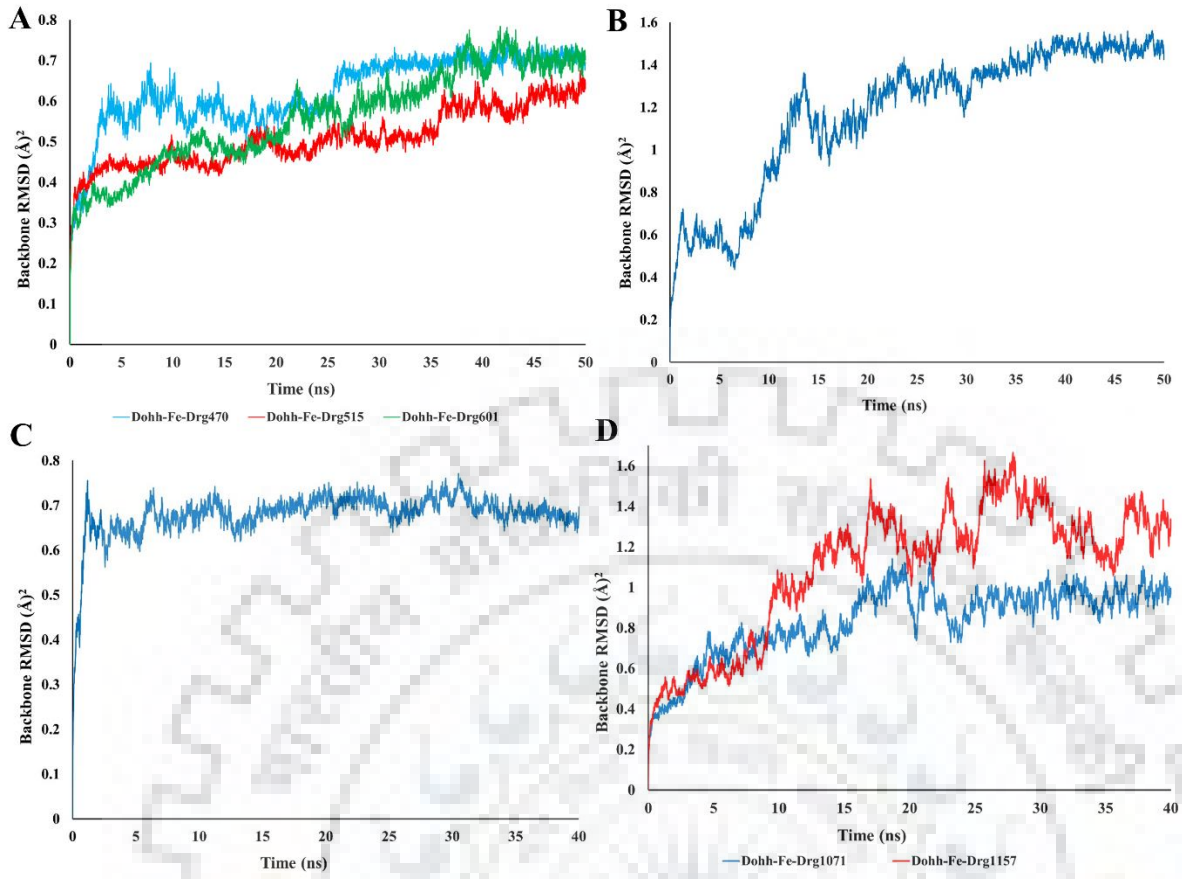

Figure 4.22: The MD simulations of the *Ld*DOHH-inhibitor docked complexes. **(A)** and **(D)** are showing the simulation of the complexes of the inhibitors labeled below the graphs. **(B)** and **(C)** are the MD graphs of the compounds 712 and 751 respectively.

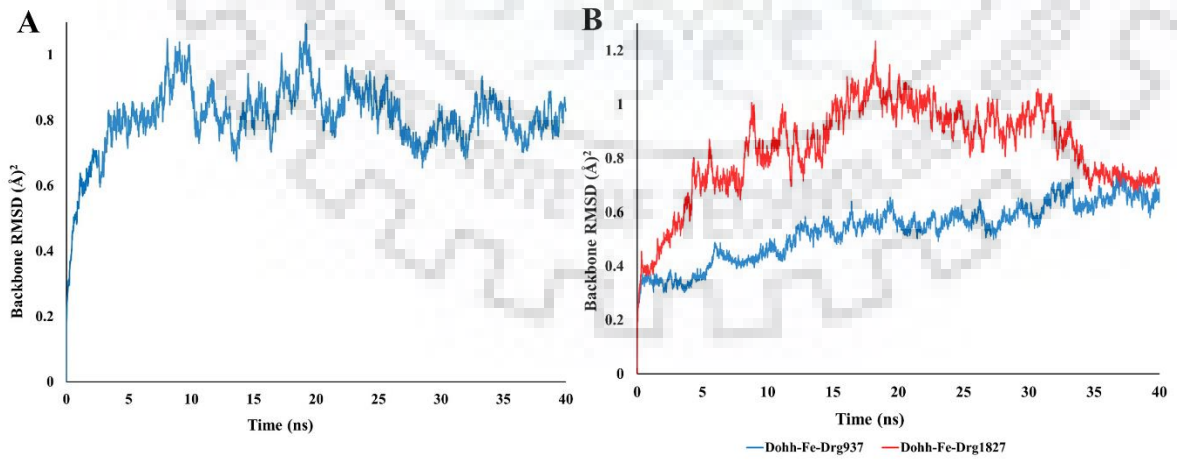

Figure 4.23: The MD simulations of the *Ld*DOHH-inhibitor docked complexes, part2. **(A)** showing the RMSD graph for the simulation of the *Ld*DOHH complex with the compound 1366. **(B)** showing the simulations of the *Ld*DOHH complexes with the compounds labeled at the bottom of the graph.

4.4. Conclusions:

The *Ld*DOHH protein was purified to highest homogeneity in His6-tagged and non-tagged forms, and used for crystallization experiments. We obtained poor quality crystals and subsequently the three different C-terminal truncations were made in order to increase the crystallization probabilities. The *Ld*DOHH protein was characterized biochemically for its oligomeric forms in solution and secondary structural contents. The protein was modeled and analysed by comparing with its human counterpart, and found certain loop insertions which are structurally differing at the active site regions. The protein model was also used for pharmacophore based virtual screening and obtained 16 hit compounds among which compounds 43, 712 and 1366 are stabilizing the structure by making intricate hydrogen bonding networks within the active site. Hence these molecules maybe further investigated for their anti-leishmanial activities.

The FabI, the isoform I of ENR, from *Moraxella catarrhalis* (*Mc*FabI) was characterized for its biochemical and structural molecular features using X-ray crystallography and other biochemical & biophysical tools. The crystal structures of *Mc*FabI protein in its apo and ternary complex forms, *Mc*FabI-NAD-TCL and *Mc*FabI-NAD-EST, were obtained and analysed for the active site elements in comparison with homologous proteins from other pathogenic bacteria and assessed for their usefulness in the understanding of designing broad-spectrum antimicrobials. The biochemical attributes of *Mc*FabI were also analysed and compared with the homologous proteins. By using the virtual screening tools, we obtained few inhibitor lead molecules and observed that the female sex hormone 17-β estradiol (E2) also binding with high energies in the active site of *Mc*FabI and hence their interactions were analysed biochemically and structurally. These analyses revealed that E2 is binding with a kD value of 5 µM to the enzyme and inhibiting its catalytic activity with a ki value of 38 µM. It is also observed that E2 is inhibiting 60% of the *M. catarrhalis* microbial growth at a concentration of 100 µM. These results are indicating that the direct antimicrobial actions of estradiol may be contributing to the sex differences in the resistance to infections in many species and supporting the well-established fact that females are more resistant to infections than their male counterparts.

Further studies have to be carried out to determine the in vivo antimicrobial actions of estradiol, within the physiological hormonal milieu, at its physiological concentrations. The studies have to be extended to other sex hormones also to confirm their antimicrobials roles and any similar contribution to sex differences in order to understand the roots of sex differences in resistance to infections. The antimicrobial roles of estradiol also have to be checked against other pathogenic bacteria. The structural features of the *Mc*FabI may be exploited in designing structure based broad-spectrum antimicrobials.

The OXA-58 structure was obtained in complex with the carbapenem mimetic 6α-HMP in a stable acyl-enzyme species form. We analysed the structural features and observed the inward movements of α3/α5- and β6/β7-loops harboring the Phe113/Phe114 and Met225 residues, respectively, involving in the formation of a hydrophobic bridge over the active site upon binding of the carbapenem mimetic 6α-HMP. The loop movements trigger the realignment of the side chains of those residues and forms the hydrophobic bridge which plays roles in

substrate recognition and subsequent catalysis. These features of the OXA-58-6α-HMP acyl-enzyme complex, are indicating that the plasticity of the active site elements is essential for the β-lactam recognition and its catalysis by the OXA-58 β-lactamase enzyme. The three different conformations observed for the side chain hydroxyl group of the hydroxyalkyl side chain of the carbapenem β-lactams and their structural mimetics play crucial roles in the substrate recognition by the β-lactamase enzymes. These three conformations (two rotamers of 6α-HMP and the virtually identical rotamers of meropenem and doripenem) are indicating the conformational sampling of the side chain hydroxyl group of the hydroxyalkyl moiety and also showing a sequence of key events that may take place during the carbapenem catalysis that is going to happen subsequently. A deacylation step in β-lactam catalysis by OXA β-lactamases requires that a water molecule be in hydrogen bond distance from the carboxylysine active-site residue (Lys-86) and the carbonyl moiety of the acyl-enzyme species. The proposed flow of catalytic events suggests that class D β-lactamases may have acquired carbapenemase activity by selecting a rotamer conformation that allows not simply retention of the deacylating water molecule but its retention in the position between the carboxylysine and the carbonyl of the acyl-enzyme complex, as required for catalytic deacylation.

The crystal structures obtained for the K86A, F113A, F114I, M225A and M225T point mutations of *Ab*OXA-58 are showing that the hydrophobic bridge is formed even in the absence of one of the phenyl alanine residues or the mutated methionine residues. And the hydrophobic bridge formation over the active sites of mutant proteins is supporting the results showing the catalytic activity of these proteins and concluding that these point mutant proteins of *Ab*OXA-58 are catalytically activity but with decreased catalytic efficiencies. Further studies are needed to confirm the active site plasticity and catalytic activity (β-lactam hydrolysis) retention in the presence of other point mutation variants including Ile260 mutations and double mutants including the simultaneous mutation of the residues from both the α3/α5- and β6/β7-loops. The understanding of these catalytic features of OXA-58 also helps in making strategies in designing structure based novel inhibitors against the carbapenemases.

The DOHH protein from *Leishmania donovani* (*Ld*DOHH) protein was purified to highest homogeneity in His6-tagged and non-tagged forms, and characterized biochemically for its oligomeric forms in solution and secondary structural contents. We obtained poor quality crystals and subsequently the three different C-terminal truncations were made in order to increase the crystallization probabilities, but haven't got the crystals and protein diffraction yet. The protein was modelled and analysed by comparing with its human counterpart, and found

certain loop insertions which are structurally differing at the active site regions. The protein model was also used for pharmacophore based virtual screening and obtained 16 hit compounds among which compounds 43, 712 and 1366 are stabilizing the structure by making intricate hydrogen bonding networks within the active site. Hence these molecules maybe further investigated for their anti-leishmanial activities. Further crystallization optimization experiments have to be carried out to obtain the crystal structure of *Ld*DOHH which may further help us in discovering structure based anti-leishmanial drugs.

1. Sender R, Fuchs S, Milo R. 2016. Are We Really Vastly Outnumbered? Revisiting the Ratio of Bacterial to Host Cells in Humans. Cell 164:337–340.

2. Daszak P, Cunningham AA, Hyatt AD. 2000. Emerging Infectious Diseases of Wildlife-Threats to Biodiversity and Human Health. Science 287:443–449.

3. GBD 2013 Mortality and Causes of Death Collaborators. 2015. Global, regional, and national age–sex specifi c all-cause and cause-specifi c mortality for 240 causes of death, 1990–2013: a systematic analysis for the Global Burden of Disease Study 2013. Lancet 385:117–71.

4. Rice LB. 2008. Federal Funding for the Study of Antimicrobial Resistance in Nosocomial Pathogens: No ESKAPE. J Infect Dis 197:1079–1081.

5. Khan HA, Baig FK, Mehboob R. 2017. Nosocomial infections: Epidemiology, prevention, control and surveillance. Asian Pac J Trop Biomed 7:478–482.

6. Saxena AK, Azad CS. 2018. Neglected tropical bacterial diseases. Top Med Chem 29:169–244.

7. Savioli L, Daumerie D. 2017. WHO leadership is essential for the elimination of NTDs. Lancet 390:2765.

8. Domínguez-Andrés J, Joosten LA, Netea MG. 2019. Induction of innate immune memory: the role of cellular metabolism. Curr Opin Immunol 56:10–16.

9. Powers JH. 2004. Antimicrobial drug development – the past, the present, and the future. Clin Microbiol Infect 10:23–31.

10. Aminov R. 2017. History of antimicrobial drug discovery: Major classes and health impact. Biochem Pharmacol 133:4–19.

11. Kumar Sg, Adithan C, Harish B, Roy G, Malini A, Sujatha S. 2013. Antimicrobial resistance in India: A review. J Nat Sci Biol Med 4:286.

12. Takahashi Y, Tatsuma T. 2014. Metal Oxides and Hydroxides as Rechargeable Materials for Photocatalysts with Oxidative Energy Storage Abilities. Electrochemistry 82:749–751.

13. Magiorakos AP, Srinivasan A, Carey RB, Carmeli Y, Falagas ME, Giske CG, Harbarth S, Hindler JF, Kahlmeter G, Olsson-Liljequist B, Paterson DL, Rice LB, Stelling J, Struelens MJ, Vatopoulos A, Weber JT, Monnet DL. 2012. Multidrug-resistant, extensively drug-resistant and pandrug-resistant bacteria: An international expert proposal for interim standard definitions for acquired resistance. Clin Microbiol Infect 18:268–281.

14. Furtado GH, Nicolau DP. 2010. Overview perspective of bacterial resistance. Expert Opin Ther Pat 20:1273–1276.

15. Cox G, Wright GD. 2013. Intrinsic antibiotic resistance: Mechanisms, origins, challenges and solutions. Int J Med Microbiol 303:287–292.

16. Finch R, Hunter PA. 2006. Antibiotic resistance - Action to promote new technologies: Report of an EU Intergovernmental Conference held in Birmingham, UK, 12-13 December 2005. J Antimicrob Chemother 58:12–13.

17. Purrello SM, Garau J, Giamarellos E, Mazzei T, Pea F, Soriano A, Stefani S. 2016. Methicillin-resistant *Staphylococcus aureus* infections: A review of the currently available treatment options. J Glob Antimicrob Resist 7:178–186.

18. Gould IM. 2013. Treatment of bacteraemia: Meticillin-resistant *Staphylococcus aureus* (MRSA) to vancomycin-resistant S. aureus (VRSA). Int J Antimicrob Agents 42:S17–S21.

19. Hayakawa K, Marchaim D, Palla M, Gudur UM, Pulluru H, Bathina P, Alshabani K, Govindavarjhulla A, Mallad A, Abbadi DR, Chowdary D, Kakarlapudi H, Guddati H, Das M, Kannekanti N, Vemuri P, Doddamani R, Mundra VRR, Guddeti RR, Policherla R, Bai S, Lohithaswa S, Shashidharan SP, Chidurala S, Diviti S, Sukayogula K, Joseph M, Pogue JM, Lephart PR, Martin ET, Rybak MJ, Kaye KS. 2013. Epidemiology of vancomycin-resistant *Enterococcus faecalis*: A case-case-control study. Antimicrob Agents Chemother 57:49–55.

20. Lautenbach E, Polk RE. 2007. Resistant gram-negative bacilli: A neglected healthcare crisis? Am J Heal Pharm 64:3–22.

21. Cassir N, Rolain JM, Brouqui P. 2014. A new strategy to fight antimicrobial resistance: The revival of old antibiotics. Front Microbiol 5:1–15.

22. Younis W, Thangamani S, Seleem MN. 2015. Reporposing non-antimicrobial drugs and clinical molecules to treat bacterial infections. Curr Pharm Des 21(28):4106-4111.

23. Bassetti M, Righi E. 2015. New antibiotics and antimicrobial combination therapy for the treatment of gram-negative bacterial infections. Curr Opin Crit Care 21:402–411.

24. Bassetti M, Righi E. 2015. Development of novel antibacterial drugs to combat multiple resistant organisms. Langenbeck's Arch Surg 400:153–165.

25. Lounnas V, Ritschel T, Kelder J, McGuire R, Bywater RP, Foloppe N. 2013. Current Progress in Structure-Based Rational Drug Design Marks a New Mindset in Drug Discovery. Comput Struct Biotechnol J 5:e201302011.

26. Śledź P, Caflisch A. 2018. Protein structure-based drug design: from docking to molecular dynamics. Curr Opin Struct Biol 48:93–102.

27. Schneider G, Fechner U. 2005. Computer-based de novo design of drug-like molecules. Nat Rev Drug Discov 4:649–663.

28. Heifetz A, Barker O, Verquin G, Wimmer N, Meutermans W, Pal S, Law RJ, Whittaker M. 2013. Fighting obesity with a sugar-based library: Discovery of novel MCH-1R antagonists by a new computational-VAST approach for exploration of GPCR binding sites. J Chem Inf Model 53:1084–1099.

29. Winter A, Higueruelo AP, Marsh M, Sigurdardottir A, Pitt WR, Blundell TL. 2012. Biophysical and computational fragment-based approaches to targeting protein-protein interactions: Applications in structure-guided drug discovery. Q Rev Biophys 45:383–426.

30. Mashalidis EH, S´ledz´ P, Lang S, Abell C. 2013. A three-stage biophysical screening cascade for fragment-based drug discovery. Nature Protocols 8(11):2309-2324.

31. Doak BC, Norton RS, Scanlon MJ. 2016. The ways and means of fragment-based drug design. Pharmacol Ther 167:28–37.

32. Lee CH, Huang HC, Juan HF. 2011. Reviewing ligand-based rational drug design: The search for an ATP synthase inhibitor. Int J Mol Sci 12:5304–5318.

33. Acharya C, Coop A, Polli JE, MacKerell Jr AD. 2011. Recent Advances in Ligand-Based Drug Design: Relevance and Utility of the Conformationally Sampled Pharmacophore Approach. Curr Comput Aided Drug Des. 7(1):10–22.

34. Waring MJ, Arrowsmith J, Leach AR, Leeson PD, Mandrell S, Owen RM, Pairaudeau G, Pennie WD, Pickett SD, Wang J, Wallace O, Weir A. 2015. An analysis of the attrition of drug candidates from four major pharmaceutical companies. Nat Rev Drug Discov 14:475–486.

35. Murphy TF, Parameswaran GI. 2009. *Moraxella catarrhalis,* a Human Respiratory Tract Pathogen. Clin Infect Dis 49:124–131.

36. Wijers CDM, Chmiel JF, Gaston BM. 2017. Bacterial infections in patients with primary ciliary dyskinesia: Comparison with cystic fibrosis. Chron Respir Dis 14:392–406.

37. De Vries SPW, Van Hijum SAFT, Schueler W, Riesbeck K, Hays JP, Hermans PWM, Bootsma HJ. 2010. Genome analysis of *Moraxella catarrhalis* strain RH4, a human respiratory tract pathogen. J Bacteriol 192:3574–3583.

38. Wilkinson TMA, Aris E, Bourne S, Clarke SC, Peeters M, Pascal TG, Schoonbroodt S, Tuck AC, Kim V, Ostridge K, Staples KJ, Williams N, Williams A, Wootton S, Devaster JM. 2017. A prospective, observational cohort study of the seasonal dynamics of airway pathogens in the aetiology of exacerbations in COPD. Thorax 919–927.

39. Ramadan MO, Ibrahim IS, Shaheen AM, Ali WE. 2017. Significance of *Moraxella catarrhalis* as a causative organism of lower respiratory tract infections. Egypt J Chest Dis Tuberc 66:459–464.

40. Enright MC, McKenzie H. 1997. *Moraxella* (*Branhamella*) *catarrhalis* - clinical and molecular aspects of a rediscovered pathogen. J. Med. Microbiol. 46:360-371.

41. Verduin CM, Hol C, Fleer A, Dijk H van, Belkum A Van. 2002. *Moraxella catarrhalis*: from Emerging to Established Pathogen. Clinical Microbiology Reviews 15(1):125–144.

42. Murphy TF, Brauer AL, Grant BJB, Sethi S. 2005. *Moraxella catarrhalis* in Chronic Obstructive Pulmonary Disease. Am J Respir Crit Care Med 172:195–199.

43. Kaur R, Morris M, Pichichero ME. 2017. Epidemiology of Acute Otitis Media in the Postpneumococcal Conjugate Vaccine Era. Pediatrics 140:e20170181.

44. Ngo CC, Massa HM, Thornton RB, Cripps AW. 2016. Predominant bacteria detected from the middle ear fluid of children experiencing otitis media: A systematic review. PLoS One 11:1–26.

45. Gómez Garcés JL, Arbol Linde F. 1991. Pneumonia caused by *Branhamella catarrhalis*. A well- documented case. Enferm Infecc Microbiol Clin. 9(1):65-6.

46. Ariza-Prota MA, Pando-Sandoval A, García-Clemente M, Fole-Vázquez D, Casan P. 2016. Community-Acquired *Moraxella catarrhalis* Bacteremic Pneumonia: Two Case Reports and Review of the Literature. Case Rep Pulmonol 2016:1–3.

47. Ahmed A, Broides A, Givon-Lavi N, Peled N, Dagan R, Greenberg D. 2008. Clinical and laboratory aspects of *Moraxella catarrhalis* bacteremia in children. Pediatr Infect Dis J 27:459–461.

48. Sano N, Matsunaga S, Akiyama T, Nakashima Y, Kusaba K, Nagasawa Z, Koizumi S, Goto M, Miyamoto H. 2010. *Moraxella catarrhalis* bacteraemia associated with prosthetic vascular graft infection. J Med Microbiol 59:245–250.

49. Funaki T, Inoue E, Miyairi I. 2016. Clinical characteristics of the patients with bacteremia due to *Moraxella catarrhalis* in children: A case-control study. BMC Infect Dis 16:1–10.

50. Guthrie R, Bakenhaster K, Nelson R, Woskobnick R. 1988. *Branhamella catarrhalis* sepsis: A case report and review of the literature. J Infect Dis 158:907–908.

51. Westendorp ICD, Tiemessen MA, de Jong M, Soomers A, Wakelkamp IMMJ, Boersma WG. 2005. *Moraxella catarrhalis* sepsis in a patient with juvenile spinal muscle atrophy. Neth J Med 63:227–229.

52. Daele JJ. 1997. Chronic Sinusitis in Children. Acta Otorhinolaryngol Belg 51(4):285-304.

53. Marom T, Alvarez-Fernandez PE, Jennings K, Patel JA, McCormick DP, Chonmaitree T. 2014. Acute Bacterial Sinusitis Complicating Viral Upper Respiratory Tract Infection in Young Children. Pediatr Infect Dis J. 33(8):803–808.

54. Yongshou J. 2000. *Moraxella catarrhalis* meningitis: a case report. Chinese Medical Journal 113(4):381-382.

55. Nigrovic LE, Kuppermann N, Malley R. 2008. Children with bacterial meningitis presenting to the emergency department during the pneumococcal conjugate vaccine era. Acad Emerg Med 15:522–528.

56. Franco J, Ossenkopp J, Peñarroja G. 2017. *Moraxella catarrhalis* meningitis during certolizumab pegol treatment. Med Clin (Barc) 149:2387.

57. Leung AK, Hon KL, Wong AHC, Wong AS. 2018. Bacterial conjunctivitis in childhood: etiology, clinical manifestations, diagnosis, and management. Recent Pat Inflamm Allergy Drug Discov 12 (2):120-127

58. Shaikh N, Hoberman A, Kearney DH, Yellon R. 2011. Tympanocentesis in Children with Acute Otitis Media. N Engl J Med 364:e4.

59. Pichichero ME. 2000. Recurrent and persistent otitis media. Pediatr Infect Dis J 19:911–916.

60. Granath A. 2017. Recurrent Acute Otitis Media: What Are the Options for Treatment and Prevention? Curr Otorhinolaryngol Rep 5:93–100.

61. Qureshi H, Sharafkhaneh A, Hanania NA. 2014. Chronic obstructive pulmonary disease exacerbations: Latest evidence and clinical implications. Ther Adv Chronic Dis 5:212–227.

62. Pavord ID, Jones PW, Burgel PR, Rabe KF. 2016. Exacerbations of COPD. Int J COPD 11:21–30.

63. Viniol C, Vogelmeier CF. 2018. Exacerbations of COPD. Eur Respir Rev 27.

64. Wirth T, Morelli G, Kusecek B, Van Belkum A, Van Der Schee C, Meyer A, Achtman M. 2007. The rise and spread of a new pathogen: Seroresistant *Moraxella catarrhalis*. Genome Res 17:1647–1656.

65. Earl JP, De Vries SPW, Ahmed A, Powell E, Schultz MP, Hermans PWM, Hill DJ, Zhou Z, Constantinidou CI, Hu FZ, Bootsma HJ, Ehrlich GD. 2016. Comparative genomic analyses of the *Moraxella catarrhalis* serosensitive and seroresistant lineages demonstrate their independent evolution. Genome Biol Evol 8:955–974.

66. Sethi S, Murphy TF. 2008. Infection in the Pathogenesis and Course of Chronic Obstructive Pulmonary Disease. N Engl J Med 359:2355–2365.

67. Bernhard S, Spaniol V, Aebi C. 2012. Molecular pathogenesis of infections caused by *Moraxella catarrhalis* in children. Swiss Med Wkly 142:1–9.

68. de Vries SPW, Eleveld MJ, Hermans PWM, Bootsma HJ. 2013. Characterization of the Molecular Interplay between *Moraxella catarrhalis* and Human Respiratory Tract Epithelial Cells. PLoS One 8:1–10.

69. Buskirk SW, Lafontaine ER. 2014. *Moraxella catarrhalis* expresses a cardiolipin synthase that impacts adherence to human epithelial cells. J Bacteriol 196:107–120.

70. Wang W, Joslin SN, Pybus C, Evans AS, Lichaa F, Brautigam CA, Hansen EJ. 2014. Identification of an outer membrane lipoprotein involved in nasopharyngeal colonization by *Moraxella catarrhalis* in an animal model. Infect Immun 82:2287–2299.

71. Singh B, Alvarado-Kristensson M, Johansson M, Hallgren O, Westergren-Thorsson G, Mörgelin M, Riesbeck K. 2016. The respiratory pathogen *Moraxella catarrhalis* targets collagen for maximal adherence to host tissues. MBio 7:1–11.

72. Singh B, Al-Jubair T, Voraganti C, Andersson T, Mukherjee O, Su YC, Zipfel P, Riesbeck K. 2015. *Moraxella catarrhalis* binds plasminogen to evade host innate immunity. Infect Immun 83:3458–3469.

73. Paulsson M, Riesbeck K. 2018. How bacteria hack the matrix and dodge the bullets of immunity. Eur Respir Rev 27:1–8.

74. Volgers C, Benedikter BJ, Grauls GE, Savelkoul PHM, Stassen FRM. 2017. Immunomodulatory role for membrane vesicles released by THP-1 macrophages and respiratory pathogens during macrophage infection. BMC Microbiol 17:1–14.

75. Luke NR, Jurcisek JA, Bakaletz LO, Campagnari AA. 2007. Contribution of *Moraxella catarrhalis* type IV pili to nasopharyngeal colonization and biofilm formation. Infect Immun 75:5559–5564.

76. Verhaegh SJC, Lebon A, Saarloos JA, Verbrugh HA, Jaddoe VWV, Hofman A, Hays JP, Moll HA, van Belkum A. 2010. Determinants of *Moraxella catarrhalis* colonization in healthy Dutch children during the first 14 months of life. Clin Microbiol Infect 16:992–997.

77. Verhaegh SJC, Snippe ML, Levy F, Verbrugh HA, Jaddoe VWV, Hofman A, Moll HA, Van Belkum A, Hays JP. 2011. Colonization of healthy children by *Moraxella catarrhalis* is characterized by genotype heterogeneity, virulence gene diversity and co-colonization with *Haemophilus influenzae*. Microbiology 157:169–178.

78. Perez AC, Pang B, King LB, Tan L, Murrah KA, Reimche JL, Wren JT, Richardson SH, Ghandi U, Swords WE. 2014. Residence of *Streptococcus pneumoniae* and *Moraxella catarrhalis* within polymicrobial biofilm promotes antibiotic resistance and bacterial persistence *in vivo*. Pathog Dis 70:280–288.

79. Pearson MM, Laurence CA, Guinn SE, Hansen EJ. 2006. Biofilm formation by *Moraxella catarrhalis in vitro*: Roles of the UspA1 adhesin and the Hag hemagglutinin. Infect Immun 74:1588–1596.

80. Pearson MM, Hansen EJ. 2007. Identification of gene products involved in biofilm production by *Moraxella catarrhalis* ETSU-9 *in vitro*. Infect Immun 75:4316–4325.

81. Matejka KM, Bremer PJ, Tompkins GR, Brooks HJL. 2012. Antibiotic susceptibility of *Moraxella catarrhalis* biofilms in a continuous flow model. Diagn Microbiol Infect Dis 74:394–398.

82. Blondeau JM, Vaughan D, Laskowski R, Borsos S. 2001. Susceptibility of Canadian isolates of *Haemophilus influenzae*, *Moraxella catarrhalis* and *Streptococcus pneumoniae* to oral antimicrobial agents. Int J Antimicrob Agents 17:457–464.

83. White AR, Kaye C, Poupard J, Pypstra R, Woodnutt G, Wynne B. 2004. Augmentin(R) (amoxicillin/clavulanate) in the treatment of community-acquired respiratory tract

infection: a review of the continuing development of an innovative antimicrobial agent. J Antimicrob Chemother 53(S1):i3–i20.

84. Roland PS, Kreisler LS, Reese B, Anon JB, Lanier B, Conroy PJ, Wall GM, Dupre SJ, Potts S, Hogg G, Stroman DW, Mclean C. 2004. Topical Ciprofloxacin/Dexamethasone Otic Suspension Is Superior to Ofloxacin Otic Solution in the Treatment of Children With Acute Otitis Media With Otorrhea Through Tympanostomy Tubes. Pediatrics 113(1):e40–e46.

85. Kitzis MD, Goldstein FW, Miegi M, Acar JF. 1999. In-vitro activity of levofloxacin, a new fluoroquinolone: Evaluation against *Haemophilus influenzae* and *Moraxella catarrhalis*. J Antimicrob Chemother 43:21–26.

86. Swanson RN, Lainez-ventosilla A, Salvo MC De, Dunne MW, Amsden GW. 2005. Once-Daily Azithromycin for 3 Days Compared with Clarithromycin for 10 Days for Acute Exacerbation of Chronic Bronchitis: A Multicenter, Double-Blind, Randomized Study. Treat Respir Med 4(1):31-39.

87. Sethi S, Anzueto A, Farrell DJ. 2005. Antibiotic activity of telithromycin and comparators against bacterial pathogens isolated from 3,043 patients with acute exacerbation of chronic bronchitis. Ann Clin Microbiol Antimicrob 4:1–7.

88. Yoshida K, Okimoto N, Kishimoto M, Fukano H, Hara H, Yoneyama H, Moriya O, Kawanishi M, Kimura M, Matsushima T, Niki Y. 2011. Efficacy and safety of moxifloxacin for community-acquired bacterial pneumonia based on pharmacokinetic analysis. J Infect Chemother 17:678–685.

89. Kuzman I, Bezlepko A, Kondova Topuzovska I, Rókusz L, Iudina L, Marschall HP, Petri T. 2014. Efficacy and safety of moxifloxacin in community acquired pneumonia: Prospective, multicenter, observational study (CAPRIVI). BMC Pulm Med 14:1–14.

90. Liu KX, Xu B, Wang J, Zhang J, Ding HB, Ariani F, Qu JM, Lin QC. 2014. Efficacy and safety of moxifloxacin in acute exacerbations of chronic bronchitis and COPD: A systematic review and meta-analysis. J Thorac Dis 6:221–229.

91. Bandet T, Whitehead S, Blondel-Hill E, Wagner K, Cheeptham N. 2014. Susceptibility of clinical *Moraxella catarrhalis* isolates in British Columbia to six empirically prescribed antibiotic agents. Can J Infect Dis Med Microbiol 25:155–158.

92. Božić DD, Pavlović B, Milovanović J, Jotić A, Čolović J, Ćirković I. 2018. Antibiofilm effects of amoxicillin–clavulanic acid and levofloxacin in patients with chronic rhinosinusitis with nasal polyposis. Eur Arch Oto-Rhino-Laryngology 275:2051–2059.

93. Flamm RK, Rhomberg PR, Huband MD, Farrell DJ. 2016. *In vitro* activity of delafloxacin tested against isolates of *Streptococcus pneumoniae*, *Haemophilus influenzae*, and *Moraxella catarrhalis*. Antimicrob Agents Chemother 60:6381–6385.

94. Brien MAO, Prosser LA, Paradise JL, Ray GT, Kurs-lasky M, Hinrichsen VL, Mehta J, Kathleen D, Lieu TA. 2014. New Vaccines Against Otitis Media : Projected.

95. Ren D, Yu S, Gao S, Peng D, Petralia RS, Muszynski A, Carlson RW, Robbins JB, Tsai CM, Lim DJ, Gu XX. 2011. Mutant lipooligosaccharide-based conjugate vaccine demonstrates a broad-spectrum effectiveness against *Moraxella catarrhalis*. Vaccine 29:4210–4217.

96. Yang M, Johnson A, Murphy TF. 2011. Characterization and evaluation of the *Moraxella catarrhalis* oligopeptide permease A as a mucosal vaccine antigen. Infect Immun 79:846–857.

97. Prymula R. 2009. Re: Global serotype distribution among *Streptococcus pneumoniae* isolates causing otitis media in children: Potential implications for pneumococcal conjugate vaccines. Vaccine 27:4739–4740.

98. Pumarola F, Marès J, Losada I, Minguella I, Moraga F, Tarragó D, Aguilera U, Casanovas JM, Gadea G, Trías E, Cenoz S, Sistiaga A, García-Corbeira P, Pirçon JY, Marano C, Hausdorff WP. 2013. Microbiology of bacteria causing recurrent acute otitis media (AOM) and AOM treatment failure in young children in Spain: Shifting pathogens in the post-pneumococcal conjugate vaccination era. Int J Pediatr Otorhinolaryngol 77:1231–1236.

99. Su YC, Hallström BM, Bernhard S, Singh B, Riesbeck K. 2013. Impact of sequence diversity in the *Moraxella catarrhalis* UspA2/UspA2H head domain on vitronectin binding and antigenic variation. Microbes Infect 15:375–387.

100. Saito R, Nonaka S, Fujinami Y, Matsuoka S, Nakajima S, Nishiyama H, Okamura N. 2014. The frequency of BRO β-lactamase and its relationship to antimicrobial susceptibility and serum resistance in *Moraxella catarrhalis*. J Infect Chemother 20:6–8.

101. Shaikh SBU, Ahmed Z, Arsalan SA, Shafiq S. 2015. Prevalence and resistance pattern of *Moraxella catarrhalis* in community-acquired lower respiratory tract infections. Infection and Drug Resistance 8:263–267.

102. Sillanpää S, Sipilä M, Hyöty H, Rautiainen M, Laranne J. 2016. Antibiotic resistance in pathogens causing acute otitis media in Finnish children. Int J Pediatr Otorhinolaryngol 85:91–94.

103. Schmitz FJ, Beeck A, Perdikouli M, Boos M, Mayer S, Scheuring S, Köhrer K, Verhoef J, Fluit AC. 2002. Production of BRO β-lactamases and resistance to complement in European *Moraxella catarrhalis* isolates. J Clin Microbiol 40:1546–1548.

104. Esel D, Ay-Altintop Y, Yagmur G, Gokahmetoglu S, Sumerkan B. 2007. Evaluation of susceptibility patterns and BRO β-lactamase types among clinical isolates of *Moraxella catarrhalis*. Clin Microbiol Infect 13:1023–1025.

105. Saito R, Miharu Y, Matsuoka S, Nonaka S, Fujinami Y, Okamura N. 2015. The outer membrane protein CD is associated with resistance to penicillins in *Moraxella catarrhalis*. J Glob Antimicrob Resist 3:224–225.

106. Yamada K, Arai K, Saito R. 2017. Antimicrobial susceptibility to β-lactam antibiotics and production of BRO β-lactamase in clinical isolates of *Moraxella catarrhalis* from a Japanese hospital. J Microbiol Immunol Infect 50:386–389.

107. Yamada K, Saito R. 2014. Molecular analysis of low-level fluoroquinolone resistance in clinical isolates of *Moraxella catarrhalis*. J Med Microbiol 63:1066–1070.

108. Iwata S, Sato Y, Toyonaga Y, Hanaki H, Sunakawa K. 2015. Genetic analysis of a pediatric clinical isolate of *Moraxella catarrhalis* with resistance to macrolides and quinolones. J Infect Chemother 21:308–311.

109. Yamada K, Saito R, Muto S, Kashiwa M, Tamamori Y, Fujisakia S. 2017. Molecular Characterization of Fluoroquinolone-Resistant *Moraxella catarrhalis* Variants Generated *In vitro* by Stepwise Selection. Antimicrob Agents Chemother 61(10):e01336-17.

110. Nakai H, Sato T, Uno T, Furukawa E, Kawamura M, Takahashi H, Watanabe A, Fujimura S. 2018. Mutant selection window of four quinolone antibiotics against clinical isolates of *Streptococcus pneumoniae*, *Haemophilus influenzae* and *Moraxella catarrhalis*. J Infect Chemother 24:83–87.

111. Stogios PJ, Cox G, Zubyk HL, Evdokimova E, Wawrzak Z, Wright GD, Savchenko A. 2018. Substrate Recognition by a Colistin Resistance Enzyme from *Moraxella catarrhalis*. ACS Chem Biol 13:1322–1332.

112. Wei W, Srinivas S, Lin J, Tang Z, Wang S, Ullah S, Kota VG, Feng Y. 2018. Defining ICR-Mo, an intrinsic colistin resistance determinant from *Moraxella osloensis*. PLoS Genet 14(5):e1007389.

113. AbuOun M, Stubberfield EJ, Duggett NA, Kirchner M, Dormer L, Nunez-Garcia J, Randall LP, Lemma F, Crook DW, Teale C, Smith RP, Anjum MF. 2017. mcr-1 and mcr-2 variant genes identified in *Moraxella* species isolated from pigs in Great Britain from 2014 to 2015. J Antimicrob Chemother 72:2745–2749.

114. Vester B, Douthwaite S. 2001. Macrolide Resistance Conferred by Base Substitutions in 23S rRNA. Antimicrobial Agents and Chemotherapy 45(1):1–12.

115. Flamm RK, Sader HS, Farrell DJ, Jones RN. 2012. Macrolide and tetracycline resistance among *Moraxella catarrhalis* isolates from 2009 to 2011. Diagn Microbiol Infect Dis 74:198–200.

116. Liu Y, Xu H, Xu Z, Kudinha T, Fan X, Xiao M, Kong F, Sun H, Xu Y. 2015. High-Level Macrolide-Resistant *Moraxella catarrhalis* and Development of an Allele-Specific PCR Assay for Detection of 23S rRNA Gene A2330T Mutation: A Three-Year Study at a Chinese Tertiary Hospital. Microb Drug Resist 21:507–511.

117. Liu YL, Li DF, Xu HP, Xiao M, Cheng JW, Zhang L, Xu ZP, Chen XX, Zhang G, Kudinha T, Kong F, Gong YP, Wang XY, Zhang YX, Wu HL, Xu YC. 2016. Use of next

generation sequence to investigate potential novel macrolide resistance mechanisms in a population of *Moraxella catarrhalis* isolates. Sci Rep 6:1–12.

118. Zhang Y, Zhang F, Wang H, Zhao C, Wang Z, Cao B, Du Y, Feng X, Hu Y, Hu B, Ji P, Liu Z, Liu Y, Liao W, Lu J, Sun H, Wang Z, Xu X, Xu X, Yang Q, Yu Y, Zhang R, Zhuo C. 2016. Antimicrobial susceptibility of *Streptococcus pneumoniae*, *Haemophilus influenzae* and *Moraxella catarrhalis* isolated from community-acquired respiratory tract infections in China: Results from the CARTIPS Antimicrobial Surveillance Program. J Glob Antimicrob Resist 5:36–41.

119. Liu YL, Xiao M, Cheng JW, Xu HP, Xu ZP, Ye S, Zhang WJ, Kudinha T, Kong F, Xu YC. 2017. *Moraxella catarrhalis* macrolide-resistant isolates are highly concentrated in two MLST clonal complexes -CCN10 and CC363. Front Microbiol 8:1–6.

120. Du Y, Zhou H, Wang F, Liang S, Cheng L, Du X, Pang F, Tian J, Zhao J, Kan B, Xu J, Li J, Zhang F. 2017. Multilocus sequence typing-based analysis of *Moraxella catarrhalis* population structure reveals clonal spreading of drug-resistant strains isolated from childhood pneumonia. Infect Genet Evol 56:117–124.

121. Murphy TF. 2005. Vaccine development for non-typeable *Haemophilus influenzae* and *Moraxella catarrhalis*: Progress and challenges. Expert Rev Vaccines 4:843–853.

122. Mawas F, Mei MH, Corbel MJ. 2009. Current progress with *Moraxella catarrhalis* antigens as vaccine candidates. Expert Rev Vaccines 8:77–90.

123. Murphy TF. 2009. Vaccine development for *Moraxella catarrhalis*: Rationale, approaches and challenges. Expert Rev Vaccines 8:655–658.

124. Yassin GM, Amin MA, Attia AS. 2016. Immunoinformatics Identifies a Lactoferrin Binding Protein A Peptide as a Promising Vaccine with a Global Protective Prospective Against *Moraxella catarrhalis*. J Infect Dis 213:1938–1945.

125. Ren D, Pichichero ME. 2016. Vaccine targets against *Moraxella catarrhalis*. Expert Opin Ther Targets 20:19–33.

126. Ren D, Almudevar AL, Murphy TF, Lafontaine ER, Campagnari AA, Luke-Marshall N, Pichichero ME. 2017. Serum antibody response to *Moraxella catarrhalis* proteins in stringently defined otitis prone children. Vaccine. pii: S0264-410X(17)30935-0.

127. Murphy TF, Brauer AL, Johnson A, Wilding GE, Koszelak-Rosenblum M, Malkowski MG. 2017. A Cation-Binding Surface Protein as a Vaccine Antigen To Prevent *Moraxella catarrhalis* Otitis Media and Infections in Chronic Obstructive Pulmonary Disease. Clin Vaccine Immunol 24(9):e00130-17.

128. Shaffer TL, Balder R, Buskirk SW, Hogan RJ, Lafontaine ER. 2013. Use of the Chinchilla Model to Evaluate the Vaccinogenic Potential of the *Moraxella catarrhalis* Filamentous Hemagglutinin-like Proteins MhaB1 and MhaB2. PLoS One 8(7):e67881.

129. Perez AC, Murphy TF. 2017. A *Moraxella catarrhalis* vaccine to protect against otitis media and exacerbations of COPD: An update on current progress and challenges. Hum Vaccines Immunother 13:2322–2331.

130. Pettigrew MM, Alderson MR, Bakaletz LO, Barenkamp SJ, Hakansson AP, Mason KM, Nokso-Koivisto J, Patel J, Pelton SI, Murphy TF. 2017. Panel 6: Vaccines. Otolaryngol - Head Neck Surg (United States) 156:S76–S87.

131. Perez AC, Murphy TF. 2017. Potential impact of a *Moraxella catarrhalis* vaccine in COPD. Vaccine.

132. Luke-Marshall NR, Mang TS, Hansen LA, Campagnari AA. 2014. *Moraxella catarrhalis* is susceptible to antimicrobial photodynamic therapy with Photofrin. Lasers Surg Med 46:712–717.

133. Tan TT, Riesbeck K. 2007. Current progress of adhesins as vaccine candidates for *Moraxella catarrhalis*. Expert Rev Vaccines 6:949–956.

134. Su Y, Singh B, Riesbeck K. 2012. *Moraxella catarrhalis*: from interactions with the host immune system to vaccine development. Future Microbiol. 7(9):1073–1100.

135. Murphy TF, Kirkham C, Johnson A, Brauer AL, Koszelak-Rosenblum M, Malkowski MG. 2016. Sulfate-binding protein, CysP, is a candidate vaccine antigen of *Moraxella catarrhalis*. Vaccine 34:3855–3861.

136. Blakeway L V., Tan A, Peak IRA, Seib KL. 2017. Virulence determinants of *Moraxella catarrhalis*: Distribution and considerations for vaccine development. Microbiol (United Kingdom) 163:1371–1384.

137. Augustyniak D, Seredyński R, McClean S, Roszkowiak J, Roszniowski B, Smith DL, Drulis-Kawa Z, MacKiewicz P. 2018. Virulence factors of *Moraxella catarrhalis* outer membrane vesicles are major targets for cross-reactive antibodies and have adapted during evolution. Sci Rep 8:1–15.

138. Or YS, Clark RF, Wang S, Chu DTW, Nilius AM, Flamm RK, Mitten M, Ewing P, Alder J, Ma Z. 2000. Design, synthesis, and antimicrobial activity of 6-O-substituted ketolides active against resistant respiratory tract pathogens [2]. J Med Chem 43:1045–1049.

139. Payne DJ, Miller WH, Berry V, Brosky J, Burgess WJ, Chen E, DeWolf WE, Fosberry AP, Greenwood R, Head MS, Heerding DA, Janson CA, Jaworski DD, Keller PM, Manley PJ, Moore TD, Newlander KA, Pearson S, Polizzi BJ, Qiu X, Rittenhouse SF, Slater-Radosti C, Salvers KL, Seefeld MA, Smyth MG, Takata DT, Uzinskas IN, Vaidya K, Wallis NG, Winram SB, Yuan CCK, Huffman WF. 2002. Discovery of a novel and potent class of fabI-directed antibacterial agents. Antimicrob Agents Chemother 46:3118–3124.

140. Doña I, Blanca-López N, Torres MJ, García-Campos J, García-Núñez I, Gómez F, Salas M, Rondón C, Canto MG, Blanca M. 2012. Drug hypersensitivity reactions: Response patterns, drug involved, and temporal variations in a large series of patients. J Investig Allergol Clin Immunol 22:363–371.

141. Norrby SR, Nord CE, Finch R. 2005. Lack of development of new antimicrobial drugs: A potential serious threat to public health. Lancet Infect Dis 5:115–119.

142. Payne DJ, Gwynn MN, Holmes DJ, Pompliano DL. 2007. Drugs for bad bugs: Confronting the challenges of antibacterial discovery. Nat Rev Drug Discov 6:29–40.

143. Miller JR, Dunham S, Mochalkin I, Banotai C, Bowman M, Buist S, Dunkle B, Hanna D, Harwood HJ, Huband MD, Karnovsky A, Kuhn M, Limberakis C, Liu JY, Mehrens S, Mueller WT, Narasimhan L, Ogden A, Ohren J, Prasad JVNV, Shelly JA, Skerlos L, Sulavik M, Thomas VH, Vanderroest S, Wang L, Wang Z, Whitton A, Zhu T, Stover CK. 2009. A class of selective antibacterials derived from a protein kinase inhibitor pharmacophore. Proc Natl Acad Sci U S A 106:1737–1742.

144. Donadio S, Maffioli S, Monciardini P, Sosio M, Jabes D. 2010. Antibiotic discovery in the twenty-first century: Current trends and future perspectives. J Antibiot (Tokyo) 63:423–430.

145. Mobegi FM, van Hijum SAFT, Burghout P, Bootsma HJ, de Vries SPW, van der Gaast-de Jongh CE, Simonetti E, Langereis JD, Hermans PWM, de Jonge MI, Zomer A. 2014. From microbial gene essentiality to novel antimicrobial drug targets. BMC Genomics 15(958):1-11.

146. Fernandes P, Martens E. 2017. Antibiotics in late clinical development. Biochem Pharmacol 133:152–163.

147. Murphy TF, Brauer AL, Johnson A, Kirkham C. 2016. Atp-binding cassette (abc) transporters of the human respiratory tract pathogen, *Moraxella catarrhalis*: Role in virulence. PLoS One 11:1–14.

148. Heath RJ, White SW, Rock CO. 2002. Inhibitors of fatty acid synthesis as antimicrobial chemotherapeutics. Appl Microbiol Biotechnol 58:695–703.

149. Campbell JW, Cronan Jr. JE. 2001. Bacterial Fatty Acid Biosynthesis: Targets for Antibacterial Drug Discovery. Annu. Rev. Microbiol. 55:305–32.

150. Lu JZ, Lee PJ, Waters NC, Prigge ST. 2005. Fatty Acid synthesis as a target for antimalarial drug discovery. Comb Chem High Throughput Screen 8:15–26.

151. Wright HT, Reynolds KA. 2007. Antibacterial targets in fatty acid biosynthesis. Curr Opin Microbiol 10:447–453.

152. Puig T, Porta R, Colomer R. 2009. Fatty acid synthase: a new anti-tumor target. Med Clin (Barc). 132(9):359-63.

153. Johansson P, Mulinacci B, Koestler C, Vollrath R, Oesterhelt D, Grininger M. 2009. Multimeric Options for the Auto-Activation of the Saccharomyces cerevisiae FAS Type I Megasynthase. Structure 17:1063–1074.

154. Flavin R, Peluso S, Nguyen PL, Loda M. 2010. Fatty acid synthase as a potential therapeutic target in cancer. Future Oncol. 6(4):551–562.

155. Płoskoń E, Arthur CJ, Evans SE, Williams C, Crosby J, Simpson TJ, Crump MP. 2008. A mammalian type I fatty acid synthase acyl carrier protein domain does not sequester acyl chains. J Biol Chem 283:518–528.

156. Schweizer E, Hofmann J. 2004. Microbial Type I Fatty Acid Synthases (FAS): Major Players in a Network of Cellular FAS Systems. Microbiology and Molecular Biology Reviews 68(3):501–517.

157. Ciccarelli L, Connell SR, Enderle M, Mills DJ, Vonck J, Grininger M. 2013. Structure and conformational variability of the *Mycobacterium tuberculosis* fatty acid synthase multienzyme complex. Structure 21:1251–1257.

158. Boehringer D, Ban N, Leibundgut M. 2013. 7.5-Å cryo-EM structure of the mycobacterial fatty acid synthase. J Mol Biol 425:841–849.

159. Enderle M, Mccarthy A, Paithankar KS, Grininger M. 2015. Crystallization and X-ray diffraction studies of a complete bacterial fatty-acid synthase type I. Acta Crystallogr Sect Struct Biol Commun 71:1401–1407.

160. Elad N, Baron S, Peleg Y, Albeck S, Grunwald J, Raviv G, Shakked Z, Zimhony O, Diskin R. 2018. Structure of Type-I *Mycobacterium tuberculosis* fatty acid synthase at 3.3 Å resolution. Nat Commun 9:1–6.

161. White SW, Zheng J, Zhang Y-M, Rock CO. 2005. the Structural Biology of Type Ii Fatty Acid Biosynthesis. Annu Rev Biochem 74:791–831.

162. Rock CO, Cronan JE. 1996. Biochimica et Biophysica fatty acid biosynthesis. Biochim Biophys Fat acid Biosynth 1302:1–16.

163. Waller RF, Ralph SA, Reed MB, Su V, Douglas JD, Minnikin DE, Cowman AF, Besra GS, McFadden GI. 2003. A type II pathway for fatty acid biosynthesis presents drug targets in *Plasmodium falciparum*. Antimicrob Agents Chemother 47:297–301.

164. Zhang YM, White SW, Rock CO. 2006. Inhibiting bacterial fatty acid synthesis. J Biol Chem 281:17541–17544.

165. Wang Y, Ma S. 2013. Recent advances in inhibitors of bacterial fatty acid synthesis type II (FASII) system enzymes as potential antibacterial agents. ChemMedChem 8:1589–1608.

166. Yao J, Abdelrahman YM, Robertson RM, Cox J V., Belland RJ, White SW, Rock CO. 2014. Type II fatty acid synthesis is essential for the replication of *Chlamydia trachomatis*. J Biol Chem 289:22365–22376.

167. Wallace J, Bowlin NO, Mills DM, Saenkham P, Kwasny SM, Opperman TJ, Williams JD, Rock CO, Bowlin TL, Moir DT. 2015. Discovery of bacterial fatty acid synthase type II inhibitors using a novel cellular bioluminescent reporter assay. Antimicrob Agents Chemother 59:5775–5787.

168. Zhang YM, Lu YJ, Rock CO. 2004. The reductase steps of the type II fatty acid synthase as antimicrobial targets. Lipids 39:1055–1060.

169. Soares Da Costa TP, Nanson JD, Forwood JK. 2017. Structural characterisation of the fatty acid biosynthesis enzyme FabF from the pathogen *Listeria monocytogenes*. Sci Rep 7:1–9.

170. Kumar V, Sharma A, Pratap S, Kumar P. 2018. Characterization of isoflavonoids as inhibitors of β-hydroxyacyl-acyl carrier protein dehydratase (FabZ) from *Moraxella catarrhalis*: Kinetics, spectroscopic, thermodynamics and *in silico* studies. Biochim Biophys Acta Gen Subj. 1862(3):726-744.

171. Heath RJ, Yu YT, Shapiro MA, Olson E, Rock CO. 1998. Broad spectrum antimicrobial biocides target the FabI component of fatty acid synthesis. J Biol Chem 273:30316–30320.

172. Tasdemir D, Topaloglu B, Perozzo R, Brun R, O'Neill R, Carballeira NM, Zhang X, Tonge PJ, Linden A, Rüedi P. 2007. Marine natural products from the Turkish sponge Agelas oroides that inhibit the enoyl reductases from *Plasmodium falciparum*, *Mycobacterium tuberculosis* and *Escherichia coli*. Bioorganic Med Chem 15:6834–6845.

173. Lu H, Tonge PJ. 2008. Inhibitors of FabI, an enzyme drug target in the bacterial fatty acid biosynthesis pathway. Acc Chem Res 41:11–20.

174. Zitko J, Doležal M. 2016. Enoyl acyl carrier protein reductase inhibitors: an updated patent review (2011 – 2015). Expert Opin Ther Pat 26:1079–1094.

175. Turnowsky F, Fuchs K, Jeschek C, Hogenauer G. 1989. envM genes of *Salmonella typhimurium* and *Escherichia coli*. J Bacteriol 171(12):6555–6565.

176. Bergler H, Wallner P, Ebeling A, Leitinger B, Fuchsbichler S, Aschauer H, Kollenz G, Hogenauer G, Turnowsky F. 1994. Protein EnvM Is the NADH-dependent Enoyl-ACP Reductase (FabI) of *Escherichia coli*. J Biol Chem 269(8):5493-5496.

177. Rafferty JB, Simon JW, Baldock C, Artymiuk PJ, Baker PJ, Stuitje AR, Slabas AR, Rice DW. 1995. Common themes in redox chemistry emerge from the X-ray structure of oilseed rape (*Brassica napus*) enoyl acyl carrier protein reductase. Structure 3:927–938.

178. Heath RJ, Rock CO. 1995. Enoyl-acyl carrier protein reductase (fabI) plays a determinant role in completing cycles of fatty acid elongation in *Escherichia coli*. J Biol Chem 270:26538–26542.

179. Heath RJ, Su N, Murphy CK, Rock CO. 2000. The enoyl-[acyl-carrier-protein] reductases FabI and FabL from *Bacillus subtilis*. J Biol Chem 275:40128–40133.

180. Heath RJ, Rock C o. 2000. A triclosan-resistant bacterial enzyme. Nature 406:145.

181. Massengo-Tiassé RP, Cronan JE. 2008. *Vibrio cholerae* FabV defines a new class of enoyl-acyl carrier protein reductase. J Biol Chem 283:1308–1316.

182. Yao J, Ericson ME, Frank MW, Rock CO. 2016. Enoyl-acyl carrier protein reductase I (FabI) is essential for the intracellular growth of *Listeria monocytogenes*. Infect Immun 84:3597–3607.

183. Neckles C, Pschibul A, Lai CT, Hirschbeck M, Kuper J, Davoodi S, Zou J, Liu N, Pan P, Shah S, Daryaee F, Bommineni GR, Lai C, Simmerling C, Kisker C, Tonge PJ. 2016. Selectivity of Pyridone- and Diphenyl Ether-Based Inhibitors for the *Yersinia pestis* FabV Enoyl-ACP Reductase. Biochemistry 55:2992–3006.

184. Cummings JE, Kingry LC, Rholl DA, Schweizer HP, Tonge PJ, Slayden RA. 2014. The *Burkholderia pseudomallei* enoyl-acyl carrier protein reductase fabI1 is essential for *in*

vivo growth and is the target of a novel chemotherapeutic with efficacy. Antimicrob Agents Chemother 58:931–935.

185. Zhu L, Bi H, Ma J, Hu Z, Zhang W, Cronan JE, Wang H. 2013. The two functional enoyl-acyl carrier protein reductases of *Enterococcus faecalis* do not mediate triclosan resistance. MBio 4:1–10.

186. Ha BH, Shin SC, Moon JH, Keum G, Kim CW, Kim EEK. 2017. Structural and biochemical characterization of FabK from *Thermotoga maritima*. Biochem Biophys Res Commun 482:968–974.

187. Baldock C, Rafferty JB, Sedelnikova SE, Baker PJ, Stuitje AR, Slabas AR, Hawkes TR, Rice DW. 1996. A mechanism of drug action revealed by structural studies of Enoyl reductase. Science 274:2107–2110.

188. Baldock C, Rafferty JB, Stuitje AR, Slabas AR, Rice DW. 1998. The X-ray structure of *Escherichia coli* enoyl reductase with bound NAD+at 2.1 Å resolution. J Mol Biol 284:1529–1546.

189. Qiu X, Janson CA, Court RI, Smyth MG, Payne DJ, Abdel-Meguid SS. 1999. Molecular basis for triclosan activity involves a flipping loop in the active site. Protein Sci 8:2529–2532.

190. Rafi S, Novichenok P, Kolappan S, Zhang X, Stratton CF, Rawat R, Kisker C, Simmerling C, Tonge PJ. 2006. Structure of acyl carrier protein bound to FabI, the FASII enoyl reductase from *Escherichia coli*. J Biol Chem 281:39285–39293.

191. Dessen A, Quémard A, Blanchard JS, Jr WRJ, Sacchettini JC, Dessen A, Quemard A, Blanchard JS, Jr WRJ, Sacchettinit JC. 2017. Crystal Structure and Function of the Isoniazid Target of *Mycobacterium tuberculosis*. Science 267:1638–1641.

192. Rozwarski DA, Grant GA, Barton DHR, Jacobs WR, Sacchettini JC. 1998. Modification of the NADH of the isoniazid target (InhA) from *Mycobacterium tuberculosis*. Science 279:98–102.

193. Rozwarski DA, Vilchèze C, Sugantino M, Bittman R, Sacchettini JC. 1999. Crystal structure of the *Mycobacterium tuberculosis* enoyl-ACP reductase, InhA, in complex with NAD+and a C16 fatty acyl substrate. J Biol Chem 274:15582–15589.

194. McMurry LM, Mcdermott PF, Levy SB. 1999. Genetic evidence that InhA of *Mycobacterium smegmatis* is a target for triclosan. Antimicrob Agents Chemother 43:711–713.

195. Li HJ, Lai CT, Pan P, Yu W, Liu N, Bommineni GR, Garcia-Diaz M, Simmerling C, Tonge PJ. 2014. A structural and energetic model for the slow-onset inhibition of the *Mycobacterium tuberculosis* ENoyl-ACP reductase InhA. ACS Chem Biol 9:986–993.

196. Manjunatha UH, Rao SPS, Kondreddi RR, Christian G, Camacho LR, Tan BH, Ng SH, Ng PS, Ma NL, Lakshminarayana B, Herve M, Barnes SW, Yu W, Kuhen K, Blasco F, Beer D, Walker JR, Tonge PJ, Glynne R, Smith W, Diagana TT. 2015. Direct inhibitors of InhA active against *Mycobacterium tuberculosis*. Sci Transl Med. 7(269):269ra3.

197. Spagnuolo LA, Eltschkner S, Yu W, Daryaee F, Davoodi S, Knudson SE, Allen EKH, Merino J, Pschibul A, Moree B, Thivalapill N, Truglio JJ, Salafsky J, Slayden RA, Kisker C, Tonge PJ. 2017. Evaluating the Contribution of Transition-State Destabilization to Changes in the Residence Time of Triazole-Based InhA Inhibitors. J Am Chem Soc 139:3417–3429.

198. Priyadarshi A, Kim EE, Hwang KY. 2010. Structural insights into *Staphylococcus aureus* enoyl-ACP reductase (Fabl), in complex with NADP end triclosan. Proteins Struct Funct Bioinforma 78:480–486.

199. Schiebel J, Chang A, Lu H, Baxter M V., Tonge PJ, Kisker C. 2012. *Staphylococcus aureus* FabI: Inhibition, Substrate Recognition, and Potential Implications for *In vivo* Essentiality. Structure 20:802–813.

200. Kaplan N, Albert M, Awrey D, Bardouniotis E, Berman J, Clarke T, Dorsey M, Hafkin B, Ramnauth J, Romanov V, Schmid MB, Thalakada R, Yethon J, Pauls HW. 2012. Mode of action, *in vitro* activity, and *in vivo* efficacy of AFN-1252, a selective antistaphylococcal fabi inhibitor. Antimicrob Agents Chemother 56:5865–5874.

201. Lee JH, Park AK, Chi YM, Jeong ASW. 2015. Crystal structures of *Pseudomonas aeruginosa* Enoyl-ACP reductase (FabI) in the presence and absence of NAD+ and triclosan. Bull Korean Chem Soc 36:322–326.

202. Schiebel J, Chang A, Shah S, Lu Y, Liu L, Pan P, Hirschbeck MW, Tareilus M, Eltschkner S, Yu W, Cummings JE, Knudson SE, Bommineni GR, Walker SG, Slayden RA, Sotriffer CA, Tonge PJ, Kisker C. 2014. Rational design of broad spectrum antibacterial activity based on a clinically relevant enoyl-acyl carrier protein (ACP) reductase inhibitor. J Biol Chem 289:15987–16005.

203. Schiebel J, Chang A, Merget B, Bommineni GR, Yu W, Spagnuolo LA, Baxter M V., Tareilus M, Tonge PJ, Kisker C, Sotriffer CA. 2015. An Ordered Water Channel in *Staphylococcus aureus* FabI: Unraveling the Mechanism of Substrate Recognition and Reduction. Biochemistry 54:1943–1955.

204. Li W, Liu Z, Yang J. 2011. Marine market forecasting using extension neural network. ICIC Express Lett 5:497–502.

205. Kim KH, Ha BH, Kim SJ, Hong SK, Hwang KY, Kim EE. 2011. Crystal structures of enoyl-ACP reductases i (FabI) and III (FabL) from *B. subtilis*. J Mol Biol 406:403–415.

206. Kim SJ, Ha BH, Kim KH, Hong SK, Shin KJ, Suh SW, Kim EEK. 2010. Dimeric and tetrameric forms of enoyl-acyl carrier protein reductase from *Bacillus cereus*. Biochem Biophys Res Commun 400:517–522.

207. Tipparaju SK, Mulhearn DC, Klein GM, Chen Y, Tapadar S, Bishop MH, Yang S, Chen J, Ghassemi M, Santarsiero BD, Cook JL, Johlfs M, Mesecar AD, Johnson ME, Kozikowski AP. 2008. Design and Synthesis of Aryl Ether Inhibitors of the *Bacillus anthracis* Enoyl-ACP Reductase. ChemMedChem 3:1250–1268.

208. Kim HT, Kim S, Na BK, Chung J, Hwang E, Hwang KY. 2017. Structural insights into the dimer-tetramer transition of FabI from *Bacillus anthracis*. Biochem Biophys Res Commun 493:28–33.

209. Hoang TT, Schweizer HP. 1999. Characterization of *Pseudomonas aeruginosa* enoyl-acyl carrier protein reductase (FabI): A target for the antimicrobial triclosan and its role in acylated homoserine lactone synthesis. J Bacteriol 181:5489–5497.

210. Lu H, England K, am Ende C, Truglio JJ, Luckner S, Reddy BG, Marlenee NL, Knudson SE, Knudson DL, Bowen RA, Kisker C, Slayden RA, Tonge PJ. 2009. Slow-Onset

Inhibition of the FabI Enoyl Reductase from Francisella tularensis : Residence Time and *in vivo* Activity. ACS Chem Biol 4:221–231.

211. Mehboob S, Truong K, Santarsiero BD, Johnson ME. 2010. Structure of the *Francisella tularensis* enoyl-acyl carrier protein reductase (FabI) in complex with NAD+ and triclosan. Acta Crystallogr Sect F Struct Biol Cryst Commun 66:1436–1440.

212. Otero JM, Nol AJ, Guardado-Calvo P, Llamas-Saiz AL, Wende W, Schierling B, Pingoud A, Van Raaij MJ. 2012. High-resolution structures of *Thermus thermophilus* enoyl-acyl carrier protein reductase in the apo form, in complex with NAD+ and in complex with NAD+ and triclosan. Acta Crystallogr Sect F Struct Biol Cryst Commun 68:1139–1148.

213. Jiang L, Gao Z, Li Y, Wang S, Dong Y. 2014. Crystal structures and kinetic properties of enoyl-acyl carrier protein reductase i from *Candidatus Liberibacter asiaticus*. Protein Sci 23:366–377.

214. Yao J, Abdelrahman YM, Robertson RM, Cox J V., Belland RJ, White SW, Rock CO. 2014. Type II fatty acid synthesis is essential for the replication of *Chlamydia trachomatis*. J Biol Chem 289:22365–22376.

215. Roujeinikova A, Sedelnikova S, De Boer GJ, Stuitje AR, Slabas AR, Rafferty JB, Rice DW. 1999. Inhibitor binding studies on enoyl reductase reveal conformational changes related to substrate recognition. J Biol Chem 274:30811–30817.

216. Fawcett T, Copse CL, Simon JW, Slabas AR. 2000. Kinetic mechanism of NADH-enoyl-ACP reductase from *Brassica napus*. FEBS Lett 484:65–68.

217. Perozzo R, Kuo M, Sidhu ABS, Valiyaveettil JT, Bittman R, Jacobs WR, Fidock DA, Sacchettini JC. 2002. Structural elucidation of the specificity of the antibacterial agent triclosan for malarial enoyl acyl carrier protein reductase. J Biol Chem 277:13106–13114.

218. Freundlich JS, Wang F, Tsai HC, Kuo M, Shieh HM, Anderson JW, Nkrumah LJ, Valderramos JC, Yu M, Kumar TRS, Valderramos SG, Jacobs WR, Schiehser GA, Jacobus DP, Fidock DA, Sacchettini JC. 2007. X-ray structural analysis of *Plasmodium falciparum* enoyl acyl carrier protein reductase as a pathway toward the optimization of triclosan antimalarial efficacy. J Biol Chem 282:25436–25444.

219. Maity K, Banerjee T, Prabakaran N, Surolia N, Surolia A, Suguna K. 2011. Effect of substrate binding loop mutations on the structure, kinetics, and inhibition of enoyl acyl carrier protein reductase from *Plasmodium falciparum*. IUBMB Life 63:30–41.

220. Muench SP, Prigge ST, Zhu L, Kirisits MJ, Roberts CW, Wernimont S, McLeod R, Rice DW. 2006. Expression, purification and preliminary crystallographic analysis of the *Toxoplasma gondii* enoyl reductase. Acta Crystallogr Sect F Struct Biol Cryst Commun 62:604–606.

221. LU JZ, MUENCH SP, ALLARY M, CAMPBELL S, ROBERTS CW, MUI E, McLEOD RL, RICE DW, PRIGGE ST. 2007. Type I and type II fatty acid biosynthesis in *Eimeria tenella*: enoyl reductase activity and structure. Parasitology 134:790–795.

222. Moir DT. 2005. Identification of inhibitors of bacterial enoyl-acyl carrier protein reductase. Curr Drug Targets Infect Disord 5:297–305.

223. Hoagland DT, Liu J, Lee RB, Lee RE. 2016. New agents for the treatment of drug-resistant *Mycobacterium tuberculosis*. Adv Drug Deliv Rev 102:55–72.

224. Karlowsky JA, Kaplan N, Hafkin B, Hoban DJ, Zhanel GG. 2009. AFN-1252, a FabI inhibitor, demonstrates a *Staphylococcus*-specific spectrum of activity. Antimicrob Agents Chemother 53:3544–3548.

225. Escaich S, Prouvensier L, Saccomani M, Durant L, Oxoby M, Gerusz V, Moreau F, Vongsouthi V, Maher K, Morrissey I, Soulama-Mouze C. 2011. The MUT056399 inhibitor of FabI is a new antistaphylococcal compound. Antimicrob Agents Chemother 55:4692–4697.

226. Martínez-Hoyos M, Perez-Herran E, Gulten G, Encinas L, Álvarez-Gómez D, Alvarez E, Ferrer-Bazaga S, García-Pérez A, Ortega F, Angulo-Barturen I, Rullas-Trincado J, Blanco Ruano D, Torres P, Castañeda P, Huss S, Fernández Menéndez R, González del Valle S, Ballell L, Barros D, Modha S, Dhar N, Signorino-Gelo F, McKinney JD, García-Bustos JF, Lavandera JL, Sacchettini JC, Jimenez MS, Martín-Casabona N, Castro-Pichel J, Mendoza-Losana A. 2016. Antitubercular drugs for an old target: GSK693 as a promising InhA direct inhibitor. EBioMedicine 8:291–301.

227. Payne DJ, Miller WH, Berry V, Brosky J, Burgess WJ, Chen E, DeWolf WE, Fosberry AP, Greenwood R, Head MS, Heerding DA, Janson CA, Jaworski DD, Keller PM, Manley PJ, Moore TD, Newlander KA, Pearson S, Polizzi BJ, Qiu X, Rittenhouse SF, Slater-Radosti C, Salvers KL, Seefeld MA, Smyth MG, Takata DT, Uzinskas IN, Vaidya K, Wallis NG, Winram SB, Yuan CCK, Huffman WF. 2002. Discovery of a novel and potent class of fabI-directed antibacterial agents. Antimicrob Agents Chemother 46:3118–3124.

228. Tipparaju SK, Joyasawal S, Forrester S, Mulhearn DC, Pegan S, Johnson ME, Mesecar AD, Kozikowski AP. 2008. Design and synthesis of 2-pyridones as novel inhibitors of the *Bacillus anthracis* enoyl-ACP reductase. Bioorg Med Chem Lett 18:3565–3569.

229. Lu XY, You QD, Chen YD. 2010. Recent Progress in the Identification and Development of InhA Direct Inhibitors of *Mycobacterium tuberculosis*. Mini-Reviews Med Chem 10:182–193.

230. Pan P, Tonge PJ. 2012. Targeting InhA, the FASII Enoyl-ACP Reductase: SAR Studies on Novel Inhibitor Scaffolds. Curr Top Med Chem. 12(7):672–693.

231. Pauli I, Dos Santos RN, Rostirolla DC, Martinelli LK, Ducati RG, Timmers LFSM, Basso LA, Santos DS, Guido RVC, Andricopulo AD, Norberto De Souza O. 2013. Discovery of new inhibitors of *Mycobacterium tuberculosis* InhA enzyme using virtual screening and a 3D-pharmacophore-based approach. J Chem Inf Model 53:2390–2401.

232. Holas O, Ondrejcek P, Dolezal M. 2015. *Mycobacterium tuberculosis* enoyl-acyl carrier protein reductase inhibitors as potential antituberculotics: Development in the past decade. J Enzyme Inhib Med Chem 30:629–648.

233. Perryman AL, Yu W, Wang X, Ekins S, Forli S, Li SG, Freundlich JS, Tonge PJ, Olson AJ. 2015. A virtual screen discovers novel, fragment-sized inhibitors of *Mycobacterium tuberculosis* InhA. J Chem Inf Model 55:645–659.

234. Soutter HH, Centrella P, Clark MA, Cuozzo JW, Dumelin CE, Guie M-A, Habeshian S, Keefe AD, Kennedy KM, Sigel EA, Troast DM, Zhang Y, Ferguson AD, Davies G, Stead ER, Breed J, Madhavapeddi P, Read JA. 2016. Discovery of cofactor-specific, bactericidal *Mycobacterium tuberculosis* InhA inhibitors using DNA-encoded library technology. Proc Natl Acad Sci 113:E7880–E7889.

235. Harding CM, Hennon SW, Feldman MF. 2018. Uncovering the mechanisms of *Acinetobacter baumannii* virulence. Nat Rev Microbiol 16:91–102.

236. Peleg AY, Seifert H, Paterson DL. 2008. *Acinetobacter baumannii*: Emergence of a successful pathogen. Clin Microbiol Rev 21(3):538–582.

237. Howard A, O'Donoghue M, Feeney A, Sleator RD. 2012. *Acinetobacter baumannii*: An emerging opportunistic pathogen. Virulence 3(3):243–250.

238. Antunes LCS, Visca P, Towner KJ. 2014. *Acinetobacter baumannii*: Evolution of a global pathogen. Pathog Dis 71:292–301.

239. Jacobs AC, Thompson MG, Black CC, Kessler JL, Clark LP, McQueary CN, Gancz HY, Corey BW, Moon JK, Si Y, Owen MT, Hallock JD, Kwak YI, Summers A, Li CZ, Rasko DA, Penwell WF, Honnold CL, Wise MC, Waterman PE, Lesho EP, Stewart RL, Actis LA, Palys TJ, Craft DW, Zurawski DV. 2014. AB5075, a highly virulent isolate of *Acinetobacter baumannii*, as a model strain for the evaluation of pathogenesis and antimicrobial treatments. mBio 5(3):e01076-14.

240. Weinstein RA, Gaynes R, Edwards JR. 2005. Overview of Nosocomial Infections Caused by Gram-Negative Bacilli. Clin Infect Dis 41:848–854.

241. Joung MK, Kwon KT, Kang CI, Cheong HS, Rhee J young, Jung DS, Chung SM, Lee JA, Moon S youn, Ko KS, Chung DR, Lee NY, Song JH, Peck KR. 2010. Impact of inappropriate antimicrobial therapy on outcome in patients with hospital-acquired pneumonia caused by *Acinetobacter baumannii*. J Infect 61:212–218.

242. Restrepo MI, Sc M, Anzueto A. 2009. The Role of Gram-Negative Bacteria in Healthcare-Associated Pneumonia. Semin Respir Crit Care Med 30:61–66

243. Francesca L, Claudia V, Gianfranco D. 2014. Biofilm formation in *Acinetobacter baumannii*. New Microbiol 37:119–127.

244. CDC. 1996. CDC Definitions of Nosocomial Infections. Infect Control 1–20.

245. Weingarten CM, Rybak MJ, Jahns BE, Stevenson JG, Brown WJ, Levine DP. 1999. Evaluation of *Acinetobacter baumannii* infection and colonization, and antimicrobial treatment patterns in an urban teaching hospital. Pharmacotherapy 19:1080–1085.

246. Ntusi NBA, Badri M, Khalfey H, Whitelaw A, Oliver S, Piercy J, Raine R, Joubert I, Dheda K. 2012. ICU-Associated *Acinetobacter baumannii* Colonisation/Infection in a High HIV-Prevalence Resource-Poor Setting. PLoS One 7:1–7.

247. Cunha BA. 2010. Optimal Therapy for Multidrug-Resistant *Acinetobacter baumannii*. Emerging Infectious Diseases 16(1):170-171.

248. Fishbain J, Peleg AY. 2010. Treatment of *Acinetobacter* infections. Clinical Infectious Diseases 51(1):79–84.

249. Rodríguez-Baño J, Martí S, Soto S, Fernández-Cuenca F, Cisneros JM, Pachón J, Pascual A, Martínez-Martínez L, McQueary C, Actis LA, Vila J. 2008. Biofilm formation in *Acinetobacter baumannii*: associated features and clinical implications. Clin Microbiol Infect 14:276–278.

250. Lee HW, Koh YM, Kim J, Lee JC, Lee YC, Seol SY, Cho DT. 2008. Capacity of multidrug-resistant clinical isolates of *Acinetobacter baumannii* to form biofilm and adhere to epithelial cell surfaces. Clin Microbiol Infect 14:49–54.

251. Gaddy JA, Actis LA. 2009. Regulation of *Acinetobacter baumannii* biofilm formation. Future Microbiol 4:273–278.

252. Brossard KA, Campagnari AA. 2012. The *Acinetobacter baumannii* biofilm-associated protein plays a role in adherence to human epithelial cells. Infect Immun 80:228–233.

253. Espinal P, Martí S, Vila J. 2012. Effect of biofilm formation on the survival of *Acinetobacter baumannii* on dry surfaces. J Hosp Infect 80:56–60.

254. Gurung J, Khyriem AB, Banik A, Lyngdoh WV, Choudhury B, Bhattacharyya P. 2013. Association of biofilm production with multidrug resistance among clinical isolates of *Acinetobacter baumannii* and *Pseudomonas aeruginosa* from intensive care unit. Indian J Crit Care Med. 17(4):214–218.

255. Francesca L, Claudia V, Gianfranco D. 2014. Biofilm formation in *Acinetobacter baumannii*. New Microbiol 37:119–127.

256. Babapour E, Haddadi A, Mirnejad R, Angaji SA, Amirmozafari N. 2016. Biofilm formation in clinical isolates of nosocomial *Acinetobacter baumannii* and its relationship with multidrug resistance. Asian Pac J Trop Biomed 6:528–533.

257. Qi L, Li H, Zhang C, Liang B, Li J, Wang L, Du X, Liu X, Qiu S, Song H. 2016. Relationship between antibiotic resistance, biofilm formation, and biofilm-specific resistance in *Acinetobacter baumannii*. Front Microbiol 7:483:1–10.

258. Greene C, Vadlamudi G, Newton D, Foxman B, Xi C. 2016. The influence of biofilm formation and multidrug resistance on environmental survival of clinical and environmental isolates of *Acinetobacter baumannii*. Am J Infect Control 44:e65–e71.

259. Bardbari AM, Arabestani MR, Karami M, Keramat F, Alikhani MY, Bagheri KP. 2017. Correlation between ability of biofilm formation with their responsible genes and MDR patterns in clinical and environmental *Acinetobacter baumannii* isolates. Microb Pathog 108:122–128.

260. Bergogne-Bérézin E and Towner, J K. 1996. Acinetobacter spp . as Nosocomial Pathogens : Microbiological , Clinical , and Epidemiological Features. Clin Microbiol Rev 9:148–165.

261. Fzal-Shah MA and Livermore DM. 1998. Worldwide emergence of carbapenem-resistant Acinetobacter spp . J Antimicrob Chemother 41: 576–577.

262. Kempf M, Rolain JM. 2012. Emergence of resistance to carbapenems in *Acinetobacter baumannii* in Europe: Clinical impact and therapeutic options. Int J Antimicrob Agents 39:105–114.

263. Peleg AY, Seifert H, Paterson DL. 2008. *Acinetobacter baumannii*: Emergence of a successful pathogen. Clin Microbiol Rev 21:538–582.

264. Jain R, Danziger LH. 2004. Multidrug-resistant Acinetobacter infections: An emerging challenge to clinicians. Ann Pharmacother 38:1449–1459.

265. Katragkou A, Roilides E. 2005. Successful Treatment of Multidrug-Resistant *Acinetobacter baumannii* Central Nervous System Infections with Colistin. J Clin Microbiol 43(9):4916–4917.

266. Bassetti M, Righi E, Esposito S, Petrosillo N, Nicolini L. 2008. Drug treatment for multidrug-resistant *Acinetobacter baumannii* infections. Future Microbiol 3(6):649-660.

267. Neonakis IK, Spandidos DA, Petinaki E. 2011. Confronting multidrug-resistant *Acinetobacter baumannii*: A review. Int J Antimicrob Agents 37:102–109.

268. Richards JJ, Reed CS, Melander C. 2008. Effects of N-pyrrole substitution on the anti-biofilm activities of oroidin derivatives against *Acinetobacter baumannii*. Bioorganic Med Chem Lett 18:4325–4327.

269. Runci F, Bonchi C, Frangipani E, Visaggio D, Visca P. 2017. *Acinetobacter baumannii* biofilm formation in human serum and disruption by gallium. Antimicrob Agents Chemother 61:1–8.

270. Tuon FF, Rocha JL, Merlini AB. 2015. Combined therapy for multi-drug-resistant *Acinetobacter baumannii* infection – is there evidence outside the laboratory? J Med Microbiol 64:951–959.

271. Beda Daniela IM, Acosta Liudmila V, Daniel AZ, Vazquez Rafael V, Escamilla Eduardo L, Badillo Raymundo R, Rodriguez Zulueta AP. 2017. Strategies of Treatment for Extensively Drug-Resistant *Acinetobacter baumannii* Infections: Single Centre Experience. J Infect Dis Med 02:1–6.

272. Rizk NA, Kanafani ZA, Tabaja HZ, Kanj SS. 2017. Extended infusion of beta-lactam antibiotics: optimizing therapy in critically-ill patients in the era of antimicrobial resistance. Expert Rev Anti Infect Ther 15:645–652.

273. Dellit TH, Owens RC, McGowan JE, Gerding DN, Weinstein RA, Burke JP, Huskins WC, Paterson DL, Fishman NO, Carpenter CF, Brennan PJ, Billeter M, Hooton TM. 2007. Infectious Diseases Society of America and the Society for Healthcare Epidemiology of America Guidelines for Developing an Institutional Program to Enhance Antimicrobial Stewardship. Clin Infect Dis 44:159–177.

274. Swe Swe-Han K, Mlisana KP, Pillay M. 2017. Analysis of clinical and microbiological data on *Acinetobacter baumannii* strains assist the preauthorization of antibiotics at the patient level for an effective antibiotic stewardship program. J Infect Public Health 10:608–616.

275. Karaiskos I, Giamarellou H. 2014. Multidrug-resistant and extensively drug-resistant Gram-negative pathogens: current and emerging therapeutic approaches. Expert Opin Pharmacother 15:1351–1370.

276. Paton R, Miles RS, Hood J AS. 1993. ARI- 1: beta-lactamase-mediated imipenem resistance in *Acinetobacter baumannii*. Int J Antimicrob Agents 2:81–88.

277. Okpara AU, Maswoswe JJ. 1994. Emergence of multidrug-resistant isolates of *Acinetobacter baumannii*. Am J Hosp Pharm 51:2671–2675.

278. Zhang Y-Y, Liang Z-X, Li C-S, Chang Y, Ma X-Q, Yu L, Chen L-A. 2018. Whole-Genome Analysis of an Extensively Drug-Resistant *Acinetobacter baumannii* Strain XDR-BJ83: Insights into the Mechanisms of Resistance of an ST368 Strain from a Tertiary Care Hospital in China. Microb Drug Resist 00:mdr.2017.0246.

279. Hujer KM, Hujer AM, Hulten EA, Bajaksouzian S, Adams JM, Donskey CJ, Ecker DJ, Massire C, Eshoo MW, Sampath R, Thomson JM, Rather PN, Craft DW, Fishbain JT, Ewell AJ, Jacobs MR, Paterson DL, Bonomo RA. 2006. Analysis of antibiotic resistance genes in multidrug-resistant Acinetobacter sp. isolates from military and civilian patients treated at the Walter Reed Army Medical Center. Antimicrob Agents Chemother 50:4114–4123.

280. Lolans K, Rice TW, Munoz-Price LS, Quinn JP. 2006. Multicity outbreak of carbapenem-resistant *Acinetobacter baumannii* isolates producing the carbapenemase OXA-40. Antimicrob Agents Chemother 50:2941–2945.

281. Kempf M, Rolain JM. 2012. Emergence of resistance to carbapenems in *Acinetobacter baumannii* in Europe: Clinical impact and therapeutic options. Int J Antimicrob Agents 39:105–114.

282. Fouad M, Attia AS, Tawakkol WM, Hashem AM. 2013. Emergence of carbapenem-resistant *Acinetobacter baumannii* harboring the OXA-23 carbapenemase in intensive care units of Egyptian hospitals. Int J Infect Dis 17:e1252–e1254.

283. Sung JY, Koo SH, Kim S, Kwon GC. 2016. Persistence of multidrug-resistant *Acinetobacter baumannii* isolates harboring blaOXA-23 and bap for 5 years. J Microbiol Biotechnol 26:1481–1489.

284. Rolain JM, Diene SM, Kempf M, Gimenez G, Robert C, Raoult D. 2013. Real-time sequencing to decipher the molecular mechanism of resistance of a clinical pan-drug-resistant *Acinetobacter baumannii* isolate from Marseille, France. Antimicrob Agents Chemother 57:592–596.

285. Zhu Y, Yi Y, Liu F, Lv N, Yang X, Li J, Hu Y, Zhu B. 2014. Distribution and molecular profiling of class 1 integrons in MDR *Acinetobacter baumannii* isolates and whole genome-based analysis of antibiotic resistance mechanisms in a representative strain. Microbiol Res 169:811–816.

286. Huang C, Long Q, Qian K, Fu T, Zhang Z, Liao P, Xie J. 2015. Resistance and integron characterization of *Acinetobacter baumannii* in a teaching hospital in Chongqing, China. New Microbes New Infect 8:103–108.

287. Bhatt P, Tandel K, Shete V, Rathi KR. 2015. Burden of extensively drug-resistant and pandrug-resistant Gram-negative bacteria at a tertiary-care centre. New Microbes New Infect 8:166–170.

288. Pagano M, Martins AF, Barth AL. 2016. Mobile genetic elements related to carbapenem resistance in *Acinetobacter baumannii*. Brazilian J Microbiol 47:785–792.

289. Goudarzi H, Azad M, Seyedjavadi SS, Azimi H, Salimi Chirani A, Fallah Omrani V, Goudarzi M. 2016. Characterization of integrons and associated gene cassettes in *Acinetobacter baumannii* strains isolated from intensive care unit in Tehran, Iran. J Acute Dis 5:386–392.

290. Infection N, Denis S. 2016. Characterisation and antimicrobial resistance of sepsis pathogens in neonates born in tertiary care centres in Delhi, India: a cohort study. Lancet Glob Heal 4:e752–e760.

291. Neves FC, Clemente WT, Lincopan N, Paião ID, Neves PR, Romanelli RM, Lima SSS, Paiva LF, Mourão PHO, Nobre-Junior VA. 2016. Clinical and microbiological characteristics of OXA-23- and OXA-143-producing *Acinetobacter baumannii* in ICU patients at a teaching hospital, Brazil. Brazilian J Infect Dis 20:556–563.

292. Rolain JM, Loucif L, Al-Maslamani M, Elmagboul E, Al-Ansari N, Taj-Aldeen S, Shaukat A, Ahmedullah H, Hamed M. 2016. Emergence of multidrug-resistant

Acinetobacter baumannii producing OXA-23 Carbapenemase in Qatar. New Microbes New Infect 11:47–51.

293. Deylam Salehi M, Ferdosi-Shahandashti E, Yahyapour Y, Khafri S, Pournajaf A, Rajabnia R. 2017. Integron-Mediated Antibiotic Resistance in *Acinetobacter baumannii* Isolated from Intensive Care Unit Patients, Babol, North of Iran. Biomed Res Int 2017.

294. Jajoo M, Manchanda V, Chaurasia S, Jeeva Sankar M, Gautam H, Agarwal R, Yadav CP, Aggarwal KC, Chellani H, Ramji S, Deb M, Gaind R, Kumar S, Arya S, Sreenivas V, Kapil A, Mathur P, Rasaily R, Deorari AK, Paul VK. 2018. Alarming rates of antimicrobial resistance and fungal sepsis in outborn neonates in North India. PLoS One 13:1–16.

295. Agyepong N, Govinden U, Owusu-Ofori A, Essack SY. 2018. Multidrug-resistant gram-negative bacterial infections in a teaching hospital in Ghana. Antimicrob Resist Infect Control 7:1–8.

296. Poirel L, Nordmann P. 2006. Carbapenem resistance in *Acinetobacter baumannii*: Mechanisms and epidemiology. Clin Microbiol Infect 12:826–836.

297. Gordon NC, Wareham DW. 2010. Multidrug-resistant *Acinetobacter baumannii*: mechanisms of virulence and resistance. Int J Antimicrob Agents 35:219–226.

298. Esterly JS, Richardson CL, Eltoukhy NS, Qi C, Scheetz MH. 2011. Genetic mechanisms of antimicrobial resistance of *Acinetobacter baumannii*. Ann Pharmacother 45:218–228.

299. Zarrilli R, Pournaras S, Giannouli M, Tsakris A. 2013. Global evolution of multidrug-resistant *Acinetobacter baumannii* clonal lineages. Int J Antimicrob Agents 41:11–19.

300. Potron A, Poirel L, Nordmann P. 2015. Emerging broad-spectrum resistance in *Pseudomonas aeruginosa* and *Acinetobacter baumannii*: Mechanisms and epidemiology. Int J Antimicrob Agents 45:568–585.

301. Farajnia S, Azhari F, Alikhani MY, Hosseini MK, Peymani A, Sohrabi N. 2013. Prevalence of PER and VEB type extended spectrum betalactamases among multidrug resistant *Acinetobacter baumannii* isolates in North-West of Iran. Iran J Basic Med Sci 16:751–755.

302. Singla P. 2014. Co-production of ESBL and AmpC β-Lactamases in Clinical Isolates of A. baumannii and A. lwoffii in a Tertiary Care Hospital From Northern India. J Clin Diagnostic Res 8:8–11.

303. Mak JK, Kim MJ, Pham J, Tapsall J, White PA. 2009. Antibiotic resistance determinants in nosocomial strains of multidrug-resistant *Acinetobacter baumannii*. J Antimicrob Chemother 63:47–54.

304. Giammanco A, Calà C, Fasciana T, Dowzicky MJ. 2017. Global Assessment of the Activity of Tigecycline against Multidrug-Resistant Gram-Negative Pathogens between 2004 and 2014 as Part of the Tigecycline Evaluation and Surveillance Trial. mSphere 2:e00310-16.

305. Soltani B, Heidari H, Ebrahim-Saraie HS, Hadi N, Mardaneh J, Motamedifar M. 2018. Molecular characteristics of multiple and extensive drug-resistant *Acinetobacter baumannii* isolates obtained from hospitalized patients in Southwestern Iran. Infez Med 26:67–76.

306. Zhang J, Wang J, Chen L, Yassin AK, Kelly P, Butaye P, Li J, Gong J, Cattley R, Qi K, Wang C. 2018. Housefly (Musca domestica) and blow fly (Protophormia terraenovae) as vectors of bacteria carrying colistin resistance genes. Appl Environ Microbiol 84:1–8.

307. Verma P, Maurya P, Tiwari M, Tiwari V. 2017. In-silico interaction studies suggest RND efflux pump mediates polymyxin resistance in *Acinetobacter baumannii*. J Biomol Struct Dyn 1–9.

308. Machado D, Antunes J, Simões A, Perdigão J, Couto I, McCusker M, Martins M, Portugal I, Pacheco T, Batista J, Toscano C, Viveiros M. 2018. Contribution of efflux to colistin heteroresistance in a multidrug resistant *Acinetobacter baumannii* clinical isolate. J Med Microbiol 67:740–749.

309. Karalewitz APA, Millera SI. 2018. Multidrug-resistant *Acinetobacter baumannii* chloramphenicol resistance requires an inner membrane permease. Antimicrob Agents Chemother 62.

310. Penwell WF, Shapiro AB, Giacobbe RA, Gu RF, Gao N, Thresher J, McLaughlin RE, Huband MD, DeJonge BLM, Ehmann DE, Miller AA. 2015. Molecular mechanisms of

sulbactam antibacterial activity and resistance determinants in *Acinetobacter baumannii*. Antimicrob Agents Chemother 59:1680–1689.

311. Jaruratanasirikul S, Wongpoowarak W, Wattanavijitkul T, Sukarnjanaset W, Samaeng M, Nawakitrangsan M, Ingviya N. 2016. Population pharmacokinetics and pharmacodynamics modeling to optimize dosage regimens of sulbactam in critically ill patients with severe sepsis caused by *Acinetobacter baumannii*. Antimicrob Agents Chemother 60:7236–7244.

312. Wang YC, Kuo SC, Yang YS, Lee YT, Chiu CH, Chuang MF, Lin JC, Chang FY, Chen TL. 2016. Individual or combined effects of meropenem, imipenem, sulbactam, colistin, and tigecycline on biofilm-embedded *Acinetobacter baumannii* and biofilm architecture. Antimicrob Agents Chemother 60:4670–4676.

313. Durand-Réville TF, Guler S, Comita-Prevoir J, Chen B, Bifulco N, Huynh H, Lahiri S, Shapiro AB, McLeod SM, Carter NM, Moussa SH, Velez-Vega C, Olivier NB, McLaughlin R, Gao N, Thresher J, Palmer T, Andrews B, Giacobbe RA, Newman J V., Ehmann DE, De Jonge B, O'Donnell J, Mueller JP, Tommasi RA, Miller AA. 2017. ETX2514 is a broad-spectrum β-lactamase inhibitor for the treatment of drug-resistant Gram-negative bacteria including *Acinetobacter baumannii*. Nat Microbiol 2.

314. Barnes MD, Bethel CR, Rutter JD, Akker F Van Den, Papp-Wallace KM, Bonomo RA. 2017. The Novel β-Lactamase Inhibitor, ETX-2514, in Combination with Sulbactam Effectively Inhibits *Acinetobacter baumannii*. Open Forum Infect Dis 4:S368–S368.

315. Mushtaq S, Vickers A, Woodford N, Livermore DM. 2017. WCK 4234, a novel diazabicyclooctane potentiating carbapenems against Enterobacteriaceae, Pseudomonas and Acinetobacter with class A, C and D β-lactamases. J Antimicrob Chemother 72:1688–1695.

316. Sader HS, Rhomberg PR, Flamm RK, Jones RN, Castanheira M. 2017. WCK 5222 (cefepime/zidebactam) antimicrobial activity tested against Gram-negative organisms producing clinically relevant β-lactamases. J Antimicrob Chemother 72:1696–1703.

317. Vázquez-Ucha JC, Maneiro M, Martínez-Guitián M, Buynak J, Bethel CR, Bonomo RA, Bou G, Poza M, González-Bello C, Beceiro A. 2017. Activity of the ß-Lactamase

inhibitor LN-1-255 against carbapenem-hydrolyzing class D ß-Lactamases from *Acinetobacter baumannii*. Antimicrob Agents Chemother 61:1–17.

318. Ruggiero M, Papp-Wallace KM, Taracila MA, Mojica MF, Bethel CR, Rudin SD, Zeiser ET, Gutkind G, Bonomo RA, Power P. 2017. Exploring the landscape of diazabicyclooctane (DBO) inhibition: Avibactam inactivation of PER-2 β-Lactamase. Antimicrob Agents Chemother 61:1–28.

319. Lenhard JR, Smith NM, Bulman ZP, Tao X, Thamlikitkul V, Shin BS, Nation RL, Li J, Bulitta JB, Tsuji BT. 2017. High-Dose Ampicillin-Sulbactam Combinations Combat Polymyxin-Resistant *Acinetobacter baumannii* in a Hollow-Fiber Infection Model. Antimicrob Agents Chemother 61:1–6.

320. Chen H, Liu Q, Chen Z, Li C. 2017. Efficacy of sulbactam for the treatment of *Acinetobacter baumannii* complex infection: A systematic review and meta-analysis. J Infect Chemother 23:278–285.

321. Zhao Y, Prideaux B, Nagasaki Y, Lee MH, Chen P-Y, Blanc L, Ho H, Clancy CJ, Nguyen MH, Dartois V, Perlin DS. 2017. Unraveling Drug Penetration of Echinocandin Antifungals at the Site of Infection in an Intra-abdominal Abscess Model. Antimicrob Agents Chemother 61:88–89.

322. Madadi-Goli N, Moniri R, Bagheri-Josheghani S, Dasteh-Goli N. 2017. Sensitivity of levofloxacin in combination with ampicillin-sulbactam and tigecycline against multidrug-resistant *Acinetobacter baumannii*. Iran J Microbiol 9:19–25.

323. Makris D, Petinaki E, Tsolaki V, Manoulakas E, Mantzarlis K, Apostolopoulou O, Sfyras D, Zakynthinos E. 2018. Colistin versus colistin combined with ampicillin-sulbactam for multiresistant *Acinetobacter baumannii* ventilator-associated pneumonia treatment: An open-label prospective study. Indian J Crit Care Med 22:67-77.

324. Leelasupasri S, Santimaleeworagun W, Jitwasinkul T. 2018. Antimicrobial Susceptibility among Colistin, Sulbactam, and Fosfomycin and a Synergism Study of Colistin in Combination with Sulbactam or Fosfomycin against Clinical Isolates of Carbapenem-Resistant *Acinetobacter baumannii*. J Pathog 2018:1–5.

325. Fan B, Guan J, Wang X, Cong Y. 2016. Activity of colistin in combination with meropenem, tigecycline, fosfomycin, fusidic acid, rifampin or sulbactam against extensively drug-resistant *Acinetobacter baumannii* in a murine thigh-infection model. PLoS One 11:1–12.

326. Ye JJ, Lin HS, Yeh CF, Wu YM, Huang PY, Yang CC, Huang CT, Lee MH. 2016. Tigecycline-based versus sulbactam-based treatment for pneumonia involving multidrug-resistant Acinetobacter calcoaceticus-*Acinetobacter baumannii* complex. BMC Infect Dis 16:1–11.

327. Shameem M, Mir MA. 2016. Management of pneumonia and blood stream infections with new antibiotic adjuvant entity (ceftriaxone + sulbactam + disodium edetate)- a novel way to spare carbapenems. J Clin Diagnostic Res 10:LC23-LC27.

328. Shapiro AB. 2017. Kinetics of Sulbactam Hydrolysis by β-Lactamases, and Kinetics of β-Lactamase Inhibition by Sulbactam. Antimicrob Agents Chemother 61:1–10.

329. Li T, Sheng M, Gu T, Zhang Y, Yirepanjiang A, Li Y. 2018. *In vitro* assessment of cefoperazone-sulbactam based combination therapy for multidrug-resistant *Acinetobacter baumannii* isolates in China. J Thorac Dis 10:1370–1376.

330. Liu X, Zheng H, Zhang W, Shen Z, Zhao M, Chen Y, Sun L, Shi J, Zhang J. 2016. Tracking cefoperazone/sulbactam resistance development *In vivo* in a. baumannii isolated from a patient with hospital-acquired pneumonia by whole-genome sequencing. Front Microbiol 7:1–9.

331. Leclercq R, Cantón R, Brown DFJ, Giske CG, Heisig P, Macgowan AP, Mouton JW, Nordmann P, Rodloff AC, Rossolini GM, Soussy CJ, Steinbakk M, Winstanley TG, Kahlmeter G. 2013. EUCAST expert rules in antimicrobial susceptibility testing. Clin Microbiol Infect 19:141–160.

332. Ramirez MS, Don M, Merkier AK, Bistué AJS, Zorreguieta A, Centrón D, Tolmasky ME. 2010. Naturally competent *Acinetobacter baumannii* clinical isolate as a convenient model for genetic studies. J Clin Microbiol 48:1488–1490.

333. Wilharm G, Piesker J, Laue M, Skiebe E. 2013. DNA Uptake by the nosocomial pathogen *Acinetobacter baumannii* occurs during movement along wet surfaces. J Bacteriol 195:4146–4153.

334. He X, Lu F, Yuan F, Jiang D, Zhao P, Zhu J, Cheng H, Cao J, Lu G. 2015. Biofilm formation caused by clinical *Acinetobacter baumannii* isolates is associated with overexpression of the AdeFGH efflux pump. Antimicrob Agents Chemother 59:4817–4825.

335. Wright MS, Iovleva A, Jacobs MR, Bonomo RA, Adams MD. 2016. Genome dynamics of multidrug-resistant *Acinetobacter baumannii* during infection and treatment. Genome Med 8:1–12.

336. Wolf J. 2018. Induction of *Acinetobacter baumannii* Natural Competence 5–7.

337. Khan S, Beattie TK, Knapp CW. 2016. Relationship between antibiotic- and disinfectant-resistance profiles in bacteria harvested from tap water. Chemosphere 152:132–141.

338. Crépin S, Ottosen EN, Peters K, Smith SN, Himpsl SD, Vollmer W, Mobley HLT. 2018. The lytic transglycosylase MltB connects membrane homeostasis and *in vivo* fitness of *Acinetobacter baumannii*. Mol Microbiol. 109(6):745-762.

339. Pakharukova N, Tuittila M, Paavilainen S, Malmi H, Parilova O, Teneberg S, Knight SD, Zavialov A V. 2018. Structural basis for *Acinetobacter baumannii* biofilm formation. Proc Natl Acad Sci 115:5558–5563.

340. Kattan JN, Villegas M V., Quinn JP. 2008. New developments in carbapenems. Clin Microbiol Infect 14:1102–1111.

341. Westly E. 2012. India moves to tackle antibiotic resistance. Nature 489:192.

342. Mezzatesta ML, Caio C, Gona F, Cormaci R, Salerno I, Zingali T, Denaro C, Gennaro M, Quattrone C, Stefani S. 2014. Carbapenem and multidrug resistance in Gram-negative bacteria in a single centre in Italy: Considerations on *in vitro* assay of active drugs. Int J Antimicrob Agents 44:112–116.

343. Bassetti M, Righi E. 2015. New antibiotics and antimicrobial combination therapy for the treatment of gram-negative bacterial infections. Curr Opin Crit Care 21:402–411.

344. Knirsch C, Alemayehu D, Botgros R, Comic-Savic S, Friedland D, Holland TL, Merchant M, Noel GJ, Pelfrene E, Reith C, Santiago J, Tiernan R, Tenearts P, Goldsack JC, Fowler Jr VJ. 2016. Improving Conduct and Feasibility of Clinical Trials to Evaluate Antibacterial Drugs to Treat Hospital-Acquired Bacterial Pneumonia and Ventilator-Associated Bacterial Pneumonia: Recommendations of the Clinical Trials Transformation Initiative Antibacterial Drug Development Project Team. Clinical Infectious Diseases 63(S2):S29–36.

345. Alvarez-Marin R, Aires-de-Sousa M, Nordmann P, Kieffer N, Poirel L. 2017. Antimicrobial activity of octenidine against multidrug-resistant Gram-negative pathogens. Eur J Clin Microbiol Infect Dis 36:2379–2383.

346. Bader MS, Loeb M, Brooks AA. 2017. An update on the management of urinary tract infections in the era of antimicrobial resistance. Postgrad Med 129:242–258.

347. Domalaon R, Yang X, Lyu Y, Zhanel GG, Schweizer F. 2017. Polymyxin B3-Tobramycin Hybrids with *Pseudomonas aeruginosa*-Selective Antibacterial Activity and Strong Potentiation of Rifampicin, Minocycline, and Vancomycin. ACS Infect Dis 3:941–954.

348. Mahmoudi M, Zhou X. 2016. Finding optimal solutions for vehicle routing problem with pickup and delivery services with time windows: A dynamic programming approach based on state-space-time network representations. Transp Res Part B Methodol 89:19–42.

349. Boonyanugomol W, Kraisriwattana K, Rukseree K, Boonsam K, Narachai P. 2017. *In vitro* synergistic antibacterial activity of the essential oil from Zingiber cassumunar Roxb against extensively drug-resistant *Acinetobacter baumannii* strains. J Infect Public Health 10:586–592.

350. Zhang Z-G, Chen F, Chen J-Z. 2018. Introducing an antibiotic stewardship program in a pediatric center in China. World J Pediatr 14:274–279.

351. Tiwari V, Mishra N, Gadani K, Solanki PS, Shah NA, Tiwari M. 2018. Mechanism of anti-bacterial activity of zinc oxide nanoparticle against Carbapenem-Resistant *Acinetobacter baumannii*. Front Microbiol 9:1–10.

352. Norsigian CJ, Kavvas E, Seif Y, Palsson BO, Monk JM. 2018. iCN718, an updated and improved genome-scale metabolic network reconstruction of *Acinetobacter baumannii* AYE. Front Genet 9:1–9.

353. Verma P, Tiwari M, Tiwari V. 2018. *In silico* high-throughput virtual screening and molecular dynamics simulation study to identify inhibitor for AdeABC efflux pump of *Acinetobacter baumannii*. J Biomol Struct Dyn 36:1182–1194.

354. Avery LM, Nicolau DP. 2018. Investigational drugs for the treatment of infections caused by multidrug-resistant Gram-negative bacteria. Expert Opinion on Investigational Drugs 27(4):325-338.

355. Kidd JM, Kuti JL, Nicolau DP. 2018. Novel pharmacotherapy for the treatment of hospital-acquired and ventilator-associated pneumonia caused by resistant gram-negative bacteria. Expert Opin Pharmacother 19:397–408.

356. Velkov T, Dai C, Ciccotosto GD, Cappai R, Hoyer D, Li J. 2018. Polymyxins for CNS infections: Pharmacology and neurotoxicity. Pharmacol Ther 181:85–90.

357. Waite RD, Stewart JE, Stephen AS, Allaker RP. 2018. Activity of a nitric oxide-generating wound treatment system against wound pathogen biofilms. Int J Antimicrob Agents 52:338–343.

358. Rahman H, Khan I, Hussain A, Shahat AA, Tawab A, Qasim M, Adnan M, Al-Said MS, Ullah R, Khan SN. 2018. Glycyrrhiza glabra HPLC fractions: identification of Aldehydo Isoophiopogonone and Liquirtigenin having activity against multidrug resistant bacteria. BMC Complement Altern Med 18:140.

359. Singh R, Vora J, Nadhe SB, Wadhwani SA, Shedbalkar UU, Chopade BA. 2018. Antibacterial Activities of Bacteriagenic Silver Nanoparticles Against Nosocomial *Acinetobacter baumannii*. J Nanosci Nanotechnol 18:3806–3815.

360. Di Bonaventura I, Baeriswyl S, Capecchi A, Gan BH, Jin X, Siriwardena TN, He R, Köhler T, Pompilio A, Di Bonaventura G, Van Delden C, Javor S, Reymond JL. 2018. An antimicrobial bicyclic peptide from chemical space against multidrug resistant Gram-negative bacteria. Chem Commun 54:5130–5133.

361. Zhang J, Li W, Chen J, Qi W, Wang F, Zhou Y. 2018. Impact of biofilm formation and detachment on the transmission of bacterial antibiotic resistance in drinking water distribution systems. Chemosphere 203:368–380.

362. Chung PY. 2018. Current Technology in the Discovery and Development of Novel Antibacterials. Curr Drug Targets 19 (7):832–840.

363. Zhao F, Lan X-Q, Du Y, Chen P-Y, Zhao J, Zhao F, Lee W-H, Zhang Y. 2018. King cobra peptide OH-CATH30 as a potential candidate drug through clinic drug-resistant isolates. Zoological Research 39(2):87–96.

364. Lewis RH, Sharpe JP, Swanson JM, Fabian TC, Croce MA, Magnotti LJ. 2018. Reinventing the Wheel: Impact of Prolonged Antibiotic Exposure on Multi-Drug Resistant Ventilator-Associated Pneumonia in Trauma Patients. J Trauma Acute Care Surg 85:256–262.

365. Wieland K, Chhatwal P, Vonberg RP. 2018. Nosocomial outbreaks caused by *Acinetobacter baumannii* and *Pseudomonas aeruginosa*: Results of a systematic review. Am J Infect Control 46:643–648.

366. Fleeman RM, Debevec G, Antonen K, Adams JL, Santos RG, Welmaker GS, Houghten RA, Giulianotti MA, Shaw LN. 2018. Identification of a novel polyamine scaffold with potent efflux pump inhibition activity toward multi-drug resistant bacterial pathogens. Front Microbiol 9:1–16.

367. Lee HY, Hsu SY, Hsu JF, Chen CL, Wang YH, Chiu CH. 2018. Risk factors and molecular epidemiology of *Acinetobacter baumannii* bacteremia in neonates. J Microbiol Immunol Infect 51:367–376.

368. Skariyachan S, Manjunath M, Bachappanavar N. 2018. Screening of potential lead molecules against prioritised targets of multi-drug-resistant-*Acinetobacter baumannii* – insights from molecular docking, molecular dynamic simulations and *in vitro* assays. J Biomol Struct Dyn 1102:1–24.

369. Qin Y, Zhang J, Wu L, Zhang D, Fu L, Xue X. 2018. Comparison of the treatment efficacy between tigecycline plus high-dose cefoperazone-sulbactam and tigecycline

monotherapy against ventilator-associated pneumonia caused by extensively drug-resistant *Acinetobacter baumannii*. Int J Clin Pharmacol Ther 56:120–129.

370. Lin J, Wang R, Chen J. 2018. Tigecycline-induced acute pancreatitis in a renal transplant patient: a case report and literature review. BMC Infect Dis 18:201.

371. Karumathil DP, Nair MS, Gaffney J, Kollanoor-Johny A, Venkitanarayanan K. 2018. Trans-Cinnamaldehyde and eugenol increase *Acinetobacter baumannii* sensitivity to beta-lactam antibiotics. Front Microbiol 9:1–10.

372. Akhter S, Lund BA, Ismael A, Langer M, Isaksson J, Christopeit T, Leiros HKS, Bayer A. 2018. A focused fragment library targeting the antibiotic resistance enzyme - Oxacillinase-48: Synthesis, structural evaluation and inhibitor design. Eur J Med Chem 145:634–648.

373. Bush K, Bradford PA. 2016. β-Lactams and β-Lactamase Inhibitors: An Overview. Cold Spring Harb Perspect Med 6:a025247.

374. El-Gamal MI, Brahim I, Hisham N, Aladdin R, Mohammed H, Bahaaeldin A. 2017. Recent updates of carbapenem antibiotics. Eur J Med Chem 131:185–195.

375. Docquier JD, Mangani S. 2018. An update on β-lactamase inhibitor discovery and development. Drug Resist Updat 36:13–29.

376. Papp-Wallace KM, Nguyen NQ, Jacobs MR, Bethel CR, Barnes MD, Kumar V, Bajaksouzian S, Rudin SD, Rather PN, Bhavsar S, Ravikumar T, Deshpande PK, Patil V, Yeole R, Bhagwat SS, Patel M V., Van Den Akker F, Bonomo RA. 2018. Strategic Approaches to Overcome Resistance against Gram-Negative Pathogens Using β-Lactamase Inhibitors and β-Lactam Enhancers: Activity of Three Novel Diazabicyclooctanes WCK 5153, Zidebactam (WCK 5107), and WCK 4234. J Med Chem 61:4067–4086.

377. Hamilton-Miller JMT. 1999. β-lactams: variations on a chemical theme, with some surprising biological results. Journal of Antimicrobial Chemotherapy 44:729-734.

378. Holten KB, Onusko EM. 2000. Appropriate prescribing of oral beta-lactam antibiotics. Am Fam Physician 62:611–620.

379. Fernandes R, Amador P, Prudêncio C. 2013. β-Lactams: Chemical structure, mode of action and mechanisms of resistance. Rev Med Microbiol 24:7–17.

380. Birnbaum J, Kahan FM, Kropp H, Macdonald JS. 1985. Carbapenems, a new class of beta-lactam antibiotics. Am J Med 78:3–21.

381. Sp C, Pa T, Dm C. 1987. Imipenem / cilastatin . A review of its antibacterial activity , pharmacokinetic properties and therapeutic efficacy . Drugs 33(3):183-241.

382. Walker G. 2009. Globalizing Environmental Justice. Glob Soc Policy An Interdiscip J Public Policy Soc Dev 9:355–382.

383. Shah PM, Isaacs RD. 2003. Ertapenem, the first of a new group of carbapenems. J Antimicrob Chemother 52:538–542.

384. Fisher JF, Meroueh SO, Mobashery S. 2005. Bacterial resistance to β-lactam antibiotics: Compelling opportunism, compelling opportunity. Chem Rev 105:395–424.

385. Zhanel GG, Johanson C, Embil JM, Noreddin A, Gin A, Vercaigne L, Hoban DJ. 2005. Ertapenem: Review of a new carbapenem. Expert Rev Anti Infect Ther 3:23–39.

386. Dalhoff A, Janjic N, Echols R. 2006. Redefining penems. Biochem Pharmacol 71:1085–1095.

387. Rodloff AC, Goldstein EJC, Torres A. 2006. Two decades of imipenem therapy. J Antimicrob Chemother 58:916–929.

388. Zhanel GG, Wiebe R, Hoban D, Karlowsky JA. 2007. Comparative review of the carbapenems. Drugs 67(7):1027-1052.

389. Burkhardt O, Derendorf H, Welte T. 2007. Ertapenem: the new carbapenem 5 years after first FDA licensing for clinical practice. Expert Opin Pharmacother 8:237–256.

390. Nicolau DP. 2008. Carbapenems: a potent class of antibiotics. Expert Opin Pharmacother 9(1):23–37.

391. Kattan JN, Villegas MV, Quinn JP. 2008. New developments in carbapenems. Clin Microbiol Infect 14: 1102–1111.

392. Reddy P, Chadaga S, Noskin GA. 2009. Antibiotic considerations in the treatment of multidrug-resistant (MDR) pathogens: A case-based review. J Hosp Med 4:8–15.

393. Bassetti M, Nicolini L, Esposito S, Righi E, Viscoli C. 2009. Current Status of Newer Carbapenems. Curr Med Chem 16:564–575.

394. Matthews SJ, Lancaster JW. 2009. Doripenem monohydrate, a broad-spectrum carbapenem antibiotic. Clin Ther 31:42–63.

395. Shakil S, Danishuddin M, Khan AU. 2009. Doripenem Versus Bacteria: An Emerging Battleground. J Chemother 21:482–492.

396. Gamal M, Oh C-H. 2010. Current Status of Carbapenem Antibiotics. Curr Top Med Chem 10:1882–1897.

397. Papp-Wallace KM, Endimiani A, Taracila MA, Bonomo RA. 2011. Carbapenems: Past, present, and future. Antimicrob Agents Chemother 55:4943–4960.

398. Hilliard JJ, Melton JL, Hall LR, Abbanat D, Fernandez J, Ward CK, Bunting RA, Barron A, Lynch AS, Flamm RK. 2011. Comparative effects of carbapenems on bacterial load and host immune response in a Klebsiella pneumoniae murine pneumonia model. Antimicrob Agents Chemother 55(2):836–844.

399. Hawkey PM, Livermore DM. 2012. Carbapenem antibiotics for serious infections. BMJ 344:1–7.

400. Vardakas KZ, Tansarli GS, Rafailidis PI, Falagas ME. 2012. Carbapenems versus alternative antibiotics for the treatment of bacteraemia due to enterobacteriaceae producing extended-spectrum β-lactamases: A systematic review and meta-analysis. J Antimicrob Chemother 67:2793–2803.

401. Bryan J. 2014. Carbapenems have stood the test of time so far but resistance is emerging. Pharm J 292:292.

402. June CM, Vaughan RM, Ulberg LS, Bonomo RA, Witucki LA, Leonard DA. 2014. A fluorescent carbapenem for structure function studies of penicillin-binding proteins, β-lactamases, and β-lactam sensors. Anal Biochem 463:70–74.

403. Yao Q, Wang J, Cui T, Yang Z, Su M, Zhao P, Yan H, Zhan Y, Yang H. 2016. Antibacterial properties of tebipenem pivoxil tablet, a new oral carbapenem preparation against a variety of pathogenic bacteria *in vitro* and *in vivo*. Molecules 21(62):1-14.

404. Poirel L, Nordmann P. 2005. Acquired carbapenem-hydrolyzing β-lactamases and their genetic support - an update. Med Chem Rev--Online 2:183–195.

405. Héritier C, Poirel L, Lambert T, Nordmann P. 2005. Contribution of acquired carbapenem-hydrolyzing oxacillinases to carbapenem resistance in *Acinetobacter baumannii*. Antimicrob Agents Chemother 49:3198–3202.

406. Queenan AM, Bush K. 2007. Carbapenemases: The versatile β-lactamases. Clin Microbiol Rev 20:440–458.

407. Walther-Rasmussen J, Høiby N. 2007. Class A carbapenemases. J Antimicrob Chemother 60:470–482.

408. Zarrilli R, Giannouli M, Tomasone F, Triassi M, Tsakris A. 2009. Carbapenem resistance in *Acinetobacter baumannii*: The molecular epidemic features of an emerging problem in health care facilities. J Infect Dev Ctries 3:335–341.

409. Girlich D, Poirel L, Nordmann P. 2010. Novel ambler class A carbapenem-hydrolyzing β-lactamase from a Pseudomonas fluorescens isolate from the Seine River, Paris, France. Antimicrob Agents Chemother 54:328–332.

410. Diene SM, Rolain JM. 2014. Carbapenemase genes and genetic platforms in Gram-negative bacilli: Enterobacteriaceae, Pseudomonas and Acinetobacter species. Clin Microbiol Infect 20:831–838.

411. Djahmi N, Dunyach-Remy C, Pantel A, Dekhil M, Sotto A, Lavigne JP. 2014. Epidemiology of carbapenemase-producing enterobacteriaceae and *Acinetobacter baumannii* in Mediterranean countries. Biomed Res Int 2014.

412. Nordmann P, Poirel L. 2014. The difficult-to-control spread of carbapenemase producers among Enterobacteriaceae worldwide. Clin Microbiol Infect 20:821–830.

413. Ehlers MM, Hughes JM, Kock MM. 2012. Prevalence of Carbapenemases in *Acinetobacter baumannii*. Antibiot Resist Bact - A Contin Chall New Millenn.

414. Jeon JH, Lee JH, Lee JJ, Park KS, Karim AM, Lee CR, Jeong BC, Lee SH. 2015. Structural basis for carbapenem-hydrolyzing mechanisms of carbapenemases conferring antibiotic resistance. Int J Mol Sci 16:9654–9692.

415. Karampatakis T, Antachopoulos C, Tsakris A, Roilides E. 2017. Molecular epidemiology of carbapenem-resistant *Acinetobacter baumannii* in Greece: An extended review (2000-2015). Future Microbiol 12:801–815.

416. Rodríguez CH, Nastro M, Famiglietti A. 2018. Carbapenemases in *Acinetobacter baumannii*. Review of their dissemination in Latin America. Rev Argent Microbiol 50:327–333.

417. Lamotte-Brasseur J, Dive G, Dideberg O, Charlier P, Frere JM, Ghuysen JM. 1991. Mechanism of acyl transfer by the class A serine beta-lactamase of Streptomyces albus G. Biochem J 279:213–221.

418. Adachi H, Ohta T, Matsuzawa H. 1991. Site-directed mutants, at position 166, of RTEM-I ??-lactamase that form a stable acyl-enzyme intermediate with penicillin. J Biol Chem 266:3186–3191.

419. Strynadka NCJ, Adachi H, Jensen SE, Johns K, Sielecki A, Betzel C, Sutoh K, James MNG. 1992. Molecular structure of the acyl-enzyme intermediate in β-lactam hydrolysis at 1.7 Å resolution. Nature 359:700–705.

420. Banerjee S, Pieper U, Kapadia G, Pannell LK, Herzbere O. 1998. Role of the Ω-loop in the activity, substrate specificity, and structure of class A β-lactamase. Biochemistry 37:3286–3296.

421. Golemi D, Maveyraud L, Ishiwata A, Tramer S, Miyashita K, Nagase T, Massova I, Mourey L, Samama J-P, Mobashery S. 2000. 6-(Hydroxyalkyl)penicillanates as Probes for Mechanisms of β-Lactamases. J Antibiot 53(10):1022–1027.

422. Golemi D, Maveyraud L, Vakulenko S, Tranier S, Ishiwata A, Kotra LP, Samama JP, Mobashery S. 2000. The first structural and mechanistic insights for class D β-lactamases: Evidence for a novel catalytic process for turnover of β-lactam antibiotics [14]. J Am Chem Soc 122:6132–6133.

423. Golemi D, Maveyraud L, Vakulenko S, Samama J, Mobashery S. 2001. Critical involvement of a carbamylated lysine in catalytic function of class D β-lactamases. Proc. Natl. Acad. Sci 98:14280-14285.

424. Maveyraud L, Golemi-Kotra D, Ishiwata A, Meroueh O, Mobashery S, Samama JP. 2002. High-resolution X-ray structure of an acyl-enzyme species for the class D OXA-10, β-lactamase. J Am Chem Soc 124:2461–2465.

425. Golemi-Kotra D, Meroueh SO, Kim C, Vakulenko SB, Bulychev A, Stemmler AJ, Stemmler TL, Mobashery S. 2004. The importance of a critical protonation state and the fate of the catalytic steps in class A ??-lactamases and penicillin-binding proteins. J Biol Chem 279:34665–34673.

426. Page MGP. 2008. Extended-spectrum β-lactamases: Structure and kinetic mechanism. Clin Microbiol Infect 14:63–74.

427. Testero SA, O'Daniel PI, Shi Q, Lee M, Hesek D, Ishiwata A, Noll BC, Mobashery S. 2009. Regiospecific Syntheses of 6α-(1 R -Hydroxyoctyl)penicillanic Acid and 6β-(1 R -Hydroxyoctyl)penicillanic Acid as Mechanistic Probes of Class D β-Lactamases. Org Lett 11:2515–2518.

428. Verma V, Testero SA, Amini K, Wei W, Liu J, Balachandran N, Monoharan T, Stynes S, Kotra LP, Golemi-Kotra D. 2011. Hydrolytic mechanism of OXA-58 enzyme, a carbapenem-hydrolyzing class D β-lactamase from *Acinetobacter baumannii*. J Biol Chem 286:37292–37303.

429. Docquier, J. D. Mangani S. 2015. Structure-Function Relationships of Class D Carbapenemases. Curr Drug Targets 17:1061–1071.

430. Brown S, Amyes S. 2006. OXA β-lactamases in Acinetobacter: The story so far. J Antimicrob Chemother 57:1–3.

431. Lee K, Kim MN, Choi TY, Cho SE, Lee S, Whang DH, Yong D, Chong Y, Woodford N, Livermore DM. 2009. Wide dissemination of OXA-type carbapenemases in clinical Acinetobacter spp. isolates from South Korea. Int J Antimicrob Agents 33:520–524.

432. Hall LMC, Livermore DM, Gur D, Akova M, Akalin HE. 1993. OXA-11, an Extended-Spectrum Variant of OXA-10 (PSE-2), B-Lactamase from *Pseudomonas aeruginosa*. Antimicrob Agents Chemother 37:1637–1644.

433. Danel F, Hall LM, Gur D, Livermore DM, Choi E-H, Kim J, Kim J-H, Kim E-C. 1997. OXA-15, an extended-spectrum variant of OXA-2 beta-lactamase, isolated from a *Pseudomonas aeruginosa* strain. Antimicrob Agents Chemother 41:785–90.

434. Philippon LN, Naas T, Bouthors AT, Barakett V, Nordmann P. 1997. OXA-18, a class D clavulanic acid-inhibited extended-spectrum β-lactamase from *Pseudomonas aeruginosa*. Antimicrob Agents Chemother 41(10):2188–2195.

435. Danel F, Hall LMC, Gur D, Livermore DM. 1998. OXA-16, a further extended-spectrum variant of OXA-10 beta-lactamase, from two *Pseudomonas aeruginosa* isolates. Antimicrob Agents Chemother 42:3117–3122.

436. Naas T, Sougakoff W, Casetta A, Nordmann P. 1998. Molecular characterization of OXA-20, a novel class D β-lactamase, and its integron from *Pseudomonas aeruginosa*. Antimicrob Agents Chemother 42:2074–2083.

437. Maveyraud L, Golemi D, Kotra LP, Tranier S, Vakulenko S, Mobashery S, Samama JP. 2000. Insights into class D β-lactamases are revealed by the crystal structure of the OXA10 enzyme from *Pseudomonas aeruginosa*. Structure 8:1289–1298.

438. Paetzel M , Danel F, de Castro L, Mosimann SC, Page MG, Strynadka NC. 2000. Crystal structure of the class D beta-lactamase OXA-10. Nat Struct Biol. 7(10):918-25.

439. Afzal-Shah M, Woodford N, Livermore DM. 2001. Characterization of OXA-25, OXA-26, and OXA-27, Molecular Class D -Lactamases Associated with Carbapenem Resistance in Clinical Isolates of *Acinetobacter baumannii*. Antimicrob Agents Chemother 45:583–588.

440. Pernot L, Frénois F, Rybkine T, L'Hermite G, Petrella S, Delettré J, Jarlier V, Collatz E, Sougakoff W. 2001. Crystal structures of the class D β-lactamase OXA-13 in the native form and in complex with meropenem. J Mol Biol 310:859–874.

441. Sun T. 2003. Comparison of β-lactamases of classes A and D: 1.5-A crystallographic structure of the class D OXA-1 oxacillinase. Protein Sci 12:82–91.

442. Dalla-Costa LM, Coelho JM, Souza HAPHM, Castro MES, Stier CJN, Bragagnolo KL, Rea-Neto A, Penteado-Filho SR, Livermore DM, Woodford N. 2003. Outbreak of Carbapenem-Resistant *Acinetobacter baumannii* Producing the OXA-23 Enzyme in Curitiba, Brazil. Journal of Clinical Microbiology 41(7):3403–3406.

443. Brown S, Young HK, Amyes SGB. 2005. Characterisation of OXA-51, a novel class D carbapenemase found in genetically unrelated clinical strains of *Acinetobacter baumannii* from Argentina. Clin Microbiol Infect 11:15–23.

444. Poirel L, Marque´ S, He´ritier C, Segonds C, Chabanon G, Nordmann P. 2005. OXA-58, a Novel Class D β-Lactamase Involved in Resistance to Carbapenems in *Acinetobacter baumannii*. Antimicrobial Agents and Chemotherapy 49(1):202–208.

445. Vahaboglu H, Budak F, Kasap M, Gacar G, Torol S, Karadenizli A, Kolayli F, Eroglu C. 2006. High prevalence of OXA-51-type class D β-lactamases among ceftazidime-resistant clinical isolates of Acinetobacter spp.: Co-existence with OXA-58 in multiple centres. J Antimicrob Chemother 58:537–542.

446. Poirel L, Lebessi E, Héritier C, Patsoura A, Foustoukou M, Nordmann P. 2006. Nosocomial spread of OXA-58-positive carbapenem-resistant *Acinetobacter baumannii* isolates in a paediatric hospital in Greece. Clin Microbiol Infect 12:1138–1141.

447. Tsakris A, Ikonomidis A, Pournaras S, Spanakis N, Markogiannakis A. 2006. Carriage of OXA-58 but not of OXA-51 β-lactamase gene correlates with carbapenem resistance in *Acinetobacter baumannii*. J Antimicrob Chemother 58:1097–1099.

448. Coelho J, Woodford N, Afzal-Shah M, Livermore D. 2006. Occurrence of OXA-58-like carbapenemases in Acinetobacter spp. collected over 10 years in three continents. Antimicrob Agents Chemother 50:756–758.

449. Santillana E, Beceiro A, Bou G, Romero A. 2007. Crystal structure of the carbapenemase OXA-24 reveals insights into the mechanism of carbapenem hydrolysis. Proc Natl Acad Sci 104:5354–5359.

450. Evans BA, Hamouda A, Towner KJ, Amyes SGB. 2008. OXA-51-like β-lactamases and their association with particular epidemic lineages of *Acinetobacter baumannii*. Clin Microbiol Infect 14:268–275.

451. Schneider KD, Karpen ME, Bonomo RA, Leonard DA, Powers RA. 2009. The 1.4 Å crystal structure of the class D β-lactamase OXA-1 complexed with doripenem. Biochemistry 48:11840–11847.

452. Baurin S, Vercheval L, Bouillenne F, Falzone C, Brans A, Jacquamet L, Ferrer JL, Sauvage E, Dehareng D, Frère JM, Charlier P, Galleni M, Kerff F. 2009. Critical role of tryptophan 154 for the activity and stability of class D β-lactamases. Biochemistry 48:11252–11263.

453. Docquier JD, Calderone V, De Luca F, Benvenuti M, Giuliani F, Bellucci L, Tafi A, Nordmann P, Botta M, Rossolini GM, Mangani S. 2009. Crystal Structure of the OXA-48 β-Lactamase Reveals Mechanistic Diversity among Class D Carbapenemases. Chem Biol 16:540–547.

454. Boo TW, Crowley B. 2009. Detection of blaOXA-58 and blaOXA-23-like genes in carbapenem-susceptible Acinetobacter clinical isolates: Should we be concerned? J Med Microbiol 58:839–841.

455. Higgins PG, Poirel L, Lehmann M, Nordmann P, Seifert H. 2009. OXA-143, a novel carbapenem-hydrolyzing class D β-lactamase in *Acinetobacter baumannii*. Antimicrob Agents Chemother 53:5035–5038.

456. Johnson JW, Gretes M, Goodfellow VJ, Marrone L, Heynen ML, Strynadka NCJ, Dmitrienko GI. 2010. Cyclobutanone analogues of β-lactams revisited: Insights into conformational requirements for inhibition of serine- and metallo-β- lactamases. J Am Chem Soc 132:2558–2560.

457. Vercheval L, Bauvois C, di Paolo A, Borel F, Ferrer J-L, Sauvage E, Matagne A, Frère J-M, Charlier P, Galleni M, Kerff F. 2010. Three factors that modulate the activity of class D β-lactamases and interfere with the post-translational carboxylation of Lys ^{70}. Biochem J 432:495–506.

458. Docquier JD, Benvenuti M, Calderone V, Giuliani F, Kapetis D, De Luca F, Rossolini GM, Mangani S. 2010. Crystal structure of the narrow-spectrum OXA-46 class D ??-lactamase: Relationship between active-site lysine carbamylation and inhibition by polycarboxylates. Antimicrob Agents Chemother 54:2167–2174.

459. Figueiredo S, Poirel L, Seifert H, Mugnier P, Benhamou D, Nordmann P. 2010. OXA-134, a naturally occurring carbapenem-hydrolyzing class D β-lactamase from Acinetobacter lwoffii. Antimicrob Agents Chemother 54:5372–5375.

460. Karah N, Giske CG, Sundsfjord A, Samuelsen Ø. 2011. A Diversity of OXA-Carbapenemases and Class 1 Integrons Among Carbapenem-Resistant *Acinetobacter baumannii* Clinical Isolates from Sweden Belonging to Different International Clonal Lineages. Microb Drug Resist 17:545–549.

461. De Luca F, Benvenuti M, Carboni F, Pozzi C, Rossolini GM, Mangani S, Docquier J-D. 2011. Evolution to carbapenem-hydrolyzing activity in noncarbapenemase class D -lactamase OXA-10 by rational protein design. Proc Natl Acad Sci 108:18424–18429.

462. Schneider KD, Ortega CJ, Renck NA, Bonomo RA, Powers RA, Leonard DA. 2011. Structures of the class D carbapenemase OXA-24 from *Acinetobacter baumannii* in complex with doripenem. J Mol Biol 406:583–594.

463. de Figueiredo DQ, dos Santos KRN, Pereira EM, Schuenck RP, de Mendonça-Souza CRV, Teixeira LM, de Mondino SSB. 2011. First report of the blaOXA-58gene in a clinical isolate of *Acinetobacter baumannii* in rio de Janeiro, Brazil. Mem Inst Oswaldo Cruz 106:368–370.

464. Hocquet D, Colomb M, Dehecq B, Belmonte O, Courvalin P, Plésiat P, Meziane-Cherif D. 2011. Ceftazidime-hydrolysing β-lactamase OXA-145 with impaired hydrolysis of penicillins in *Pseudomonas aeruginosa*. J Antimicrob Chemother 66:1745–1750.

465. Poirel L, Castanheira M, Carrër A, Rodriguez CP, Jones RN, Smayevsky J, Nordmann P. 2011. OXA-163, an OXA-48-related class D β-lactamase with extended activity toward expanded-spectrum cephalosporins. Antimicrob Agents Chemother 55:2546–2551.

466. Sevillano E, Fernández E, Bustamante Z, Zabalaga S, Rosales I, Umaran A, Gallego L. 2012. Emergence and clonal dissemination of carbapenem-hydrolysing OXA-58-producing *Acinetobacter baumannii* isolates in Bolivia. J Med Microbiol 61:80–84.

467. Kaitany KCJ, Klinger N V., June CM, Ramey ME, Bonomo RA, Powers RA, Leonard DA. 2013. Structures of the class D carbapenemases OXA-23 and OXA-146: Mechanistic

basis of activity against carbapenems, extended-spectrum cephalosporins, and aztreonam. Antimicrob Agents Chemother 57:4848–4855.

468. Smith CA, Antunes NT, Stewart NK, Toth M, Kumarasiri M, Chang M, Mobashery S, Vakulenko SB. 2013. Structural basis for carbapenemase activity of the OXA-23 β-Lactamase from *Acinetobacter baumannii*. Chem Biol 20:1107–1115.

469. Higgins PG, Pérez-Llarena FJ, Zander E, Fernández A, Bou G, Seifert H. 2013. OXA-235, a novel class D β-lactamase involved in resistance to carbapenems in *Acinetobacter baumannii*. Antimicrob Agents Chemother 57:2121–2126.

470. Smith CA, Antunes NT, Toth M, Vakulenko SB. 2014. Crystal structure of carbapenemase OXA-58 from *Acinetobacter baumannii*. Antimicrob Agents Chemother 58:2135–2143.

471. Lahiri SD, Mangani S, Jahić H, Benvenuti M, Durand-Reville TF, De Luca F, Ehmann DE, Rossolini GM, Alm RA, Docquier J-D. 2015. Molecular Basis of Selective Inhibition and Slow Reversibility of Avibactam against Class D Carbapenemases: A Structure-Guided Study of OXA-24 and OXA-48. ACS Chem Biol 10:591–600.

472. King DT, King AM, Lal SM, Wright GD, Strynadka NCJ. 2016. Molecular Mechanism of Avibactam-Mediated β-Lactamase Inhibition. ACS Infect Dis 1:175–184.

473. Wu W, He Y, Lu J, Lu Y, Wu J, Liu Y. 2015. Transition of blaOXA-58-like to blaOXA-23-like in *Acinetobacter baumannii* clinical isolates in Southern China: An 8-year study. PLoS One 10(9):e0137174.

474. Saino H, Sugiyabu T, Ueno G, Yamamoto M, Ishii Y, Miyano M. 2015. Crystal Structure of OXA-58 with the Substrate-Binding Cleft in a Closed State: Insights into the Mobility and Stability of the OXA-58 Structure. PLoS One 10(12):e0145869.

475. Stojanoski V, Chow DC, Fryszczyn B, Hu L, Nordmann P, Poirel L, Sankaran B, Prasad BVV, Palzkill T. 2015. Structural basis for different substrate profiles of two closely related class D β-lactamases and their inhibition by halogens. Biochemistry 54:3370–3380.

476. Krasauskas R, Labeikyte D, Markuckas A, Povilonis J, Armalyte J, Plančiuniene R, Kavaliauskas P, Sužiedeliene E. 2015. Purification and characterization of a new β-

lactamase OXA-205 from *Pseudomonas aeruginosa*. Ann Clin Microbiol Antimicrob 14:1–8.

477. Staude MW, Leonard DA, Peng JW. 2016. Expanded Substrate Activity of OXA-24/40 in Carbapenem-Resistant *Acinetobacter baumannii* Involves Enhanced Binding Loop Flexibility. Biochemistry 55:6535–6544.

478. Mueck FG, Roesch S, Scherr M, Fischer F, Geyer L, Peschel O, Maxien D, Grabherr S, Wirth S. 2015. How low can we go in contrast-enhanced CT imaging of the chest?: A dose-finding cadaver study using the model-based iterative image reconstruction approach. Acad Radiol 22:345–356.

479. Pratap S, Katiki M, Gill P, Kumar P, Golemi-Kotra D. 2016. Active-site plasticity is essential to carbapenem hydrolysis by OXA-58 class D β-lactamase of *Acinetobacter baumannii*. Antimicrob Agents Chemother 60:75–86.

480. Meziane-Cherif D, Bonnet R, Haouz A, Courvalin P. 2016. Structural insights into the loss of penicillinase and the gain of ceftazidimase activities by OXA-145 β-lactamase in *Pseudomonas aeruginosa*. J Antimicrob Chemother 71:395–402.

481. Lohans CT, Wang DY, Jorgensen C, Cahill ST, Clifton IJ, McDonough MA, Oswin HP, Spencer J, Domene C, Claridge TDW, Brem J, Schofield CJ. 2017. 13C-Carbamylation as a mechanistic probe for the inhibition of class D β-lactamases by avibactam and halide ions. Org Biomol Chem 15:6024–6032.

482. Toth M, Smith CA, Antunes NT, Stewart NK, Maltz L, Vakulenko SB. 2017. The role of conserved surface hydrophobic residues in the carbapenemase activity of the class D β-lactamases. Acta Crystallogr Sect D Struct Biol 73:692–701.

483. Lund BA, Thomassen AM, Carlsen TJO, Leiros HKS. 2017. Structure, activity and thermostability investigations of OXA-163, OXA-181 and OXA-245 using biochemical analysis, crystal structures and differential scanning calorimetry analysis. Acta Crystallogr Sect FStructural Biol Commun 73:579–587.

484. Leungtongkam U, Thummeepak R, Wongprachan S, Thongsuk P, Kitti T, Ketwong K, Runcharoen C, Chantratita N, Sitthisak S. 2018. Dissemination of bla OXA-23 , bla OXA-

24 , bla OXA-58 , and bla NDM-1 Genes of *Acinetobacter baumannii* Isolates from Four Tertiary Hospitals in Thailand. Microb Drug Resist 24:55–62.

485. Lund BA, Thomassen AM, Nesheim BHB, Carlsen TJO, Isaksson J, Christopeit T, Leiros H-KS. 2018. The biological assembly of OXA-48 reveals a dimer interface with high charge complementarity and very high affinity. FEBS J 1-15.

486. Harper TM, June CM, Taracila MA, Bonomo RA, Powers RA, Leonard DA. 2018. Multiple substitutions lead to increased loop flexibility and expanded specificity in *Acinetobacter baumannii* carbapenemase OXA-239. Biochemical Journal 475:273–288.

487. Desjeux P. 1996. Leishmaniasis. Clin Dermatol 14:417–423.

488. Herwaldt BL. 1999. Leishmaniasis. Lancet 354:1191-1199.

489. Desjeux P. 2001. The increase in risk factors for leishmaniasis worldwide. Transactions of the royal society of tropical medicine and hygiene 95:239-243.

490. Hubálek Z. 2003. Emerging Human Infectious Diseases: Anthroponoses, Zoonoses, and Sapronoses. Emerg Infect Dis 9:403–404.

491. Desjeux P. 2004. Leishmaniasis: Current situation and new perspectives. Comp Immunol Microbiol Infect Dis 27:305–318.

492. Blasco Morente G, Rodríguez-Granger J, Tercedor Sánchez J, Latorre Fuentes JM. 2014. Old World Leishmaniasis on the Ear Lobe: A Rare Site. Actas Dermo-Sifiliográficas (English Ed) 105:628–630.

493. Burza S, Croft SL, Boelaert M. 2018. Leishmaniasis. Lancet 392:951–970.

494. Otranto D. 2018. Arthropod-borne pathogens of dogs and cats: From pathways and times of transmission to disease control. Vet Parasitol 251:68–77.

495. Rogers ME, Bates PA. 2007. Leishmania manipulation of sand fly feeding behavior results in enhanced transmission. PLoS Pathog 3:0818–0825.

496. Joshi RS, Joshi SR, Deepa T, Swapnil B. 2014. Visceral leishmaniasis - a case report. Online Int Interdiscip Res J 4:86–90.

497. Tanner CE. 1996. Immunobiology of visceral leishmaniasis. Clin Immunol Immunopathol 78:105–111.

498. Kirstein OD, Skrip L, Abassi I, Iungman T, Horwitz BZ, Gebresilassie A, Spitzova T, Waitz Y, Gebre-Michael T, Volf P, Hailu A, Warburg A. 2018. A fine scale eco-epidemiological study on endemic visceral leishmaniasis in north ethiopian villages. Acta Trop 183:64–77.

499. Shrestha M, Pandey BD, Maharjan J, Dumre SP, Tiwari PN, Manandhar K Das, Pun SB, Pandey K. 2018. Visceral leishmaniasis from a non-endemic Himalayan region of Nepal. Parasitol Res 117:2323–2326.

500. Stauch A, Sarkar RR, Picado A, Ostyn B, Sundar S, Rijal S, Boelaert M, Dujardin JC, Duerr HP. 2011. Visceral leishmaniasis in the indian subcontinent: Modelling epidemiology and control. PLoS Negl Trop Dis 5(11):e14055:1–12.

501. Poché DM, Grant WE, Wang HH. 2016. Visceral Leishmaniasis on the Indian Subcontinent: Modelling the Dynamic Relationship between Vector Control Schemes and Vector Life Cycles. PLoS Negl Trop Dis 10(8):e0004868:1–32.

502. Steverding D. 2017. The history of leishmaniasis. Parasites and Vectors 10:82:1–10.

503. Abdullah AYM, Dewan A, Shogib MRI, Rahman MM, Hossain MF. 2017. Environmental factors associated with the distribution of visceral leishmaniasis in endemic areas of Bangladesh: Modeling the ecological niche. Trop Med Health 45:1–15.

504. WHO. 2013. Leishmaniasis Burden Distribution.

505. Pigott DM, Bhatt S, Golding N, Duda KA, Battle KE, Brady OJ, Messina JP, Balard Y, Bastien P, Pratlong F, Brownstein JS, Freifeld CC, Mekaru SR, Gething PW, George DB, Myers MF, Reithinger R, Hay SI. 2014. Global distribution maps of the Leishmaniases. Elife 3:e02851:1–21.

506. Ready PD. 2014. Epidemiology of visceral leishmaniasis. Clinical Epidemiology 6:147–154.

507. Heras-Mosteiro J, Monge-Maillo B, Pinart M, Lopez Pereira P, Reveiz L, Garcia-Carrasco E, Campuzano Cuadrado P, Royuela A, Mendez Roman I, López-Vélez R. 2017.

Interventions for Old World cutaneous leishmaniasis. Cochrane Database Syst Rev 2017, Issue 12. Art. No.: CD005067.

508. Hooja S, Jindal A, Sharma B, Vyas N. 2014. First reported cases of diffuse cutaneous leishmaniasis in human immunodeficiency virus positive patients in Jaipur District of Rajasthan, India. Trop Parasitol 4(1):50-52.

509. El Alem MMM, Hakkour M, Hmamouch A, Halhali M, Delouane B, Habbari K, Fellah H, Sadak A, Sebti F. 2018. Risk factors and prediction analysis of cutaneous leishmaniasis due to *Leishmania tropica* in Southwestern Morocco. Infect Genet Evol 61:84–91.

510. Reithinger R, Dujardin J-C, Louzir H, Pirmez C, Alexander B, Brooker S. 2007. Cutaneous leishmaniasis. Lancet Infect Dis 7:581–96.

511. de Vries HJC, Reedijk SH, Schallig HDFH. 2015. Cutaneous Leishmaniasis: Recent Developments in Diagnosis and Management. Am J Clin Dermatol 16:99–109.

512. Sangueza OP, Sangueza JM, Stiller MJ, Sangueza P. 1993. Mucocutaneous leishmaniasis: A clinicopathologic classification. J Am Acad Dermatol 28:927–932.

513. Ahluwalia S, Lawn SD, Kanagalingam J, Grant H, Lockwood DNJ. 2004. Mucocutaneous leishmaniasis: an imported infection among travellers to central and South America. BMJ 329:842–844.

514. Palumbo E. 2010. Treatment strategies for mucocutaneous leishmaniasis. J Glob Infect Dis 2(2):147–150.

515. Diniz JLCP, Costa MO da R, Gonçalves DU. 2011. Mucocutaneous leishmaniasis: Clinical markers in presumptivediagnosis. Braz J Otorhinolaryngol 77:380–384.

516. Daulatabad D, Singal A, Dhawan A, Pandhi D, Sharma S. 2015. Mucocutaneous leishmaniasis caused by *Leishmania donovani* infection in an Indian man. Int J Dermatol 54:680–684.

517. Martínez DY, Verdonck K, Kaye PM, Adaui V, Polman K, Llanos-Cuentas A, Dujardin JC, Boelaert M. 2018. Tegumentary leishmaniasis and coinfections other than HIV. PLoS Negl Trop Dis 12:1–20.

518. Zijlstra EE, Musa AM, Khalil EAG, El Hassan IM, El-Hassan AM. 2003. Post-kala-azar dermal leishmaniasis. Lancet Infect Dis 3:87–98.

519. Rathi SK, Pandhi RK, Chopra P, Khanna N. 2005. Post-kala-azar dermal leishmaniasis: a histopathological study. Indian J Dermatol Venereol Leprol 71:250–253.

520. Ganguly S, Mukhopadhyay D, Das NK, Chaduvula M, Sadhu S, Chatterjee U, Rahman M, Goswami RP, Guha SK, Modak D, Mallik S, Gonju D, Pramanik N, Barbhuiya JN, Saha B, Chatterjee M. 2010. Enhanced lesional foxp3 expression and peripheral anergic lymphocytes indicate a role for regulatory T cells in indian post-kala-azar dermal leishmaniasis. J Invest Dermatol 130:1013–1022.

521. Zijlstra EE, Alvar J. 2012. The Post Kala-azar Dermal Leishmaniasis (PKDL) Atlas. A manual for health workers 1–216.

522. WHO. 2012. Post-kala-azar dermal leishmaniasis: a manual for case management and control. Report of a WHO consulative Meeting Kolkata, India.

523. Mukhopadhyay D, Dalton JE, Kaye PM, Chatterjee M. 2014. Post kala-azar dermal leishmaniasis: An unresolved mystery. Trends Parasitol 30:65–74.

524. Ganguly S, Saha P, Chatterjee M, Roy S, Ghosh TK, Guha SK, Kundu PK, Bera DK, Basu N, Maji AK. 2015. PKDL—A Silent Parasite Pool for Transmission of Leishmaniasis in Kala-azar Endemic Areas of Malda District, West Bengal, India. PLoS Negl Trop Dis 9(10):e0004138:1–13.

525. Trindade MAB, Silva LL da C, Braz LMA, Amato VS, Naafs B, Sotto MN. 2015. Post-kala-azar dermal leishmaniasis and leprosy: Case report and literature review. BMC Infect Dis 15:543:1–8.

526. Zijlstra EE. 2016. The immunology of post-kala-azar dermal leishmaniasis (PKDL). Parasites and Vectors 9:464:1–9.

527. Rock KS, Pandey A, Ndeffo-Mbah ML, Atkins KE, Lumbala C, Galvani A, Keeling MJ. 2017. Data-driven models to predict the elimination of sleeping sickness in former Equateur province of DRC. Epidemics 18:101–112.

528. Desjeux P, Piot B, O'Neill K, Meert JP. 2001. [Co-infections of leishmania/HIV in south Europe]. Med Trop (Mars). 61(2):187-93.

529. Ababa A. 2007. Report of the Fifth Consultative Meeting on Leishmania/HIV Coinfection. Ethiopia, 20–22 March 2007.

530. Alvar J, Aparicio P, Aseffa A, Den Boer M, Cañavate C, Dedet JP, Gradoni L, Ter Horst R, López-Vélez R, Moreno J. 2008. The relationship between leishmaniasis and AIDS: The second 10 years. Clin Microbiol Rev 21:334–359.

531. Demarchi IG, Silveira TGV, Ferreira ICP, Lonardoni MVC. 2012. Effect of HIV protease inhibitors on New World Leishmania. Parasitol Int 61:538–544.

532. Andreani G, Lodge R, Richard D, Tremblay MJ. 2012. Mechanisms of interaction between protozoan parasites and HIV. Curr Opin HIV AIDS 7(3):276–282.

533. Okwor I, Uzonna JE. 2013. The immunology of Leishmania/HIV co-infection. Immunol Res 56(1):163–171.

534. Van Griensven J, Diro E, Lopez-Velez R, Boelaert M, Lynen L, Zijlstra E, Dujardin JC, Hailu A. 2013. HIV-1 protease inhibitors for treatment of visceral leishmaniasis in HIV-co-infected individuals. Lancet Infect Dis 13:251–259.

535. Cota GF, de Sousa MR, de Mendonça ALP, Patrocinio A, Assunção LS, de Faria SR, Rabello A. 2014. Leishmania-HIV Co-infection: Clinical Presentation and Outcomes in an Urban Area in Brazil. PLoS Negl Trop Dis 8(4):e2816:1–7.

536. Zijlstra EE. 2014. PKDL and Other Dermal Lesions in HIV Co-infected Patients with Leishmaniasis: Review of Clinical Presentation in Relation to Immune Responses. PLoS Negl Trop Dis 8(11):e3258.

537. van Griensven J, Zijlstra EE, Hailu A. 2014. Visceral Leishmaniasis and HIV Coinfection: Time for Concerted Action. PLoS Negl Trop Dis 8(8):e3023:1–2.

538. Monge-Maillo B, Norman FF, Cruz I, Alvar J, López-Vélez R. 2014. Visceral Leishmaniasis and HIV Coinfection in the Mediterranean Region. PLoS Negl Trop Dis 8(8):e3021.

539. Lindoso JAL, Cunha MA, Queiroz IT, Moreira CHV. 2016. Leishmaniasis–HIV coinfection: Current challenges. HIV/AIDS - Res Palliat Care 8:147–156.

540. Coutinho JVSC, dos Santos FS, Ribeiro RDSP, Oliveira IBB, Dantas VB, Santos ABFS, Tauhata JR. 2017. Visceral leishmaniasis and Leishmaniasis-HIV coinfection: Comparative study. Rev Soc Bras Med Trop 50:670–674.

541. Leite de Sousa-Gomes M, Romero GAS, Werneck GL. 2017. Visceral leishmaniasis and HIV/AIDS in Brazil: Are we aware enough? PLoS Negl Trop Dis 11(9):e0005772:1–13.

542. Alvarenga DLR, Silva AH dos S, Fiuza JA, Gaze ST, de Oliveira JG, Oliveira RC, Calzavara-Silva CE, Pascoal-Xavier MA, Alves ÉAR. 2018. HIV aspartyl protease inhibitors modify the percentage of activated leukocytes, as well as serum levels of IL-17A and NO during experimental leishmaniasis. Int Immunopharmacol 60:179–188.

543. Quaresma PF, Murta SMF, de Castro Ferreira E, da Rocha-Lima ACVM, Xavier AAP, Gontijo CMF. 2009. Molecular diagnosis of canine visceral leishmaniasis: Identification of Leishmania species by PCR-RFLP and quantification of parasite DNA by real-time PCR. Acta Trop 111:289–294.

544. Leal GG de A, Carneiro M, Pinheiro A da C, Marques LA, Ker HG, Reis AB, Coura-Vital W. 2018. Risk profile for Leishmania infection in dogs coming from an area of visceral leishmaniasis reemergence. Prev Vet Med 150:1–7.

545. Paz GF, Rugani JMN, Marcelino AP, Gontijo CMF. 2018. Implications of the use of serological and molecular methods to detect infection by Leishmania spp. in urban pet dogs. Acta Trop 182:198–201.

546. Travi BL, Cordeiro-da-Silva A, Dantas-Torres F, Miró G. 2018. Canine visceral leishmaniasis: Diagnosis and management of the reservoir living among us. PLoS Negl Trop Dis 12:1–13.

547. Rogers ME, Ilg T, Nikolaev A V., Ferguson MAJ, Bates PA. 2004. Transmission of cutaneous leishmaniasis by sand flies is enhanced by regurgitation of fPPG. Nature 430:463–467.

548. Croft A, Taylor N, Rodenhurst K. 2006. Sandflies and leishmaniasis. Lancet 367:112.

549. Bates PA. 2008. Leishmania sand fly interaction: progress and challenges. Curr Opin Microbiol 11(4): 340–344.

550. Gálvez R, Descalzo MA, Miró G, Jiménez MI, Martín O, Dos Santos-Brandao F, Guerrero I, Cubero E, Molina R. 2010. Seasonal trends and spatial relations between environmental/meteorological factors and leishmaniosis sand fly vector abundances in Central Spain. Acta Trop 115:95–102.

551. Dostálová A, Volf P. 2012. Leishmania development in sand flies: Parasite-vector interactions overview. Parasites and Vectors 5:1–12.

552. Tiwary P, Kumar D, Singh RP, Rai M, Sundar S. 2012. Prevalence of Sand Flies and *Leishmania donovani* Infection in a Natural Population of Female *Phlebotomus argentipes* in Bihar State, India. Vector-Borne Zoonotic Dis 12:467–472.

553. Picado A, Dash AP, Bhattacharya S, Boelaert M. 2012. Vector control interventions for Visceral Leishmaniasis elimination initiative in South Asia, 2005-2010. Indian J Med Res 136:22–31.

554. Chowdhury R, Kumar V, Mondal D, Das ML, Das P, Dash AP, Kroeger A. 2016. Implication of vector characteristics of Phlebotomus argentipes in the kala-azar elimination programme in the Indian sub-continent. Pathog Glob Health 110:87–96.

555. Dhiman RC, Yadav RS. 2016. Insecticide resistance in phlebotomine sandflies in Southeast Asia with emphasis on the Indian subcontinent. Infect Dis Poverty 5:1–10.

556. Zorrilla V, De Los Santos MB, Espada L, Santos R del P, Fernandez R, Urquia A, Stoops CA, Ballard SB, Lescano AG, Vásquez GM, Valdivia HO. 2017. Distribution and identification of sand flies naturally infected with Leishmania from the Southeastern Peruvian Amazon. PLoS Negl Trop Dis 11(11):e0006029:1–14.

557. Poché DM, Garlapati RB, Mukherjee S, Torres-Poché Z, Hasker E, Rahman T, Bharti A, Tripathi VP, Prakash S, Chaubey R, Poché RM. 2018. Bionomics of Phlebotomus argentipes in villages in Bihar, India with insights into efficacy of IRS-based control measures. PLoS Negl Trop Dis 12(1):e0006168:1–20.

558. Wheeler RJ, Gluenz E, Gull K. 2011. The cell cycle of Leishmania: Morphogenetic events and their implications for parasite biology. Mol Microbiol 79:647–662.

559. Colmenares M, Kar S, Goldsmith-Pestana K, McMahon-Pratt D. 2002. Mechanisms of pathogenesis: differences amongst Leishmania species. Trans R Soc Trop Med Hyg 96:S3–S7.

560. Das NK, Sandhya S, Vishnu Vivek G, Kumar R, Singh AK, Bal SK, Kumari S, Mukhopadhyay CK. 2018. *Leishmania donovani* inhibits ferroportin translation by modulating FBXL5-IRP2 axis for its growth within host macrophages. Cell Microbiol 20:1–14.

561. Mahmoudzadeh-Niknam H, McKerrow JH. 2004. *Leishmania tropica*: Cysteine proteases are essential for growth and pathogenicity. Exp Parasitol 106:158–163.

562. Bañuls AL, Hide M, Prugnolle F. 2007. Leishmania and the Leishmaniases: A Parasite Genetic Update and Advances in Taxonomy, Epidemiology and Pathogenicity in Humans. Adv Parasitol 64: 1–109, 455–458.

563. Malla N, Mahajan RC. 2006. Pathophysiology of visceral leishmaniasis - Some recent concepts. Indian J Med Res 123:267–274.

564. Naderer T, McConville MJ. 2011. Intracellular growth and pathogenesis of *Leishmania* parasites. Essays Biochem 51:81–95.

565. Ameen M. 2010. Cutaneous leishmaniasis: Advances in disease pathogenesis, diagnostics and therapeutics. Clin Exp Dermatol 35:699–705.

566. Oghumu S, Natarajan G, Satoskar AR. 2015. Pathogenesis of Leishmaniasis in Humans. Parasit Infect 337–348.

567. Karimi A, Alborzi A, Amanati A. 2016. Visceral Leishmaniasis: An Update and Literature Review. Arch Pediatr Infect Dis. 4(3):e31612.

568. Suman SS, Amit A, Singh KP, Gupta P, Equbal A, Kumari A, Topno RK, Ravidas V, Pandey K, Bimal S, Das P, Ali V. 2018. Cytosolic tryparedoxin of *Leishmania donovani* modulates host immune response in visceral leishmaniasis. Cytokine 108:1–8.

569. Scott P, Novais FO. 2016. Cutaneous leishmaniasis: Immune responses in protection and pathogenesis. Nat Rev Immunol 16:581–592.

570. Loeuillet C, Bañuls AL, Hide M. 2016. Study of Leishmania pathogenesis in mice: Experimental considerations. Parasites and Vectors 9:1–12.

571. Masoudzadeh N, Mizbani A, Taslimi Y, Mashayekhi V, Mortazavi H, Sadeghipour P, Ardekani HM, Rafati S. 2017. *Leishmania tropica* infected human lesions: Whole genome transcription profiling. Acta Trop 176:236–241.

572. Alam MN, Chakraborti S, Paik D, Bagchi A, Chakraborti T. 2018. Functional attribution of LdISP, an endogenous serine protease inhibitor from *Leishmania donovani* in promoting infection. Biochimie 147:105–113.

573. Spath GF, Garraway LA, Turco SJ, Beverley SM. The role(s) of lipophosphoglycan (LPG) in the establishment of *Leishmania major* infections in mammalian hosts. PNAS 100(16):9536–9541.

574. Nylén S, Sacks D. 2007. Interleukin-10 and the pathogenesis of human visceral leishmaniasis. Trends Immunol 28:378–384.

575. Favila MA, Geraci NS, Jayakumar A, Hickerson S, Mostrom J, Turco SJ, Beverley SM, McDowell MA. 2015. Differential Impact of LPG-and PG-Deficient *Leishmania major* Mutants on the Immune Response of Human Dendritic Cells. PLoS Negl Trop Dis 9(12):e0004238:1–28.

576. Forestier C-L, Gao Q, Boons G-J. 2015. Leishmania lipophosphoglycan: how to establish structure-activity relationships for this highly complex and multifunctional glycoconjugate? Front Cell Infect Microbiol 4(193):1–7.

577. Leenders ACAP, Reiss P, Portegies P, Clezy K, Hop WCJ, Hoy J, Borleffs JCC, Allworth T, Kauffmann RH, Jones P, Kroon FP, Verbrugh HA, De Marie S. 1997. Liposomal amphotericin B (AmBisome) compared with amphotericin and both followed by oral fluconazole in the treatment of AIDS-associated cryptococcal meningitis. Aids 11:1463–1471.

578. Sundar S, Goyal AK, More DK, Singh MK, Murray HW. 1998. Treatment of antimony-unresponsive Indian visceral leishmaniasis with ultra-short courses of amphotericin-B-lipid complex. Ann Trop Med Parasitol 92:755–764.

579. Coukell AJ, Brogden RN. 1998. Liposomal amphotericin B: Therapeutic use in the management of fungal infections and visceral leishmaniasis. Drugs 55:585–612.

580. Sundar S, Rai M. 2002. Advances in the treatment of leishmaniasis. Curr Opin Infect Dis 15(6):593–598.

581. Sundar S, Jha TK, Thakur CP, Engel J, Sindermann H, Fischer C, Junge K, Bryceson A, Berman J. 2002. Oral Miltefosine for Indian Visceral Leishmaniasis. N Engl J Med 347:1739–1746.

582. Rosenthal E, Marty P. 2002. Treatment of visceral leishmaniasis: a review of current treatment practices. Expert Opin Pharmacother 3:1101–1108.

583. Berman J. 2003. Current treatment approaches to leishmaniasis. Curr Opin Infect Dis 16:397–401.

584. Sangraula H, Sharma KK, Rijal S, Dwivedi S, Koirala S. 2003. Orally effective drugs for kala-azar (visceral leishmaniasis): focus on miltefosine and sitamaquine. J Assoc Physicians India 51:686–690.

585. Rosenthal E, Marty P. 2013. Recent understanding in the treatment of visceral leishmaniasis. J Postgrad Med 49:61–8.

586. Murray HW. 2004. Progress in the treatment of a neglected infectious disease: Visceral leishmaniasis. Expert Rev Anti Infect Ther 2:279–292.

587. Berman J. 2005. Clinical status of agents being developed for leishmaniasis. Expert Opin Investig Drugs 14:1337–1346.

588. Murray HW. 2004. Treatment of visceral leishmaniasis in 2004. Am J Trop Med Hyg 71:787–794.

589. Dorlo TPC, Eggelte TA, Beijnen JH, de Vries PJ. 2006. [Miltefosine: a new remedy for leishmaniasis]. Miltefosine een nieuw Geneesm voor leishmaniasis 150:2697–2701.

590. Minodier P, Parola P. 2007. Cutaneous leishmaniasis treatment. Travel Med Infect Dis 5:150–158.

591. Minodier P, Noel G, Blanc P, Uters M, Retornaz K, Garnier JM. 2007. [Treatment of visceral leishmaniasis in children]. Med Trop (Mars) 67:73–78.

592. Gradoni L, Soteriadou K, Louzir H, Dakkak A, Toz SO, Jaffe C, Dedet JP, Campino L, Cañavate C, Dujardin JC. 2008. Drug regimens for visceral leishmaniasis in Mediterranean countries. Trop Med Int Heal 13:1272–1276.

593. Berman JD, Badaro R, Thakur CP, Wasunna KM, Behbehani K, Davidson R, Kuzoe F, Pang L, Weerasuriya K, Bryceson ADM. 1998. Efficacy and safety of liposomal amphotericin B (AmBisome) for visceral leishmaniasis in endemic developing countries. Bull World Health Organ 76:25–32.

594. Santos DO, Coutinho CER, Madeira MF, Bottino CG, Vieira RT, Nascimento SB, Bernardino A, Bourguignon SC, Corte-Real S, Pinho RT, Rodrigues CR, Castro HC. 2008. Leishmaniasis treatment - A challenge that remains: A review. Parasitol Res 103:1–10.

595. Palumbo E. 2008. Oral miltefosine treatment in children with visceral leishmaniasis: a brief review. Braz J Infect Dis 12:2–4.

596. Berman J (Josh). 2008. Treatment of leishmaniasis with miltefosine: 2008 status. Expert Opin Drug Metab Toxicol 4:1209–1216.

597. Al-Natour SH. 2009. Update in the treatment of cutaneous leishmaniasis. J Family Community Med 16(2):41–47.

598. Rosenthal E, Delaunay P, Jeandel PY, Haas H, Pomares-Estran C, Marty P. 2009. Liposomal amphotericin B as treatment for visceral leishmaniasis in Europe, 2009. Med Mal Infect 39(10):741–744.

599. Moen MD, Lyseng-Williamson KA, Scott LJ. 2009. Liposomal amphotericin B: A review of its use as empirical therapy in febrile neutropenia and in the treatment of invasive fungal infections. Drugs 69(3):361–392.

600. Frézard F, Demicheli C, Ribeiro RR. 2009. Pentavalent antimonials: New perspectives for old drugs. Molecules 14:2317–2336.

601. Olliaro P, Darley S, Laxminarayan R, Sundar S. 2009. Cost-effectiveness projections of single and combination therapies for visceral leishmaniasis in Bihar, India. Trop Med Int Heal 14:918–925.

602. Paila YD, Saha B, Chattopadhyay A. 2010. Amphotericin B inhibits entry of *Leishmania donovani* into primary macrophages. Biochem Biophys Res Commun 399:429–433.

603. Frézard F, Demicheli C. 2010. New delivery strategies for the old pentavalent antimonial drugs. Expert Opin Drug Deliv 7:1343–1358.

604. Palumbo E. 2010. Visceral leishmaniasis in children: a review. Minerva Pediatr. 62(4):389-95.

605. Murray HW. 2010. Treatment of visceral leishmaniasis in 2010: Direction from Bihar State, India. Future Microbiol 5:1301–1303.

606. Olliaro PL. 2010. Drug combinations for visceral leishmaniasis. Curr Opin Infect Dis 23:595–602.

607. Rybniker J, Goede V, Mertens J, Ortmann M, Kulas W, Kochanek M, Benzing T, Arribas JR, Fätkenheuer G. 2010. Treatment of visceral leishmaniasis with intravenous pentamidine and oral fluconazole in an HIV-positive patient with chronic renal failure - a case report and brief review of the literature. Int J Infect Dis 14:522–525.

608. Moore EM, Lockwood DN. 2010. Treatment of Visceral Leishmaniasis. J Glob Infect Dis. 2(2):151–158.

609. Boecken G, Sunderkötter C, Bogdan C, Weitzel T, Fischer M, Müller A, Löbermann M, Anders G, Von Stebut E, Schunk M, Burchard G, Grobusch M, Bialek R, Harms-Zwingenberger G, Fleischer B, Pietras M, Faulde M, Erkens K. 2011. Diagnosis and therapy of cutaneous and mucocutaneous Leishmaniasis in Germany. JDDG - (Suppl. 8): 1–51.

610. Shakya N, Sane SA, Shankar S, Gupta S. 2011. Effect of Pam3Cys induced protection on the therapeutic efficacy of miltefosine against experimental visceral leishmaniasis. Peptides 32:2131–2133.

611. Tiuman TS, Santos AO, Ueda-Nakamura T, Filho BPD, Nakamura CV. 2011. Recent advances in leishmaniasis treatment. Int J Infect Dis 15:e525–e532.

612. Stauch A, Sarkar RR, Picado A, Ostyn B, Sundar S, Rijal S, Boelaert M, Dujardin JC, Duerr HP. 2011. Visceral leishmaniasis in the indian subcontinent: Modelling epidemiology and control. PLoS Negl Trop Dis 5(11):e14055:1–12.

613. Sundar S, Sinha PK, Rai M, Verma DK, Nawin K, Alam S, Chakravarty J, Vaillant M, Verma N, Pandey K, Kumari P, Lal CS, Arora R, Sharma B, Ellis S, Strub-Wourgaft N, Balasegaram M, Olliaro P, Das P, Modabber F. 2011. Comparison of short-course multidrug treatment with standard therapy for visceral leishmaniasis in India: An open-label, non-inferiority, randomised controlled trial. Lancet 377:477–486.

614. Musa A, Khalil E, Hailu A, Olobo J, Balasegaram M, Omollo R, Edwards T, Rashid J, Mbui J, Musa B, Abuzaid AA, Ahmed O, Fadlalla A, El-Hassan A, Mueller M, Mucee G, Njoroge S, Manduku V, Mutuma G, Apadet L, Lodenyo H, Mutea D, Kirigi G, Yifru S, Mengistu G, Hurissa Z, Hailu W, Weldegebreal T, Tafes H, Mekonnen Y, Makonnen E, Ndegwa S, Sagaki P, Kimutai R, Kesusu J, Owiti R, Ellis S, Wasunna M. 2012. Sodium stibogluconate (ssg) and paromomycin combination compared to ssg for visceral leishmaniasis in east africa: A randomised controlled trial. PLoS Negl Trop Dis 6(6): e1674:1-10.

615. Nahidi Y, Maleki M, Tafaghodi M, Karimi G, Raftari S. 2012. Comparison of intralesional two percent zinc sulfate and glucantime injection in treatment of acute cutaneous leishmaniasis. Indian J Dermatol 57(2):118–122.

616. Freitas-Junior LH, Chatelain E, Kim HA, Siqueira-Neto JL. 2012. Visceral leishmaniasis treatment: What do we have, what do we need and how to deliver it? Int J Parasitol Drugs Drug Resist 2:11–19.

617. Hamill RJ. 2013. Amphotericin B formulations: A comparative review of efficacy and toxicity. Drugs 73:919–934.

618. Lezama-Dávila CM, Pan L, Isaac-Márquez AP, Terrazas C, Oghumu S, Isaac-Márquez R, Pech-Dzib M, Barbi J, Calomeni E, Parinandi N, Kinghorn AD, Satoskar AR. 2014. Pentalinon andrieuxii root extract is effective in the topical treatment of cutaneous leishmaniasis caused by *Leishmania mexicana*. Phyther Res 28:909–916.

619. Corral MJ, González-Sánchez E, Cuquerella M, Alunda JM. 2014. *In Vitro* synergistic effect of amphotericin B and allicin on *Leishmania donovani* and L. infantum. Antimicrob Agents Chemother 58:1596–1602.

620. Albergante L, Timmis J, Beattie L, Kaye PM. 2013. A Petri Net Model of Granulomatous Inflammation: Implications for IL-10 Mediated Control of *Leishmania donovani* Infection. PLoS Comput Biol 9(11):e1003334:1-13.

621. Pandey K, Singh D, Lal C, Das V, Das P. 2013. Fatal acute pancreatitis in a patient with visceral leishmaniasis during miltefosine treatment. J Postgrad Med 59(4):306-308.

622. Masmoudi A, Hariz W, Marrekchi S, Amouri M, Turki H. 2013. Old World cutaneous leishmaniasis: Diagnosis and treatment. J Dermatol Case Rep 7(2):31–41.

623. Corral MJ, González-Sánchez E, Cuquerella M, Alunda JM. 2014. *In Vitro* synergistic effect of amphotericin B and allicin on *Leishmania donovani* and L. infantum. Antimicrob Agents Chemother 58:1596–1602.

624. Nagle AS, Khare S, Kumar AB, Supek F, Buchynskyy A, Mathison CJN, Chennamaneni NK, Pendem N, Buckner FS, Gelb MH, Molteni V. 2014. Recent developments in drug discovery for leishmaniasis and human african trypanosomiasis. Chem Rev 114:11305–11347.

625. Bhattacharya SK, Dash AP. 2016. Treatment of visceral leishmaniasis: Options and choice. Lancet Infect Dis 16:142–143.

626. Dorlo TPC, Ostyn BA, Uranw S, Dujardin JC, Boelaert M. 2016. Treatment of visceral leishmaniasis: Pitfalls and stewardship. Lancet Infect Dis 16:777–778.

627. Sundar S, Singh A. 2016. Recent developments and future prospects in the treatment of visceral leishmaniasis. Ther Adv Infect Dis 3:98–109.

628. No JH. 2016. Visceral leishmaniasis: Revisiting current treatments and approaches for future discoveries. Acta Trop 155:113–123.

629. den Boer M, Davidson RN. 2006. Treatment options for visceral leishmaniasis. Expert Rev Anti Infect Ther 4:187–97.

630. Voak AA, Harris A, Qaiser Z, Croft SL, Seifert K. 2017. Treatment of experimental visceral leishmaniasis with single-dose liposomal amphotericin B – pharmacodynamics and biodistribution at different stages of disease. Antimicrob Agents Chemother 61. 00497-17.

631. Aronson N, Herwaldt BL, Libman M, Pearson R, Lopez-Velez R, Weina P, Carvalho E, Ephros M, Jeronimo S, Magill A. 2017. Diagnosis and treatment of leishmaniasis: Clinical practice guidelines by the infectious diseases society of America (IDSA) and the American Society of tropical medicine and hygiene (ASTMH). Am J Trop Med Hyg 96:24–45.

632. Jesus JA, Fragoso TN, Yamamoto ES, Laurenti MD, Silva MS, Ferreira AF, Lago JHG, Gomes GS, Passero LFD. 2017. Therapeutic effect of ursolic acid in experimental visceral leishmaniasis. Int J Parasitol Drugs Drug Resist 7:1–11.

633. Ansari MY, Dikhit MR, Sahoo GC, Ali V, Das P. 2017. Recent advancement and treatment of leishmaniasis based on pharmacoinformatics approach: Current and future outlook. Gene Reports 9:86–97.

634. Kimutai R, Musa AM, Njoroge S, Omollo R, Alves F, Hailu A, Khalil EAG, Diro E, Soipei P, Musa B, Salman K, Ritmeijer K, Chappuis F, Rashid J, Mohammed R, Jameneh A, Makonnen E, Olobo J, Okello L, Sagaki P, Strub N, Ellis S, Alvar J, Balasegaram M, Alirol E, Wasunna M. 2017. Safety and Effectiveness of Sodium Stibogluconate and Paromomycin Combination for the Treatment of Visceral Leishmaniasis in Eastern Africa: Results from a Pharmacovigilance Programme. Clin Drug Investig 37:259–272.

635. Rocha LG, Almeida JRGS, Macêdo RO, Barbosa-Filho JM. 2005. A review of natural products with antileishmanial activity. Phytomedicine 12:514–535.

636. Singh SK, Bimal S, Narayan S, Jee C, Bimal D, Das P, Bimal R. 2011. *Leishmania donovani*: Assessment of leishmanicidal effects of herbal extracts obtained from plants in the visceral leishmaniasis endemic area of Bihar, India. Exp Parasitol 127:552–558.

637. Sen R, Chatterjee M. 2011. Plant derived therapeutics for the treatment of Leishmaniasis. Phytomedicine 18:1056–1069.

638. Singh N, Mishra BB, Bajpai S, Singh RK, Tiwari VK. 2014. Natural product based leads to fight against leishmaniasis. Bioorganic Med Chem 22:18–45.

639. Machado M, Dinis AM, Santos-Rosa M, Alves V, Salgueiro L, Cavaleiro C, Sousa MC. 2014. Activity of Thymus capitellatus volatile extract, 1,8-cineole and borneol against Leishmania species. Vet Parasitol 200:39–49.

640. Jaafari MR, Behravan J, Abde-Emami J, Saghafi-Khadem F, Ramezani M. 2006. Evaluation of leishmanicidal effect of Euphorbia bungei Boiss extract by *in vitro* leishmanicidal assay using promastigotes of *Leishmania major*. Int J Pharmacol 2:569–573.

641. Akbarzadeh T, Sabourian R, Saeedi M, Rezaeizadeh H, Khanavi M, Ardekani MRS. 2015. Liver tonics: Review of plants used in Iranian traditional medicine. Asian Pac J Trop Biomed 5:170–181.

642. Dayakar A, Chandrasekaran S, Veronica J, Sundar S, Maurya R. 2015. *In vitro* and *in vivo* evaluation of anti-leishmanial and immunomodulatory activity of Neem leaf extract in *Leishmania donovani* infection. Exp Parasitol 153:45–54.

643. Ullah N, Nadhman A, Siddiq S, Mehwish S, Islam A, Jafri L, Hamayun M. 2016. Plants as Antileishmanial Agents: Current Scenario. Phyther Res 30:1905–1925.

644. Soosaraei M, Fakhar M, Hosseini Teshnizi S, Ziaei Hezarjaribi H, Banimostafavi ES. 2017. Medicinal plants with promising antileishmanial activity in Iran: a systematic review and meta-analysis. Ann Med Surg 21:63–80.

645. Odonne G, Houël E, Bourdy G, Stien D. 2017. Treating leishmaniasis in Amazonia: A review of ethnomedicinal concepts and pharmaco-chemical analysis of traditional treatments to inspire modern phytotherapies. J Ethnopharmacol 199:211–230.

646. Zahedifard F, Rafati S. 2018. Prospects for antimicrobial peptide-based immunotherapy approaches in Leishmania control. Expert Rev Anti Infect Ther 16:461–469.

647. Baranwal A, Chiranjivi AK, Kumar A, Dubey VK, Chandra P. 2018. Design of commercially comparable nanotherapeutic agent against human disease-causing parasite, Leishmania. Sci Rep 8(1):8814.

648. Bahar K, Dowlati Y, Shidani B, Alimohammadian MH, Khamesipour A, Ehsasi S, Hashemi-Feshariu R, Ale-Agha S, Modabber F. 1996. Comparative Safety and Immunogenicity Trial of Two Killed *Leishmania major* Vaccines With or Without BCG in Human Volunteers. Clinics in Dermatology 14:489-495.

649. Melby PC, Yang J, Zhao W, Perez LE, Cheng J. 2001. *Leishmania donovani* p36(LACK) DNA vaccine is highly immunogenic but not protective against experimental visceral leishmaniasis. Infect Immun 69(8):4719–4725.

650. Handman E. 2001. Leishmaniasis: Current status of vaccine development. Clin Microbiol Rev 14(2):229–243.

651. Misra A, Dube A, Srivastava B, Sharma P, Srivastava JK, Katiyar JC, Naik S. 2001. Successful vaccination against *Leishmania donovani* infection in Indian langur using alum-precipitated autoclaved *Leishmania major* with BCG. Vaccine 19:3485–3492.

652. Alimohammadian MH, Khamesipour A, Darabi H, Firooz A, Malekzadeh S, Bahonar A, Dowlati Y, Modabber F. 2002. The role of BCG in human immune responses induced by multiple injections of autoclaved *Leishmania major* as a candidate vaccine against leishmaniasis. Vaccine 21:174–180.

653. Kamil AA, Khalil EAG, Musa AM, Modabber F, Mukhtar MM, Ibrahim ME, Zijlstra EE, Sacks D, Smith PG, Zicker F, El-Hassan AM. 2003. Alum-precipitated autoclaved *Leishmania major* plus bacille Calmette-Guérrin, a candidate vaccine for visceral leishmaniasis: Safety, skin-delayed type hypersensitivity response and dose finding in healthy volunteers. Trans R Soc Trop Med Hyg 97:365–368.

654. Mendez S, Tabbara K, Belkaid Y, Bertholet S, Verthelyi D, Klinman D, Seder RA, Sacks DL. 2003. Coinjection with CpG-containing immunostimulatory oligodeoxynucleotides reduces the pathogenicity of a live vaccine against cutaneous leishmaniasis but maintains its potency and durability. Infect Immun 71:5121–5129.

655. Tewary P, Mehta J, Sukumaran B, Madhubala R. 2004. Vaccination with Leishmania soluble antigen and immunostimulatory oligodeoxynucleotides induces specific immunity and protection against *Leishmania donovani* infection. FEMS Immunol Med Microbiol 42:241–248.

656. Tewary P, Sukumaran B, Saxena S, Madhubala R. 2004. Immunostimulatory oligodeoxynucleotides are potent enhancers of protective immunity in mice immunized with recombinant ORFF leishmanial antigen. Vaccine 22:3053–3060.

657. Arora SK, Pal NS, Mujtaba S. 2005. *Leishmania donovani*: Identification of novel vaccine candidates using human reactive sera and cell lines. Exp Parasitol 109:163–170.

658. Kedzierski L, Zhu Y, Handman E. 2006. Leishmania vaccines: Progress and problems. Parasitology 133:S87–S112.

659. Garg R, Gupta SK, Tripathi P, Hajela K, Sundar S, Naik S, Dube A. 2006. *Leishmania donovani*: Identification of stimulatory soluble antigenic proteins using cured human and hamster lymphocytes for their prophylactic potential against visceral leishmaniasis. Vaccine 24:2900–2909.

660. Launois P, Tacchini-Cottier F, Kieny MP. 2008. Cutaneous leishmaniasis: Progress towards a vaccine. Expert Rev Vaccines 7:1277–1287.

661. Kumari S, Samant M, Khare P, Sundar S, Sinha S, Dube A. 2008. Induction of Th1-type cellular responses in cured/exposed Leishmania-infected patients and hamsters against polyproteins of soluble *Leishmania donovani* promastigotes ranging from 89.9 to 97.1 kDa. Vaccine 26:4813–4818.

662. Kumari S, Samant M, Misra P, Khare P, Sisodia B, Shasany AK, Dube A. 2008. Th1-stimulatory polyproteins of soluble *Leishmania donovani* promastigotes ranging from 89.9 to 97.1 kDa offers long-lasting protection against experimental visceral leishmaniasis. Vaccine 26:5700–5711.

663. Bhardwaj S, Vasishta RK, Arora SK. 2009. Vaccination with a novel recombinant Leishmania antigen plus MPL provides partial protection against L. donovani challenge in experimental model of visceral leishmaniasis. Exp Parasitol 121:29–37.

664. Kedzierski L, Sakthianandeswaren A, Curtis J, Andrews P, Junk P, Kedzierska K. 2009. Leishmaniasis: Current Treatment and Prospects for New Drugs and Vaccines. Curr Med Chem 16:599–614.

665. Kedzierski L. 2010. Leishmaniasis vaccine: Where are we today? J Glob Infect Dis 2(2):177–185.

666. Mizbani A, Taheri T, Zahedifard F, Taslimi Y, Azizi H, Azadmanesh K, Papadopoulou B, Rafati S. 2009. Recombinant Leishmania tarentolae expressing the A2 virulence gene as a novel candidate vaccine against visceral leishmaniasis. Vaccine 28:53–62.

667. da Silva RAA, Tavares NM, Costa D, Pitombo M, Barbosa L, Fukutani K, Miranda JC, de Oliveira CI, Valenzuela JG, Barral A, Soto M, Barral-Netto M, Brodskyn C. 2011. DNA vaccination with KMP11 and Lutzomyia longipalpis salivary protein protects hamsters against visceral leishmaniasis. Acta Trop 120:185–190.

668. Kedzierski L. 2011. Leishmaniasis. Human Vaccines 7(11):1204-1214.

669. Nagill R, Kaur S. 2011. Vaccine candidates for leishmaniasis: A review. Int Immunopharmacol 11:1464–1488.

670. Das A, Ali N. 2012. Vaccine development against *Leishmania donovani*. Front Immunol 3:1–19.

671. Datta S, Adak R, Chakraborty P, Haldar AK, Bhattacharjee S, Chakraborty A, Roy S, Manna M. 2012. Radio-attenuated leishmanial parasites as immunoprophylactic agent against experimental murine visceral leishmaniasis. Exp Parasitol 130:39–47.

672. Gupta R, Kushawaha PK, Tripathi CDP, Sundar S, Dube A. 2012. A novel recombinant *Leishmania donovani* p45, a partial coding region of methionine aminopeptidase, generates protective immunity by inducing a Th1 stimulatory response against experimental visceral leishmaniasis. Int J Parasitol 42:429–435.

673. Mahmood K, Akhter N, Eldeirawi K, Önal E, Christman JW, Carley DW, Herdegen JJ. 2009. Prevalence of type 2 diabetes in patients with obstructive sleep apnea in a multi-ethnic sample. J Clin Sleep Med 5:215–221.

674. Louzir H, Aoun K, Späth GF, Laouini D, Prina E, Victoir K, Bouratbine A. 2013. Leishmania epidemiology, diagnosis, chemotherapy and vaccination approaches in the international network of Pasteur Institutes. Med Sci (Paris). 29(12):1151–60.

675. Guha R, Gupta D, Rastogi R, Vikram R, Krishnamurthy G, Bimal S, Roy S, Mukhopadhyay A. 2013. Vaccination with leishmania hemoglobin receptor-encoding DNA protects against visceral leishmaniasis. Sci Transl Med 5(202):202ra121:1–11.

676. Rezvan H, Moafi M. 2015. An overview on Leishmania vaccines: A narrative review article. Vet Res forum 6(1):1–7.

677. Katebi A, Gholami E, Taheri T, Zahedifard F, Habibzadeh S, Taslimi Y, Shokri F, Papadopoulou B, Kamhawi S, Valenzuela JG, Rafati S. 2015. Leishmania tarentolae secreting the sand fly salivary antigen PpSP15 confers protection against *Leishmania major* infection in a susceptible BALB/c mice model. Mol Immunol 67:501–511.

678. Giersing BK, Dastgheyb SS, Modjarrad K, Moorthy V. 2016. Status of vaccine research and development of vaccines for *Staphylococcus aureus*. Vaccine 34:2962–2966.

679. Duthie MS, Pereira L, Favila M, Hofmeyer KA, Reed SJ, Metangmo S, Townsend S, Laurance JD, Picone A, Misquith A, Hossain F, Ghosh P, Khan MAA, Guderian J, Bailor HR, Liang H, Vergara J, Oliveira F, Howard RF, Kamhawi S, Mondal Di, Coler RN, Valenzuela JG, Reed SG. 2017. A defined subunit vaccine that protects against vector-borne visceral leishmaniasis. Vaccines 2(23):1–8.

680. Osman M, Mistry A, Keding A, Gabe R, Cook E, Forrester S, Wiggins R, Di Marco S, Colloca S, Siani L, Smith DF, Aebischer T, Kaye PM, Lacey CJ. 2017. A third generation vaccine for human visceral leishmaniasis and post kala azar dermal leishmaniasis: First-in-human trial of ChAd63-KH. PLoS Negl Trop Dis 11:1–24.

681. Müller KE, Solberg CT, Aoki JI, Floeter-Winter LM, Nerland AH. 2018. Developing a vaccine for leishmaniasis: How biology shapes policy. Tidsskr den Nor Laegeforening 138.

682. Haimeur A, Guimond C, Pilote S, Mukhopadhyay R, Rosen BP, Poulin R, Ouellette M. 1999. Elevated levels of polyamines and trypanothione resulting from overexpression of the ornithine decarboxylase gene in arsenite-resistant Leishmania. Molecular Microbiology 34(4):726–735.

683. Sundar S. 2001. Drug resistance in Indian visceral leishmaniasis. Tropical Medicine and International Health 6(11):849–854.

684. Croft SL. 2001. Monitoring drug resistance in leishmaniasis. Tropical Medicine and International Health 6(11):899–905.

685. Ouellette M, Drummelsmith J, Papadopoulou B. 2004. Leishmaniasis: Drugs in the clinic, resistance and new developments. Drug Resist Updat 7:257–266.

686. Croft SL, Sundar S, Fairlamb AH. 2006. Drug Resistance in Leishmaniasis. Clinical Microbiology Reviews 19(1):111–126.

687. Rojas R, Valderrama L, Valderrama M, Varona MX, Saravia NG, Saravia NG, Varona MX, Valderrama M, Ouellette M, Valderrama L. 2006. Resistance to Antimony and Treatment Failure in Human Leishmania (Viannia) Infection. J Infect Dis 193:1375–1383.

688. Janvier F, Morillon M, Olliaro P. 2008. Visceral leishmaniasis: clinical sensitivity and resistance to various therapeutic agents. Med Trop (Mars) 68(1):89–101.

689. Jhingran A, Chawla B, Saxena S, Barrett MP, Madhubala R. 2009. Paromomycin: Uptake and resistance in *Leishmania donovani*. Mol Biochem Parasitol 164:111–117.

690. Vélez ID, Colmenares LM, Muñoz CA. 2009. Two cases of visceral leishmaniasis in Colombia resistant to meglumine antimonial treatment. Rev Inst Med Trop Sao Paulo 51(4):231–236.

691. Purkait B, Kumar A, Nandi N, Sardar AH, Das S, Kumar S, Pandey K, Ravidas V, Kumar M, De T, Singh D, Das P. 2012. Mechanism of amphotericin B resistance in clinical isolates of *Leishmania donovani*. Antimicrob Agents Chemother 56:1031–1041.

692. de Melo EC, Fortaleza CMCB. 2013. Challenges in the Therapy of Visceral Leishmaniasis in Brazil: A Public Health Perspective. J Trop Med 2013:319234:1–5.

693. Ponte-Sucre A, Gamarro F, Dujardin JC, Barrett MP, López-Vélez R, García-Hernández R, Pountain AW, Mwenechanya R, Papadopoulou B. 2017. Drug resistance and treatment failure in leishmaniasis: A 21st century challenge. PLoS Negl Trop Dis 11(12):e0006052:1–24.

694. Singh J, Khan MI, Singh Yadav SP, Srivastava A, Sinha KK, Ashish, Das P, Kundu B. 2017. L-Asparaginase of *Leishmania donovani*: Metabolic target and its role in Amphotericin B resistance. Int J Parasitol Drugs Drug Resist 7:337–349.

695. Abhishek K, Sardar AH, Das S, Kumar A, Ghosh AK, Singh R, Saini S, Mandal A, Verma S, Kumar A, Purkait B, Dikhit MR, Das P. 2017. Phosphorylation of Translation Initiation Factor 2-Alpha in *Leishmania donovani* under Stress Is Necessary for Parasite Survival. Mol Cell Biol 37(1): e00344-16:1–19.

696. Rastrojo A, García-Hernández R, Vargas P, Camacho E, Corvo L, Imamura H, Dujardin JC, Castanys S, Aguado B, Gamarro F, Requena JM. 2018. Genomic and transcriptomic alterations in *Leishmania donovani* lines experimentally resistant to antileishmanial drugs. Int J Parasitol Drugs Drug Resist 8:246–264.

697. Alexander B, Maroli M. 2003. Control of phlebotomine sandflies. Med Vet Entomol 17:1–18.

698. Surendran SN, Karunaratne SHPP, Adamsn Z, Hemingway J, Hawkes NJ. 2005. Molecular and biochemical characterization of a sand fly population from Sri Lanka: evidence for insecticide resistance due to altered esterases and insensitive acetylcholinesterase. Bull Entomol Res 95:371–380.

699. Ostyn B, Vanlerberghe V, Picado A, Dinesh DS, Sundar S, Chappuis F, Rijal S, Dujardin JC, Coosemans M, Boelaert M, Davies C. 2008. Vector control by insecticide-treated nets in the fight against visceral leishmaniasis in the Indian subcontinent, what is the evidence? Trop Med Int Heal 13(8):1073–1085.

700. Hassan MM, Widaa SO, Osman OM, Numiary MSM, Ibrahim MA, Abushama HM. 2012. Insecticide resistance in the sand fly, Phlebotomus papatasi from Khartoum State, Sudan. Parasites and Vectors 5:46:1–10.

701. Joshi AB, Das ML, Akhter S, Chowdhury R, Mondal D, Kumar V, Das P, Kroeger A, Boelaert M, Petzold M. 2009. Chemical and environmental vector control as a contribution to the elimination of visceral leishmaniasis on the Indian subcontinent: Cluster randomized controlled trials in Bangladesh, India and Nepal. BMC Med 7:54:1–9.

702. Yaghoobi-Ershadi MR. 2016. Control of Phlebotomine Sand Flies in Iran : A Review Article. J Arthropod-Borne Dis 10(4):429–444.

703. Gomes B, Purkait B, Deb RM, Rama A, Singh RP, Foster GM, Coleman M, Kumar V, Paine M, Das P, Weetman D. 2017. Knockdown resistance mutations predict DDT

resistance and pyrethroid tolerance in the visceral leishmaniasis vector Phlebotomus argentipes. PLoS Negl Trop Dis 11(4):e0005504:1–14.

704. Chappuis F, Sundar S, Hailu A, Ghalib H, Rijal S, Peeling RW, Alvar J, Boelaert M. 2007. Visceral leishmaniasis: What are the needs for diagnosis, treatment and control? Nat Rev Microbiol 5:S7–S16.

705. Joshi AB, Narain JP, Prasittisuk C, Bhatia R, Hashim G, Jorge A, Banjara M, Kroeger A. 2008. Can visceral leishmaniasis be eliminated from Asia? J Vector Borne Dis 45:105–111.

706. Mondal D, Singh SP, Kumar N, Joshi A, Sundar S, Das P, Siddhivinayak H, Kroeger A, Boelaert M. 2009. Visceral leishmaniasis elimination programme in India, Bangladesh, and Nepal: Reshaping the case finding/case management strategy. PLoS Negl Trop Dis 3(1):e355:1–8.

707. Buckner FS, Waters NC, Avery VM. 2012. Recent highlights in anti-protozoan drug development and resistance research. Int J Parasitol Drugs Drug Resist 2:230–235.

708. Picado A, Dash AP, Bhattacharya S, Boelaert M. 2012. Vector control interventions for Visceral Leishmaniasis elimination initiative in South Asia, 2005-2010. Indian J Med Res 136:22–31.

709. Bhunia GS, Kesari S, Chatterjee N, Kumar V, Das P. 2013. The Burden of Visceral Leishmaniasis in India: Challenges in Using Remote Sensing and GIS to Understand and Control. Infectious Diseases 2013(675846):1–14.

710. Akbari M, Oryan A, Hatam G. 2017. Application of nanotechnology in treatment of leishmaniasis: A Review. Acta Trop 172:86–90.

711. Torres-Guerrero E, Quintanilla-Cedillo MR, Ruiz-Esmenjaud J, Arenas R. 2017. Leishmaniasis: a review. F1000Research 6:750:1-15.

712. Zijlstra EE, Alves F, Rijal S, Arana B, Alvar J. 2017. Post-kala-azar dermal leishmaniasis in the Indian subcontinent: A threat to the South-East Asia Region Kala-azar Elimination Programme. PLoS Negl Trop Dis 11:1–16.

713. Le Rutte EA, Chapman LAC, Coffeng LE, Jervis S, Hasker EC, Dwivedi S, Karthick M, Das A, Mahapatra T, Chaudhuri I, Boelaert MC, Medley GF, Srikantiah S, Hollingsworth TD, de Vlas SJ. 2017. Elimination of visceral leishmaniasis in the Indian subcontinent: a comparison of predictions from three transmission models. Epidemics 18:67–80.

714. Hirve S, Kroeger A, Matlashewski G, Mondal D, Banjara MR, Das P, Be-Nazir A, Arana B, Olliaro P. 2017. Towards elimination of visceral leishmaniasis in the Indian subcontinent—Translating research to practice to public health. PLoS Negl Trop Dis 11(10):e0005889:1–25.

715. Ram S. 2018. India's Contribution and Research Impact Leishmaniasis Research: A Bibliometric Analysis. J Scientometr Res 7(1):38–44.

716. Le Rutte EA, Chapman LAC, Coffeng LE, Ruiz-Postigo JA, Olliaro PL, Adams ER, Hasker EC, Boelaert MC, Hollingsworth TD, Medley GF, De Vlas SJ. 2018. Policy recommendations from transmission modeling for the elimination of visceral leishmaniasis in the indian subcontinent. Clin Infect Dis 66(S4):S301–S308.

717. Sundar S, Rai M. 2002. Laboratory diagnosis of visceral leishmaniasis. Clinical and Diagnostic Laboratory Immunology 9(5):951–958.

718. Schönian G, Nasereddin A, Dinse N, Schweynoch C, Schallig HDFH, Presber W, Jaffe CL. 2003. PCR diagnosis and characterization of Leishmania in local and imported clinical samples. Diagn Microbiol Infect Dis 47:349–358.

719. Reithinger R, Dujardin JC. 2007. Molecular diagnosis of leishmaniasis: Current status and future applications. J Clin Microbiol 45(1):21–25.

720. Vaish M, Mehrotra S, Chakravarty J, Sundar S. 2011. Noninvasive molecular diagnosis of human visceral leishmaniasis. J Clin Microbiol 49(5):2003–2005.

721. Srividya G, Kulshrestha A, Singh R, Salotra P. 2012. Diagnosis of visceral leishmaniasis: Developments over the last decade. Parasitol Res 110:1065–1078.

722. Matlashewski G, Das VNR, Pandey K, Singh D, Das S, Ghosh AK, Pandey RN, Das P. 2013. Diagnosis of Visceral Leishmaniasis in Bihar India: Comparison of the rK39 Rapid Diagnostic Test on Whole Blood Versus Serum. PLoS Negl Trop Dis 7(5):e2233:1–4.

723. De Ruiter CM, Van Der Veer C, Leeflang MMG, Deborggraeve S, Lucas C, Adams ER. 2014. Molecular tools for diagnosis of visceral leishmaniasis: Systematic review and meta-analysis of diagnostic test accuracy. J Clin Microbiol 52:3147–3155.

724. Abass E, Kang C, Martinkovic F, Semião-Santos SJ, Sundar S, Walden P, Piarroux R, El Harith A, Lohoff M, Steinhoff U. 2015. Heterogeneity of *Leishmania donovani* parasites complicates diagnosis of visceral leishmaniasis: Comparison of different serological tests in three endemic regions. PLoS One 10(3):e0116408:1–13.

725. Sakkas H, Gartzonika C, Levidiotou S. 2016. Laboratory diagnosis of human Visceral Leishmaniasis. J Vector Borne Dis 53:8–16.

726. Moreira OC, Yadon ZE, Cupolillo E. 2018. The applicability of real-time PCR in the diagnostic of cutaneous leishmaniasis and parasite quantification for clinical management: Current status and perspectives. Acta Trop 184:29–37.

727. Al-Jawabreh A, Dumaidi K, Ereqat S, Nasereddin A, Azmi K, Al-Jawabreh H, Al-Laham N, Abdeen Z. 2018. A comparison of the efficiency of three sampling methods for use in the molecular and conventional diagnosis of cutaneous leishmaniasis. Acta Trop 182:173–177.

728. Bangert M, Flores-Chávez MD, Llanes-Acevedo IP, Arcones C, Chicharro C, García E, Ortega S, Nieto J, Cruz I. 2018. Validation of rK39 immunochromatographic test and direct agglutination test for the diagnosis of Mediterranean visceral leishmaniasis in Spain. PLoS Negl Trop Dis 12(3):e0006277:1–12.

729. Anfossi L, Di Nardo F, Profiti M, Nogarol C, Cavalera S, Baggiani C, Giovannoli C, Spano G, Ferroglio E, Mignone W, Rosati S. 2018. A versatile and sensitive lateral flow immunoassay for the rapid diagnosis of visceral leishmaniasis. Anal Bioanal Chem 410:4123–4134.

730. Sundar S, Singh OP. 2018. Molecular Diagnosis of Visceral Leishmaniasis. Mol Diagnosis Ther 22:443–457.

731. Mukhtar M, Ali SS, Boshara SA, Albertini A, Monnerat S, Bessell P, Mori Y, Kubota Y, Ndung'u JM, Cruz I. 2018. Sensitive and less invasive confirmatory diagnosis of visceral

leishmaniasis in Sudan using loop-mediated isothermal amplification (LAMP). PLoS Negl Trop Dis 12(2):e0006264:1–14.

732. Drugs for Neglected Diseases initiative (DNDi) news letter No18. June 2009.

733. WHO Technical Report Series ; no. 949. Control of the leishmaniases. Report of a meeting of the WHO Expert Committee on the Control of Leishmaniases, Geneva, 22–26 March 2010.

734. Report of the sixth meeting of the WHO Strategic and Technical Advisory Group for Neglected Tropical Diseases (STAG-NTD). Salle D, WHO headquarters, Geneva, Switzerland, 29–30 April 2013.

735. Ghana Neglected Tropical Diseases Programme. Master plan. Five-year strategic plan, 2013-2017.

736. Nigeria Master Plan for Neglected Tropical Diseases (NTDs) 2013-2017. 22 March 2012.

737. Seddoh A, Onyeze A, Gyapong J, Holt J, Bundy D. 2013. Towards an Investment Case for Neglected Tropical Diseases: Including new analysis of the cost of intervening against preventable NTDs in sub-Saharan Africa.

738. Burki T. 2014. Vector borne disease: India's ambition to eliminate visceral leishmaniasis. With the introduction of a new drug, can the new government keep its promise to rid India of kala azar? BMJ 349:1–3.

739. Asian leishmaniac initiatives. Issue #1- 2015: summarized by KP Chang (11-15) from PI-provided Information. Worldleish: An International Congress on *Leishmania* and Leishmaniasis. International A. 2019. Worldleish 2013–2015.

740. Investing to overcome the global impact of neglected tropical diseases. Third WHO report on neglected tropical diseases 2015.

741. Accelerating progress on HIV, tuberculosis, malaria, hepatitis and neglected tropical diseases. A new agenda for 2016–2030.

742. Access to Medicine Index 2016.

743. WHO Weekly epidemiological record No 22, 2016, 91, 285–296.

744. World Health Organization. 2016. Process of validation of elimination of kala-azar as a public health problem in South-East Asia.

745. Neglected tropical diseases Visceral leishmaniasis : WHO publishes validation document as countries approach elimination 2016.

746. World Health Organization. 2016. Process of validation of elimination of kala-azar as a public health problem in South-East Asia.

747. Accelerated plan for Kala-azar elimination 2017. Directorate, National vector borne disease control programme.

748. WHO. 2014. Uniting to combat NTDs. Delivering on Promises and Driving Progress 2013.

749. WHO Weekly epidemiological record No 38, 2017, 92, 557–572.

750. Elimination of Kala-azar: Report of the Fourth Meeting of the Regional Technical Advisory Group (RTAG) Kathmandu, Nepal, 12 - 14 July 2011.

751. Davidson RN, Croft SL. 1993. Recent advances in the treatment of visceral leishmaniasis. Trans R Soc Trop Med Hyg 87(2):130–1, 141.

752. Berman JD. 1997. Human leishmaniasis: Clinical, diagnostic, and chemotherapeutic developments in the last 10 years. Clin Infect Dis 24:684–703.

753. Minodier P, Retornaz K, Horelt A, Garnier JM. 2003. Liposomal amphotericin B in the treatment of visceral leishmaniasis in immunocompromised patients. Fundamental and Clinical Pharmacology 17:183–188.

754. Maroli M, Khoury C. 2004. Prevention and control of leishmaniasis vectors: current approaches. Parassitologia. 46(1-2):211-215.

755. Singh S, Sivakumar R. 2004. Challenges and new discoveries in the treatment of leishmaniasis. J Infect Chemother 10:307–315.

756. Machado PRL, Ribeiro CS, França-Costa J, Dourado MEF, Trinconi CT, Yokoyama-Yasunaka JKU, Malta-Santos H, Borges VM, Carvalho EM, Uliana SRB. 2018.

Tamoxifen and meglumine antimoniate combined therapy in cutaneous leishmaniasis patients: a randomised trial. Trop Med Int Heal 23:936–942.

757. Gradoni L, Ascenzi P. 2004. Nitric oxide and anti-protozoan chemotherapy. Parassitologia 46(1-2):101–103.

758. Kafetzis DA, Velissariou IM, Stabouli S, Mavrikou M, Delis D, Liapi G. 2005. Treatment of paediatric visceral leishmaniasis: Amphotericin B or pentavalent antimony compounds? Int J Antimicrob Agents 25:26–30.

759. Frézard F, Demicheli C, Ribeiro RR. 2009. Pentavalent Antimonials: New Perspectives for Old Drugs. Molecules 14:2317-2336.

760. Neelagiri S, Kumar IS, Singh S. 2010. Tools for Antileishmanial Drug Discovery and Drug Development. Current research and information on pharmaceuticals sciences (CRIPS) 11(2):22-28.

761. Frézard F, Demicheli C. 2010. New delivery strategies for the old pentavalent antimonial drugs. Expert Opin Drug Deliv 7(12):1343–1358.

762. Seifert K. 2011. Structures, Targets and Recent Approaches in Anti-Leishmanial Drug Discovery and Development. Open Med Chem J 5:31–39.

763. Treiger Borborema SE, Schwendener RA, Osso Junior JA, De Andrade Junior HF, Do Nascimento N. 2011. Uptake and antileishmanial activity of meglumine antimoniate-containing liposomes in Leishmania (Leishmania) major-infected macrophages. Int J Antimicrob Agents 38:341–347.

764. Borborema SET, Osso JA, de Andrade HF, do Nascimento N. 2016. Antimonial drugs entrapped into phosphatidylserine liposomes: Physicochemical evaluation and antileishmanial activity. Rev Soc Bras Med Trop 49:196–203.

765. Reis LES, Fortes de Brito RC, Cardoso JM de O, Mathias FAS, Aguiar Soares RDO, Carneiro CM, de Abreu Vieira PM, Ramos GS, Frézard FJG, Roatt BM, Reis AB. 2017. Mixed Formulation of Conventional and Pegylated Meglumine Antimoniate-Containing Liposomes Reduces Inflammatory Process and Parasite Burden in Leishmania infantum-Infected BALB/c Mice. Antimicrob Agents Chemother 61(11):e00962-17:1–13.

766. Zulfiqar B, Shelper TB, Avery VM. 2017. Leishmaniasis drug discovery: recent progress and challenges in assay development. Drug Discov Today 22:1516–1531.

767. Borborema SET, Osso Junior JA, Tempone AG, de Andrade Junior HF, do Nascimento N. 2018. Pharmacokinetic of meglumine antimoniate encapsulated in phosphatidylserine-liposomes in mice model: A candidate formulation for visceral leishmaniasis. Biomed Pharmacother 103:1609–1616.

768. Castro RS, de Amorim IFG, Pereira RA, Silva SM, Pinheiro LJ, Pinto AJW, Azevedo EG, Demicheli C, Caliari MMV, Mosser DM, Michalick MSM, Frezard FJG, Tafuri WL. 2018. Hepatic fibropoiesis in dogs naturally infected with Leishmania (Leishmania) infantum treated with liposome-encapsulated meglumine antimoniate and allopurinol. Vet Parasitol 250:22–29.

769. Imming P, Sinning C, Meyer A. 2006. Drugs, their targets and the nature and number of drug targets. Nat Rev Drug Discov 5:821–834.

770. Spiro Z, Kovacs IA, Csermely P. 2008. Drug-therapy networks and the prediction of novel drug targets. J Biol 7:20:1-8.

771. Rask-Andersen M, Almén MS, Schiöth HB. 2011. Trends in the exploitation of novel drug targets. Nat Rev Drug Discov 10:579–590.

772. Guru PY, Agrawal AK, Singha UK, Singhal A, Gupta CM. 1989. Drug targeting in *Leishmania donovani* infections using tuftsin-bearing liposomes as drug vehicles. FEBS Lett 245:204–208.

773. Roberts SC, Tancer MJ, Polinsky MR, Michael Gibson K, Heby O, Ullman B. 2004. Arginase plays a pivotal role in polyamine precursor metabolism in Leishmania: Characterization of gene deletion mutants. J Biol Chem 279:23668–23678.

774. Opperdoes FR, Coombs GH. 2007. Metabolism of Leishmania: proven and predicted. Trends Parasitol 23:149–158.

775. McConville MJ, de Souza D, Saunders E, Likic VA, Naderer T. 2007. Living in a phagolysosome; metabolism of Leishmania amastigotes. Trends Parasitol 23(8):368–375.

776. Wanasen N, Soong L. 2008. L-arginine metabolism and its impact on host immunity against Leishmania infection. Immunol Res 41:15–25.

777. Chavali AK, Whittemore JD, Eddy JA, Williams KT, Papin JA. 2008. Systems analysis of metabolism in the pathogenic trypanosomatid *Leishmania major*. Mol Syst Biol 4:177:1-19.

778. Chawla B, Madhubala R. 2010. Drug targets in Leishmania. J Parasit Dis 34(1):1–13.

779. Brannigan JA, Smith BA, Yu Z, Brzozowski AM, Hodgkinson MR, Maroof A, Price HP, Meier F, Leatherbarrow RJ, Tate EW, Smith DF, Wilkinson AJ. 2010. N-myristoyltransferase from *Leishmania donovani*: structural and functional characterisation of a potential drug target for visceral leishmaniasis. J Mol Biol 396:985–999.

780. Pan J, Guo XM, Chen M, Tan X. 2008. A new method of electrocardiograph signals detection in remote monitoring. J Clin Rehabil Tissue Eng Res 12:1713–1715.

781. Duncan R, Gannavaram S, Dey R, Debrabant A, Lakhal-Naouar I, Nakhasi HL. 2011. Identification and Characterization of Genes Involved in *Leishmania* Pathogenesis: The Potential for Drug Target Selection. Mol Biol Int 428486:1–10.

782. Singh N, Kumar M, Singh RK. 2012. Leishmaniasis: Current status of available drugs and new potential drug targets. Asian Pac J Trop Med 5:485–497.

783. Rachidi N, Taly JF, Durieu E, Leclercq O, Aulner N, Prina E, Pescher P, Notredame C, Meijer L, Späth GF. 2014. Pharmacological assessment defines *Leishmania donovani* casein kinase 1 as a drug target and reveals important functions in parasite viability and intracellular infection. Antimicrob Agents Chemother 58:1501–1515.

784. Walkinshaw M. 2014. Multiple chemical scaffolds inhibit a promising Leishmania drug target. IUCrJ 1:202–203.

785. Capasso C, Supuran CT. 2015. Bacterial, fungal and protozoan carbonic anhydrases as drug targets. Expert Opin Ther Targets 19(12):1689-704.

786. Vermelho AB, Capaci GR, Rodrigues IA, Cardoso VS, Mazotto AM, Supuran CT. 2017. Carbonic anhydrases from Trypanosoma and Leishmania as anti-protozoan drug targets. Bioorganic Med Chem 25:1543–1555.

787. Kieffer C, Cohen A, Verhaeghe P, Paloque L, Hutter S, Castera-Ducros C, Laget M, Rault S, Valentin A, Rathelot P, Azas N, Vanelle P. 2015. Antileishmanial pharmacomodulation in 8-nitroquinolin-2(1H)-one series. Bioorganic Med Chem 23:2377–2386.

788. Das M, Saha G, Saikia AK, Dubey VK. 2015. Novel agents against miltefosine-unresponsive *Leishmania donovani*. Antimicrob Agents Chemother 59:7826–7829.

789. Guillon J, Cohen A, Das RN, Boudot C, Gueddouda NM, Moreau S, Ronga L, Savrimoutou S, Basmaciyan L, Tisnerat C, Mestanier S, Rubio S, Amaziane S, Dassonville-Klimpt A, Azas N, Courtioux B, Mergny JL, Mullié C, Sonnet P. 2018. Design, synthesis, and antiprotozoal evaluation of new 2,9-bis[(substituted-aminomethyl)phenyl]-1,10-phenanthroline derivatives. Chem Biol Drug Des 91:974–995.

790. Tonelli M, Gabriele E, Piazza F, Basilico N, Parapini S, Tasso B, Loddo R, Sparatore F, Sparatore A. 2018. Benzimidazole derivatives endowed with potent antileishmanial activity. J Enzyme Inhib Med Chem 33:210–226.

791. Shokri A, Akhtari J, Keighobadi M, Fakhar M, Teshnizi SH, Emami S, Sadjjadian S. 2017. Promising antileishmanial effectiveness of doxorubicin and Doxil against *Leishmania major*: An *in vitro* assay. Asian Pac J Trop Med 10:544–548.

792. Chowdhury SR, Kumar A, Godinho JLP, De Macedo Silva ST, Zuma AA, Saha S, Kumari N, Rodrigues JCF, Sundar S, Dujardin JC, Roy S, De Souza W, Mukhopadhyay S, Majumder HK. 2017. Voacamine alters Leishmania ultrastructure and kills parasite by poisoning unusual bi-subunit topoisomerase IB. Biochem Pharmacol 138:19–30.

793. Mijiddorj B, Kaneda S, Sato H, Kitahashi Y, Javkhlantugs N, Naito A, Ueda K, Kawamura I. 2018. The role of D-allo-isoleucine in the deposition of the anti-Leishmania peptide bombinin H4 as revealed by ^{31}P solid-state NMR, VCD spectroscopy, and MD simulation. Biochim Biophys Acta - Proteins Proteomics 1866:789–798.

794. da Silva Cardoso V, Vermelho AB, Ricci Junior E, Almeida Rodrigues I, Mazotto AM, Supuran CT. 2018. Antileishmanial activity of sulphonamide nanoemulsions targeting the β-carbonic anhydrase from Leishmania species. J Enzyme Inhib Med Chem 33:850–857.

795. Nocentini A, Cadoni R, Dumy P, Supuran CT, Winum JY. 2018. Carbonic anhydrases from Trypanosoma cruzi and *Leishmania donovani* chagasi are inhibited by benzoxaboroles. J Enzyme Inhib Med Chem 33:286–289.

796. Romero AH, López SE, Rodríguez N, Oviedo H. 2018. Antileishmanial activity, structure-activity relationship of series of 2-(trifluoromethyl)benzo[*b*][1,8]naphthyridin-4(1*H*)-ones. Arch Pharm (Weinheim) 351:e1800094.

797. Fonseca-Berzal C, Ibáñez-Escribano A, Vela N, Cumella J, Nogal-Ruiz JJ, Escario JA, da Silva PB, Batista MM, Soeiro M de NC, Sifontes-Rodríguez S, Meneses-Marcel A, Gómez-Barrio A, Arán VJ. 2018. Antichagasic, Leishmanicidal, and Trichomonacidal Activity of 2-Benzyl-5-nitroindazole-Derived Amines. ChemMedChem 13:1246–1259.

798. Valdivieso E, Mejías F, Torrealba C, Benaim G, Kouznetsov V V., Sojo F, Rojas-Ruiz FA, Arvelo F, Dagger F. 2018. *In vitro* 4-Aryloxy-7-chloroquinoline derivatives are effective in mono- and combined therapy against *Leishmania donovani* and induce mitocondrial membrane potential disruption. Acta Trop 183:36–42.

799. Pedron J, Boudot C, Hutter S, Bourgeade-Delmas S, Stigliani JL, Sournia-Saquet A, Moreau A, Boutet-Robinet E, Paloque L, Mothes E, Laget M, Vendier L, Pratviel G, Wyllie S, Fairlamb A, Azas N, Courtioux B, Valentin A, Verhaeghe P. 2018. Novel 8-nitroquinolin-2(1H)-ones as NTR-bioactivated antikinetoplastid molecules: Synthesis, electrochemical and SAR study. Eur J Med Chem 155:135–152.

800. Tejería A, Pérez-Pertejo Y, Reguera RM, Balaña-Fouce R, Alonso C, González M, Rubiales G, Palacios F. 2018. Substituted 1,5-naphthyridine derivatives as novel antileishmanial agents. Synthesis and biological evaluation. Eur J Med Chem 152:137–147.

801. Upadhyay A, Kushwaha P, Gupta S, Dodda RP, Ramalingam K, Kant R, Goyal N, Sashidhara KV. 2018. Synthesis and evaluation of novel triazolyl quinoline derivatives as potential antileishmanial agents. Eur J Med Chem 154:172–181.

802. Chen KY, Liu AY-C. 1997. Biochemistry and Function of Hypusine Formation on Eukaryotic Initiation Factor 5A. Biological signals 6:105–109.

803. Park MH. 2006. The Post-Translational Synthesis of a Polyamine-Derived Amino Acid, Hypusine, in the Eukaryotic Translation Initiation Factor 5A (eIF5A). J Biochem 139(2):161–169.

804. Zanelli CF, Valentini SR. 2007. Is there a role for eIF5A in translation? Amino Acids 33:351–358.

805. Costa-Neto CM, Parreiras-e-Silva LT, Ruller R, Oliveira EB, Miranda A, Oliveira L, Ward RJ. 2006. Molecular modeling of the human eukaryotic translation initiation factor 5A (eIF5A) based on spectroscopic and computational analyses. Biochem Biophys Res Commun 347:634–640.

806. Kaiser AE, Gottwald AM, Wiersch CS, Maier WA, Seitz HM. 2003. Spermidine metabolism in parasitic protozoa - a comparison to the situation in prokaryotes, viruses, plants and fungi. Folia Parasitol (Praha) 50(1):3–18.

807. Tong Y, Park I, Hong B-S, Nedyalkova L, Tempel W, Park H-W. 2009. Crystal structure of human eIF5A1: Insight into functional similarity of human eIF5A1 and eIF5A2. Proteins Struct Funct Bioinforma 75:1040–1045.

808. Ober D, Harms R, Witte L, Hartmann T. 2003. Molecular Evolution by Change of Function : Alkaloid-specific homospermidine synthase retained all properties of deoxyhypusine synthase except binding the eIF5A precursor protein. J Biol Chem 278(15):12805–12812.

809. Lee YB, Joe YA, Wolff EC, Dimitriadis EK, Park MH. 1999. Complex formation between deoxyhypusine synthase and its protein substrate, the eukaryotic translation initiation factor 5A (eIF5A) precursor. Biochem. J. 340:273-281.

810. Kaiser A, Hammels I, Gottwald A, Nassar M, Zaghloul MS, Motaal BA, Hauber J, Hoerauf A. 2007. Modification of eukaryotic initiation factor 5A from Plasmodium vivax by a truncated deoxyhypusine synthase from *Plasmodium falciparum*: An enzyme with dual enzymatic properties. Bioorg Med Chem 15:6200–6207.

811. Umland TC, Wolff EC, Park MH, Davies DR. 2004. A New Crystal Structure of Deoxyhypusine Synthase Reveals the Configuration of the Active Enzyme and of an Enzyme·NAD·Inhibitor Ternary Complex. J Biol Chem 279(27):28697–28705.

812. Njuguna JT, Nassar M, Hoerauf A, Kaiser AE. 2006. Cloning, expression and functional activity of deoxyhypusine synthase from Plasmodium vivax. BMC Microbiol 6(91):1–7.

813. Chawla B, Jhingran A, Singh S, Tyagi N, Park MH, Srinivasan N, Roberts SC, Madhubala R. 2010. Identification and Characterization of a Novel Deoxyhypusine Synthase in *Leishmania donovani*. J Biol Chem 285(1):453–463.

814. Wolff EC, Lee SB, Park MH. 2011. Assay of Deoxyhypusine Synthase Activity. Methods Mol Biol. 720:195–205.

815. Kaiser A. 2012. Translational control of eIF5A in various diseases. Amino Acids 42:679–684.

816. Nguyen S, Jones DC, Wyllie S, Fairlamb AH, Phillips MA. 2013. Allosteric Activation of Trypanosomatid Deoxyhypusine Synthase by a Catalytically Dead Paralog. J Biol Chem 288:15256–15267.

817. Jakus J, Wolff EC, Park MH, Folk JE. 1993. Features of the spermidine-binding site of deoxyhypusine synthase as derived from inhibition studies: Effective inhibition by bis- and mono-guanylated diamines and polyamines. J Biol Chem 268:13151–13159.

818. Park MH, Wolff EC, Lee YB, Folk JE. 1994. Antiproliferative effects of inhibitors of deoxyhypusine synthase. J Biol Chem 269:27827–27832.

819. Lee YB, Park MH, Folk JE. 1995. Diamine and Triamine Analogs and Derivatives as Inhibitors of Deoxyhypusine Synthase: Synthesis and Biological Activity. J Med Chem 38:3053–3061.

820. Shi XP, Yin KC, Ahern J, Davis LJ, Stern AM, Waxman L. 1996. Effects of N1-guanyl-1,7-diaminoheptane, an inhibitor of deoxyhypusine synthase, on the growth of tumorigenic cell lines in culture. Biochim Biophys Acta - Mol Cell Res 1310:119–126.

821. Chen ZP, Yan YP, Ding QJ, Knapp S, Potenza JA, Schugar HJ, Chen KY. 1996. Effects of inhibitors of deoxyhypusine synthase on the differentiation of mouse neuroblastoma and erythroleukemia cells. Cancer Lett 105:233–239.

822. Lee YB, Folk JE. 1998. Branched-chain and unsaturated 1,7-Diaminoheptane derivatives as deoxyhypusine synthase inhibitors. Bioorg Med Chem 6:253–270.

823. Lee Y, Kim HK, Park HE, Park MH, Joe YA. 2002. Effect of N1-guanyl-1,7-diaminoheptane, an inhibitor of deoxyhypusine synthase, on endothelial cell growth, differentiation and apoptosis. Mol Cell Biochem. 237(1-2):69-76.

824. Park J-H, Wolff EC, Folk JE, Park MH. 2003. Reversal of the Deoxyhypusine Synthesis Reaction: Generation of Spermidine or Homospermidine from Deoxyhypusine by Deoxyhypusine Synthase. J Biol Chem 278(35):32683–32691.

825. Kaiser A, Gottwald A, Maier W, Seitz HM. 2003. Targeting enzymes involved in spermidine metabolism of parasitic protozoa? a possible new strategy for anti-parasitic treatment. Parasitol Res 91:508–516.

826. Specht S, Sarite SR, Hauber I, Hauber J, Görbig UF, Meier C, Bevec D, Hoerauf A, Kaiser A. 2008. The guanylhydrazone CNI-1493: an inhibitor with dual activity against malaria—inhibition of host cell pro-inflammatory cytokine release and parasitic deoxyhypusine synthase. Parasitol Res 102:1177–1184.

827. Abbruzzese A, Park MH, Folk JE. 1986. Deoxyhypusine hydroxylase from rat testis. Partial purification and characterization. J Biol Chem 261:3085–3089.

828. Csonga R, Ettmayer P, Auer M, Eckerskorn C, Eder J, Klier H. 1996. Evaluation of the metal ion requirement of the human deoxyhypusine hydroxylase from HeLa cells using a novel enzyme assay. FEBS Lett 380:209–214.

829. Clement PMJ, Hanauske-Abel HM, Wolff EC, Kleinman HK, Park MH. 2002. The antifungal drug ciclopirox inhibits deoxyhypusine and proline hydroxylation, endothelial cell growth and angiogenesis *in vitro*. Int J Cancer 100:491–498.

830. Kim YS, Kang KR, Wolff EC, Bell JK, McPhie P, Park MH. 2006. Deoxyhypusine Hydroxylase Is an Fe(II)-dependent, Heat-repeat Enzyme. J Biol Chem 281:13217–13225.

831. Park J-H, Aravind L, Wolff EC, Kaevel J, Kim YS, Park MH. 2006. Molecular cloning, expression, and structural prediction of deoxyhypusine hydroxylase: A HEAT-repeat-containing metalloenzyme. Proc Natl Acad Sci 103(1):51–56.

832. Kang KR, Kim YS, Wolff EC, Park MH. 2007. Specificity of the Deoxyhypusine Hydroxylase-Eukaryotic Translation Initiation Factor (eIF5A) Interaction. J Biol Chem 282:8300–8308.

833. Cano VSP, Jeon GA, Johansson HE, Henderson CA, Park J-H, Valentini SR, Hershey JWB, Park MH. 2008. Mutational analyses of human eIF5A-1 - identification of amino acid residues critical for eIF5A activity and hypusine modification. FEBS J 275:44–58.

834. Vu VV., Emerson JP, Martinho M, Kim YS, Munck E, Park MH, Que L. 2009. Human deoxyhypusine hydroxylase, an enzyme involved in regulating cell growth, activates O2 with a nonheme diiron center. Proc Natl Acad Sci 106(35):14814–14819.

835. Park JH, Wolff EC, Park MH. 2011. Assay of Deoxyhypusine Hydroxylase Activity. Methods Mol Biol. 720:207–216.

836. Chawla B, Kumar RR, Tyagi N, Subramanian G, Srinivasan N, Park MH, Madhubala R. 2012. A Unique Modification of the Eukaryotic Initiation Factor 5A Shows the Presence of the Complete Hypusine Pathway in *Leishmania donovani*. PLoS One 7(3):e33138:1-12.

837. Han Z, Sakai N, Böttger LH, Klinke S, Hauber J, Trautwein AX, Hilgenfeld R. 2015. Crystal Structure of the Peroxo-diiron(III) Intermediate of Deoxyhypusine Hydroxylase, an Oxygenase Involved in Hypusination. Structure 23:882–892.

838. Park MH, Cooper HL, Folk JE. 1982. The biosynthesis of protein-bound hypusine (N epsilon -(4-amino-2-hydroxybutyl)lysine). Lysine as the amino acid precursor and the intermediate role of deoxyhypusine (N epsilon -(4-aminobutyl)lysine). J Biol Chem 257(12):7217–22.

839. Abbruzzese A, Park MH, Beninati S, Folk JE. 1989. Inhibition of deoxyhypusine hydroxylase by polyamines and by a deoxyhypusine peptide. Biochim Biophys Acta - Protein Struct Mol Enzymol 997:248–255.

840. Abbruzzese A, Hanauske-Abel HM, Park MH, Henke S, Folk JE. 1991. The active site of deoxyhypusyl hydroxylase: use of catecholpeptides and their component chelator and peptide moieties as molecular probes. Biochim Biophys Acta - Protein Struct Mol Enzymol 1077:159–166.

841. Andrus L, Szabo P, Grady RW, Hanauske AR, Huima-Byron T, Slowinska B, Zagulska S, Hanauske-Abel HM. 1998. Antiretroviral effects of deoxyhypusyl hydroxylase inhibitors: a hypusine-dependent host cell mechanism for replication of human immunodeficiency virus type 1 (HIV-1). Biochem Pharmacol 55:1807–18.

842. Dong Z, Arnold RJ, Yang Y, Park MH, Hrncirova P, Mechref Y, Novotny M V., Zhang J-T. 2005. Modulation of Differentiation-related Gene 1 Expression by Cell Cycle Blocker Mimosine, Revealed by Proteomic Analysis. Mol Cell Proteomics 4:993–1001.

843. Hoque M, Hanauske-Abel HM, Palumbo P, Saxena D, D'Alliessi Gandolfi D, Park M, Pe'ery T, Mathews MB. 2009. Inhibition of HIV-1 gene expression by Ciclopirox and Deferiprone, drugs that prevent hypusination of eukaryotic initiation factor 5A. Retrovirology 6:90:1-17.

844. Kerscher B, Nzukou E, Kaiser A. 2010. Assessment of deoxyhypusine hydroxylase as a putative, novel drug target. Amino Acids 38:471–477.

845. von Koschitzky I, Kaiser A. 2013. Chemical profiling of deoxyhypusine hydroxylase inhibitors for antimalarial therapy. Amino Acids 45:1047–1053.

846. Lou B, Fan J, Wang K, Chen W, Zhou X, Zhang J, Lin S, Lv F, Chen Y. 2013. N1-guanyl-1,7-diaminoheptane (GC7) enhances the therapeutic efficacy of doxorubicin by inhibiting activation of eukaryotic translation initiation factor 5A2 (eIF5A2) and preventing the epithelial–mesenchymal transition in hepatocellular carcinoma cells. Exp Cell Res 319:2708–2717.

847. Atemnkeng VA, Pink M, Schmitz-Spanke S, Wu X-J, Dong L-L, Zhao K-H, May C, Laufer S, Langer B, Kaiser A. 2013. Deoxyhypusine Hydroxylase from Plasmodium vivax, the Neglected Human Malaria Parasite: Molecular Cloning, Expression and Specific Inhibition by the 5-LOX Inhibitor Zileuton. PLoS One 8(3):e58318:1-12.

848. von Koschitzky I, Gerhardt H, Lämmerhofer M, Kohout M, Gehringer M, Laufer S, Pink M, Schmitz-Spanke S, Strube C, Kaiser A. 2015. New insights into novel inhibitors against deoxyhypusine hydroxylase from *Plasmodium falciparum*: compounds with an iron chelating potential. Amino Acids 47:1155–1166.

849. Gupta N, Arora S, Kundra S. 2011. *Moraxella catarrhalis* as a respiratory pathogen. Indian J Pathol Microbiol 54(4):769–71.

850. Leone M, Honstettre A, Lepidi H, Capo C, Bayard F, Raoult D, Mege J-L. 2004. Effect of Sex on Coxiella burnetii Infection: Protective Role of 17β-Estradiol. J Infect Dis 189:339–345.

851. Giefing-Kröll C, Berger P, Lepperdinger G, Grubeck-Loebenstein B. 2015. How sex and age affect immune responses, susceptibility to infections, and response to vaccination. Aging Cell 14:309–321.

852. Roved J, Westerdahl H, Hasselquist D. 2017. Sex differences in immune responses: Hormonal effects, antagonistic selection, and evolutionary consequences. Horm Behav 88:95–105.

853. vom Steeg LG, Klein SL. 2016. SeXX Matters in Infectious Disease Pathogenesis. PLOS Pathog 12(2):e1005374:1-6.

854. Neyrolles O, Quintana-Murci L. 2009. Sexual Inequality in Tuberculosis. PLoS Med 6(12):e1000199:1-6.

855. Zuk M, McKean KA. 1996. Sex differences in parasite infections: Patterns and processes. Int J Parasitol 26:1009–1024.

856. vom Steeg LG, Klein SL. 2017. Sex Steroids Mediate Bidirectional Interactions Between Hosts and Microbes. Horm Behav 88:45–51.

857. Goodman M, Naiman DQ, LaKind JS. 2018. Systematic review of the literature on triclosan and health outcomes in humans. Crit Rev Toxicol 48:1–51.

858. Yueh M-F, Tukey RH. 2016. Triclosan: A Widespread Environmental Toxicant with Many Biological Effects. Annu Rev Pharmacol Toxicol 56:251–272.

859. Feng Y, Zhang P, Zhang Z, Shi J, Jiao Z, Shao B. 2016. Endocrine Disrupting Effects of Triclosan on the Placenta in Pregnant Rats. PLoS One 11:e0154758.

860. Wang C-F, Tian Y. 2015. Reproductive endocrine-disrupting effects of triclosan: Population exposure, present evidence and potential mechanisms. Environ Pollut 206:195–201.

861. Dinwiddie M, Terry P, Chen J. 2014. Recent Evidence Regarding Triclosan and Cancer Risk. Int J Environ Res Public Health 11:2209–2217.

862. Lee H, Hwang K, Nam K, Kim H, Choi K. 2014. Progression of Breast Cancer Cells Was Enhanced by Endocrine-Disrupting Chemicals, Triclosan and Octylphenol, via an

Estrogen Receptor-Dependent Signaling Pathway in Cellular and Mouse Xenograft Models. Chem Res Toxicol 27:834–842.

863. Axelstad M, Boberg J, Vinggaard AM, Christiansen S, Hass U. 2013. Triclosan exposure reduces thyroxine levels in pregnant and lactating rat dams and in directly exposed offspring. Food Chem Toxicol 59:534–540.

864. Roy JR, Chakraborty S, Chakraborty TR. 2009. Estrogen-like endocrine disrupting chemicals affecting puberty in humans-a review. Med Sci Monit 15(6):RA137-45.

865. Huang H, Du G, Zhang W, Hu J, Wu D, Song L, Xia Y, Wang X. 2014. The *in vitro* estrogenic activities of triclosan and triclocarban. J Appl Toxicol 34:1060–1067.

866. Gee RH, Charles A, Taylor N, Darbre PD. 2008. Oestrogenic and androgenic activity of triclosan in breast cancer cells. J Appl Toxicol 28:78–91.

867. Tanaka S, Hasegawa S, Hishinuma F, Kurata S. 1989. Estrogen can regulate the cell cycle in the early G1 phase of yeast by increasing the amount of adenylate cyclase mRNA. Cell 57:675–681.

868. Kumar V, Balomajumder C, Roy P. 2008. Disruption of LH-induced testosterone biosynthesis in testicular Leydig cells by triclosan: Probable mechanism of action. Toxicology 250:124–131.

869. Li H, Zhao Y, Chen L, Su Y, Li X, Jin L, Ge R-S. 2017. Triclocarban and Triclosan Inhibit Human Aromatase via Different Mechanisms. Biomed Res Int 2017(8284097):1–7.

870. Ci-qing Z. 1986. Nonlinear bendings of unsymmetrically layered anisotropic rectangular plates. Appl Math Mech 7:1063–1081.

871. Wang X, Chen X, Feng X, Chang F, Chen M, Xia Y, Chen L. 2016. Triclosan causes spontaneous abortion accompanied by decline of estrogen sulfotransferase activity in humans and mice. Sci Rep 5:18252.

872. Rowland SS, Falkler WA, Bashirelahi N. 1992. Identification of an estrogen-binding protein in *Pseudomonas aeruginosa*. J Steroid Biochem Mol Biol 42:721–7.

873. Sugarman B, Mummaw N. 1990. Oestrogen binding by and effect of oestrogen on trichomonads and bacteria. J Med Microbiol 32:227–232.

874. Madani ND, Malloy PJ, Rodriguez-Pombo P, Krishnan A V., Feldman D. 1994. *Candida albicans* estrogen-binding protein gene encodes an oxidoreductase that is inhibited by estradiol. Proc Natl Acad Sci 91:922–926.

875. Chopra S, Matsuyama K, Hutson C, Madrid P. 2011. Identification of antimicrobial activity among FDA-approved drugs for combating *Mycobacterium abscessus* and *Mycobacterium chelonae*. J Antimicrob Chemother 66:1533–1536.

876. Wira CR, Patel M V., Ghosh M, Mukura L, Fahey J V. 2011. Innate Immunity in the Human Female Reproductive Tract: Endocrine Regulation of Endogenous Antimicrobial Protection Against HIV and Other Sexually Transmitted Infections. Am J Reprod Immunol 65:196–211.

877. Fahey J V., Wright JA, Shen L, Smith JM, Ghosh M, Rossoll RM, Wira CR. 2008. Estradiol selectively regulates innate immune function by polarized human uterine epithelial cells in culture. Mucosal Immunol 1(4):317–325.

878. Medina-Estrada I, López-Meza JE, Ochoa-Zarzosa A. 2016. Anti-Inflammatory and Antimicrobial Effects of Estradiol in Bovine Mammary Epithelial Cells during *Staphylococcus aureus* Internalization. Mediators Inflamm 2016:1–16.

879. W Patt M, Conte L, Blaha M, J Plotkin B. 2018. Steroid hormones as interkingdom signaling molecules: Innate immune function and microbial colonization modulation. AIMS Mol Sci 5:117–130.

880. Sugarman B, Mummaw N. 1988. The Effect of Hormones on Trichomonas vaginalis. Journal of General Microbiology 134:1623–1628.

881. Otwinowski Z, Minor W. 1997. [20] Processing of X-ray diffraction data collected in oscillation mode. Methods in Enzymology 276:307–326.

882. Kabsch W. 2010. XDS. Acta Crystallogr Sect D Biol Crystallogr 66:125–132.

883. Vagin A, Teplyakov A. 2010. Molecular replacement with MOLREP. Acta Crystallogr Sect D Biol Crystallogr 66:22–25.

884. Long F, Vagin AA, Young P, Murshudov GN. 2008. BALBES : a molecular-replacement pipeline. Acta Crystallogr Sect D Biol Crystallogr 64:125–132.

885. Collaborative Computational Project N 4. 1994. The CCP4 suite: programs for protein crystallography. Acta Crystallogr Sect D Biol Crystallogr 50:760–763.

886. Winn MD, Ballard CC, Cowtan KD, Dodson EJ, Emsley P, Evans PR, Keegan RM, Krissinel EB, Leslie AGW, McCoy A, McNicholas SJ, Murshudov GN, Pannu NS, Potterton EA, Powell HR, Read RJ, Vagin A, Wilson KS. 2011. Overview of the CCP 4 suite and current developments. Acta Crystallogr Sect D Biol Crystallogr 67:235–242.

887. Murshudov GN, Skubák P, Lebedev AA, Pannu NS, Steiner RA, Nicholls RA, Winn MD, Long F, Vagin AA. 2011. REFMAC 5 for the refinement of macromolecular crystal structures. Acta Crystallogr Sect D Biol Crystallogr 67:355–367.

888. Adams PD, Afonine P V., Bunkóczi G, Chen VB, Davis IW, Echols N, Headd JJ, Hung L-W, Kapral GJ, Grosse-Kunstleve RW, McCoy AJ, Moriarty NW, Oeffner R, Read RJ, Richardson DC, Richardson JS, Terwilliger TC, Zwart PH. 2010. PHENIX : a comprehensive Python-based system for macromolecular structure solution. Acta Crystallogr Sect D Biol Crystallogr 66:213–221.

889. Echols N, Grosse-Kunstleve RW, Afonine P V., Bunkóczi G, Chen VB, Headd JJ, McCoy AJ, Moriarty NW, Read RJ, Richardson DC, Richardson JS, Terwilliger TC, Adams PD. 2012. Graphical tools for macromolecular crystallography in PHENIX. J Appl Crystallogr 45:581–586.

890. Emsley P, Cowtan K. 2004. Coot : model-building tools for molecular graphics. Acta Crystallogr Sect D Biol Crystallogr 60:2126–2132.

891. Davis IW, Leaver-Fay A, Chen VB, Block JN, Kapral GJ, Wang X, Murray LW, Arendall WB, Snoeyink J, Richardson JS, Richardson DC. 2007. MolProbity: all-atom contacts and structure validation for proteins and nucleic acids. Nucleic Acids Res 35:W375–W383.

892. Sievers F, Wilm A, Dineen D, Gibson TJ, Karplus K, Li W, Lopez R, McWilliam H, Remmert M, Soding J, Thompson JD, Higgins DG. 2011. Fast, scalable generation of high-quality protein multiple sequence alignments using Clustal Omega. Mol Syst Biol 7:539:1–6.

893. McWilliam H, Li W, Uludag M, Squizzato S, Park YM, Buso N, Cowley AP, Lopez R. 2013. Analysis Tool Web Services from the EMBL-EBI. Nucleic Acids Res 41:W597–W600.

894. Li W, Cowley A, Uludag M, Gur T, McWilliam H, Squizzato S, Park YM, Buso N, Lopez R. 2015. The EMBL-EBI bioinformatics web and programmatic tools framework. Nucleic Acids Res 43:W580–W584.

895. Robert X, Gouet P. 2014. Deciphering key features in protein structures with the new ENDscript server. Nucleic Acids Res 42:W320–W324.

896. The PyMOL Molecular Graphics System, Version 1.3 Schrödinger, LLC.

897. Dassault Systèmes BIOVIA, Discovery Studio, 4.5, San Diego: Dassault Systèmes, 2015.

898. Pettersen EF, Goddard TD, Huang CC, Couch GS, Greenblatt DM, Meng EC, Ferrin TE. 2004. UCSF Chimera–A visualization system for exploratory research and analysis. J Comput Chem 25:1605–1612.

899. Holm L, Rosenstrom P. 2010. Dali server: conservation mapping in 3D. Nucleic Acids Res 38:W545–W549.

900. Holm L, Laakso LM. 2016. Dali server update. Nucleic Acids Res 44:W351–W355.

901. Krissinel E, Henrick K. 2007. Inference of Macromolecular Assemblies from Crystalline State. J Mol Biol 372:774–797.

902. Morris GM, Huey R, Lindstrom W, Sanner MF, Belew RK, Goodsell DS, Olson AJ. 2009. AutoDock4 and AutoDockTools4: Automated docking with selective receptor flexibility. J Comput Chem 30:2785–2791.

903. Trott O, Olson AJ. 2010. AutoDock Vina: Improving the speed and accuracy of docking with a new scoring function, efficient optimization, and multithreading. J Comput Chem 31(2):455–461.

904. Al-Balas Q, Hassan M, Al-Oudat B, Alzoubi H, Mhaidat N, Almaaytah A. 2012. Generation of the First Structure-Based Pharmacophore Model Containing a Selective “Zinc Binding Group” Feature to Identify Potential Glyoxalase-1 Inhibitors. Molecules 17:13740–13758.

905. Arooj M, Sakkiah S, Kim S, Arulalapperumal V, Lee KW. 2013. A Combination of Receptor-Based Pharmacophore Modeling and amp; QM Techniques for Identification of Human Chymase Inhibitors. PLoS One 8:e63030.

906. Seidel T, Ibis G, Bendix F, Wolber G. 2010. Strategies for 3D pharmacophore-based virtual screening. Drug Discov Today Technol 7(4):e221–e228.

907. Napper AD, Sivendran S. 2011. Miniaturized High-Throughput Fluorescent Assay for Conversion of NAD(P)H to NAD(P). Curr Protoc Chem Biol. 3(2):790–795.

908. Moynié L, Hope AG, Finzel K, Schmidberger J, Leckie SM, Schneider G, Burkart MD, Smith AD, Gray DW, Naismith JH. 2016. A Substrate Mimic Allows High-Throughput Assay of the FabA Protein and Consequently the Identification of a Novel Inhibitor of *Pseudomonas aeruginosa* FabA. J Mol Biol 428:108–120.

909. Wayne P. 2016. Performance Standards for Antimicrobial Susceptibility Testing An informational supplement for global application developed through the Clinical and Laboratory Standards Institute.

910. Tawfick MM, El-borhamy MI. 2017. PCR-RFLP-Based Detection of Mutations in the Chromosomal Fluoroquinolone Targets gyrA and parC Genes of Acinetobacter baumanii Clinical Isolates from a Tertiary Hospital in Cairo, Egypt. American Journal of Microbiological Research 5(2):37-43.

911. Rich RL, Hoth LR, Geoghegan KF, Brown TA, LeMotte PK, Simons SP, Hensley P, Myszka DG. 2002. Kinetic analysis of estrogen receptor/ligand interactions. Proc Natl Acad Sci 99(13):8562–8567.

912. Abraham MJ, Murtola T, Schulz R, Páll S, Smith JC, Hess B, Lindahl E. 2015. GROMACS: High performance molecular simulations through multi-level parallelism from laptops to supercomputers. SoftwareX 1–2:19–25.

913. Roujeinikova A, Levy CW, Rowsell S, Sedelnikova S, Baker PJ, Minshull CA, Mistry A, Colls JG, Camble R, Stuitje AR, Slabas AR, Rafferty JB, Pauptit RA, Viner R, Rice DW. 1999. Crystallographic analysis of triclosan bound to enoyl reductase. J Mol Biol 294:527–535.

914. Payne DJ, Miller WH, Berry V, Brosky J, Burgess WJ, Chen E, DeWolf WE, Fosberry AP, Greenwood R, Head MS, Heerding DA, Janson CA, Jaworski DD, Keller PM, Manley PJ, Moore TD, Newlander KA, Pearson S, Polizzi BJ, Qiu X, Rittenhouse SF, Slater-Radosti C, Salyers KL, Seefeld MA, Smyth MG, Takata DT, Uzinskas IN, Vaidya K, Wallis NG, Winram SB, Yuan CCK, Huffman WF. 2002. Discovery of a Novel and Potent Class of FabI-Directed Antibacterial Agents. Antimicrob Agents Chemother 46(10):3118–3124.

915. Leenders F, Tesdorpf JG, Markus M, Engel T, Seedorf U, Adamski J. 1996. Porcine 80-kDa Protein Reveals Intrinsic 17-Hydroxysteroid Dehydrogenase, Fatty Acyl-CoA-hydratase/Dehydrogenase, and Sterol Transfer Activities. J Biol Chem 271(10):5438–5442.

916. Venkatesan R, Sah-Teli SK, Awoniyi LO, Jiang G, Prus P, Kastaniotis AJ, Hiltunen JK, Wierenga RK, Chen Z. 2014. Insights into mitochondrial fatty acid synthesis from the structure of heterotetrameric 3-ketoacyl-ACP reductase/3R-hydroxyacyl-CoA dehydrogenase. Nat Commun 5:4805.

917. Shafqat N, Marschall H-U, Filling C, Nordling E, Wu X-Q, Björk L, Thyberg J, Mårtensson E, Salim S, Jörnvall H, Oppermann U. 2003. Expanded substrate screenings of human and Drosophila type 10 17β-hydroxysteroid dehydrogenases (HSDs) reveal multiple specificities in bile acid and steroid hormone metabolism: characterization of multifunctional 3α/7α/7β/17β/20β/21-HSD. Biochem J 376:49–60.

918. Moon Y-A, Horton JD. 2003. Identification of Two Mammalian Reductases Involved in the Two-carbon Fatty Acyl Elongation Cascade. J Biol Chem 278(9):7335–7343.

919. Lukacik P, Keller B, Bunkoczi G, Kavanagh K, Hwa Lee W, Adamski J, Oppermann U. 2007. Structural and biochemical characterization of human orphan DHRS10 reveals a novel cytosolic enzyme with steroid dehydrogenase activity. Biochem J 402:419–427.

920. Persson B, Krook M, Jornvall H. 1991. Characteristics of short-chain alcohol dehydrogenases and related enzymes. Eur J Biochem 200:537–543.

921. Baker ME. 1995. Unusual evolution of 11β- and 17β-steroid and retinol dehydrogenases. BioEssays 18(1):63-70.

922. Benach J, Filling C, Oppermann UCT, Roversi P, Bricogne G, Berndt KD, Jörnvall H, Ladenstein R. 2002. Structure of Bacterial 3β/17β-Hydroxysteroid Dehydrogenase at 1.2 Å Resolution: A Model for Multiple Steroid Recognition. Biochemistry 41:14659–14668.

923. Baker ME. 1991. Genealogy of regulation of human sex and adrenal function, prostaglandin action, snapdragon and petunia flower colors, antibiotics, and nitrogen fixation: functional diversity from two ancestral dehydrogenases. Steroids 56:354–360.

924. Roe CR, Kaplan NO. 1969. Purification and substrate specificities of bacterial hydroxysteroid dehydrogenases. Biochemistry 8(12):5093–5103.

925. Yu Y, Liu C, Wang B, Li Y, Zhang H. 2015. Characterization of 3,17β-hydroxysteroid dehydrogenase in Comamonas testosteroni. Chem Biol Interact 234:221–228.

926. Kurakado S, Kurogane R, Sugita T. 2017. 17β-Estradiol inhibits estrogen binding protein-mediated hypha formation in *Candida albicans*. Microb Pathog 109:151–155.

927. Amirshahi A, Wan C, Beagley K, Latter J, Symonds I, Timms P. 2011. Modulation of the *Chlamydia trachomatis In vitro* transcriptome response by the sex hormones estradiol and progesterone. BMC Microbiol 11:150.

928. Chotirmall SH, Smith SG, Gunaratnam C, Cosgrove S, Dimitrov BD, O'Neill SJ, Harvey BJ, Greene CM, McElvaney NG. 2012. Effect of Estrogen on *Pseudomonas* Mucoidy and Exacerbations in Cystic Fibrosis. N Engl J Med 366:1978–1986.

929. Kumar S, Stecher G, Tamura K. 2016. MEGA7: Molecular Evolutionary Genetics Analysis Version 7.0 for Bigger Datasets. Mol Biol Evol. 33(7):1870-4.

930. Ishida T, Kinoshita K. 2007. PrDOS: prediction of disordered protein regions from amino acid sequence. Nucleic Acids Res 35:W460–W464.

931. Linding R, Jensen LJ, Diella F, Bork P, Gibson TJ, Russell RB. 2003. Protein disorder prediction: implications for structural proteomics. Structure 11(11):1453-9.

932. Linding R, Russell RB, Neduva V, Gibson TJ. 2003. GlobPlot: Exploring protein sequences for globularity and disorder. Nucleic Acids Res. 31(13):3701-8.

933. Gasteiger E, Hoogland C, Gattiker A, Duvaud S, Wilkins MR, Appel RD, Bairoch A. 2005. Protein Identification and Analysis Tools on the ExPASy Server. (In) John M. Walker (ed): The Proteomics Protocols Handbook, Humana Press (2005). pp. 571-607.

934. Sali A , Blundell TL. 1993. Comparative protein modelling by satisfaction of spatial restraints. J Mol Biol. 234(3):779-815.

935. Laskowski RA, MacArthur MW, Moss DS, Thornton JM. 1993. PROCHECK: a program to check the stereochemical quality of protein structures. J. Appl. Cryst. 26:283-291.

936. Colovos C1, Yeates TO. 1993. Verification of protein structures: patterns of nonbonded atomic interactions. Protein Sci. 9:1511-9.

937. Pontius J1, Richelle J, Wodak SJ. 1996. Deviations from standard atomic volumes as a quality measure for protein crystal structures. J Mol Biol. 264(1):121-36.

938. Bowie JU1, Lüthy R, Eisenberg D. 1991. A method to identify protein sequences that fold into a known three-dimensional structure. Science. 253(5016):164-70.

939. van Aalten DM1, Bywater R, Findlay JB, Hendlich M, Hooft RW, Vriend G. 1996. PRODRG, a program for generating molecular topologies and unique molecular descriptors from coordinates of small molecules. J Comput Aided Mol Des. 10(3):255-62.

940. Schüttelkopf AW1, van Aalten DM. 2004. PRODRG: a tool for high-throughput crystallography of protein-ligand complexes. Acta Crystallogr D Biol Crystallogr. 60(Pt 8):1355-63.